November 2023

AN INVESTIGATION OF THE ROLE OF AMYGDALAR CIRCUITS IN THE PRODUCTION OF SOCIAL BEHAVIOR

Joseph FD Dwyer
University of Massachusetts Amherst

AN INVESTIGATION OF THE ROLE OF AMYGDALAR CIRCUITS IN THE PRODUCTION OF SOCIAL BEHAVIOR

A Dissertation Presented

by

JOSEPH DWYER

Submitted to the Graduate School of the
University of Massachusetts Amherst in partial fulfillment
of the requirements for the degree of

DOCTOR OF PHILOSOPHY

September 2023

Neuroscience & Behavior Graduate Program

AN INVESTIGATION OF THE ROLE OF AMYGDALAR CIRCUITS IN THE PRODUCTION OF SOCIAL BEHAVIOR

A Dissertation Presented

by

JOSEPH DWYER

Approved as to style and content by:

_____
Joseph Bergan, Chair

_____
Luke Remage-Healey, Member

_____
Karine Fenelon, Member

_____
Stephanie Padilla, Member

_____
Luke Remage- Healey,
Graduate Program Director
Neuroscience and Behavior Program

DEDICATION

For my brother Phil, who helped me do everything except science.

ACKNOWLEDGMENTS

Thanks to the Bergan lab and to Dr. Bergan in particular, who believed in me enough to let an undergrad play around with tissue, high voltages, and dangerously strong magnets with little to no supervision. I also need to acknowledge the help and support of my committee and my wife. In particular my wife because if I don't, she will hit me.

I also want to thank my family who have always been very supportive of me, even when I told them in 2013 that I wouldn't get a job until 2023.

ABSTRACT

AN INVESTIGATION OF THE ROLE OF AMYGDALAR CIRCUITS IN THE PRODUCTION OF SOCIAL BEHAVIOR

SEPTEMBER 2023

JOSEPH DWYER, B.S., UNIVERSITY OF MASSACHUSETTS AMHERST

Ph.D., UNIVERSITY OF MASSACHUSETTS AMHERST

Directed by: Professor Joseph F. Bergan

Adaptive social behaviors allow animals to survive, thrive, and successfully reproduce. These behaviors, including mating, parenting, affiliation, and aggression, can be stereotyped in response to specific stimuli but often display sex-specific, and interoceptive-dependent variations in their execution. A conserved set of brain regions collectively known as the social behavior network (SBN) interprets sensory information about social cues and generates an appropriate behavioral response. In this dissertation I present 5 chapters. Chapter 1 introduces historical research focusing on the neural circuits that drive social behavior and the potential impact of environmental factors on the activity of these circuits. Chapter 2 describes a new technique that uses magnetohydrodynamic-based tissue clearing to investigate intact neural circuits rapidly and efficiently. Chapter 3 uses this approach to interrogate the synaptic connections of a primary hub for social sensory integration, the medial amygdala (MeA). I focused on neurons in the MeA that express an enzyme that plays an important role in the development of sex-specific social behaviors: aromatase and identified the sources of synaptic input to this population. These inputs included regions involved in maintaining metabolic homeostasis, production of socio-sexual behaviors, fear/anxiety, parenting, and aggressive behaviors –suggesting an expanded view of social behavior production. I demonstrate that the brain regions involved in the production of social behavior have broad access to internal physiological and external environmental information. Chapter 4, demonstrates the impact of external environmental factors on the behaviors produced in response to a social stimulus, as well as, on the early sensory representation of these stimuli in the AOB. Predator presence influences an animals' responses to conspecific stimuli even when not presented concurrently. This effect was observed in males and females and in response to male and female stimuli, demonstrating a generalizable impact of environmental conditions on the sensory representation of social stimuli. Chapter 5 summarizes these findings in a broader context, arguing for an expanded role for the SBN in integrating internal and external environmental information with sensory perceptions of social stimuli to produce appropriate behavioral response for not only a specific social stimulus, but a specific environmental context.

TABLE OF CONTENTS

Page

LIST OF TABLES

Table Page

LIST OF FIGURES

Figure Page

CHAPTER 1

INVESTIGATING THE ROLE OF THE MEA IN INTEGRATING ENVIRONMENTAL AND SENSORY INFORMATION TO DRIVE SOCIAL BEHAVIORS

Introduction

Adaptive social behaviors are produced in response to other animals, and in accord with an animal's internal physiological state and external environment (Newmann, et al., 1999; Iwasa, et al., 2018; Krebs and Kroodsma, 1980). For example, a malnourished mouse will engage in more risky foraging behaviors that would be maladaptive to a well-fed mouse (Padilla, et al., 2016). Starvation also changes aggressive and reproductive behaviors of a mouse (Iwasa, et al., 2018; Padilla, et al., 2016). Underlying this concept is the profound interconnections between areas of the brain that drive social behavior and those that work to determine internal homeostasis and environmental factors (Dwyer, et al., 2022). While social behaviors are produced in response to specific social stimuli, a complex, and interconnected network of brain regions work together to 'decide' whether a specific social behavior is appropriate for a given situation.

Neural circuits that mediate social behavior

Many species of animals rely on social interaction to increase their evolutionary fitness. Social behaviors allow animals to communicate necessary information within their own species, as well as between species throughout the animal kingdom (Darwin,

1871; Greene and Marler, 1979). This socio-sexual recognition is integral to reproductive, parental, and aggressive behaviors, and represents a fundamental set of behaviors in the animal kingdom (Darwin, 1871). These behaviors work collectively towards the goal of improving evolutionary fitness of the species (Tinbergen, 1951). While anatomical and physiological evolution can require hundreds of generations to adapt to a change in the environment, behavioral adaptation can occur within a single generation (Baier and Hoekstra, 1914). By selecting specifically for adaptive behaviors, environmental pressures can drive genetically similar animals to exhibit unique behaviors (Baier and Hoekstra, 1914). This allows animals that are otherwise indistinguishable to exhibit sometimes radical differences in behavior (Baier and Hoekstra, 1914).

Nearly all sensory systems have been linked to social behavior (Keller, et al., 2006a; 2006b; Pomerantz, et al., 1983; Contreras and Agmo, 1993; Strasser and Dixon, 1986). In the songbird, auditory signals are used to communicate species, individual identity, territorial ownership, and readiness to mate (Marler, 1961). In bats, echolocation is used to coordinate hunting and identify individual group members (Dina, et al., 2020). Mormyrid weakly electric fish use a technique called ‘electrolocation’ to identify conspecifics based on their distinct electrical signaling patterns (Worm, et al., 2018). In humans, visual cues produced in the face and hands provide information about another’s identity and emotional state (Haxby, et al., 2002). In mice, social behavior relies particularly strongly on chemosensory cues (Raisman, 1972; Winans and Scalia 1970). This broad utilization of sensory information to drive social interactions across even highly specialized sensory modalities highlights just how integral social behaviors are to survival.

Along with many other vertebrates, mice use a complex mix of semiochemicals, known as pheromones, to communicate social information and to produce social behaviors (Stowers, et al., 2002; Chamero, et al., 2007). For example, major urinary proteins produced by the male mouse are both necessary and sufficient to produce male-male-aggression (Chamero, et al., 2007; Stowers, et al., 2002). Similarly, the production of sulfated steroids in the urine of female mice is used to communicate the physiological status of the pheromone-producing animal to male and female conspecifics (Nodari, et al., 2008). These chemicals are endogenously produced in specialized glands that allow the mouse to secrete pheromones most commonly through their tears and in their urine (Stowers, et al., 2002; Chamero, et al., 2007). The level of production of many pheromones varies with the internal state of the mouse and along its development. Specifically, during puberty, a surge in sex-specific hormones drives a subsequent surge in the production of sex-specific pheromones (Stowers, et al., 2015; Ferrero, et al., 2013).

While it is tempting to view these chemicals as keys used to produce a single, specific behavior, the resultant behaviors also depend on the state of the animal receiving the signal. For example, a juvenile animal will not respond to sex-specific mating cues in the same way that an adult animal will. Likewise, a male animal will not respond to male specific pheromones the same way that a female will. These developmental and sex-specific responses are reliable and can be predictive of future behavior (Chamero, et al., 2007).

In the mouse, the vomeronasal organ (VNO) detects and transduces non-volatile pheromones (Dulac and Torello, 2003; Wysocki, 1981; Wysocki and Lepri, 1991). The VNO is a small cylindrical organ, the inner surface of which is covered in hundreds of

different types of vomeronasal receptor-expressing cells that recognize hundreds of individual pheromones and convert them into neural signals (Dulac and Torello, 2003).

The mouse VNO is organized into two layers, corresponding to the two major families of vomeronasal receptors. The apical layer expresses mainly V1R receptors, and the basal layer expresses mainly V2R receptors (Perez-Gomez, et al., 2014). While both receptor classes bind to pheromones, V1R receptors are more represented in circuits that drive social behavior, which suggests an outsized role for this subfamily in the production of social behavior (Hammen, et al., 2014; Isogai, et al., 2011).

Pheromone sensing cells in the VNO that express the same receptor subtype send excitatory projections to large neuropil-filled clusters known as glomeruli (Mombaerts, et al., 1996). These glomeruli aggregate individual pheromonal signals, which are then received individually or as groups of multiple receptor-expressing signals in individual mitral and tufted cells in the accessory olfactory bulb (AOB) (Del Punta, et al., 2002; Wagner, et al., 2006). Vomeronasal receptor segregation is maintained through the AOB as incoming projections from the apical layer are gathered in glomeruli in the anterior AOB, while incoming projections from the basal layer are gathered in glomeruli in the posterior AOB (Petrovich, et al., 2001). These glomeruli send these vomeronasal signals to the mitral and tufted cells in the mitral and tufted cell layer of the AOB (Petrovich, et al., 2001).

In the mouse these mitral and tufted cells provide the primary sensory input to a network of brain regions that is dedicated to executing social behaviors in all vertebrate species examined thus far (Goodson and Kingsbury, 2013; Newmann, et al., 1999;

O'Connell and Hofmann, 2012). First coined by Sarah Newman in 1999, the SBN grew out of an earlier concept known as the 'extended amygdala' (Newman, et al 1999; Olmos, et al., 1985). While elucidating the cellular makeup of the ventral forebrain of rats, they found a series of rings of very similar cells in the medial and central amygdala, bed nucleus of the stria terminalis, and substantia innominate (de Olmos, et al., 1985). It was hypothesized that the similarity of cell populations in these regions indicates a shared function (de Olmos, et al., 1985). While this hypothesis was largely speculatory, future research showed a similar organizational network of behaviorally relevant nuclei, the SBN (Newman, et al., 1999; Goodson and Kingsbury, 2013; O'Connell and Hofmann, 2012). Using the sexual behavior of the male rat it was found that a series of six highly interconnected nuclei displayed functional and anatomical continuity. This included not only specific stimulus responses, but also sexual dimorphisms in anatomy and behavioral correlates along with responses to endogenous hormones. The extended amygdala (including the medial amygdala and BNST), lateral septum (LS), medial preoptic area (mPOA), midbrain, anterior hypothalamus (AH), and ventromedial hypothalamus (VMH) work in concert to drive and maintain social behavior and are each required to produce appropriate social behavior (Goodson and Kingsbury, 2013; Newman, et al., 1999; O'Connell and Hofmann, 2012).

These regions, or homologous regions, are found in all vertebrates and play an outsized role in the modulating social behavior in animals including poison dart frogs (Fisher, et al., 2019), fish (Butler, et al., 2018), birds (Goodson, et al., 2005), and other mammalian species (Goodson and Kingsbury, 2013; Kollack-Walker, et al., 1997; O'Connell and Hofmann, 2012).

The MeA exhibits robust control over social behaviors and is required for an animal to engage in numerous social behaviors (Cooke, et al., 1999; Schwarz, et al., 2008: Unger, et al., 2015). A particularly robust example of this control is role that aromatase-expressing neurons in the MeA play in the production of aggressive behavior in males and females (Unger, et al., 2015; Padilla, et al., 2016). A single population of neurons in the MeA were shown to be necessary for intermale aggression in males and maternal aggression in females (Unger, et al., 2015). These two behaviors are sex-specific, indicating that the MeA plays an important role in the production of these sex-specific behaviors.

Indeed, when recording neural activity in the MeA of males and females, each sex displays different firing patterns to the same social stimulus (Bergan, et al., 2014). Most notably, the rate of firing of neurons in the MeA increases in response to pheromones from opposite sex conspecifics than same sex conspecifics, resulting in distinct firing patterns in each sex (Bergan, et al., 2014). Differential firing of MeA neurons depends on aromatase activity in those neurons, suggesting that aromatase expressing cells in the MeA may play an integral role in accurately recognizing and acting on the social information communicated by pheromones (Bergan, et al., 2014; Cooke, et al., 1999; Schwarz, et al., 2008).

The MeA contains the single largest population of aromatase-expressing neurons in the brain (Yao, et al., 2017). Aromatase is an enzyme which converts testosterone to estradiol. It plays a critical role in establishing sex-differences in neuroanatomy, physiology, and behavior in the developing brain and into adulthood (McCarthy, et al., 2017). Aromatase plays an integral role in driving sex-specific social behaviors such as

recognition, mating, parenting, and aggression behaviors (DeAngelis, et al., 2018; Huffman, et al., 2013; Pierman, et al., 2008).

As might be expected for a region that plays such an important role in driving sexually dimorphic social behaviors, the MeA displays structural, molecular, and functional sex differences (Nishizuka and Arai, 1981; Meredith and Fernandez-Fewell, 1994; Cooke et al., 1999; Bergan et al., 2014; Billing et al., 2020; Dwyer, et al., 2022). The male MeA occupies a larger volume of the brain compared the female and shows significantly greater dendritic innervation than females (Cooke, et al., 2007). This differentiation is driven by the presence of sex-specific neonatal hormones during development (Nishizuka and Arai, 1981). When we look closely at the circuits that send sensory information to the MeA, we see differences in the density and number of connections in males as opposed to females (Billing, et al., 2020). This sexual difference in connections between the AOB and MeA are conserved in projections to the MeA from many additional brain regions (Dwyer, et al., 2022). However, while the impact of these connections on the functioning of the MeA and production of social behavior is unclear, differences in behavioral responses are mirrored in the activity of the MeA neurons (Bergan, et al, 2014). These studies show markedly different responses in the MeA of males and females when the animals are presented with the same sensory stimuli (Bergan, et al., 2014).

If we are to understand how the MeA converts these inputs into behavioral responses, we must first understand what signals are being sent, and how these signals are sent to the MeA. New work has revealed the myriad connections received by the aromatase-expressing neurons in MeA. Indeed, the MeA receives signals from scores of

different sources throughout the brain (Dwyer, et al., 2022). This inputome of the aromatase-expressing population of cells in the MeA in males and females suggest complex circuitry for modulating social behavior and suggest a network of regional innervation that both mirrors and expands beyond the traditional SBN to the integration of environmental factors in the production of social behavior (Newman, et al., 1999).

Impacts of Internal and External state on social behavior

An animal's internal and external conditions can have a profound impact on their responses to a social stimulus. Ample food and safety from predators are critical for successful mating and parenting, and these behaviors are often suppressed if these conditions are not met. We see this impact throughout many additional social behaviors (Iwasa, et al., 2018; Krebs, 1980; Creel, et al., 2014; St-Cyr, et al., 2018). In starvation conditions animals will be less likely to engage in mounting behavior and more likely to undertake riskier foraging behaviors (Iwasa, et al., 2018; Krebs, 1980). And in high predation environments, animals modify their interactions with each other, spending more time in larger groups and much less time foraging (Creel, et al., 2014; St-Cyr, et al., 2018; Padilla, et al., 2016). Indeed, the impact of environmental factors on social behavior can involve the external environment and the internal physiology of the animal including parenting and aggressive status, previous experiences, and metabolic and sexual status.

Parenting and Aggression

Both parenting and aggression are integral social behaviors that an animal must engage in to ensure that their evolutionary fitness. While the methods of care and the

caregiver vary, parental care is observed in many vertebrates (Dulac, et al., 2014). Parental care can be defined as a prolonged period of non-reciprocal caregiving by either the male parent, female parent, or both (Kohl, et al., 2016). This period of caregiving greatly increases the odds of survival for the offspring and will often lead to future reproductive success (Numan, et al 2011). This is unique from the traditional transient social interactions between adults of a species as its benefits are purely unidirectional for the parent and can have a notable impact on the behavioral responses of the parent to other animals. In mice, parenting involves nest-building, nursing, grooming, crouching, carrying, and defense against potential threats to the pups (Kohl, et al., 2016). The onset of these behaviors is dependent on a surge of hormones that is driven by pregnancy or close interaction with an actively maternal dam (Numan, et al., 1977).

Across all mammals, pregnancy and childbirth is a profound endocrine event that can cause noticeable changes in neural circuitry and have significant impacts on the production of social behavior (Moltz, et al., 1970; Numan, et al., 1977; Kohl, et al., 2016). Following childbirth, women's expectations of social support from family and community begin to change to allow for better care of the child and more support for childrearing (Negron, et al., 2014; Katz-Wise, et al., 2010). These subtle changes have large impacts on how the new mother engages with the outside world and can change the social behaviors that they see as appropriate in each context.

As an integral part of parenting behavior, aggression to defend offspring provides a clear link between parenting and aggressive behaviors. Indeed, recent studies looking at the neural basis of parenting behavior have confirmed this link by observing the interactions of male mice with their pups (Isogai, et al., 2018). A male mouse is known to

attack and kill pups that he does not recognize as his own – likely to get a reproductive advantage (Parmigiani, et al, 1994). This pup-directed aggression was localized to populations of brain regions that run parallel to and feed into the larger parenting focused nuclei (i.e. mPOA) and more aggression-associated regions (i.e. VMH) (Kohl, et al., 2016). In fact, the activation and suppression of infanticide-driving neurons in the perifornical area can act as a switch to change between infanticide and parenting responses in males to pups from another male (Isogai, et al., 2018). The circuitry associated with aggression is the same circuitry that drives parenting and infanticidal aggression. This shows the deep anatomical and behavioral connections between parenting and aggression in the brain.

In humans, we also see a connection between childbirth and infant-directed aggression in a subset of women suffering from postpartum psychosis (Pearlstein, et al., 2009). In rodent studies the neural circuitry responsible for modulating pup-directed aggression is highly interconnected with those that drive traditional parenting behaviors (Kohl, et al., 2016). While in humans, innervation between the amygdala and insular cortex was significantly decreased in patients impacted by post-partum depression (Wonch, et al., 2015). Indeed, reduced amygdalar connection and activity is a hallmark of post-partum depression studies (Nguyen, et al., 2019). Together, this suggests that there is a similar, likely homologous among mammalian species, distributed neural network that provides relevant information to the amygdala that shapes behavioral responses based on significant events (in this case childbirth).

The ventromedial hypothalamus (VMH) and medial preoptic area (mPOA) are two important brain regions that are implicated mainly in aggression and parenting

behavior respectively (Wang et al., 2015; Kim and Im, 2019; Numan, 1988). The mPOA itself is required to produce many sex-specific behaviors associated with mating and parenting (i.e., pup-gathering) by driving positive reinforcement for advantageous social interactions such as those with potential mates and those with their pups (Hu, et al., 2021; Wei, et al., 2017).

Activation of the VMH and specifically ESR1-expressing neurons in the VMH are traditionally associated with territorial aggression (Lin, et al., 2011). Pup-directed aggression, another aggression-based behavior that is inextricably linked with parenting behavior has been linked to the perifonical area (PeFA), amygdalohippocampal transition area (HATA), and VMH (Autry, et al., 2021). The connections observed between these three regions and the aromatase-expressing MeA neurons are consistent with the role of the MeA in directly reducing aggression in both males and females (Unger, et al., 2015).

Memory

In the context of social behavior, memory of previous social interactions can cause substantial changes to the way that two animals interact with one another in each context. Animals survive because they can recognize kinship and potential danger. This may seem simple, but it requires the animal to internalize a complex web of interpersonal cues with highly complex social stimuli. This allows an animal to react appropriately when they encounter novel or familiar conspecifics. In practice, this often manifests in the amount of time that one mouse will spend investigating another. Mice will typically spend less time investigating a familiar conspecific when compared to a novel conspecific (Thor, et al., 1982). This phenomenon is commonly referred to as social

recognition. The underlying thought process is that the animal will ‘remember’ an animal that it has already ‘met’ and will therefore be less interested in investigating them when compared to a totally novel animal of which nothing is ‘remembered’.

In a resident intruder paradigm, a familiar intruder will elicit a less severe response than a novel intruder (Hattori, et al., 2015). In the context of parenting, a male mouse will not immediately attack infants that it recognizes as its own (Parmigiani, et al., 1994). These differential reactions based on social recognition indicate that familiarity with a conspecific may be an important factor to integrate into a given behavioral response.

Likewise, memory has a strong impact on social behaviors in humans, which allows social behavior to be shaped by previous social interactions (Hassabis, et al., 2014). Humans use previous social interactions to create a ‘prediction’ of how they believe another individual will interact with them and use this information to ‘choose’ an appropriate social behavior for this situation (Spreng, et al., 2013). We can see the development of this social-behavior response machinery in developing adolescents. Not only is physical and cognitive nourishment a developmental necessity, but social interactions in this period also allow the adolescent to develop an appropriate array of social behaviors and learn the correct situations to use each of them (Heyes, et al., 2015).

Research has shown distinct connections between the regions of the hippocampus and the MeA (Dwyer, et al., 2022). As a hub for memory episodic memory consolidation and recall in the brain the connections between the hippocampus (Scoville and Milner, 1957) and MeA suggest a role for episodic memory in the production of social behavior

responses. We have some evidence to support this hypothesis, the hippocampal region CA2 has been implicated in modulating social state and plays a role in the deduction of social novelty (Dudek et al., 2016). These functions overlap with the roles played by the MeA in social memory and aromatase-expressing neurons in the MeA in social discrimination (Ferguson, et al., 2001; Yao, et al., 2017). This supports the idea of the MeA and hippocampal regions working together to perform memory-involved social discrimination tasks.

Metabolism

An important, if often overlooked, factor when talking about social behavior is the impact of internal homeostasis and metabolic levels. A behavior is only selected for if its cost is outweighed by its benefits (Tinbergen, 1963). Many social behaviors are highly energy consuming (e.g., territorial defense, mating, parenting) meaning that they can exact large tolls on the metabolism and homeostasis of the animal that performs them. The metabolic load of parenting is particularly large in mammals. With this in mind, it only makes sense that the production of social behavior should be mediated by the metabolic and homeostatic status of the animal that would be performing the behavior (Iwasa, et al., 2018; Padilla, et al., 2016).

In many animals, we see that starvation conditions push the animals to spend more time foraging in riskier environments (Whitham, et al., 2000; Kohler, et al., 1989; Anderson, 1986). And in humans, we can see evidence of starvation conditions profoundly influencing social behaviors (Keys, et al., 1950; Iwasa, et al., 2018). The most striking evidence of metabolic conditions impacting social behaviors was in the

Minnesota Starvation Experiment. In this study, 36 men were placed on a severe calorie restriction for six months (Keys, et al., 1950). They exhibited not just profound physiological changes, but also showed severe social behavior deficits (Keys, et al., 1950). These included a lowered sex drive and decreased social interactions in favor of social isolation (Keys, et al., 1950).

Nutrition, metabolic state, and social stress can impact the development of social behaviors and these effects are most pronounced during specific 'sensitive periods' of development. The onset of puberty is dependent on the weight of the child and can be impacted by abuse or neglect (Fisher, et al., 2014; Rutter, 1998). An extreme example of this kind of depravation is that of the Romanian orphans who were poorly fed and received virtually no social enrichment for an average of the first eight years of their lives (Rutter, 1998). These children were severely developmentally impaired, showing profound social behavior deficits and delayed puberty (Rutter, 1998). This provides a direct example of an external factor (metabolic and social stress) modulating the development and execution of social behaviors in humans.

Indeed, when we look at the projections of several metabolically relevant brain regions including the LH, VMH, and ventral premammilary nucleus (PMv), we observe direct synaptic projections to the MeA (Dwyer, et al., 2022). The LH contains a variety of neurons that modulate feeding behavior and sense the internal metabolic state of the animal (Berthoud, et al., 2011; Jordan, et al., 2010). Inputs from this region to the aromatase-expressing MeA neurons could provide invaluable information about the internal homeostasis of the animal. The PMv is a sexually dimorphic area that expresses a vast array of receptors that regulate energy balance and modulate seasonal reproductive

behaviors (Donato, et al., 2009; Donato and Elias, 2011). Inputs from these two regions suggest an interesting system where the PMv and LH both regulate energy availability and use this information to 'allow' or 'disallow' reproductive behavior depending on the metabolic state of the animal. The established inputs from these areas to the aromatase-expressing neurons of the MeA that we know are directly involved in driving social behaviors, including reproduction, present an interesting potential mechanism for metabolism impacting social behaviors.

Sociosexual Behaviors

Not only is reproductive behavior impacted by an animal's metabolic state, but reproductive behavior itself can impact other behaviors. It is fitting that the brain regions involved in modulating sexual reproduction, the most important social behavior for species survival, would have an impact on the production of other important social behaviors. The act of mating is highly complex and involves an intricate suite of neural regions working in concert under specific endogenous endocrine conditions to occur. As a social behavior it is undoubtedly the most important for the survival of the species (Darwin, 1871). Much like parenting, this behavior is highly interconnected with aggression and recognition (Hashikawa, et al., 2016).

In many animals, including humans, the prospect of reproduction can cause radical changes in both male and female behavior. Most commonly males use courtship displays to demonstrate their reproductive potential to prospective mates, which leads to often socially and metabolically expensive behavioral displays (Mitoyen, et al., 2019; Bastock., 1967). To 'court' a female, a male will engage in risky behaviors and display

extravagant possessions in an effort to display their personal social status as a potential reproductive partner (Wortham and Miller, 2017). These displays are in no way constrained to a single sex and can often depend on the population makeup to determine which sex performs the most extravagant behaviors (Wortham and Miller, 2017; Mitoyen, et al., 2019). Without the prospect of reproduction, these behaviors are undoubtedly negative. They reduce the reproductive fitness of the individual and can reduce their social and economic standing (Wortham and Miller, 2017). A subtler suite of courtship behaviors observed in humans, commonly referred to as 'flirting' are similarly unique in their ability to communicate reproductive susceptibility (Gersick, et al., 2014). This unique suite of social behaviors is a less expensive and less overt courtship proposition (Gersick, et al., 2014).

The neural correlates of these mating behaviors are best understood in the mouse. The act of mating in the mouse is a two-step process involving two sets of instinctive behaviors in the initial appetitive phase and the following consummatory phase (Tinbergen, 1951). In mice, the appetitive phase is the process of approaching a stimulus to identify it and drive a behavioral response (Tinbergen, 1951). This process is highly similar to other social behaviors including aggression and recognition highlighting the interconnectedness of these behaviors. This stage of mating activates many regions with strong connections to the aromatase-expressing MeA neurons including the VMH, cortical amygdala, and nucleus of the lateral olfactory tract.

Regions that mediate odor-driven approach and aversion, which is an essential first step to reproduction, likewise project to the aromatase-expressing MeA neurons.

Both the cortical amygdala and the nucleus of the lateral olfactory tract are understood to produce context-specific perceptions of odors with a view towards driving reproductive behavior (Tanisumi, et al., 2021) The posterolateral and posteromedial cortical amygdala receive important sensory information from the main olfactory bulb and are critical for taking this information and determining whether a given scent should be seen as aversive or attractive (Hashikawa, et al., 2016). The PMCO specifically appears to drive copulation after reception of an attractive stimulus, making it integral to reproductive behavior (Maras and Petrulis, 2008).

Sociosexual Behavior functional overlaps

While there is clear evidence showing a possible impact of inputs from regions with a highly stereotyped physiological function on the production of social behavior, there is also evidence showing that many regions that otherwise play major roles in driving fear/anxiety are also highly influential in the production of socio-sexual behavior (Dwyer, et al., 2022). This overlap suggests another possible axis in the control of social behavior by external stimuli in which an interplay between fear/anxiety and socio-sexual behavior may impact both the production of each other and of other social behaviors. In this context, we use fear/anxiety to describe the activation of a sympathetic nervous response to a given stimulus. This drives what is often referred to as the 'fight, flight, or freeze' response, which causes a radical physiological shift in the animal to prepare it to best survive a potentially life-threatening situation. The anxiety aspect of this concept is used to refer to the effects of a prolonged stressor. Prolonged stress has serious impacts on other social behaviors including parenting, reproduction, and aggression toward conspecifics (Bedoya-Perez, et al., 2019). The production of fear/anxiety behaviors is

often in response to an external threat. These threats are changes in the environment that make it more difficult for an animal to survive. In these circumstances, it is not prudent from a survival perspective to spend an incredible amount of metabolic energy that could otherwise be spent countering an incoming threat on the production and rearing of offspring. This makes it only natural that many of the areas involved in driving reproduction would work closely with those areas that modulate fear responses to ensure that reproductive behaviors are only performed when it is advantageous to reproduce. Indeed, the amygdala, being a highly heterogenous integration area, contains many of most prominent of these cell populations including the basomedial amygdala (BMA), central amygdala (CeA), and PLCO.

While we have already discussed the role of the PLCO in reproductive behavior, it also plays an important role and drives aversion to specific odors (Hashikawa, et al., 2016). This control of aversion plays an important role in determining what will be observed as a stressor and thus drives fear and anxiety. The BMA and CeA are both portions of the subcortical amydala most associated with fear conditioning and top-down control of fear and anxiety (Ciocchi, et al., 2010; Adhikari, et al., 2015). The CeA plays the clearest role in associating aversive stimuli with fear responses. It does this by increasing plasticity during aversive stimulus presentation, which allows the fear response that it traditionally drives to be tailored to a specific stimulus (Ciocchi, et al., 2010). Alternatively, the BMA uses cortical information from the medial prefrontal cortex to ‘shape’ the perception of a potentially aversive stimulus based on ‘higher-level’ cognitive information, which has the effect of modulating a potential fear response (Adhikari, et al., 2015). Both of these sets of information, the fear response and the input

shaping the fear response should help to shape a social interaction based on previous experience through their inputs to the aromatase-expressing MeA neurons.

Conclusions

While the MeA is often discussed as a brain region that receives mainly sensory input, the vast interconnection with a large network of regions inextricably linked with the production of social behavior suggests that it plays a much larger role (Dwyer, et al., 2022; Scalia and Winans, 1975). If, as seems to be the case, the MeA, and the aromatase-expressing cells in the MeA in particular, receive inputs from a host of regions, which contain relevant information that has been shown to influence the production of social behaviors, our view of the MeA must be amended. Not only does the MeA, as has been well established, receive important sensory information through the vomeronasal system, but the MeA also must integrate this sensory information with information from hundreds of other brain regions about the internal and external environments within which these stimuli exist.

Social behaviors are so important that it only makes sense that animals consider all necessary environmental variables before acting. Not only are these behaviors necessary for survival, they are also often incredibly energy intensive (Boyle, et al., 2017). Animals improve their evolutionary fitness by engaging with social behavior because of the indirect benefits received by engaging with other animals of the same groups (Boyle, et al., 2017). This is a potentially costly gamble that can incur costs. For example, in parenting, an animal expends a tremendous amount of energy supporting their young (Kohl, et al., 2016). It is not readily apparent that this is a beneficial situation

for the dam as the result is a simple increase in the odds that their pups reach adulthood. It is when we consider the indirect and evolutionary benefits of raising pups to reproductive maturity that we find a potential benefit to the an animals evolutionary fitness. In raising the pups to adulthood, dams are able to pass on their own genetic material to future generations.

The impact of animal sex on behavioral and neural responses to socially relevant stimuli in the vomeronasal system allows us to use it as a model to investigate the impacts of sex and other physiological and environmental factors on social behavior and the neural responses that underly them. When a mouse uses pheromones to communicate with a conspecific, the pheromones are recognized by receptors in the vomeronasal organ, which send input to the accessory olfactory bulb. The accessory olfactory bulb collects these signals in glomeruli which are innervated by olfactory projection neurons (mitral and tufted cells) which convey these signals to the MeA. While the broad organization of this system is similar in males and females, this circuit has been shown to produce different behaviors and neural activity in response to identical pheromone signals in males and females (Bergan, et al., 2014). While electrophysiological recordings in the MeA showed aromatase-dependent sex-differences in activity, there were no sex-differences observed in the activity of the AOB (Bergan, et al., 2014). This sensory circuit provides an evolutionarily conserved model that can be used to investigate several possible mechanisms for socially relevant chemosensory signals to be identified differentially in the MeA based-on sex and environmental conditions.

In one scenario the AOB of awake and behaving mice could display sex-specific activity in response to social stimuli. This would support a model where sensory

information is differentially received in the AOB in males and females, but from there, the connections between the AOB and aromatase-expressing MeA neurons are similar in males and females, resulting in a direct relay of this differential sensory information from the AOB to the aromatase-expressing MeA neurons.

Another possibility is that the AOB neurons exhibit similar activity patterns in males and females as well as sending similar signals to the aromatase-expressing MeA neurons in males and females. This would indicate that internal connections and region-specific properties in the aromatase-expressing population of MeA neurons were responsible for converting the signals received for similar social stimulus into different responses based on sex.

However, the model that claims the most support states that the AOB produces subtly different activity patterns in response to the same stimuli in males and females, which are amplified in the MeA and produce different signals in the MeA of males and females. This would indicate that the cells that process the same sensory information in the AOB of males and females may react largely similarly in both sexes but, through either differential MeA processing or connection patterns with the aromatase-expressing neurons in the MeA, subtle sex differences in sensory perception are accentuated in the MeA in response to similar stimuli.

Future Research

The amygdala contains heterogeneous populations of cells with an incredible breadth of anatomical and functionally distinct cell populations existing in close proximity (Yu, et al., 2023). The constellation of different, often interconnected

populations comes as no surprise given the extent to which the MeA takes in vast amounts of information and uses it to 'drive' an appropriate behavioral outcome. And, while previous research has revealed these interconnections, the specific cellular populations that perform each function are lost in such a broad analysis focusing on individual brain regions. Going forward, it should be of the utmost importance to change our framing of the MeA and amygdala at large as a single region and view it for what it is: a vast, interconnected web of cells that receive broad information and project outward together to drive social behaviors in accord with both internal and external factors.

This paradigm shift will necessitate a finer level of understanding of these cell populations. We will need to perform cell-level genomic analyses to find which populations of cells in the MeA and amygdala at large receive what information and identify the proteins produced by these cells that allows them to effectively process or receive their specific information as opposed to another's. Viewing the MeA as a single structure handicaps our understanding of how neural networks actually function *in vivo*. All the cells of a region are seldom responsible for the same function. Looking at them from our coarse level we see them as an individual node, when, in fact, they are nodes, within nodes where each cell impacts the signal a little one way or another.

Statement of Dissertation Goals

In this dissertation I will introduce three studies, which provide a framework for understanding the impact of environmental and internal physiological factors on the perception of socially relevant sensory information and the production of social behaviors. The goal of this dissertation is to present an expanded view of social behavior-

producing areas as adaptable centers that consider internal and external environmental conditions to determine an appropriate behavioral response not just for a given stimulus, but also for a given situation.

The first study in this dissertation (Chapter 2) presents a novel technique for investigating intact neural circuits. Using magnetohydrodynamic force (MHD), we were able to accelerate and improve the clarity of large tissue samples. This allowed us to identify labeled neurons deep in the brain at high resolution.

The second study (Chapter 3) uses this technique to trace the specific cells that provide neural input to the aromatase-expressing neurons of the MeA. Using rabies tracing in combination with MHD-accelerated clearing, we were able to identify and locate the specific inputs to aromatase-expressing cells throughout an entire tissue sample without damaging the internal connections by slicing.

The third study in this dissertation (Chapter 4) identifies the impact of an external stimulus (predator scent) on the behavior and neural responses of mice to conspecifics. Using conditional fiberphotometry recordings focusing on the mitral and tufted cells in the AOB that provide direct sensory input to the MeA, we were able to identify the sensory neural and social behavioral changes in environments with and without a predator present.

CHAPTER 2

ACCELERATED CLEARING AND MOLECULAR LABELING OF LARGE TISSUE SAMPLES USING MAGNETOHYDRODYNAMIC FORCE

Published as: Dwyer, J., Ramirez, M.D., Katz, P.S., Bergan, J., (2021) Accelerated clearing and molecular labeling of biological tissues using magnetohydrodynamic force. Sci Rep, (11):16462.

Abstract

Techniques used to clear biological tissue for fluorescence microscopy are essential to connect anatomical principles at levels ranging from subcellular to the whole animal. Here we report a simple and straightforward approach to efficiently render opaque tissue samples transparent and show that this approach can be modified to rapidly label intact tissue samples with antibodies for large volume fluorescence microscopy. This strategy applies a magnetohydrodynamic (MHD) force to accelerate the removal of lipids from tissue samples at least as large as an intact adult mouse brain. We also show that MHD force can be used to accelerate antibody penetration into tissue samples. This strategy complements a growing array of tools that enable high-resolution 3-dimensional anatomical analyses in intact tissues using fluorescence microscopy. MHD-accelerated clearing is simple, fast, reliable, inexpensive, provides thermal regulation, and is compatible with existing strategies for high-quality fluorescence microscopy of intact tissues.

Introduction

Advances in microscopy now allow investigation of subcellular anatomical structures while maintaining the macroscopic organization of intact tissues. Generating high-quality tissue samples is a critically important step towards achieving this goal. Most biological tissues, including the brain, are recalcitrant to large-volume microscopy without first being made optically transparent (cleared). Early methods for chemically-based tissue clearing quenched fluorescence, making tissue samples unsuitable for fluorescence microscopy (Shultze, et al., 1897; Spalteholz, et al., 1914); however, modern approaches for tissue preparation reduce light scattering without quenching fluorescence (Chung, et al., 2013; Hama, et al., 2011; Kim, et al., 2015; Renier, et al., 2016; Li, et al., 2018; Susaki, et al., 2020; Table 1). These approaches reduce light scattering primarily by removing lipids and standardizing the refractive index of the tissue sample. When combined with genetically encoded fluorophores, these approaches enable anatomical investigation with sub-micron precision at depths of at least a centimeter. Here, we present a technique that utilizes MHD force in combination with a conductive buffer and detergent to efficiently, reliably, and cost-effectively prepare high-quality cleared tissue samples for visualization with fluorescence microscopy. Importantly, MHD-based clearing minimizes thermal damage to tissue, preserves endogenous fluorescent signals, and is simple to implement.

MHD force describes a physical phenomenon also known as Lorentz force where force is generated on a charged particle in the third orthogonal direction from perpendicular electric and magnetic fields (Jamalabadi, 2014). The efficiency of MHD force to rapidly drive charged molecules into and out of tissue is a consequence of a

fundamental difference in the way that MHD fields and electrical fields act on charged particles. Electrophoresis drives cations and anions in opposite directions resulting in no net flow of buffer through a tissue sample. In contrast, MHD-forces drive cations and anions in the same direction along the third orthogonal axis resulting in a unidirectional flow of buffer through the sample itself (Figure 1C; Jamalabadi, 2014). The rapid flow of buffer through a tissue sample located within the MHD field constantly replaces heated buffer with fresh cool buffer thereby minimizing thermal damage to fluorescent molecules embedded in a large tissue sample while rapidly removing unbound molecules.

Intact tissues also present a challenge for the introduction of molecules that are needed to label molecular features deep in the sample. Based on the efficacy of MHD-accelerated clearing, we tested if MHD force could be used to propel antibodies into tissue samples. The same approach used to remove lipids and clear tissue samples also accelerated the penetration of antibodies into the tissue sample—MHD-accelerated labeling.

Using MHD-accelerated clearing, transparency of an intact mouse brain can be achieved in as little as 12 hours. MHD forces can subsequently be harnessed to drive antibodies into cleared tissues. These MHD-based approaches work in both vertebrate (shown for mouse and zebrafish) and invertebrate (shown for the nudibranch mollusk *Berghia stephanieae*) species, providing a generalizable method to render intact tissue transparent and accelerate immunohistochemical labeling for fluorescence microscopy of intact tissues. We provide plans for the construction of the MHD device, as well as a detailed protocol to ensure the successful implementation of this strategy for those interested in large-volume tissue microscopy.

Results

Effects of MHD force

MHD force produces a linear increase in flow velocity that is not observed with the application of purely electrical force (Figure 1). To quantify the effects of the MHD force, we compared the movement of sodium alginate spheres suspended in an electrically conductive buffer in response to purely electrical or MHD forces. The MHD condition produced dramatically higher velocity flow over the electrical only condition for all tested non-zero voltages and across the time course (Figure 1A; $p < 0.0001$). The difference between MHD and electric-only flow velocity increased as the applied voltage increased (Figure 1A).

Tissue Clearing/Delipidation

MHD-accelerated clearing renders an intact mouse brain transparent in as little as 12 hours (Figure 2). Both electric-only and MHD-accelerated clearing remove lipids from brain tissue and produce an increasingly transparent tissue sample with longer clearing times (Figure 2B). Tissue samples cleared using MHD-accelerated clearing were cleared more completely and quickly than electric-only clearing (30V DC; 0.35 AMPS). As the electric-only condition does not produce buffer flow independently, these trials were conducted with the assistance of a peristaltic pump (500 ml/min) with flow matched to the MHD condition to prevent tissue damage from overheating.

Because excessive heating during active clearing can denature proteins and quench fluorescence, we measured the temperature of tissue samples actively cleared

with either MHD or electric-only conditions at matched voltage, amperage, and buffer circulation (Figure 2C). Note that the buffer circulation for the MHD condition is intrinsic to the technique while a pump is required to achieve buffer flow with the electric-only condition. The temperature of brains cleared in the electric-only condition were hotter temperatures than those cleared in the MHD condition across the full range of tested voltages indicating that MHD-accelerated clearing provides additional thermal buffering ($F(1,3) = 119$, $p < 0.0001$; 2-way anova with repeated measures).

MHD-accelerated clearing reliably rendered tissue samples optically transparent while also preserving genetically encoded fluorescent proteins (Figure 3). An intact adult mouse brain conditionally expressing GFP via EnvA-G-deleted rabies virus in aromatase-expressing neurons (Watabe-Uchida et al., 2016; Yao, et al., 2017; Billing et al., 2020) was prepared using MHD-accelerated clearing. Without fluorescent labeling, the shadows of individual cells and fine subcortical architecture (e.g., anterior commissure) is visible into the very center of the tissue (Figure 3A). A population of GFP-expressing cells was easily identified in the medial amygdala (Figure 3A). Higher magnification images showed that fine processes, such as dendrites and axons, can be identified and analyzed several millimeters (3 mm) from the surface of the brain (Figure 3B). Indeed, the resolution is sufficient to reconstruct the dendritic arbors of individual neurons in three dimensions (Figure 3C; Figure 3D) and to reconstruct the path of a single axon, including axon collaterals, from the cell body, through several millimeters of brain tissue, ending at the axon terminals (Figure 3E).

Tissue Labeling

MHD-accelerated labeling improved antibody penetration and allowed labeling of large intact tissue samples (Figure 7). To confirm the specificity of antibody binding is maintained in MHD-accelerated labeling, we used an anti-vasopressin antibody in mice that expressed tdTomato in vasopressin-expressing neurons (Figure 4 A-C). Tissue was generated by crossing the Ai9 Rosa26:LSL:tdTomato reporter line (Madisen, et al., 2010) and a line where Cre recombinase is expressed under the control of the arginine vasopressin (AVP) promoter (Bendesky, et al., 2017). This produced tissue where the fluorescent reporter tdTomato was expressed under the control of the AVP promoter. After a 12-hour MHD accelerated antibody label on this tissue using an anti-AVP antibody, we observed specific co-labeling of the genetically encoded fluorophores and the anti-AVP antibody (Figure 4 A-C).

An intact adult nudibranch (*Berghia stephanieae*) (medio-lateral: 1.3 mm, dorso-ventral: 1.5 mm, anterio-posterior: 2 cm) that had been delipidated using the MHD-accelerated clearing device was incubated with an anti-serotonin (5-HT; Immunostar; 1:500) antiserum followed by a fluorescent secondary antibody (488 nm conjugated; ThermoFisher; 1:200) suspended in a high pH electrophoresis buffer (0.1 M Borate Buffer and 0.1% Triton X-100 brought to pH 9.5 with 0.1 M LiOH; Figure 8). Passive incubation for 12 hours resulted in little to no penetration into the brain (Figure 4D), whereas MHD-accelerated antibody labeling for 12 hours drove antibodies throughout the sample and revealed 5-HT expressing cell bodies and neurites (Figure 4E).

Intact zebrafish brains (medio-lateral: 3 mm; dorso-ventral: 3 mm; anterio-posterior: 6 mm) were passively delipidated in SDS for 7 days and then incubated with anti-acetylated tubulin antiserum (Immunostar; 1:500; Piperno, et al., 1985) for 12 hours to identify neural fibers (Figure 4G). Control tissue samples (no MHD force applied) showed minimal antibody penetration along the outer edge of the tissue with little fluorescence visible in the optic tectum (Figure 4F). In contrast, MHD-accelerated labeling for the same amount of time showed robust labeling of neural tracts throughout the brain (Figure 4G).

To test MHD-accelerated labeling in mammalian tissue, an anti-oxytocin (OT) antibody was applied to a cube of mouse brain (medio-lateral: 6 mm, ventro-dorsal: 6 mm, antero-posterior: 6 mm) centered on the periventricular nucleus of the hypothalamus (1:500 primary; 1:200 secondary). As above, antibodies did not effectively penetrate the tissue sample in the absence of MHD force (Figure 4H). In contrast, OT-expressing cells were clearly visible in the PVN, located deep within of tissue cube, using MHD-accelerated labeling (Figure 4I). OT-expressing neuronal processes were easily resolved and were seen to project towards the third ventricle, which is consistent with OT neuron morphology (Figure 8). Accurate OT-labeling was seen >1.8 mm from the nearest edge. The ability to visualize axonal varicosities and nuclei in OT-labeled neurons demonstrated that the MHD-accelerated labeling strategy can be used to resolve subcellular structures (Figure 4I).

Discussion

The ability to study fine anatomical structures while maintaining their native organization is necessary to reveal relationships at the wide range of scales over which biological functions occur. The MHD-accelerated protocol outlined here harnesses the strengths of hydrogel-based clearing approaches to maintain proteins and genetically encoded fluorescence in large samples (Chung, et al., 2013; Kim, et al., 2015; Susaki, et al., 2015; Lee, et al., 2016; Pan, et al., 2016). MHD accelerated clearing maintains all advantages of electric-only clearing and adds the additional MHD force to further accelerate tissue clearing without increasing the potentially damaging electric field (Table 1; Figure 2; Figure 4—Figure 7).

MHD-induced flow serves at least three purposes. First, in the case of tissue clearing it helps remove lipids from the tissue sample. Second, in the case of antibody labeling it helps push antibodies into the tissue. While MHD acts directly on electrically charged antibodies, it is also possible that the observed acceleration of antibody penetration is because MHD generates something akin to a stream of buffer flowing inside the fixed tissue. Like twigs caught in the flow of a river, antibodies and lipids could be pulled through the tissue sample allowing rapid clearing and labeling. Third, MHD driven buffer flow provides additional thermal regulation of tissue samples above that observed with electrophoretic-only approaches (Figure 1). The MHD force is produced within the tissue itself and therefore constantly pulls fresh cool buffer into the tissue sample to replace buffer that has been heated by the electrical resistance (Figure 1). Because buffer flow is inherent to the MHD process, no moving parts (e.g. pump) are required to maintain buffer flow and the resultant thermal buffering. Moreover, because

the ‘pumping’ action of MHD is produced directly from the electrical and magnetic fields, tissue damage resulting from pump failure during active clearing is almost completely eliminated with MHD-accelerated tissue clearing.

This approach does not rely on solvents that are harmful to fluorophores (e.g., methanol and hydrogen peroxide), and simplifies tissue clearing to the bare minimum components. The only obligatory requirement is that the tissue sample is held at the intersection of an electrical and a magnetic field. Thus, the strategy outlined here is clean, efficient, and adaptable (Table 1). The device itself can be 3D printed in plastic (Figure 5; Supplementary Files) making the device simple and cost-effective, roughly two-hundred dollars, to build.

The MHD-based approach described here (Figure 5; Figure 6) reliably allows rapid tissue clearing, rendering them suitable for three-dimensional fluorescent imaging. We demonstrate the efficacy of a simple MHD device by clearing dozens of mouse brains and measuring the effects of voltage and MHD-conjugation on tissue heat, clarity and time needed to achieve complete optical transparency. We also introduce the exciting possibility by labeling sea slug, zebrafish, and mouse tissue with multiple different antibodies. Each antibody protocol required no more than 4.5 mL (1:200 concentration) of labeling solution which can be collected at the end of the procedure and reused. Similarly, the buffer solution used for clearing can be reused until the pH falls below 8.2 (typically after one month of heavy use or about 20 brains). Taken together, we believe MHD-accelerated clearing and labeling provides a simple, reliable, effective, and economical approach that can also be quickly adapted to the specific needs of each experiment.

Methods

Animal Use

All vertebrate animals were handled according to a protocol approved by the UMass Amherst Institutional Animal Care and Use Committee (IACUC; protocol #2018-0014 and #2017-0060).

Measure of MHD-induced flow

A solution of sodium chloride was made in a small tank (2.5 L). Sodium chloride was slowly added to the tank until the electric conductivity of the solution matched that of the clearing solution. The clearing device was then submerged in the solution with a measured grid behind the tank to provide scale. 0V, 10V, 20V, 30V, 40V, 50V, or 60V were applied to the device and sodium alginate spheres were introduced into the tank at a constant location (N = 7). The velocity of the spheres through the device was measured. Velocity was calculated using a high-speed video taken over a calibrated grid. This process was then repeated using only an electric field (magnets were removed). Paired-sample t-tests were performed between the MHD and electric-only conditions at each voltage and a 2-way ANOVA was performed across all voltages using MATLAB. The p-values for the paired samples T-test were corrected for multiple comparisons using Bonferroni correction. Each condition was fit to a linear model using MATLAB.

Design of MHD-accelerated clearing device

The strategy for using MHD to remove lipids from tissue samples requires binding proteins and polymerizing a hydrogel, removing lipids, and matching the

refractive index of the tissue and imaging media (Figure 5A). A tissue chamber was placed into the central chamber of the MHD-accelerated clearing device (Figure 5B, C). This holds the tissue at the intersection of the electrical and magnetic fields. The clearing chamber was submerged in a large (5 L) bath of clearing solution at 37 °C and 30 VDC (0.35 Amps) was applied across the tissue for several hours (typically 16 hours for mouse brain tissue and 2 hours for intact zebrafish brains; Figure 5D).

Tissue Fixation and hydrogel polymerization

Mice were anesthetized with isoflurane, euthanized, and perfused with 0.01 M phosphate buffered saline (PBS) followed by 4% paraformaldehyde (PFA) in 0.01M PBS. Tissue was then post-fixed in 4% PFA at 4 ˚C overnight. Next, the tissue was placed in a hydrogel solution (4% acrylamide, 4% PFA, 0.05% bis acrylamide, and 0.25% VA-044 initiator suspended in 0.01 M PBS) at 4 ˚C overnight (Chung, et al., 2013; Isogai, et al., 2017). Oxygen was flushed out of hydrogel-infused tissues nitrogen gas and then the samples were polymerized by incubating them at 37 ˚C overnight (Chung, et al., 2013). Excess hydrogel was removed from the surface and tissue samples were transferred to PBS to flush hydrogel monomers.

Adult zebrafish were euthanized in 0.2 mg/ml tricaine mesylate (MS-222), decapitated, and the heads placed in 4% paraformaldehyde overnight. Heads were then placed in PBS and brains were carefully dissected, incubated in hydrogel at 4 ˚C overnight, and processed as above.

Adult nudibranchs (*Berghia stephanieae*) were anaesthetized in cold 4.5% magnesium chloride in artificial sea water for 20 minutes, pinned to a Sylgard-lined dish,

and fixed in 4% paraformaldehyde in sea water overnight at 4 ˚C. Whole animals were washed with PBS and then incubated in hydrogel at 4 ˚C overnight and processed as above.

Active Tissue Delipidation (clearing)

Tissue samples were incubated in SDS-clearing solution (10 mM sodium dodecyl sulfate in 0.1 M borate buffer, pH 8.5) for 2 days at 37 ˚C unless otherwise noted. Samples were then transferred to the MHD-accelerated clearing chamber, consisting of two interlocking cell-strainers (ThermoFisher; catalog #: 87791). This chamber was placed in the intersection of the electrical and magnetic fields in the center of the device and the chamber was lowered into a bath of 37 ˚C SDS. 30V DC were then applied across the tissue to initiate MHD-accelerated clearing (Figure 5D). After clearing, the tissue is taken out of the clearing chamber and washed in 0.1 M PBS for at least 12 hours. Of the 55 samples cleared for this paper using this technique in multiple laboratories, all achieved transparency with little physical damage.

Electrophorectic Clearing

Tissue samples were incubated in SDS-clearing solution for 2 days at 37 ˚C unless otherwise noted. Samples were then transferred to a clearing chamber, consisting of two interlocking cell-strainers (ThermoFisher; catalog #: 87791). This chamber was placed between two electrodes in the center of a MHD-accelerated clearing device, which has had magnets removed from the device. A 500ml/min peristaltic pump (Grey Beard Niagra) was then affixed to the top of the central chamber to circulate buffer across the tissue during clearing by pulling buffer from the temperature-controlled bath. The

chamber and output from the pump were lowered into a bath of 37 ˚C SDS. Direct electrical current was then applied across the tissue to initiate clearing. After clearing, the tissue was taken out of the clearing chamber and washed in 0.1 M PBS for at least 12 hours.

Clearing Temperature Measurements

Tissue was left to incubate in SDS-clearing solution for 2 days at 37 ˚C, then allowed to cool to room temperature for at least 2 hours. Tissue was then subjected to either MHD-accelerated or electrophoretic clearing (n = 6) for 30 minutes with four different voltages applied across the tissue (30, 40, 50, and 60 VDC) in a 37 ˚C SDS bath. After clearing the tissue was rapidly removed from the device and imaged with an infrared thermal imaging camera (Hti-Xintai: HT-18) on a room temperature background. The highest observed temperature from each sample was recorded and the tissue was allowed to cool down to room temperature prior to additional experiments at different voltages.

Refractive Index Matching and Light Sheet Microscopy

The tissue was transferred to “Optiview” (Isogai, et al., 2017) refractive index matching solution and incubated at 37 ˚C for at least 12 hours to achieve optical clarity through RI matching (Figure 5A; Isogai, et al., 2017). Samples were imaged at 5X or 20X magnification with a lightsheet microscope adapted for a 1.45 RI imaging solution (Zeiss Z1).

Measures of Clearing Efficacy

Tissue was left to incubate in SDS-clearing solution for 2 days at 37 ˚C. Tissue was then subjected to either MHD-accelerated or electrophoretic clearing (n = 6) for 24 hrs. Clearing was interrupted at 0hr, 6hr, 12hr, and 24hr. Tissue was washed with 0.01M PBS overnight, then equilibrated to RI 1.43 in Optiview (Isogai, et al., 2017) for at least two days at 37 ˚C. Tissue transparency was then measured by the percentage of light transmitted through the tissue suspended in an Optiview solution (Isogai, et al., 2017). Light transmission was measured using a wide-spectrum light-source and calibrated photodiode. The sample was then washed in 0.01M PBS overnight, then equilibrated to SDS-clearing solution for 2 days at 37 ˚C before clearing continued up to 24hr per sample. Data across all samples at each time were fit with a saturating exponential curve in MATLAB.

MHD-accelerated staining of fixed tissue with methylene blue

Penetration of methylene blue into a 1 cm^3 cube of homogeneous brain tissue under MHD force was tested over 1, 2, and 4 hours (N = 1). Cubes of uncleared sheep brain tissue were equilibrated to the antibody labeling buffer solution for 12 hours. The tissue was then placed at the intersection of a strong magnetic and electric field (30V DC) and submerged in a solution of methylene blue (0.1 M) buffered to pH 9.5 (37 °C). The orientation of the electric field was reversed at 15-minute intervals for 3 minutes. Three samples were labeled using this approach for 1, 2 or 4 hours. Following the stain, the tissue was bisected and imaged. A control sample was incubated in the same solution (37

°C) for 4 hours without the application of any active force. This sample was bisected and imaged as the others.

Comparative staining of methylene blue into agarose cubes as a result of various strengths of electrical force conjugated to MHD force

15 1 cm^3 of 3 % agarose were subjected to labeling methylene blue labeling by MHD force for 0, 5, 10, 15, 30, 60, or 120 minutes at varied electrical field strengths. The distance penetrated into the agarose cubes was measure after bisection and plotted against staining time with 10, 20, or 30V in a constant magnetic field.

Antibody Labeling

Delipidated tissue was placed inside of a 2-inch length of 0.25-inch diameter dialysis tubing (6 – 8 kDa); Spectrum). After equilibration, samples were incubated in an antibody solution inside dialysis tubing at the center of intersecting electrical and magnetic fields where the MHD force was strongest (Figure 6). Confining the tissue sample inside dialysis tubing reduced the volume of antibody required for labeling and protected the tissue sample and antibody solution from direct exposure to the electrodes. Magnets (Applied magnets; NB057-6-N52) were placed on the top and bottom of the MHD labeling device creating a central chamber Figure 6B). The ends of the dialysis tubing were connected to 9.5 mm diameter vinyl tubing (ThermoFisher: S504591) using 0.25-inch Leur lock barbs (Cole-Parmer; UX-45501-20) to create a torus-shaped chamber allowing the antibody solution to circulate continuously and provide an even and continuous source of antibody to the tissue sample (Figure 6). Antibody solution (4.5 mL; 0.1 M borate buffer titrated to pH 9.5 with 0.1 M LiOH, 1% heparin, 0.1% Triton X-100;

1:500 primary antibody) was transferred into the dialysis tubing using a 5 mL syringe. The labeling chamber was submerged in a 1L tub containing electrophoresis solution (0.1M Borate Buffer pH 9.5/0.1% Triton X-100 solution). A 5 mL syringe filled with the buffer solution was attached to the circulation line to maintain constant pressure inside of the dialysis tube. 60 volts DC (~0.2 Amps) was applied across the electrodes for 15 minutes, followed by 3 minutes of inactivity repeatedly for 12 hours to drive antibodies into the tissue sample. The system was held at 37 ˚C and protected from ambient light to minimize bleaching of fluorophores throughout the procedure.

Following each round of MHD-accelerated labeling, the antibody solution was replaced with a wash solution (0.1 M borate buffer titrated to pH 9.5 with 0.1 M LiOH, 1% heparin, 0.1% Triton X-100) and the tissue was exposed to 6-hours of "active washing" using the same voltage settings. Labeled tissue was then washed in 0.01 M PBS for at least 12 hours.

Traditional Immunohistochemistry

Mouse brains were dissected from highly anesthetized mice. These tissues were incubated in 4% PFA suspended in 0.01M PBS at 4°C. Tissue was sliced to 100 µm thickness on a vibratome and transferred to 0.01M PBS or the electrophoresis buffer used in MHD-accelerated labeling. Slices were blocked in 10% FBS in 0.5% TritonX-100/PBS or electrophoresis buffer at room temperature for 1 hour, then incubated in a 1:200 dilution of antibody in 10% FBS/PBS or electrophoresis buffer at room temperature for 2 hours. The tissue was then washed three times in 0.05% TritonX-100 / PBS or electrophoresis buffer for 30 minutes at room temperature.

CHAPTER 3

BRAIN-WIDE SYNAPTIC INPUTS TO AROMATASE-EXPRESSING NEURONS IN THE MEDIAL AMYGDALA SUGGEST COMPLEX CIRCUITRY FOR MODULATING SOCIAL BEHAVIOR.

Published as: Dwyer, J, Kelly, D.A., Bergan, J., (2022). Brain-Wide Synaptic Inputs to Aromatase-Expressing Neurons in the Medial Amygdala Suggest Complex Circuitry for Modulating Social Behavior. eNeuro, 9(2):ENEURO.0329-21.2021.

Abstract

Here, we reveal an unbiased view of the brain regions that provide specific inputs to aromatase-expressing cells in the medial amygdala, neurons which play an outsized role in the production of sex specific social behaviors, using rabies tracing and light-sheet microscopy. While the downstream projections from these cells are known, the specific inputs to the aromatase-expressing cells in the medial amygdala remained unknown. We observed established connections to the medial amygdala (e.g., bed nucleus of the stria terminalis and accessory olfactory bulb) indicating that aromatase neurons are a major target cell-type for efferent input including from regions associated with parenting and aggression. We also identified novel and unexpected inputs from areas involved in metabolism, fear and anxiety, and memory and cognition. These results confirm the central role of the medial amygdala in sex specific social recognition and social behavior and point to an expanded role for its aromatase-expressing neurons in the integration of multiple sensory and homeostatic factors, which are likely used to modulate many other social behaviors.

Significance Statement

Aromatase-expressing neurons in the medial amygdala play a significant role in producing critically important social behaviors including parenting, aggression, and reproduction. We used rabies tracing and light-sheet microscopy to reveal an unbiased view of many brain regions that provide direct synaptic input to aromatase neurons and observe both well-established and previously unknown inputs from areas involved in parenting and aggression, metabolism, fear and anxiety, and memory and cognition. These results confirm the central role of the medial amygdala in social recognition behavior and point to an expanded role for its aromatase-expressing neurons in the integration of multiple sensory and homeostatic factors, which can be used to modulate many other social behaviors.

Introduction

Social behaviors are necessary for communication, survival, and reproduction in species throughout the animal kingdom (Darwin, 1871; Marler, et al., 1979; Ueda et al., 2020), and depend on the integration of external and internal sensory cues. Nearly all sensory systems have been linked to social behavior (Keller, et al., 2006a; 2006b; 2006c; Pomerantz, et al., 1983; Contreras and Agmo, 1993; Strasser and Dixon, 1986). For example, the diverse, and often beautiful, vocalizations of songbirds signal their species, individual identity, territorial ownership, and readiness to mate (Marler, 1961). In humans, visual cues produced in the face and hands provide information about another's identity and emotional state (Haxby, et al., 2002). For many species, chemosensory cues are particularly important to detect, identify, and respond to social partners (Bradley, et

al., 2002; Dulac, et al., 1995; Gonzalez, et al., 2017; Keller, et al., 2006c, Schwanzel-Fukuda, et al., 1991). In mice, chemosensory information, transduced by the main olfactory epithelium and the vomeronasal organ, provides the primary sensory input to a conserved network of brain regions dedicated to executing social behaviors (Newmann, et al., 1999).

The core brain regions that make up the social behavior network (SBN) are well-established and conserved for all vertebrate species examined thus far (Goodson, 2005). However, identifying the specific neural circuits that generate social behaviors has been challenging because of both the heterogeneity of cell populations in these regions and the interwoven and reciprocal nature of both the behaviors themselves and the underlying circuits. Thus, a current goal in neuroscience is to define specific contributions of well-defined populations of neurons to circuit function and, ultimately, to behaviors. Genetic and viral tools allow precise characterization of the connections made by individual populations of neurons and have been instrumental in defining cell-type-specific wiring diagrams that mediate specific behaviors (Watabe-Uchida, et al., 2012; Menegas, et al., 2015; Kohl, et al., 2018; Wickersham, et al., 2007).

The medial amygdala (MeA), a central node in the SBN, receives sensory input directly from the accessory olfactory bulb (AOB) and the main olfactory bulb (MOB). The MeA integrates chemosensory signals with modulatory input from other brain regions (Ferguson, et al., 2001; Yao, et al., 2017) and circulating hormones (Cooke, et al., 1999; Cooke, et al., 2005) to guide behavioral responses through its projections to efferent behavioral centers (Wu, et al., 2009). MeA neurons in mice display sex differences in sensory responses to social stimuli (Bergan, et al., 2014; Samuelsen &

Meredith, 2009; Kim et al., 2017) and robust anatomical sex differences (Cooke, et al., 1999; Wu, et al., 2009; Billing et al., 2020). Social behaviors that are tightly associated with the MeA, including parenting, mate choice, and aggression, also display clear sex differences (Chen, et al., 2020; Vochteloo, et al., 1987; Yao, et al., 2017; Haller et al., 2006; Haller, 2018). Each of these behaviors are critical for survival and reproduction. Their dependence on an animal's sex, age, and neuroendocrine status offers an opportunity to understand how the function of a common neural circuit can be modified to meet the specific behavioral requirements of an individual animal.

A large population of MeA neurons express the enzyme aromatase, which converts testosterone to estradiol, is critical for aggression in both sexes, and is known to shape the pattern of sensory responses in the MeA (Unger et al., 2015; Bergan et al., 2014). To fully understand the role of aromatase neurons in social behavior, however, we must first identify the inputs they receive and the circuits they form. Past experiments have addressed the electrophysiology of MeA neurons (Binns, et al., 2005; Bergan et al., 2014; Yao et al., 2017; Meredith et al., 2004; Li, et al., 2018) as well as the efferent targets of the MeA aromatase population (Wu et al., 2009). Recently, a sex-specific connection from AOB mitral and tufted neurons to aromatase neurons of the MeA was identified using rabies-based viral tracing from aromatase neurons (Billing, et al., 2020). However, the MeA integrates information from a large network of brain regions. Here we use rabies-based circuit mapping in conjunction with whole-brain cleared tissue imaging to exhaustively characterize the sources of synaptic input to aromatase neurons in the MeA, and to identify the information channels that shape aromatase-dependent social behaviors.

Materials and Methods

Animal Use

All experiments were performed in strict compliance with the National Institute of Health. All animals were handled according to a protocol approved by the UMass Amherst Institutional Animal Care and Use Committee (IACUC; protocol #2018-0014 and #2017-0060).

Fifteen adult mice (2 to 8 months old, both male (n=9) and female (n=6)) from an existing transgenic mouse line (Cyp19a1-Cre: Jax Labs) were housed in a temperature (22°C) and light (12hr: 12hr light: dark) controlled facility, with *ad libitum* access to food and water. The Cyp19a1-Cre transgenic line was generated by BAC recombination (Yao et al., 2017); its expression pattern faithfully recapitulates endogenous aromatase expression (Yao et al., 2017) and displays no known behavioral deficits in either heterozygous or homozygous animals.

Viral injections

We used a retrograde tracing system based on the modified rabies virus (EnvA-SADΔG-EGFP; Wickersham, et al., 2007) that uses two consecutive stereotaxic injections to visualize ->MeA^{arom+}. In the first injection, 500 nl of AAV8-FLEX-TVA and AAV8-FLEX-RG-mCherry (mixed 1:1; Watabe-Uchida et al. 2012) were injected into either the left or right MeA (Bregma −1.9, Lateral 1.9, Depth 4.5 to 5.5). After 14 days, 500 nl of SADΔG-EGFP(EnvA) virus (Viral Vector Core, Salk Institute, La Jolla, CA) was injected into the MeA at the same stereotaxic coordinates (Figure 13B;

Wickersham et al. 2007). All stereotaxic injections used a cold capillary (20-micron diameter tip) coupled to a Narishige hydraulic manipulator (Wu et al., 2014). All AAV viruses were produced by the UNC Vector Core Facility (Chapel Hill, NC, United States).

The rabies virus requires the cell-surface expression of TVA to enter a cell and is therefore limited to infecting Cre-expressing neurons (Figure 13A). Once inside a neuron, the modified rabies virus requires co-expression of the envelope glycoprotein (RG) to be packaged for retrograde trans-synaptic spread. The efficiency of viral infection was determined by injecting the same viruses into double-transgenic line that labels all Cre-expressing neurons with the R26-lsl-tdTomato reporter (Figure 13C; Madisen et al., 2010). This control experiment allowed us to estimate the infection rate (percent of the target population labeled by rabies; Figure 13D).

Tissue Processing

Ten days after the final injection, animals were deeply anesthetized with isoflurane and perfused with 50ml cold PBS followed by 25 ml cold PFA (4% in PBS). The brain was extracted and post-fixed in 25 ml hydrogel (4% acrylamide, 4% PFA, 0.05% bis acrylamide, and 0.25% VA-044 initiator suspended in 0.01 M PBS; Isogai, et al., 2017) 4 ˚C overnight.

After 12 - 24 hours incubation in hydrogel, oxygen was flushed from the hydrogel by bubbling the liquid hydrogel solution with nitrogen. The tissue container was resealed and transferred to a 37°C water bath until polymerization was complete (at least two hours). Excess hydrogel was removed from the brain manually and the tissue sample was

incubated to SDS-clearing solution (10 mM sodium dodecyl sulfate in 0.1 M borate buffer, pH 8.5) for 2 days at 37 ˚C prior to MHD-accelerated clearing (Dwyer, et al, 2019).

Active clearing was performed in a 5-gallon container containing SDS-clearing solution using a custom magnetohydrodynamic (MHD) clearing device (Dwyer et al., 2019) that rapidly removed unbound lipids from the tissue sample at 37°C. Brains were cleared until bright white and translucent, which typically took 24-48 hours. Brains were then transferred to 0.01M PBS for 24 hr. Brains were transferred from PBS to an OptiView imaging solution (Isogai et al. 2017) with refractive index 1.45 and incubated at 37°C for 2 days before imaging.

Image acquisition and processing

Images were acquired with the Zeiss Z1 Lightsheet microscope (Carl Zeiss, Jena, Germany). Rabies-labeled eGFP-expressing neurons were excited with a 488 nm laser. A 561 nm and/or 647 nm laser was used to produce an autofluorescence image for subsequent background subtraction and isolation of the GFP signal. Images were collected with a 5-times magnification objective lens with PCO-Edge scMOS cameras (PCO, Kelheim, Germany). The entire brain was imaged in the horizontal orientation from both the dorsal and ventral surfaces. This produced a series of slightly overlapping 3D image stacks for each brain. 3D Image stacks were saved at 1-5 μm resolution and reconstructed to form a 3D image of the entire brain using custom MATLAB scripts (Mathworks, Natick, MA).

Cell-counting

Rabies-labeled cells were identified using a human-trained computer vision algorithm (Ilastik, Heidelberg University). Briefly, a training subset of images were annotated as ‘not tissue’, ‘unlabeled tissue’, and ‘rabies labeled neuron’ by a trained user to prepare a machine learning kernel to automatically identify rabies labeled neurons. The resulting kernel was refined over several iterations until it accurately identified rabies labeled cells. Ilastik then automatically classified each pixel in from each image based on its probability of being a member of each category. The resulting probability map for ‘rabies labeled neuron’ were segmented with ‘regionprops’ in MATLAB and the centroids of each identified neuron were identified. Automatically identified cells (ilastik, Heidelberg University) were reviewed and confirmed by a human observer for quality control.

Each identified ‘input cell’ was assigned to a brain region based on its anatomical location. Thus, each imaged brain was transformed into a list containing the numbers and positions of identified neurons in each brain region and for each experimental animal. The identified populations were interpreted as the afferent synaptic input to the target population. Our past successes with this strategy likely result from three factors: 1) Thousands of input neurons are typically labeled in each brain providing broad coverage of social circuits. 2) The genetic specificity, ‘starter neurons’, of our approach reduces variability introduced by cell-type heterogeneity and by fibers of passage at the injection site; 3) The automated analysis pipeline allows user to annotate a sample dataset, which is then used to efficiently and accurately segment all subsequent datasets into ‘input cells’, ‘starter cells’, and ‘unlabeled tissue’ in an unbiased manner (Menegas et al., 2015).

Because of the intensely bright fluorescence of EGFP driven by the EnvA-SADΔG-EGFP virus, this algorithm can identify rabies labeled neurons with more than 99% accuracy and with very few false positives.

Brain Alignment

Each reconstructed 3D brain was aligned to the common framework Allen Brain Atlas (ccfv3; Wang, et al., 2020b) using elastix (Klein, et al., 2010; Shamonin, et al., 2014). Custom MATLAB scripts (Mathworks, Natick, MA) were used to integrate user input and computer processing and produce the alignment. Transformix (Klein, et al., 2010; Shamonin, et al., 2014) was then used to migrate the identified cells in each brain to the position of the accurate brain region in the standard Allen Brain Atlas framework. This allowed us to identify the number of eGFP-expressing cells in each region of the brain in each animal.

Statistical Analysis

*S*tatistical analyses were performed using MATLAB . Means are reported with standard error of the mean. Regressions were performed in MATLAB using the “fitlm” and “predict” functions. Regions identified as providing input to MeA arom+ neurons were determined using an single sample t-test on the observed cell counts in each region with Bonferroni correction for multiple comparisons when appropriate. A second comparison was made using a single sample t-test to determine if the input from a given region exceeded the expected input based on chance using the region volume and an even distribution of cells as the chance rates. Sex differences in synaptic input were first characterized using a repeated measures ANOVA with interactions conducted in

MATLAB. Post-hoc analyses for sex differences were conducted using an exact Permutation test comparing the cell counts observed in males versus females for each region (Efron and Tibshirani, 1986). D' was calculated as a sensitivity index for distributions with different SEM by normalizing the difference in cell count means by the standard deviation of the overall distribution. All scripts required to replicate these analyses have been provided as supplementary materials.

Results

We used a previously described aromatase-cre transgenic mouse line (Yao et al., 2017) crossed with the AI9 tdTomato reporter line (Madisen, et al., 2010) to identify aromatase-expressing neurons throughout the brain (Figure 13). Consistent with previous reports, aromatase was expressed in a subset of cells largely restricted to the social behavior network with the largest population located in the posterodorsal MeA (MeApd; Figure 13C; Unger, et al., 2015; Yao, et al., 2017; Morris, et al.., 2008; Newman, et al., 1999). We cleared the intact mouse brain with a modified version of CLARITY (Dwyer et al 2019, Chung et al., 2013), and imaged the whole brain using lightsheet microscopy (Isogai et al., 2017; Menegas et al., 2015). The full brain was digitally reconstructed and aligned to the Allen reference brain to allow automated categorization by region. This approach allowed us to identify labeled neurons throughout the brain and to maintain the macroscopic organization of these cells (Figure 13C).

Population data: broad-scale brain regions

Next, we identified the inputome for aromatase-expressing neurons located in the MeApd. The MeApd of adult male and female aromatase-cre mice was sterotaxically

injected with double-floxed inverse orientation adeno-associated viruses that selectively express the EnvA receptor (TVA) and rabies glycoprotein (RG) in aromatase-expressing neurons following cre-based recombination (Figure 13A; see methods). Two weeks later, an avian G-deleted rabies virus was injected in the same location (Rabies-ΔG-eGFP). Endogenous tdtomato and eGFP-expressing 'starter neurons' were visible in the MeApd (Figure 13C). As above, rabies-infected brains were cleared, imaged with lightsheet microscopy, and aligned to the Allen reference atlas. GFP-positive neurons were automatically detected using a machine vision algorithm and manually curated to ensure accuracy (see methods; Menegas et al., 2015).

The number of neurons retrogradely labeled by rabies, which synapse directly on aromatase-expressing neurons in the MeApd (->MeA^{arom+}), were counted in all brain regions. The number of neurons labeled outside the MeA scaled linearly with the size of the initially infected 'starter neuron' population in the MeApd (Figure 13D; B = 2.6, [1.06, 4.1] 95% CI, $R^2 = 0.45$; F = 12.9, p = 0.002). Injections were performed unilaterally in either the right or left hemisphere and the vast majority of ->MeA^{arom+} neurons were ipsilateral, indicating that the circuit that provides input to aromatase-expressing neurons in the MeA is largely contained within a single hemisphere (Figure 13E; Table 1; Percentage of Ipsi cells = 98.9 ± 0.24 SEM; t-test: p = 0.0002). Consistent with previous descriptions of inputs to the MeA (Winans & Scalia; 1970; Scalia & Winans, 1975) almost the entire identified inputome was restricted to subcortical regions (99.6%; Figure 13F). Even when looking at finer regions that span the brain (e.g., hippocampal formation), we find nearly all cells confined to the most ventral areas (Figure 18A). Taken together, we found that each 'starter neuron' is associated with more

than 100 presynaptic neurons on average, and the overwhelming majority of these neurons were both ipsilateral and subcortical.

Synaptic input: coarse regions

Aligning our whole brain datasets to the Allen reference atlas allowed us to identify the location of each neuron with high specificity. An individual dataset typically had neurons distributed across many subcortical regions. An example of neurons identified in a single animal is shown in Figure 14. We divided the Allen atlas into 10 mutually exclusive brain regions spanning the full volume of the reference brain and used these regions to coarsely classify the inputome for aromatase-expressing MeApd neurons (Figure 15A,B; see methods). Only statistically significant sources of synaptic input are reported, unless otherwise noted. The majority of ->MeA^{arom+} were located in the cerebral nuclei (59.7 ± 1.4; $t(17)=10.8$, $p<0.0001$), with additional significant populations of ->MeA^{arom+} neurons in the hypothalamus (11 ± 1.1; $t(17)=2.5$,$p=0.01$), hippocampus (10 ± 0.8; $t(17)=3.26$, $p = 0.0023$), cortical subplate (8.9 ± 0.4; $t(17)=5.7$, $p<0.0001$) and olfactory regions (7.2 ± 0.35; $t(17)=5.2$,$p<0.0001$; Figure 15 B,C). A small but consistent population of ->MeA^{arom+} neurons were identified in the thalamus (1.9 ± 0.2; $t(17)=2.05$, $p = 0.03$) and midbrain (0.9 ± 0.07; $t(17)=3.4$, $p =0.0016$). Very few neurons were identified in the isocortex (0.36 ± 0.03; $t(17)=3.3$, $p=0.002$), even though the isocortex and cerebellum represent the two largest regions of the brain by volume. Inputs from the hindbrain (0.02 ± 0.003; $t(17)=1.5$,$p=0.076$) and cerebellum (0.009 ± 0.002; $t(17)=1$,$p=0.17$) did not reach statistical significance. This indicates that the densities of neurons in the isocortex, cerebellum, midbrain, and hindbrain are very low while the

densities of labeled neurons was highest in the cerebral nuclei, cortical subplate, and hypothalamus (Figure 15A; Figure 22). Because the midbrain, isocortex, hindbrain, and cerebellum each contained less than a single percent of the ->MeA^{arom+} they were excluded from the main dataset. We have included a detailed summary of all inputs from these minor regions in the supplementary materials (see Figures 23-25; Table 3). Comparison of the cell counts to cell density is included (Figures 22, 26-29).

Synaptic input: finer-scale regions

Closer investigation of five primary sources of input to the aromatase-expressing neurons in the MeApd revealed a consistent presynaptic circuit. ->MeA^{arom+} neurons in the cerebral nuclei were initially divided into the striatum (48.1 ± 1.2; t(17)=10,p<0.0001) and pallidum (11.6 ± 0.6; t(17)=4.7, p<0.0001; Figure 16A). Within the striatum, the MeA, including the 'starter neuron' population accounts for 20 ± 1.3% of the total ->MeA^{arom+} neurons in the brain (Figure 16B; t(17)=3.8, p=0.0007). Regions that border the MeA, including CEA and CP, accounted for an additional (11 ± 0.6; t(17)=4.7, p < 0.0001) and (6.6 ± 0.6; t(17)=2.6, p=0.01) percentage of the overall inputome respectively (Figure 16B). Smaller populations of ->MeA^{arom+} were identified in the IA (0.43 ± 0.04; t(17)=2.7,p=0.0078), nucleus accumbens (0.15 ± 0.014; t(17)=2.6, p=0.009), fundus of the striatum (0.11 ± 0.011; t(17)=2.5,p=0.01), lateral septal nucleus (0.15 ± 0.01; t(17)=3, p=0.0037), and septofimbrial nucleus (0.05 ± 0.006; t(17)=2.0,p=0.034) while the populations of ->MeA^{arom+} in the rest of the striatal regions were not significant (Figure 16D). The largest pallidum projections include the globus pallidus, both external (3.25 ± 0.3; t(17)=2.6,p=0.009) and internal (1.5 ± 0.12; t(17)=3.0, p=0.004) segments; the substantia innominata (2.5 ± 0.2; t(17)=3.2, p=0.0025), the bed nuclei of the stria

terminalis (0.61 ± 0.04; t(17)=3.5, p=0.001), and the diagonal band nucleus (0.5 ± 0.03; t(17)=3.6, p=0.001; Figure 16C).

The hypothalamus provided the second largest source of ->MeA^{arom+} neurons with most inputs located in the lateral (4.5 ± 0.4; t(17)=2.6, p=0.001) and medial (3.1 ± 0.4; t(17)=1.9, p=0.04) zones, with a smaller contribution from the periventricular region (1.0 ± 0.06; t(17)=3.9, p=0.0006) and the periventricular zone (0.25 ± 0.03; t(17)=2.4, p=0.01; Figure 17A). The two hypothalamic regions providing the largest number of ->MeA^{arom+} neurons to the inputome are the lateral hypothalamic area (2.0 ± 0.17; t(17)=3.0,p=0.004) and ventromedial hypothalamic nucleus (1.2 ± 0.16; t(17)=1.9, p=0.04; Figure 17A; extended data).

Both the amygdala and hippocampus are critical for memory and contain large populations of ->MeA^{arom+} neurons. Hippocampal ->MeA^{arom+} neurons are primarily located in field CA3 (6.3 ± 0.6; t(17)=2.7, p=0.007), followed by field CA1 (2.5 ± 0.2; t(17)=3.3, p = 0.002) and CA2 (0.26 ± 0.2; t(17)=2.8, p =0.006; Figure 18A). We also observed ->MeA^{arom+} cells in the hippocampal-amygdaloid transition area (0.22 ± 0.02; t(17)=2.7, p=0.00). The hippocampus is a large structure that spans nearly the entire dorsal to ventral axis of the brain. The vast majority of ->MeA^{arom+} neurons in the hippocampus were located in the posterior ventral hippocampus (Figure 18A).

The largest proportion of inputs from the cortical subplate originate in amygdalar nuclei (Figure 18B), including the posterior amygdalar nucleus (3.8 ± 0.2; t(17)=4.0, p=0.0005) and lateral amygdala (0.1 ± 0.01; t(17)=2.3, p = 0.017). The anterior and posterior basomedial (1.6 ± 0.1; t(17)=3.3, p=0.002; 1.6 ± 0.1; t(17)=3.4, p=0.002] and

anterior and posterior basolateral (0.6 ± 0.06; t(17)=2.6, p = 0.009; 0.3 ± 0.024; t(17)=2.8, p=0.006) nuclei of the amygdala also each showed ->MeA^{arom+} cells.

Within the olfactory areas (Figure 19A), the largest proportion of inputs originate in the cortical amygdalar (4.0 ± 0.3; t(17)=3.8, p=0.0007) and piriform (1.0 ± 0.06; t(17)=4.4, p = 0.0002) areas, as well as the accessory olfactory bulb (1.0 ± 0.1; t(17)=2.4,p = 0.014). Smaller contributions originate in the piriform amygdalar area (0.38 ± 0.03; t(17)=4.5, p=0.00017), the postpiriform transition area (0.34 ± 0.03; t(17)=2.8, p=0.0067).

The largest proportion of input cells originating in the thalamus (Figure 19B) come from the recticular nucleus (0.9 ± 0.15; t(17)=1.6, p =0.07) though this population was variable between individuals and not statistically significant. Additional input came from the ventral group of the dorsal thalamus (0.33 ± 0.04; t(17)=2.1, p=0.025), with smaller contributions originating from the geniculate groups of the dorsal thalamus (0.2 ± 0.03; t(17)=1.2, p=0.1) ventral thalamus (0.08 ± 0.01; t(17)=2.1,p=0.023), midline group of the dorsal thalamus (0.11 ± 0.01; t(17)=2.7, p=0.0002), and lateral group of the dorsal thalamus (0.04 ± 0.005; t(17)= 2.0, p=0.03).

Sex Differences in distribution of observed input cells

Because sex differences in the MeA, and specifically in MeA^{arom+} neurons, are well established (Cooke, et al., 2005; Yao et al., 2017; Billing et al., 2019) we investigated sex differences in synaptic input to MeA^{arom+} neurons. A regression analysis of the cell counts for all male regions against cell counts for all female regions indicated that the major regions providing synaptic input to MeA^{arom+} neurons are largely conserved

across sexes (Figure 20; $R^2 = 0.60252$; $F = 39.4127$; $p < 0.00001$; linear regression). No significant difference was observed for sex when considering all regions (ANOVA: $F = 0.04$ $p = 0.83$); however, there was a significant interaction between region and sex (ANOVA: $F = 1.81$, $p = 0.01$) indicating that a subset of brain regions displayed sex differences in projections to MeA^{arom+} neurons. Post-hoc analyses revealed nine regions that provided more input in males and one region that provided more input in females (Figure 20). MeA^{arom+} neurons received more input from the AOB, basolateral amygdala (both anterior and ventral), CA1 region of the hippocampus, piriform areas, diagonal band nucleus, and lateral preoptic area in males and more input from the ventral premammillary nucleus in females ($p<0.05$: permutation test; Table 4). Additionally, the fraction labeled neurons in the MeA, local to the injection site), was higher in females (29.2 ± 10.7) than males though this trend did not reach significance (13.0 ± 3.5; $p=0.08$: permutation test; Figure 30).

Discussion

Social behaviors require an animal to detect and respond to specific stimuli that signal the identity of a conspecific: rivals, potential mates, and offspring each demand different behavioral responses. As a central component of the social behavior network the MeA plays an important role in interpreting chemicals used to convey social information and producing appropriate behavioral responses (Newman, et al., 1999; Bakker, et al., 2002; Yao, et al., 2017). Here, we focus on a population of neurons in the MeA that express the enzyme aromatase (Naftolin et al., 1975), which has been causally linked to social behaviors (Unger et al., 2015; Lee et al., 2014; Ishii et al., 2017). In this study we identify the broad constellation of synaptic inputs that allow aromatase-expressing MeA

neurons to integrate social information. We show that these neurons receive input from an unexpectedly wide range of regions, with strong inputs from regions linked to chemosensation, memory, metabolism, and the networks underlying social behaviors and decision-making. (Figure 21)

Two regions that are classically associated with the MeA are the AOB and BNST. The MeA is often illustrated as the third node in the vomeronasal pathway: vomeronasal sensory neurons project to the AOB that in turn projects to the MeA (Winans & Scalia; 1970; Scalia & Winans, 1975). Similarly, the BNST and MeA are together considered the extended amygdala, a collective region that processes sensory and social information (Marino, et al., 2016). Using classical retrograde tracing it has been previously shown that most AOB neurons project to the MeA (De Olmos, et al., 1978; Bergan, et al., 2014, with aromatase neurons receiving input overwhelmingly from the anterior subdivision of the AOB (Billing, et al., 2019). Our tracing results demonstrate a clear input to aromatase-expressing MeA neurons from both the AOB and the BNST. However, the collective inputs from the AOB and BNST account for less than 2 percent of the overall ->MeA^{arom+} neurons observed in this study. This result should not be interpreted as evidence that few AOB neurons project to the MeA, but rather, it highlights the larger set of projections coming from areas other than the AOB and BNST. Aromatase-expressing neurons clearly have a wide-ranging role as integrators of information from inputs throughout the brain, illustrating the danger in thinking of the social behavior network as a simple feed-forward network. Moreover, our results indicate that many known *postsynaptic* targets of the MeA are also *presynaptic* inputs to aromatase expressing MeA

neurons, suggesting that the MeA forms feedback loops with many regions in the social behavior network, even at the level of the population of aromatase-expressing neurons.

Nearly all ->MeA^{arom+} neurons were located ipsilateral to the site of injection (Figure 12). This is consistent with previous findings (Canteras, et al., 1995; Bressler, et al., 1996; Bergan et al, 2014) and indicates that afferent sensory information from the left and right VNO is kept separate at least to the level of the MeA. The near complete ipsilateral bias seems surprising given the need to integrate both sides of the body in social behavior. One possibility is that chemical compounds activate each VNO similarly, reducing the need for integration between left and right sides. A second possibility is that, like the auditory system (Clemens, et al., 2015, Schnupp, et al., 2009) or visual system (Krapp, et al., 2001), internasal comparisons provide an additional line of sensory information (e.g. spatial location). In the latter case, our data suggests that internasal comparisons are likely done outside the MeA.

Despite representing more than 12.9% of the brain by volume, the cortex contained less than 0.5 percent of the total identified ->MeA^{arom+} neurons. The only exception to this rule was the piriform cortex which processes olfactory information and provided clear input to aromatase neurons in the MeA, indicating an indirect route for arom+ neurons to integrate input from the main olfactory system with 'direct' vomeronasal input from the AOB. There is also a small input from the thalamus, which may represent an alternative pathway of directing cortical information to the arom+ MeA neurons. Indeed, integration between the main olfactory and vomeronasal systems is critical for adaptive social behaviors and these data indicate that inputs from both systems converge on MeA^{arom+} with direct input from the AOB and multisynaptic input from the

MOB. Consistent with the survival value of sex, parenting, and territorial defense, the brain regions that provide input to aromatase-expressing neurons are evolutionarily old and conserved (O'Connell, et al., 2011).

The vast majority of inputs to the aromatase-expressing MeA neurons were found in cerebral nuclei, hypothalamus, hippocampal formation, cortical subplate, and associated olfactory areas. The remaining regions collectively comprise less than 1.3% of total inputs. Thus, the inputome reported in this study suggests an integration of chemosensory input, emotional processing, memory, and sociosexual behavior regulation by MeA aromatase neurons. A combination of inputs from areas that provide information about the metabolic, reproductive, and attentional status of the animal implies a strong effect of the internal status of the animal on the activity of aromatase-expressing MeA cells that are likely integrated with input from regions involved in voluntary movement and the production of social behaviors. We will briefly discuss these specific inputs by their known functions in the following sections.

Areas involved in detecting chemosensory cues to drive specific sexual discrimination and sociosexual behaviors provide strong input to aromatase-expressing MeA neurons. Inputs from the ventromedial hypothalamus (VMH), posterolateral and posteromedial cortical amygdala (PLCO, PMCO), anterior basomedial amygdala (aBMA), the nucleus of the lateral olfactory tract (LT), and AOB were identified (Nomoto and Lima 2015; Yang et al 2013; Maras and Petrulis 2008; Melis et al 2009; Hashikawa et al 2016; Moncho-Bogani et al 2005; Guo et al 2018; Hammen et al., 2014; Luo et al., 2003). This result is consistent with previous data from MeA, PLCO, AOB,

and LT which are involved in the interpretation of chemosensory signals (Vaz, et al., 2017; Root, et al., 2014; Sosulski, et al., 2011).

Research into aggression, parenting, and sex consistently implicate the ventromedial hypothalamus (Kim, et al., 2019; Wang, et al., 2015) and medial preoptic area (Numan, 1988) as control regions for these behaviors. Recent work highlights the important role of galanin-expressing neurons of the MPOA for parental behavior (Wu, et al., 2014; Kohl, et al., 2018), and a primary source of sensory input for galanin-expressing neurons is the MeA.The MPOA is necessary to produce sex-specific mating and parenting behaviors (Wei, et al., 2018). The MPOA also plays a role in driving positive reinforcement for social interactions (Hu, et al., 2021). By identifying an arom+ MeA neuron-specific interaction between the MPOA and MeA, we can propose a loop between the MeA and MPOA with the potential to mediate positive and negative sex-specific patterns in parental and direct social interaction behaviors. Additional input to arom+ MeA neurons from the perifornical area (PeFA), BNST, and amygdalohippocampal area (AHi) further strengthen the role of the identified MeA arom+ circuitry for parental behavior (Kohl, et al., 2018; Autry, et al., 2021; Lebow, et al., 2016). neurons. Combined with previous data showing afferent inputs from the MeA (Pardo-Bellever, et al., 2012; Cádiz-Moretti, et al., 2016), these data demonstrate that aromatase-expressing MeA neurons have direct access to a parenting circuit (Chen et al., 2019).

Activation of VMH neurons causes immediate territorial aggression (Lin, et al., 2011): this is believed to be, at least in part, due to the role of ESR1-expressing neurons in the VMH (Lee, et al., 2014). A distinct aggressive behavior, pup-directed aggression,

has been linked to the periforncal area (PeF; Autry, et al., 2021), amygdalohippocampal transition area (HATA), and ventromedial hypothalamus. Each of the aggression-linked regions contain neurons that project to aromatase neurons in the MeA, consistent with the observation that chemical silencing of aromatase-expressing neurons in the MeA directly reduces aggression in both male and female mice (Unger, et al., 2015).

Social interactions can be strongly influenced by fear and anxiety in both animals and people (Beery, et al., 2015; Sarnoff, et al., 1961). We found that several nodes of the amygdalar fear network send direct input to MeA aromatase neurons. The central amygdala (CeA; Ferretti et al., 2019), basomedial amygdalar nucleus (BMA), bed nucleus of the stria terminalis (BNST), and zona incerta (ZI) had some of the densest projections to the MeA in the brain; each is tightly linked to regulating anxiety and fear responses (Adhikari et al 2015; Amano et al 2010; Duvarci, et al., 2011; Chou, et al., 2018; Jasnow et al., 2006; Lee et al., 2019; Walker et al., 2003). Initially, this might suggest is that aromatase-expressing neurons are directly involved in the fear response to predators. We think this is not the case as the aromatase-expressing neurons receive sensory information from a class of V1R neurons not associated with predator responses (Billing, et al., 2020, Isogai, et al., 2011). Instead, we predict that these inputs are more likely sculpting behaviors directed towards conspecifics (mates, competitors, and pups) based on the proximity of predators (Apfelbach et al., 2005).

MeA aromatase neurons receive direct input from the hippocampus, known for its role in memory formation and consolidation (Scoville, et al., 1957). Hippocampal inputs to the MeA were not evenly distributed throughout the hippocampus, but rather were concentrated in the posterior ventral hippocampus including the HATA, CA1, CA2, and

CA3. These are also the hippocampal regions anatomically closest to the MeA. Previous data indicate that region CA2 is particularly involved in memory and spatial processing but is also highly receptive to social state and plays a role in the deduction of social novelty (Dudek, et al., 2016). Similarly, the MeA has been linked to social memory (Ferguson et al., 2001) and MeA aromatase neurons have been directly implicated in social discrimination (Yao et al., 2017). We identified direct input from the ventral tegmental area, and together these sources of input may help elevate and reinforce responses to emotionally relevant stimuli (Zikopoulos, et al., 2012). We also identified inputs from areas involved in regulation of voluntary movement suggesting a potential for gating aromatase neuron-dependent behaviors.

A broad set of identified inputs to MeA aromatase neurons are associated with metabolic regulation, including the tuberal nucleus (TN), ventral premammillary nucleus (VPM), lateral hypothalamus (LH), and ventromedial hypothalamus (VMH). However, a hallmark of social behavior is that the pattern of social behaviors observed in young animals is different from those observed in adult animals. The transition from juvenile to adult behaviors depends on metabolic constraints including body weight and fat content (Castellano, et al., 2016). The observed input from brain regions that regulate metabolic state (Luo, et al., 2018; Donato & Elias, 2011; Nisbett 1972; Berthoud and Munzberg 2011) further supports the role of the MeA as a node responsible for coordinating social behaviors in accord with internal state, reproductive readiness, environmental contexts, and reinforcement signals (Padilla et al., 2016; Harris et al., 2005; King, 2006; Ross et al., 2018). This suggests that information about sexual receptivity and readiness are

integrated with other relevant cues about conspecifics in the aromatase-expressing cells in the MeA.

In accord with the role of MeA, and aromatase neurons, in sexually dimorphic social behaviors, the MeA displays structural, molecular, and functional sex differences (Nishizuka and Arai, 1981; De Vries et al., 1984; Cooke et al., 1999; Morris et al., 2008; Bergan et al, 2014; Billing et al., 2019; McCarthy, 1994). In fact, the domestication process of creating isogenic mouse strains may have accentuated sex-differences in circuit function (Chalfin, et al., 2014; Bansal, et al., 2021). We found that the broad pattern of regional inputs to aromatase-expressing MeA neurons was conserved across males and females; however, a number of regions displayed a quantitative difference in the percentage of inputs observed in males as compared to females. Of the ten regions identified as having a quantitative sex-difference, nine had more labeled neurons in males. One possible explanation for this male bias is that the percentage of connections made by aromatase-expressing neurons inside the MeA is higher in females as compared to males. This hypothesis is partially supported by our data, which indicates more neurons labeled in the female MeA versus the male MeA; however, this trend did not reach significance. To account for variability in the levels of starter neurons infection, our analyses here rely on normalizing cell counts in each region by the overall number of identified neurons, and therefore, we cannot distinguish between a reduction in the number of local connections versus an enhancement of long-range connections.

The regions displaying sex differences provide new insights into the function of aromatase-expressing MeA circuits. The ventral premammillary nucleus was the only region identified with more neurons labeled in females and this region has recently been

identified as a critical mediator of maternal aggression (Motta, et al., 2013). This is consistent with the role of aromatase-expressing MeA neurons in aggression in female mice (Unger et al., 2015). Regions with more neurons in males are linked to fear and anxiety (Yang, Y, et al., 2017), social and contextual memory (Okuyama, et al., 2016), mate identification and olfaction (Cádiz-Morretti, B., 2016; Wang, L, 2020a), regulation of neuropeptide secretion (Brown, 2016), and male-specific sexual behavior (Schmidt, et al., 2000). Still, like the social behaviors mediated by MeA arom+ neurons in mice, the circuits that mediate these behaviors are sculpted differently in males and females, and these differences in circuit connectivity likely support sex differences in social behavior.

Conclusions

We comprehensively identified the inputome of aromatase-expressing MeA neurons, finding the sources of direct synaptic input to aromatase-expressing MeA neurons through rabies-based circuit mapping in the intact brains from transgenic animals expressing cre-recombinase under the control of the aromatase promoter. Presynaptic inputs were identified through a semiautomated algorithm, which provided an unbiased view of the circuit. Data from each individual is set in a standard reference frame that allows direct comparisons among brains, as well as to future datasets using a similar approach.

Our study confirms that known sources of synaptic input to MeA neurons (e.g., BNST and AOB) synapse specifically on arom+ neurons in the MeA. However, we also identified a broad set of subcortical inputs that have not been previously reported indicating that aromatase neurons in the MeA represent a critical node for integrating an

array of internal states for the generation of social behaviors. The broad input to aromatase neurons reveals a framework that allows the aromatase-expressing MeA neurons to occupy a critical position in the social behavior network, with a role in nearly all known social behaviors ranging from parenting and reproduction to aggression and learning. While the overall pattern of inputs was similar in males and females, specific regions displayed sex differences in connectivity with aromatase-expressing MeA neurons further solidifying the role of these neurons as a control center for sex-specific social behaviors that are critical for survival.

CHAPTER 4

AN EXPANDED ROLE FOR EARLY SENSORY AREAS IN SHAPING PERCEPTIONS OF SOCIAL STIMULI

Introduction

The presence of a predator in the environment poses a clear threat and impacts a wide array of behaviors in prey animals (Creel, et al., 2014). The American prairie dog uses an alarm sound to communicate to all surrounding prairie dogs that they perceive a predator close by (Merriam, 1902). These social signals can have profound effects on the behavior of all animals that receive them. A classic example of group dynamics in prey animals, shoaling fish from high predation environments form larger, more cohesive shoals compared to similar groups from lower predation environments (Herbert-Read, et al., 2017). In numerous mammalian species the presence of predators promotes grouping behaviors, decrease foraging, and decrease exploratory behaviors in an effort to ward off predation (Creel, et al., 2014; St-Cyr, et al., 2018; Padilla, et al., 2016).

A distributed network of regions in the brain work together to process social sensory information and to determine and execute appropriate, often sex-specific, behavioral responses to a given social stimulus (Newman, 1999; Yao, et al., 2017). This network, commonly known as the social behavior network (SBN) contains several subcortical brain regions that play an integral role in the production of social behavior, including fear and predator defense behaviors (Newmann, 1999).

While predator presence can have a prolonged impact on animal behavior more broadly and social behaviors more specifically, we know less about how the presence of a predator impacts the neural response to conspecific social stimuli (St-Cyr, et al., 2018).

Many animals produce and recognize specific semiochemicals in the environment that communicate social information about surrounding conspecifics and the presence of predators in the surrounding area (Dulac and Axel, 1995, Papes, et al., 2010). Mice rely heavily on chemosensation to interpret the social environment and guide both social interaction and communication (Bradley, et al., 2002; Keller, et al., 2006b). The majority of these chemosensory signals, sometimes referred to as pheromones or allomones, are recognized by a suite of vomeronasal receptor-expressing neurons that encircle the interior of the cylindrical vomeronasal organ which sends input to the accessory olfactory bulb. The accessory olfactory bulb (AOB) receives input from the vomeronasal organ (VNO), processes these sensory signals, and sends the resulting information via mitral and tufted cells to the social behavior network.

Previous work has shown distinct effects of predator scent on the AOB responses of both males and females in anesthetized animals (Ben-Shaul, et al., 2010; Bergan, et al., 2014). These experiments used solely urine stimuli and were not performed on awake animals (Ben-Shaul, et al., 2010; Bergan, et al., 2014). Accordingly, these experiments could not observe the neural and behavioral impact of the presence of a predator in the environment on the responses of a given animal

to conspecific stimuli. Using a genetically constrained optogenetic approach (GcaMP6s), we were able to record signals from the specific AOB mitral and tufted cells that project directly to the social behavior network in awake and behaving animals (Figure 31). This allowed us to define the contributions of sensory cells in the AOB to observed effects of stimulus origin.

Results

Behavioral Analysis

We injected 9 female and 7 male tbet:Cre mice (Tbx21-cre: Jax Labs; Figure 31A) in the AOB with a conditional GcaMP-expressing vector (AAV9:Syn:FLEX:GCaMP6s:WPRE:SV40; addgene Plasmid #:100845; Chen, et al., 2013) that only infected the cre-expressing tbet cells (Figure 31B). This produced animals where fluctuations in GCaMP fluorescence indicated neural activity in the mitral and tufted cells of the olfactory bulb (Figure 31C). Following fiber-implantation into the AOB, we were able to record neural activity in the mitral and tufted cells of the AOB mitral and tufted cells specifically in awake and behaving animals.

To minimize confounding variables in the presentation of social stimuli, we developed an automated stimulus presentation box (Figure 31D). This box allowed us to present an experimental animal with access to one of three stimuli (male conspecific, female conspecific, or predator stimulus or control) with no human interference on a computerized schedule (Figure 31E). Each animal performed six

experiments, which consisted of a series of seven stimulus presentations of each stimulus, in conditions where the predator stimulus was present and six experiments where the predator stimulus was not present (Figure 31E).

While the estrus state of the experimental and stimulus animals is an important consideration for these experiments and the estrus state of the experimental animals will be analyzed; we did not collect estrus states from the stimulus animals. Thus, differential estrus states are an important consideration that requires further investigation.

We identified the location of the experimental animal's nose during each behavioral paradigm using DeepLabCut (Mathis, et al., 2018) and then determined the amount of time that each animal spent in the proximity of the stimulus animal (Figure 32). In addition to automatic position data, both social and non-social behaviors were manually scored throughout each experiment. For example, we determined when an animal was in the vicinity of a presented stimulus animal with the head directly facing the stimulus and labeled these epochs 'social interaction'. We then combined manual scored behaviors with automatically scored position data and as expected, social interaction states were heavily skewed towards times when the experimental mouse was in close proximity with the stimulus (Figure 31G).

Looking at the distance over time for all animals, we saw that animals spent more time close to the conspecific stimuli as opposed to either the control or predator scent stimuli (Figure 33). The only exception to this pattern was that male

experimental mice spent roughly equal time near the predator stimulus and the male stimulus (Figure 33). Both males and females spent more time around female animals compared to male animals in experiments without the predator stimulus present (Figure 34). The addition of the predator stimulus, presented during different trials from the conspecific stimuli, increased the amount of time mice spent near conspecific stimuli (Figure 34C).

We did not observe differences between the sexes in the amount of time spent around the male stimulus in conditions with the predator present ($t(533) = 1.2149$, $p = 0.23$). We do see a significant increase in the amount of time a male spends near a male ($t(578) = 5.0541$, $p < 0.0001$) or female ($t(578) = 5.7206$, $p < 0.0001$) stimulus without the predator stimulus present in the trial. We also see a significant increase in the time a male animal spends near a female animal when the predator stimulus is included in the trial ($t(533) = 8.2507$, $p < 0.0001$). In these cases, experimental males spent more time close to the female stimulus than did experimental females (Figure 34C).

We also observed a trend of animals spending more time in the 'social interaction' area during predator conditions when compared to the non-predator conditions (Figure 34). When controlling for the presented stimulus we see a statistically significant increase in the time a female animal spent near a male stimulus when the predator stimulus is added ($t(578) = 5.1519$, $p < 0.0001$) as well as in the male animal when the female stimulus is presented ($t(533) = 1.9921$, $p = 0.047$). These effects represent a greater increase in the time spent by animals in the

'social interaction' area for opposite-sex stimuli (Figure 34C). There is a more measured increase in the amount of time a male ($t(533) = 1.0692$, $p = 0.29$) and female ($t(578) = 1.6697$, $p = 0.96$) spends in the 'social interaction' area of same-sex stimulus animals and a similar trend in the increase in the time spent in the vicinity of the non-animal stimulus when the control stimulus is replaced with predator scent (Figure 34C).

Neural Signals

Using the recorded fiberphotometry signal from each experimental set along with the stimulus presentation and manually scored behaviors, we were able to isolate epochs consisting of 20 seconds before to 40 seconds after each stimulus interaction. We controlled for individual differences in signal strength by calculating the z-score of fiberphotometry signal and then compared the resultant z-score responses relative to the onset of each behavior (Figure 35).

Initial observations of the fiberphotometry responses to a social interaction reveal a consistent pattern of activity across all conditions (Figure 35). Typically, a sniff produced minimal variation before the interaction and a small peak at the point of the interaction. This was followed by a sharp decrease in signal for the first 5 seconds post-interaction, and then a sharp increase in neural signal over the course of the next several seconds, which culminates in a high signal response that then fades over time (Figure 35). When comparing between responses we focused on measuring the magnitude of the post-interaction peak as a direct comparison. To determine statistical significance, we performed a two samples Kolmogorov–

Smirnov test comparing the average signals in each condition from the point of interaction (0) to 20 seconds post interaction (+20).

We compared responses to male, female, and predator stimuli in both male and female animals. While responses to male, female, and predator stimuli were much stronger than those to control, the average bulk responses to male and female stimuli were quite similar (Figure 36). Sex differences in neural responses to social interactions were small in conditions with the predator stimulus present. In these experiments we observed a 15.2% increase in peak z-score response to a male stimulus in the female animals 0.5439 when compared to the peak z-score response in male animals of 0.4721 ($ks2stat = 0.3990$; $p < 0.0001$). This effect is also observed in response to a female stimulus where the female animals displayed a 4% higher peak z-score response of 0.5381 when compared to the male animals' peak z-score response of 0.5169 ($ks2stat = 0.2045$; $p < 0.0001$; Figure 36).

In stimulus presentations where the predator stimulus is not included, we observe an increased difference in male and female neural responses to male and female stimuli, even though the magnitude of the signal is markedly reduced in both sexes. In response to a male stimulus the female animal displayed a peak z-score response of 0.2477, which represents a 66.1% increase over the male animal peak z-score response of 0.1491 ($ks2stat = 0.3840$, $p < 0.0001$). We see a similar effect in response to a female stimulus. In these conditions, the females' peak z-score response of 0.2658 represents a 43.6% increase in peak response over the male peak z-score response of 0.1851 ($ks2stat = 0.4713$, $p < 0.0001$). It is also notable

that the female animals showed a higher signal than males post interaction in response to both male and female stimuli in predator and non-predator conditions (Figure 36). However, these putative sex differences in neural signaling are subtle and were not statistically significant in the current dataset.

While the individual fiberphotometry experiments did not demonstrate differences in the response to conspecific stimuli presented in the context of predator stimuli or in a context without predator stimuli, the presence of a predator stimulus resulted in a consistent increase in the magnitude of AOB responses to all stimuli (Figure 35F). This was true even though the predator stimulus was never presented simultaneously with the conspecific stimuli. In response to all stimuli in male and female animals the peak signal following an interaction was more than doubled (Figure 37). We see a distinct, positive effect of the predator stimulus on the average neural responses. We observe 85.7 % of male animals and 71.4 % of female animals show higher peak responses to a female stimulus when the predator is present and 71.4 % of male and 85.7 % of females show higher peak responses to a male stimulus when the predator stimulus is present.

The addition of a predator stimulus resulted in a more than doubling of peak interaction responses in male and female animals. In female animals, z-score responses to a female stimulus presentation increased by 117.2% from 0.2477 to 0.538 with the addition of a predator stimulus ($ks2stat = 0.7057$; $p < 0.0001$), while responses to male stimulus presentation increased 104.6% from 0.2658 to 0.5439 with the addition of a predator stimulus ($ks2stat = 0.6035$; $p < 0.0001$). Male

animals display an even more pronounced increase in predator effects. In male animals the addition of a predator stimulus causes a 246.7% increase in peak z-score responses from 0.1491 to 0.5169 when the female stimulus was presented (ks2stat = 0.6933; $p < 0.0001$) and a 155.0% increase in peak z-score from 0.1851 to 0.4721 when the male stimulus was presented (ks2stat = 0.7456; $p < 0.0001$; Figure 37). These data demonstrate a clear and significant impact of the predator scent on neural responses to male and female social stimuli in both male and female animals.

Discussion

In this study we show that presentation of a predator stimulus impacts subsequent social interactions in which an animal engages even without the predator stimulus being available. We can see that the addition of the predator stimulus to any given experiment increases the amount of time that an animal spends near a presented stimulus (Figure 34C).

In high-predation environments, prey animals undergo behavioral changes that reduce predation (Creel, et al., 2014; Herbert-Read, et al., 2017; St-Cyr, et al., 2018). These behaviors include a lack of exploratory foraging behavior and the formation of larger-than-normal social groups (Creel, et al., 2014). Previous research has shown that maternal mice exhibit reduced foraging and increased immobility behaviors (Padilla, et al., 2016; St-Cyr, et al., 2018). Consistent with previous observations of predator-induced behavioral changes (Creel, et al., 2014; Herbert-Read, et al., 2017; St-Cyr, et al., 2018) we observed an increase in the amount of time animals spend close to conspecific stimuli (Figure 33). An increase

in time spent near conspecifics is a hallmark of a defensive behavior performed by prey animals known as grouping. In grouping, animals form larger and more cohesive groups to ward off predation (Creel, et al., 2014). Our data may show an aspect of this effect at play.

While we did not observe strong or consistent sex differences in neural responses to stimulus interactions, these data should not be seen as suggesting that sex-specific representations of social stimuli do not exist in the AOB. While our data show a limited effect of the sex of stimulus animals on neural responses, it is important to consider that our data reflect a bulk collection of neural responses. Previous research has shown that individual clusters of cells in the AOB encode sex-specific stimuli (Hammen, et al., 2014; Ben-Shaul, et al., 2010). By collecting signal fluctuations across the entire AOB we are averaging across neurons that respond specifically to male and female stimuli, and single cell resolution is critical to understand the absolute encoding of any stimulus.

Fiberphotometry responses during social interactions were larger when a predator stimulus was added to the experiment (Figure 35), and this was true in both male and female experimental animals (Figure 36). There are several, non-mutually exclusive mechanisms that could drive the observed predator-induced changes in behavior and neural activity in response to conspecific social stimuli. First, AOB neurons may recognize the presence of the predator stimulus intrinsically and increase response to conspecifics through local interactions. Second, predator odors may impact the AOB indirectly through feedback from other

brain regions. In this scenario, the presence of a predator would activate downstream, threat-detecting brain regions (e.g. the SBN) and a subset of these regions may modulate AOB responses to social stimuli, through feedback to the AOB, when a predator stimulus is present. Third, predator stimuli could change in the rate of habituation of AOB neurons to conspecific stimuli in response to the predator stimulus. By averaging responses over each interaction from each animal, we may be obscuring a natural decrease in responsiveness to conspecifics over time that is suppressed in the predator conditions. This could lead to our observed heightened responses to conspecifics in the predator conditions.

Additional recordings of downstream SBN regions that may provide reciprocal connections to the AOB may provide insight into whether these changes are mediated by interactions within the AOB or the greater SBN. Further examination of estrus states of the experimental animals in these experiments may also provide an insight into an environmental effect outside of the AOB impacting AOB responsiveness and animal behavior. Additional analysis of the order of collected data and the possible effects of trial and experiment number for each animal may also reveal a potential impact of habituation on the effect of predator stimuli on AOB responsiveness to conspecifics.

This study demonstrates that the presence or absence of a predator stimulus in a given social situation has a significant impact on the behavioral and AOB responses of an animal to a conspecific. This effect is robust and observed in males and females in response to male and female stimuli. This suggests an expanded role

of the AOB in initial processing and shaping of social stimuli before it is sent to the SBN.

Methods

Animal Use

All experiments were performed in strict compliance with the National Institute of Health. All animals were handled according to a protocol approved by the UMass Amherst Institutional Animal Care and Use Committee (IACUC; protocol #2018-0014 and #2017-0060).

Sixteen adult mice (2 to 8 months old, both female (n=9) and male (n=7)) from an existing transgenic mouse line (Tbx21-cre: Jax Labs) were housed in a temperature (22°C) and light (12hr: 12hr light: dark) controlled facility, with *ad libitum* access to food and water. The transgenic line expresses the enzyme cre-recombinase in all mitral and tufted cells in the MOB and AOB (Haddad, et al., 2013). By targeting subsequent GCaMP infection to the AOB mitral and tufted cells using a conditional vector, we were able to record activity of the specific cell populations that provide direct projections to the MeA (Scalia and Winnans, 1975). The tbx21-Cre transgenic line was generated by BAC recombination (Haddad, et al., 2013); its expression pattern faithfully recapitulates endogenous tbet expression (Haddad, et al., 2013) and displays no known behavioral deficits in either heterozygous or homozygous animals.

Surgeries

We used conditional GCaMP expression to record from active tbet-expressing neurons in the awake, behaving animal (Nakai, et al., 2001). We injected the AOB (Bregma 3.5, Lateral 1.0, Depth 1.0) of these tbet:cre mice that express cre-recombinase in all mitral and tufted cells in the MOB and AOB, with a conditional GCaMP expressing AAV virus (AAV9:Syn:FLEX:GCaMP6s:WPRE:SV40; addgene Plasmid #:100845; Chen, et al., 2013). This produced a mouse that expressed GCaMP in all the mitral and tufted cells in the AOB and MOB.

Fiberoptic implants were custom made by inserting a 10 mm length of 440 μm diameter silica optical fiber (Ploymicro, FIP400440480) into a 440 μm ceramic ferrule (Thor Labs, ADAF2) and securing with acrylic adhesive. Fibers were then implanted into the same hole used for initial injections of AOB with the conditional GCaMP (Bregma 3.5, Lateral 1.0, Depth 1.0) at the same position as the virus was itself injected. The fibers were secured to the skull using dental cement and the animal was left to rest for the next 72 hours.

Behavioral Paradigm

Animals were placed in a customized robotic stimulus presentation arena. This arena (24” by 24”) contained computer-controlled cages that rotate in three corners of the box. These contained the stimuli that the animal was to interact with. These stimuli included male and female conspecifics (2 to 8 month black6 mice) as

well as either an empty cup (control) or a cup containing a cotton square with 1 ml of 1:100 diluted fox urine in it (predator).

Experimental animals were attached to a 2-channel Doric Rotary Fiber Photometry System (Doric, RFPS_S) and placed in the box. The fluorescence signal from the GcaMP is recorded through the Doric system as the animal is recorded interacting with the animals in the small, computer-controlled cages in the corners of the box over the course of 47 minutes. During this time the opening of the various cups is pseudo-randomized over 7 repetitions with an initial 2-minute habituation and post-experimental recording phase. During a single trial one cage is opened to allow the experimental animal to interact with the animal in the cage for one minute. The cage is then closed for one minute before the following cage is opened. This continues until the animal has had the opportunity to interact with each cage seven times. Each animal performed up to six of these trials over the course of experimentation for the 'no predator' and 'predator' conditions.

Behavioral Scoring

As the animals are not constant in their interactions, we proceeded to score the exact times that the animal was performing a specific action using a custom MATLAB script-based interface (mathworks). These actions included sniffing and approaching each cup as well as monitoring the relative position of the animal in relation to the open cup. We identified an animal as engaging in social interaction when they were within a small radius of an open cage (identified visually as a 1/8 section of the box on the video). They were identified as engaging in exploratory

behavior if they were outside of this small radius of the cage or within this radius with a closed cage. A sniff was scored when an animal placed their nose inside of the cage of the stimulus animal. These sniffs were each labeled based on the identity of the stimulus they were sniffing.

Animal location was recorded from six individual points on the animal using DeepLabCut machine learning (Mathis, et al., 2018). Using the recordings of the animal's behavior in the box, the position of the animals' nose, left and right ears, torso, base of tail, and fiber implant were tracked throughout each experimental run.

Data Processing

Custom MATLAB (mathworks) scripts were used to align the signal from the Doric recording setup with the videos of the box and computers organization of stimulus presentation. Manual scoring data was then aligned to the Doric recordings, which allowed us to observe signal changes at the point of presentation. The Doric signal was normalized to a z-score to allow multiple recordings to be compared effectively.

Statistical Analyses

Paired Samples T-test

We collected all instances of possible interaction across all animals in all experimental conditions and determined the amount of time that an animal spent within 12 cm of the available stimulus. We collected these measurements for each instance of

stimulus availability and formed these measurements into groups that differed by the sex of the experimental animal, the sex of the stimulus animal, and the presence of the predator stimulus in the stimulus presentation paradigm. A paired samples t-test was performed comparing these groups to each other over all interaction opportunities in MATLAB (Mathworks) using the function 'ttest2'.

Two Sample Kolmogorov–Smirnov Test

We collected all fiberphotometry data for each instance of an animal interacting with a male or female stimulus across all experimental conditions. We isolated the epoch from the moment of interaction to 20 seconds post-interaction for each of these instances. Fiberphotometry signals were expressed as a z-score. We averaged the signal responses in groups comparing responses to each sex of stimulus animal presented with and without a predator stimulus present in the presentation paradigm to reveal an average response pattern for each condition. The kstest2 function for MATLAB (Mathworks) was performed on this 20 second epoch of the average fiberphotometry signals post interaction for each condition.

Tissue Processing:

Following the final behavioral trials, animals were deeply anesthetized with isoflurane and perfused with 50ml cold PBS followed by 25 ml cold PFA (4% in PBS). The brain was extracted and post-fixed in 25 ml PFA (4% in PBS) at 4 ˚C overnight. Tissue was sliced at 100 μm on a Leica vibratome and mounted to slides before imaging with a fluorescent microscope.

CHAPTER 5

CONCLUSIONS

These collected studies aim to better understand how the brain 'decides' which social behaviors to engage in based on social stimuli and the context in which those stimuli are presented. The first study described in this document illustrates the development of a technique that allowed us to visualize the specific circuitry responsible for driving social behaviors in response to social stimuli. Using this approach, our second study reveals that a brain region that is critical to the development of social behavior, the medial amygdala (MeA) receives inputs far beyond the previously reported sensory information (Scalia and Winnans, 1975). We identified scores of inputs from subcortical regions throughout the brain to the MeA. These regions were involved in the production of socio-sexual behaviors, parenting and aggression, memory, and the maintenance of homeostasis. These results suggest an expanded role of for the MeA, where, beyond simply responding to socially relevant sensory stimuli, the MeA itself may use a broad range of internal physiological and external environmental factors in combination with a socially relevant sensory stimulus to 'decide', an appropriate behavioral response. In the final study we investigated the role of the environment in the neural responses of awake and behaving animals to sensory social stimuli. By recording activity in the neurons of the accessory olfactory bulb (AOB), we identified that the addition of a predator into an environment where the animal can interact with male and female conspecifics altered the sensory representation of conspecific social stimuli and resulted in a change in the behavior of the animal. Taken together, these studies suggest an enhanced role for the

regions that make up the SBN and the MeA in the integration of important internal and external environmental factors with sensory stimuli to drive appropriate social behaviors.

Chapter 1

The development of the MHD-accelerated clearing and labeling approach to tissue processing was an integral step in the study of the circuits that drive social behavior in the mouse. By using MHD-accelerated clearing in conjunction with light-sheet imaging on fluorescently labeled, intact tissue samples, we were able to efficiently image circuits that work together to drive social behavior in the mouse. This approach provided higher quality tissue faster than can be achieved using other techniques. This allowed us to visualize small, fluorescently labeled cells deep within the subcortical regions of the brain without the need to thinly slice tissue. This subcellular resolution even allows for tracing of processes that connect cells together. In addition to removing lipids from tissue, we were able to drive antibodies into the tissue—allowing labeling of molecular targets in large tissue samples. Using these developments, we were able to quickly image dozens of tissue samples and identify the specific labeled cells throughout the entire brain. By revealing neural connectivity across so many samples, we were able to reveal foundational motifs of circuitry that are shared across individuals. This ability clears the way for further, more extensive circuit-mapping projects that will allow researchers to identify the foundational elements upon which the tangled web of neural connections is based.

Chapter 2

Using the newly developed MHD-accelerated clearing approach allowed us to develop an exhaustive, brain-wide inputome of the aromatase-expressing neurons in the MeA. The MeA was traditionally viewed as a relay node in the SBN that would integrate sensory information relating to social information and use this information to drive an often sex-specific behavioral response (Bergan, et al., 2014). While past research has shown clear MeA inputs from the AOB and MOB (Scalia and Winans, 1975), we reveal that the MeA receives inputs from a vast array of subcortical brain regions.

We identified that the aromatase-expressing MeA neurons receive inputs from scores of subcortical brain regions that serve a unique constellation of roles ranging from the maintenance of homeostasis, to driving parenting and aggression behaviors, to facilitating memory, fear, and anxiety responses. The distinct subcortical nature of these inputs suggests that these connections are highly conserved and points to the evolutionary importance of social behavior production across many species. It may be that these connections and perhaps the aromatase-expressing MeA neuron populations themselves are conserved across a similarly large swath of species. These data both confirm the long-established connections from the AOB, which recognizes important socially relevant sensory stimuli, and suggest an expanded network of connections that may work together to drive social behavior. The distinct connections between several regions that are integral for survival and a population of neurons involved in the production of social behaviors underscore the importance of this potentially highly conserved system of social behavior production.

Chapter 3

Using the accessory olfactory system in the mouse as a model for a socially relevant sensory stimulus driving a behavioral response, we used fiberphotometry to record from AOB activity in mice in response to male, female, and control stimuli in conditions with and without a predator stimulus present. Our results reveal an impact of predator stimuli on early sensory perception of social stimuli in the AOB. Indeed, both the behavior and neural signals driven by stimulus animals changed when a predator was included in the experiment. The mice in the predator condition exhibited increased neural responses to conspecifics and spent much more time near the stimulus animals as compared to the conditions without the predator condition. These behavioral changes are consistent with a series of defensive prey behaviors known as 'grouping' and reduced mobility. This suggests not only that the AOB reacts differently to the same stimulus when a predator is introduced in both male and female experimental animals, but also that these changes may play a role in shaping the behavior of these animals. However, it is important to consider that we have only correlations between these neural effects and behavior, and any insight into behavioral causality requires further study.

These findings present even more complexity in the brain circuitry that drives behavioral responses to socially relevant sensory stimuli. Is it possible that the MeA could use reciprocal connections with sensory processing areas along with its myriad of subcortical connections to modify sensory perceptions of social information? Reciprocity is an important feature of the SBN, where the individual nodes that comprise the network are highly interconnected (Goodson,et al., 2005; Newman, 1999). While these data only focus on a single sensory modality, the deeply conserved nature of the SBN suggests that

other sensory modalities may show similar enhancements. These questions provide an exciting foundation for future study into the role of an animal's external environment on its sensory perception.

Limitations

While the presented studies demonstrate and expanded framework for the environment around an animal to impact their response to social behavior, there are some notable limitations of these studies. In our functional assays, in which we demonstrate neural and behavioral impacts of predator scent in awake and behaving mice, we do not identify the estrus state of the experimental and stimulus mice. Females are both more receptive to mating, and more attracted to male major urinary proteins during late diestrus (Lovick, et al., 2021). It is also noteworthy that we use a novel automated stimulus presentation technique, whose impact on mouse behavior remains to be seen. An automated stimulus presentation paradigm, while eliminating possible human confounds, may introduce yet unknown, unique confounds to the stimulus presentation approach. An additional variable that may impact the neural and behavioral responses to social stimuli in our experimental mice is the relative novelty of the presented stimulus and the effects of habituation on repeated exposure to these same stimulus animals. Future analyses and experiments will need to account for these effects.

Taken from a broader perspective, our experimental model and predator stimulus themselves are limiting. While we often like to generalize mouse behavioral responses, we present only data from a single strain of mouse that is highly inbred and specifically used in laboratory studies (c57:Black6). These mice have been selectively bred for

enhanced social interaction and docility. While it is unfair to say that studies that involve the use of model organisms are without value, it is important to understand that generalizability is only achievable through further study. This critique includes our anatomical, functional, and behavioral insights into the social behavior of the mouse and demands future research into other mouse strains and other vertebrate species to confirm our results are translatable.

Future Directions

While we identified a correlation between the sensory cells that process socially relevant sensory stimuli and environmental factors in an awake and behaving animal, it remains to be seen what impact, if any these environmental factors have on the neural activity of the cells of the SBN regions that drive social behaviors. Future research should focus on understanding not only the mechanisms by which sensory perception in the accessory olfactory system is impacted by environmental factors, but also the impact of these environmental factors on the other socially relevant sensory modalities and the social processing hubs that these regions project to. By understanding the true impact of the environment on sensory perception and behavior production, we can begin to understand how the SBN cells that receive hundreds of subcortical inputs from around the brain use this information to 'decide' how to drive a specific behavior.

Implications

These studies present a new perspective on the neural circuitry that drives social behavior in response to socially relevant sensory stimuli. Beyond simply accessing information communicated from another animal through sensory signaling, we show that

the MeA has access to a wide range of information about the animal itself and the environment in which it resides. While the precise role of this information in processing inarguably socially relevant sensory stimuli and the impact of these factors on animal behavior remains unclear, we do see hints that the MeA may work to modify sensory perception in response to changes in the environment or the state of the animal. These insights highlight the need for further research into the exact functional role of the MeA in the production of social behavior in response to sensory social stimuli.

APPENDICES

APPENDIX A

FIGURES

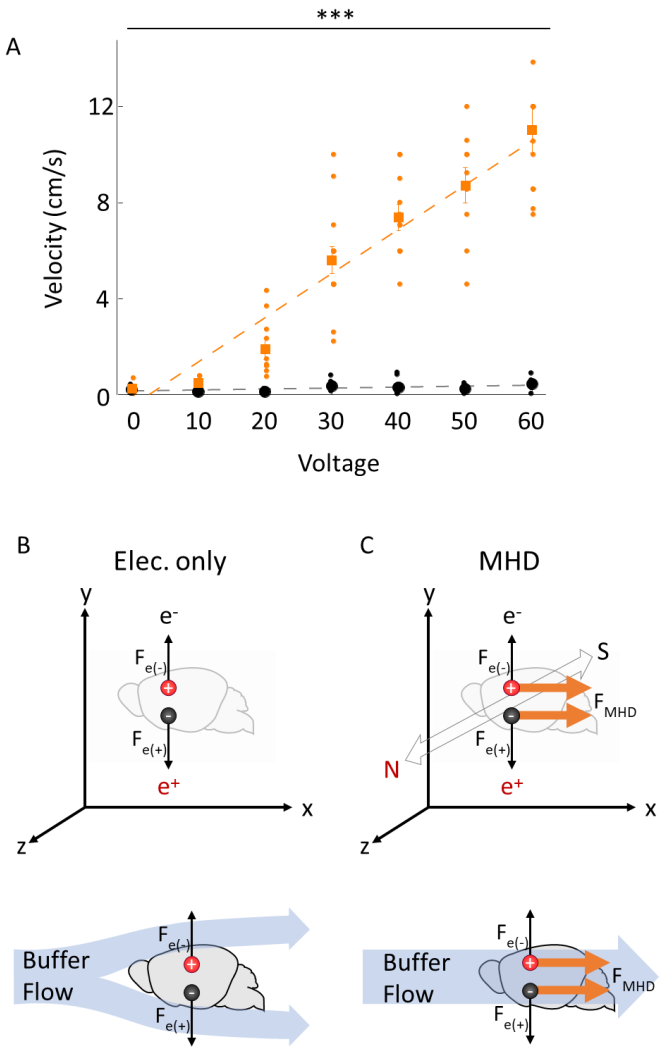

Figure 1: Comparison of voltage effects on buffer velocity between MHD and electrical forces.

(**A**) Velocity of sodium alginate spheres through the MHD-accelerated clearing device with (orange) and without a magnetic field (black; N = 7; error bars: standard error of the mean). MHD-acceleration increases produced higher velocities than electric-only across all voltages ($p < 0.0001$ (***); 2-way ANOVA ($F\{2,6\} = 38.51$; pairwise comparisons: 10 V: $p = 0.002$, 20 V: $p = 0.0005$, 30 V: $p < 0.0001$, 40 V: $p < 0.0001$, 50 V: $p < 0.0001$, 60 V: $p < 0.0001$). The MHD and electric datasets are fit to linear models $y = 0.18x - 0.48$ (orange) and $y = 0.004x + 0.15$ (grey) respectively. Illustrations of the effects of an electric field (**B**) or conjugated electric and magnetic field (**C**) on positively charged (red) or negatively charged (black) particles. The force induced on each particle by the electric field alone (black arrow) and MHD force (orange arrow) are shown as vectors. The cartoons below show the buffer flow induced by an external pump in conjunction with electrical force (**B**) or by MHD force alone (**C**). The flow of the buffer is shown as blue arrows where the MHD force (orange vector) continues to push buffer through the tissue, while the external pump produces flow around the tissue.

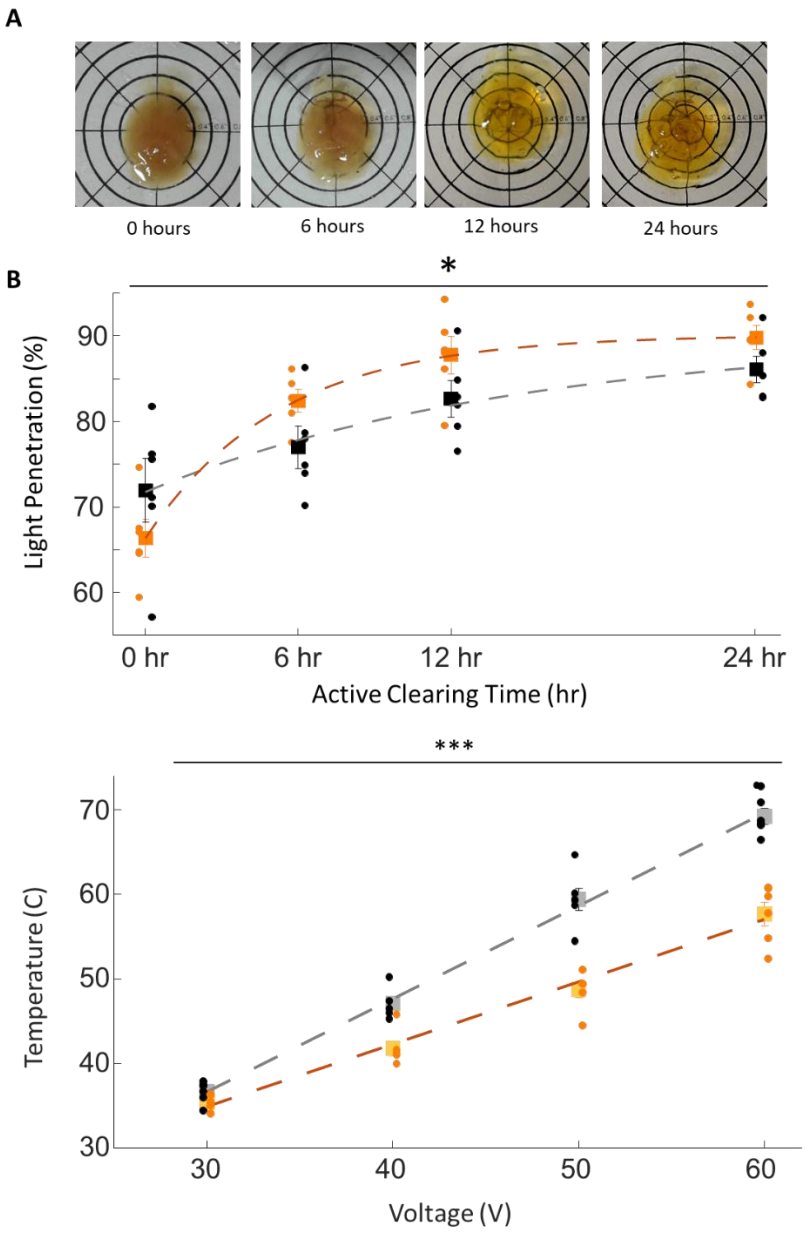

Figure 2: MHD-accelerated clearing of the intact mouse brain. (**A**) Representative examples of intact cleared brains actively cleared with MHD for 0, 6, 12, and 24 h and then equilibrated in RI-matching solution (N = 6). (**B**) Measurements of the optical transparency of mouse brains cleared using MHD force (red) or electrical force combined with a pump to circulate buffer solution (black). Transparency was measured as percentage wide-spectrum light penetration through the tissue. Both MHD and electric only data were fit to saturating exponentials (MHD: $y=89.9-18.2*e^{-0.07x}$; Electric-only: $y=90.1-23.8*e^{-0.19x}$). A significant interaction between electrical and MHD clearing over time is denoted by an asterisk $F\{2,3\} = 3.24$, $p = 0.03$. (**C**) Average peak temperature of tissue actively cleared with MHD (orange) was lower than electric-only (black) at voltages ranging from 30 to 60 V (two-way ANOVA $F\{1,3\} = 119$, $p < 0.0001$; linear fit for electric-only $y=1.1x+3.6$; linear fit for MHD: $y=0.7x+12.7$.

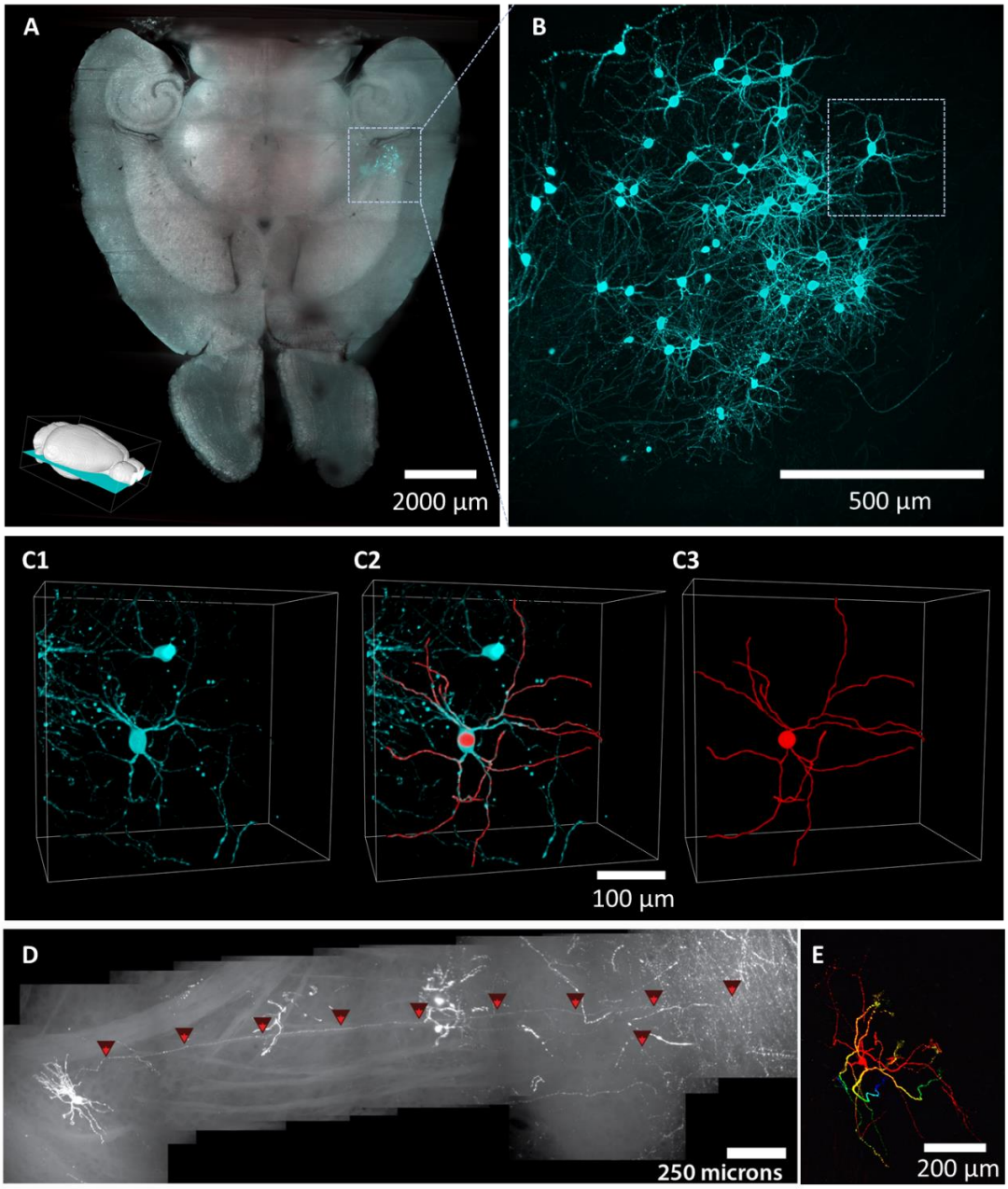

Figure 3: Light sheet microscopy with MHD-cleared tissue. (A) Optical slice of an intact mouse brain cleared using MHD-accelerated clearing (horizontal orientation; inset: position of slice). GFP-labeled cells (cyan) are clear in the medial amygdala. (B) Higher magnification image corresponding to the location of the dashed box in panel A showing individual cells and associated neural processes are visible deep within the tissue. (C) Higher magnification corresponding to the dashed box in panel B showing an isolated GFP-expressing neuron in the MeA (left), traced neural processes (right), and overlay of the fluorescent image and trace (center). (D) A depth color-coded projection of a single GFP-expressing neuron cell inside the brain (100 µm depth for projection; red: closest; blue: farthest). (E) Single axon traced from cell body to axon terminals through several millimeters of brain tissue inside the intact brain. The cells shown in (D) and (E) are not from the same sample as in (A) through (C).

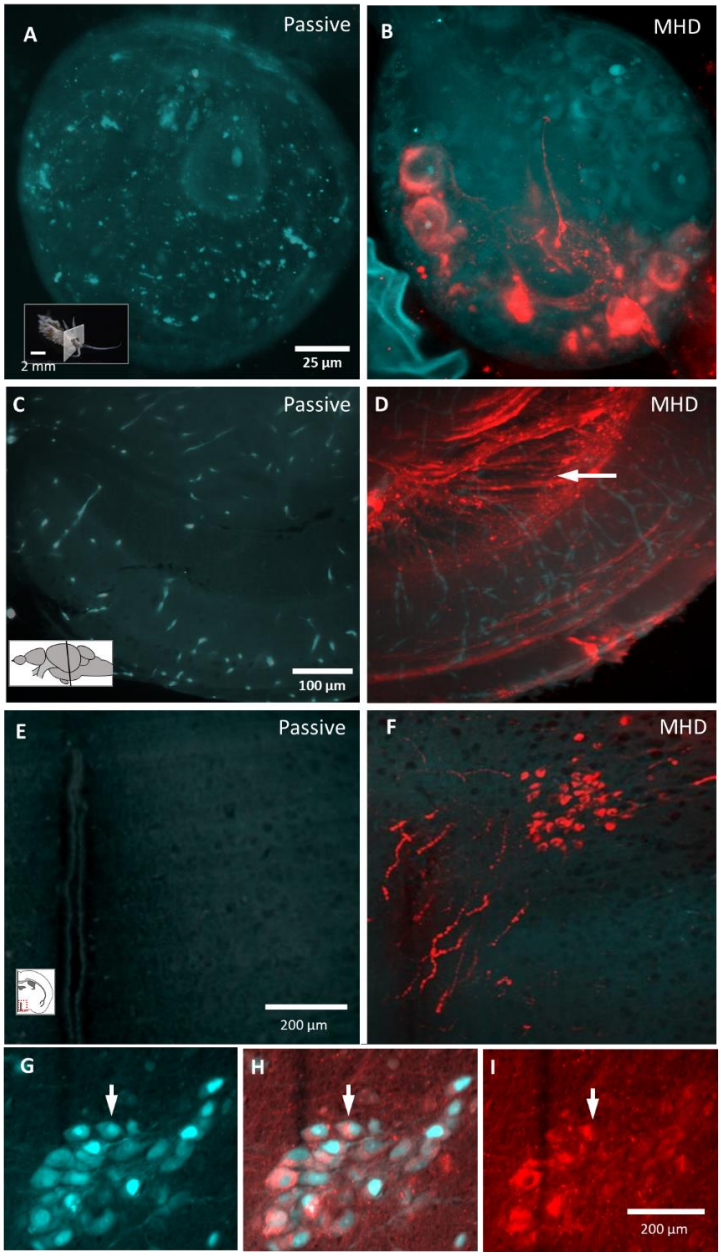

Figure 4: MHD-accelerated antibody labeling of brain tissue from sea slug, zebrafish, and mouse. (A, B) Image of an intact Berghia stephanieae pedal ganglion after passive (A) and MHD-accelerated (B) α-serotonin antibody labeling (red) with tissue autofluorescence (cyan). (C, D) Images of a cleared adult zebrafish brain (3 mm x 3 mm x 6 mm) after α-acetylated tubulin antibody labeling (red) with tissue autofluorescence (cyan; Passive labeling: C; MHD-accelerated labeling: D). (E, F) Images of cleared mouse brain sample (6 mm x 6 mm x 6 mm) after α-oxytocin labeling (red) with tissue autofluorescence (cyan; Passive labeling: E; MHD-accelerated labeling: F). (G–I) MHD-accelerated labeling of adult mouse brain sample (6 mm x 6 mm x 6 mm) after α-vasopressin antibody labeling (cyan) with genetically encoded tdTomato in vasopressin-expressing neurons (red; AVP-cre X rosa26-lsl-tdTomato; Pearson's coefficient: $r = 0.609$). Insets indicate the imaging plane.

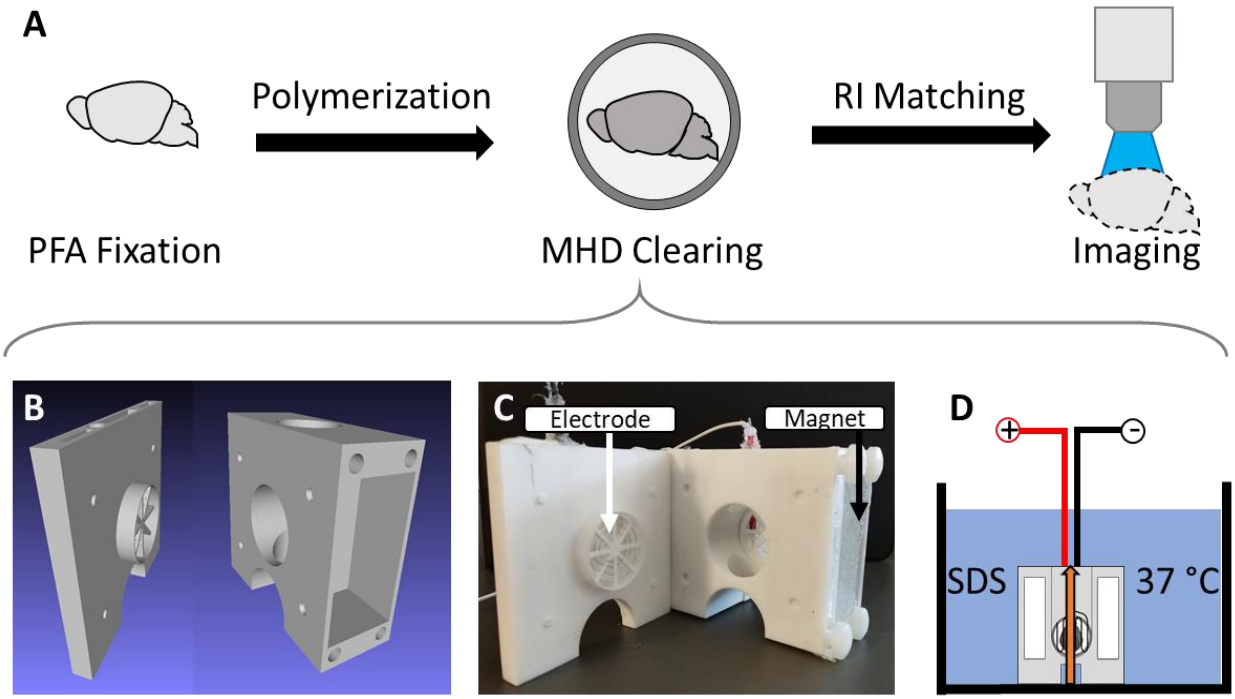

Figure 5: Overview of MHD-accelerated clearing approach. (A) Steps required to effectively clear tissue of lipids. (B) CAD diagram showing the MHD-assisted clearing device. (C) A photograph of the clearing device with tissue chamber exposed and arrows to show the location of the magnets and electrodes in the device. (D) Illustration of clearing device submerged in a container filled with detergent solution held at 37 °C. Tissue is placed in the central chamber where MHD force (orange arrow) produced from the electrical and magnetic fields simultaneously circulate the buffer solution and accelerate clearing.

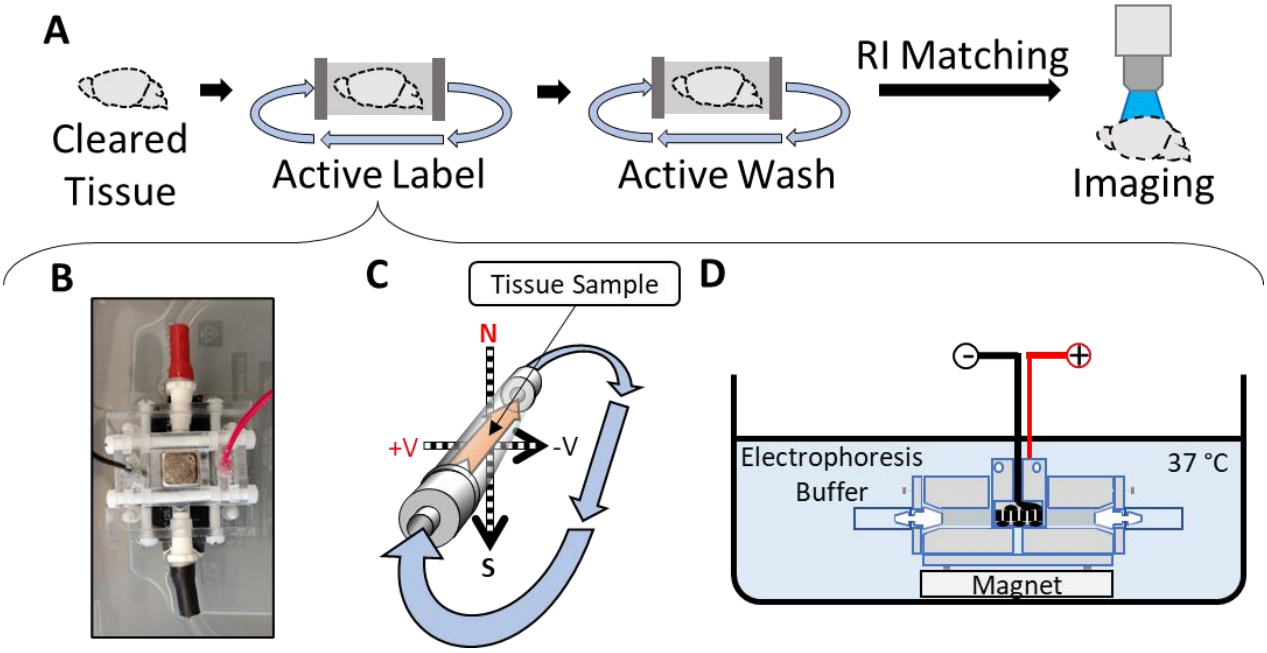

Figure 6: Overview of MHD-accelerated antibody labeling. (A) Illustration of the steps required to label and image tissue. (B) Picture of the MHD-assisted labeling device. (C) Schematic showing the tissue location inside the MHD-assisted labeling device. The direction of the MHD force is indicated by the orange arrow inside the dialysis tubing. The resulting direction of flow of the solution through the closed loop is indicated by the blue arrows. (D) Diagram of the antibody labeling device setup for a label. The device is submerged in a bath of electrophoresis buffer held at 37 °C.

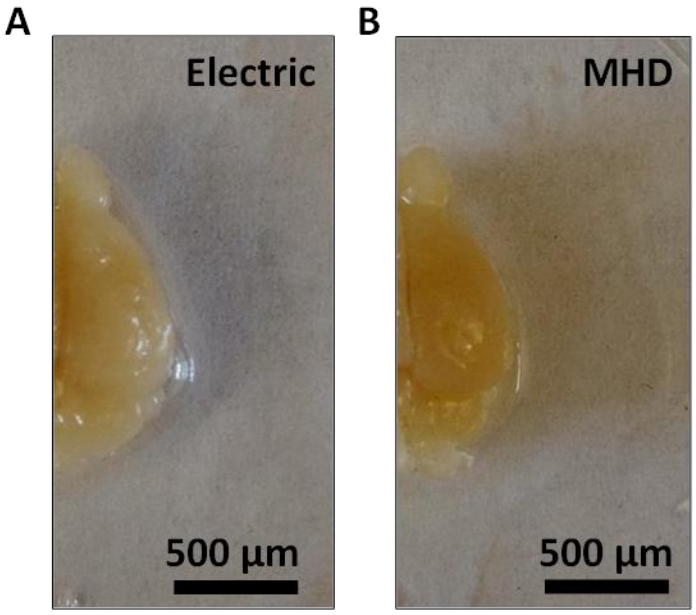

Figure 7: Images of a single brain split along the sagittal plane with one hemisphere cleared with electric-only clearing A) and the other hemisphere cleared with MHD-accelerated clearing B).

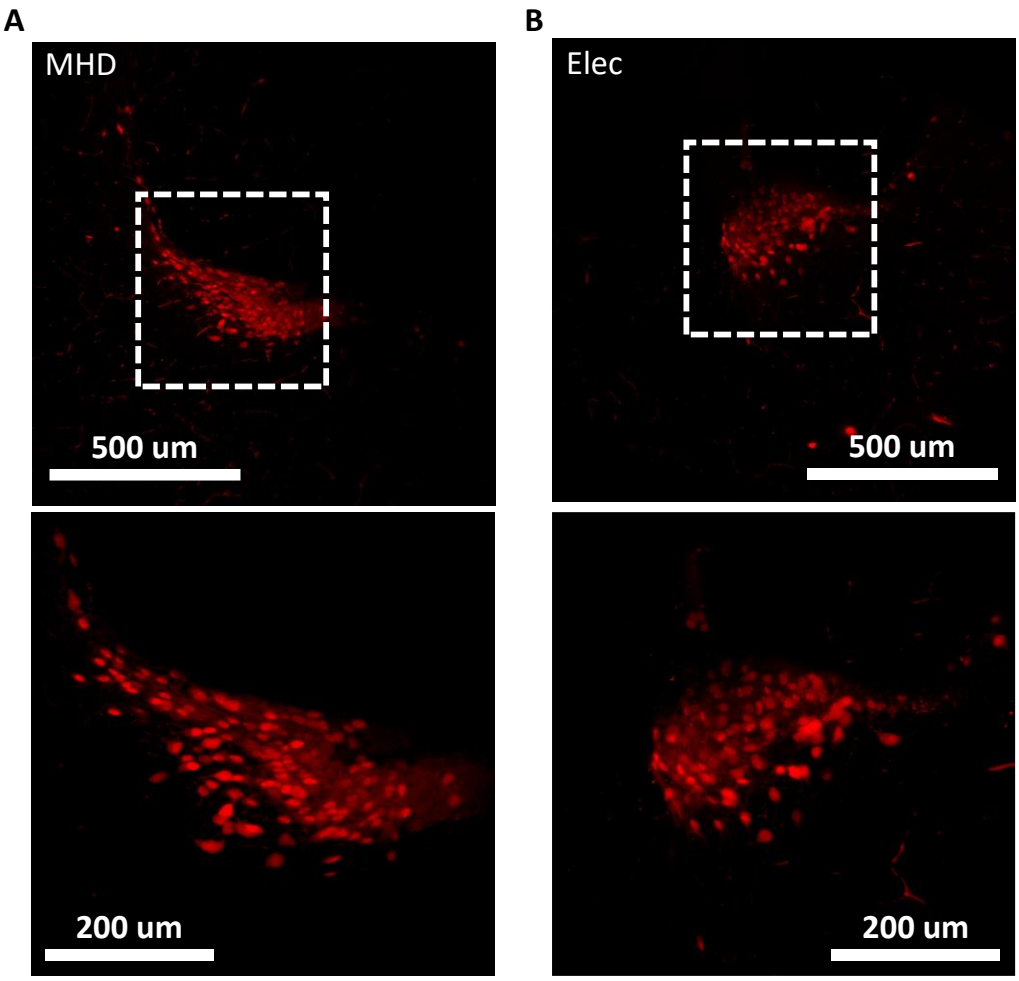

Figure 8: Images of hypothalamus neurons expressing tdTomato under the control of the AVP-promoter. A) Cell population in a brain cleared using MHD-accelerated labeling (top), and higher magnification of the dashed box in the top image (bottom). B) Cell population in a brain cleared using electric-only force (top), and higher magnification of the dashed box in the top image (bottom).

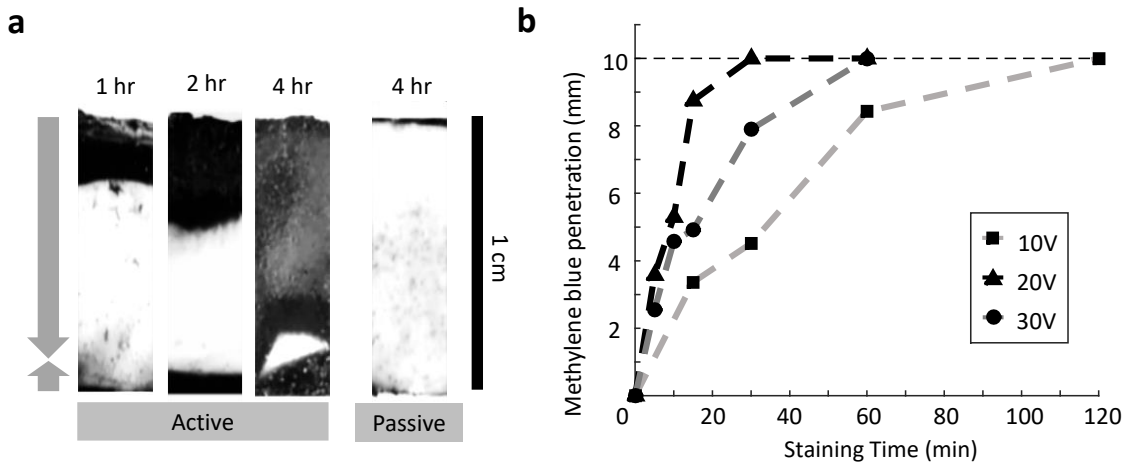

Figure 9: Overview of methylene blue penetration under MHD conditions. A) Penetration of methylene blue into a 1 cm^3 cube of homogeneous brain tissue as a result of MHD force over 1, 2, and 4 hours (N = 1). The fourth image shows a comparative 4-hour stain without MHD force. The arrows on the left-hand side of the images demonstrate the direction of the MHD force with respect to the tissue. The length of the arrows demonstrates the proportion of time when the MHD force was aimed in the direction indicated by each arrow. B) shows the comparative staining of methylene blue into agarose cubes as a result of various strengths of electrical force conjugated to MHD force. The distance the methylene blue penetrated into the agarose cubes is measured against the amount of time stained with 10, 20, or 30V conjugated to a constant magnetic field.

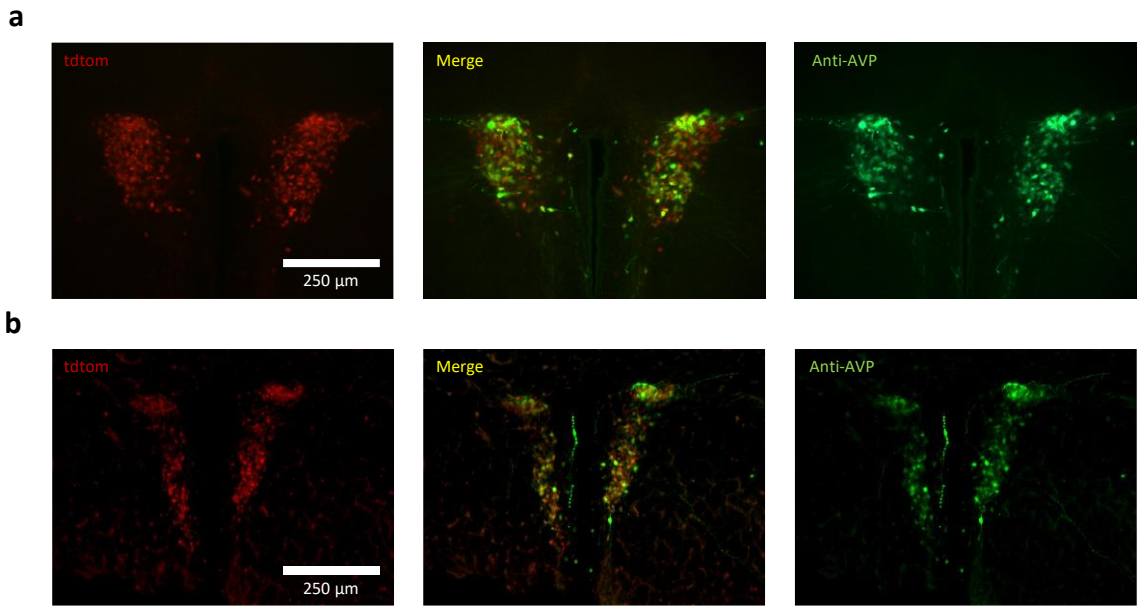

Figure 10: Demonstrated specificity of antibodies applied using MHD. Antibody labeling of a 100 µm, PFA-fixed slice from a mouse that expresses tdTomato under control of the AVP promoter (red; AVP-cre X rosa26-lsl-tdTomato) with α-vassopressin antibody (green) using a pH 7.0, PBS-based buffer A) or the pH 9.5 electrophoresis buffer used in MHD-accelerated labeling. In both A) and B) endogenous fluorescence is on the left, antibody fluorescence is on the right and a merge of the two images is in the center.

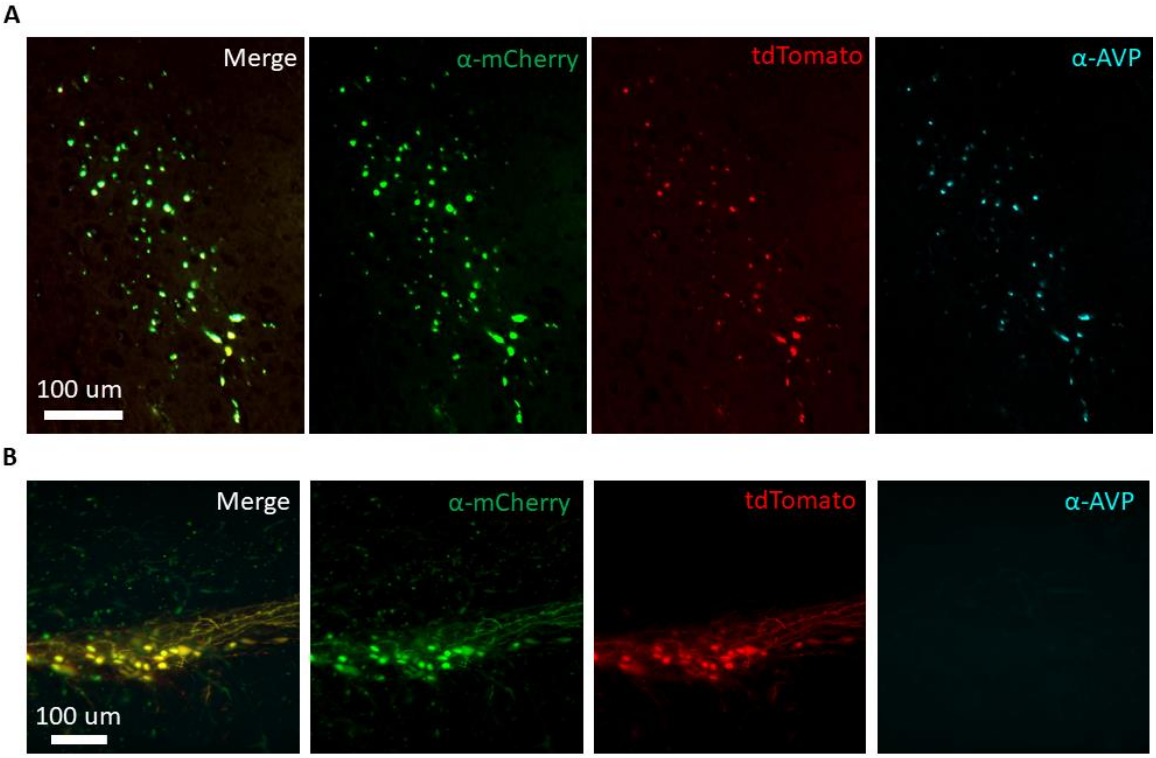

Figure 11: **MHD-accelerated antibody labeling of mouse tissue with multiple antibody probes.** A) Cells that express tdTomato (red) under the control of the AVP-promoter labeled with antibodies targeting mCherry (green) and AVP (cyan). Images from left to right show merged channels, α-mCherry antibody with Alexafluor 488 nm secondary antibody, tdTomato (Ai9) crossed with the AVP-Cre transgenic mice, and α-AVP with Alexafluor 647 nm secondary antibody (Pearson's coefficient α-mCherry to tdTomato: r = 0.67; Pearson's coefficient α-AVP to tdTomato: r = 0.64). B) tdTomato-expressing cells (red) in the mitral and tufted layer of the main olfactory bulb labeled with the same antibodies targeting mCherry (green) and AVP (cyan; panel order the same as in A). This MOB population of neurons consistently expresses tdTomato in the adult brain (likely due to developmentally restricted expression of AVP) but does not express AVP in the adult (Pearson's coefficient α-mCherry to tdTomato: r = 0.86; Pearson's coefficient α-AVP to tdTomato: r = 0.54).

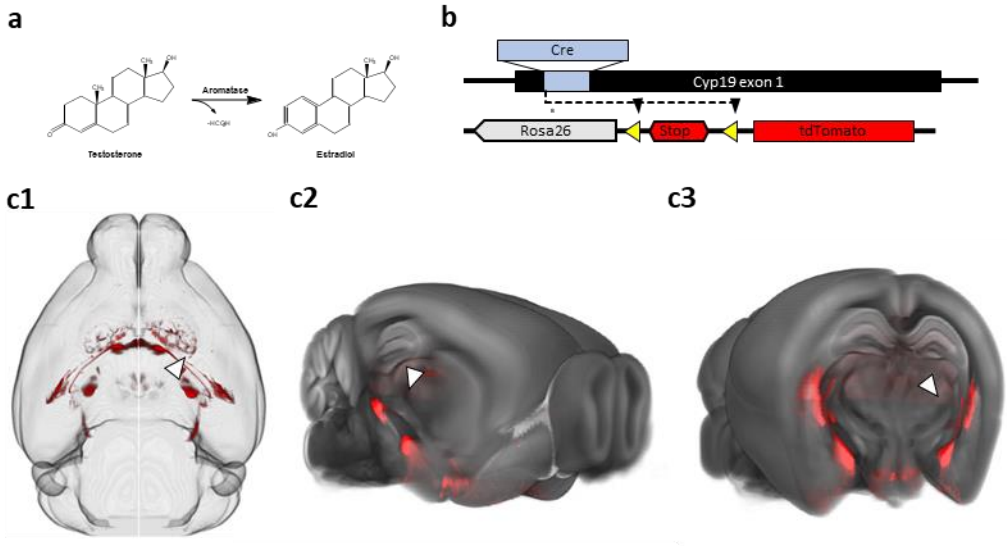

Figure 12: Identifying aromatase-expressing (arom+) neurons in the mouse brain. a, The aromatase enzyme mediates the conversion of testosterone into estradiol. b, Crossing aromatase-cre and Ai9 tdTomato reporter mice ensures that the tdTomato fluorescent protein is coexpressed with aromatase. c, A large population of aromatase-expressing cells is present in the posterodorsal MeA [arrow in (1) horizontal, (2) sagittal, and (3) coronal view].

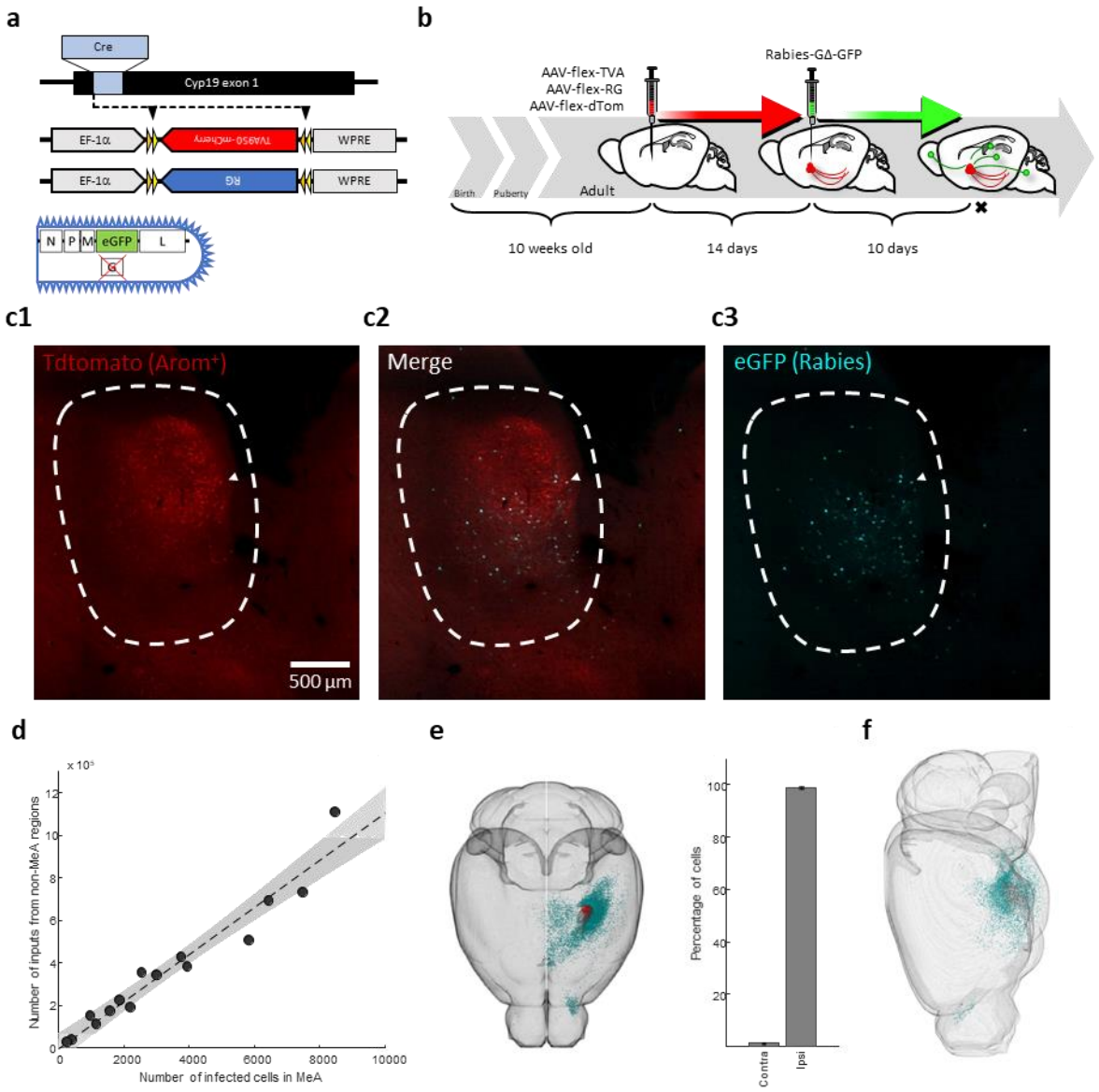

Figure 13: Mapping the inputome of arom$^+$ neurons in the MeA. ***a***, Conditional AAV vectors were injected in aromatase-cre mice to express TVA, RG, and mCherry in arom$^+$ neurons of the MeA. ***b***, Fourteen days after AAV injection, G-deleted rabies (GFP) was injected at the same stereotaxic coordinates to infect arom$^+$ starter neurons; followed by 10 d for retrograde movement of rabies from arom$^+$ neurons in the MeA to upstream neurons. ***c***, Infected starter neurons in the MeApd identified by simultaneous tdtomato and EGFP expression. ***d***, The number of neurons labeled with GFP by rabies infection outside the MeA scales linearly with the number of starter neurons infected in the MeApd. ***e***, View through the dorsal aspect of the brain showing location of starter neurons (red) and inputome (green), demonstrating that input cells are almost entirely ipsilateral to the injection site (see graph). ***f***, Lateral view of the same cells shown in panel ***e*** showing that most inputs originate from subcortical regions.

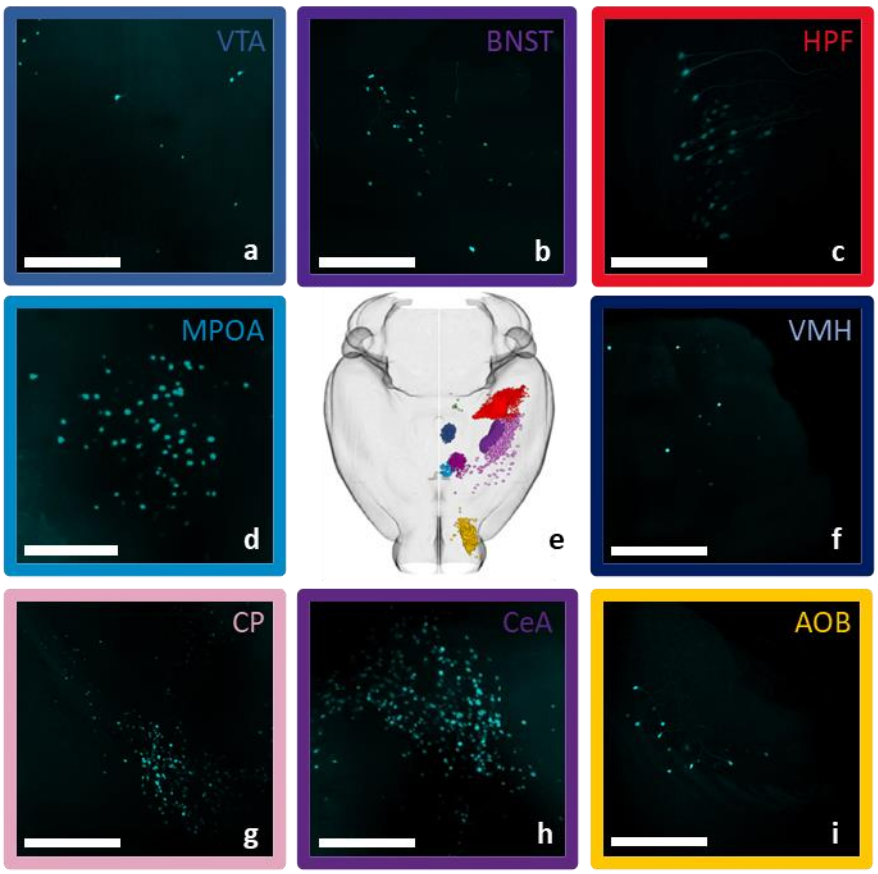

Figure 14: Input cell numbers vary across subcortical brain regions. A sampling of input cells observed in one individual after alignment to the Allen mouse brain common coordinate framework demonstrates that inputs can be localized to subcortical regions brain-wide and that input cell density varies among brain regions. ***a***, ventral tegmental area (VTA). ***b***, bed nucleus of the stria teminalis (BNST). ***c***, hippocampal formation (HPF). ***d***, medial preoptic area (MPOA). ***e***, ventromedial hypothalamus (VMH). ***f***, caudoputamen (CP). ***g***, central amygdala (CeA). ***h***, accessory olfactory bulb (AOB). Scale bars, 500 μm.

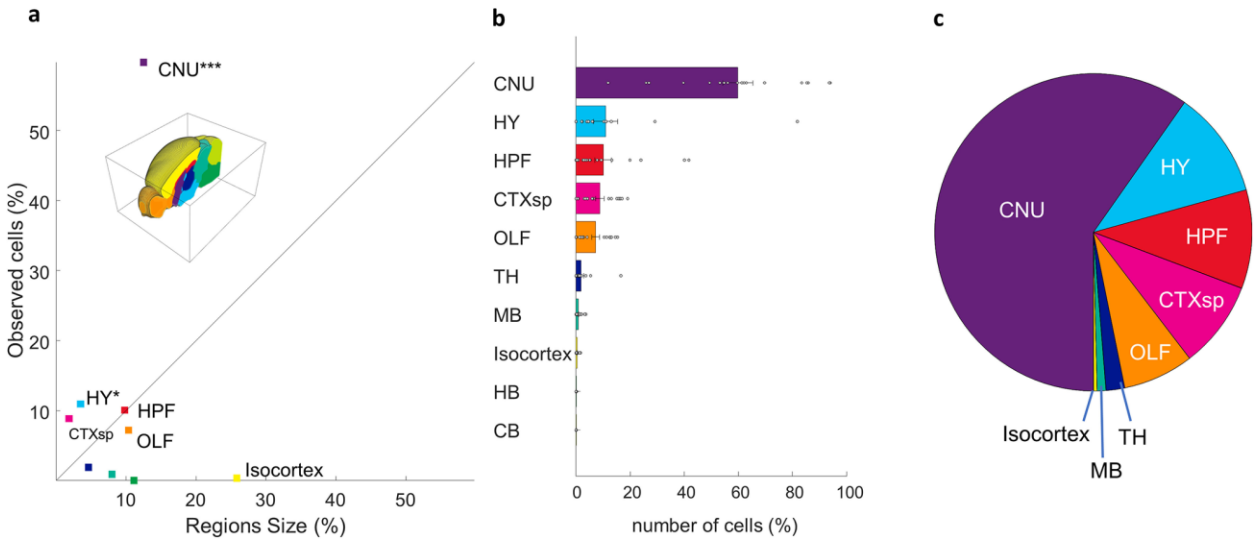

Figure 15: Coarse population count of the MeA arom$^+$ inputome. Each input cell was assigned to 1 of 10 nonoverlapping regions spanning the full volume of the reference brain. Defined regions are as follows: cerebral nuclei (CNU), hypothalamus (H), hippocampal formation (HPF), cortical subplate (CTXsp), olfactory areas (OF), thalamus (TH), midbrain (MB), isocortex, hindbrain (HB), and cerebellum (CB). ***a***, Graph showing the percentage of the average total observed input neurons found in each brain region relative to the volume of that brain region shows that some regions have either much higher or much lower density of inputs than would be expected if the cells were evenly distributed across the brain (straight line). ***b***, Percentages of the average total number of input cells found in each defined brain region. ***c***, Pie chart illustrating the proportions of inputome cells found in eight brain regions.

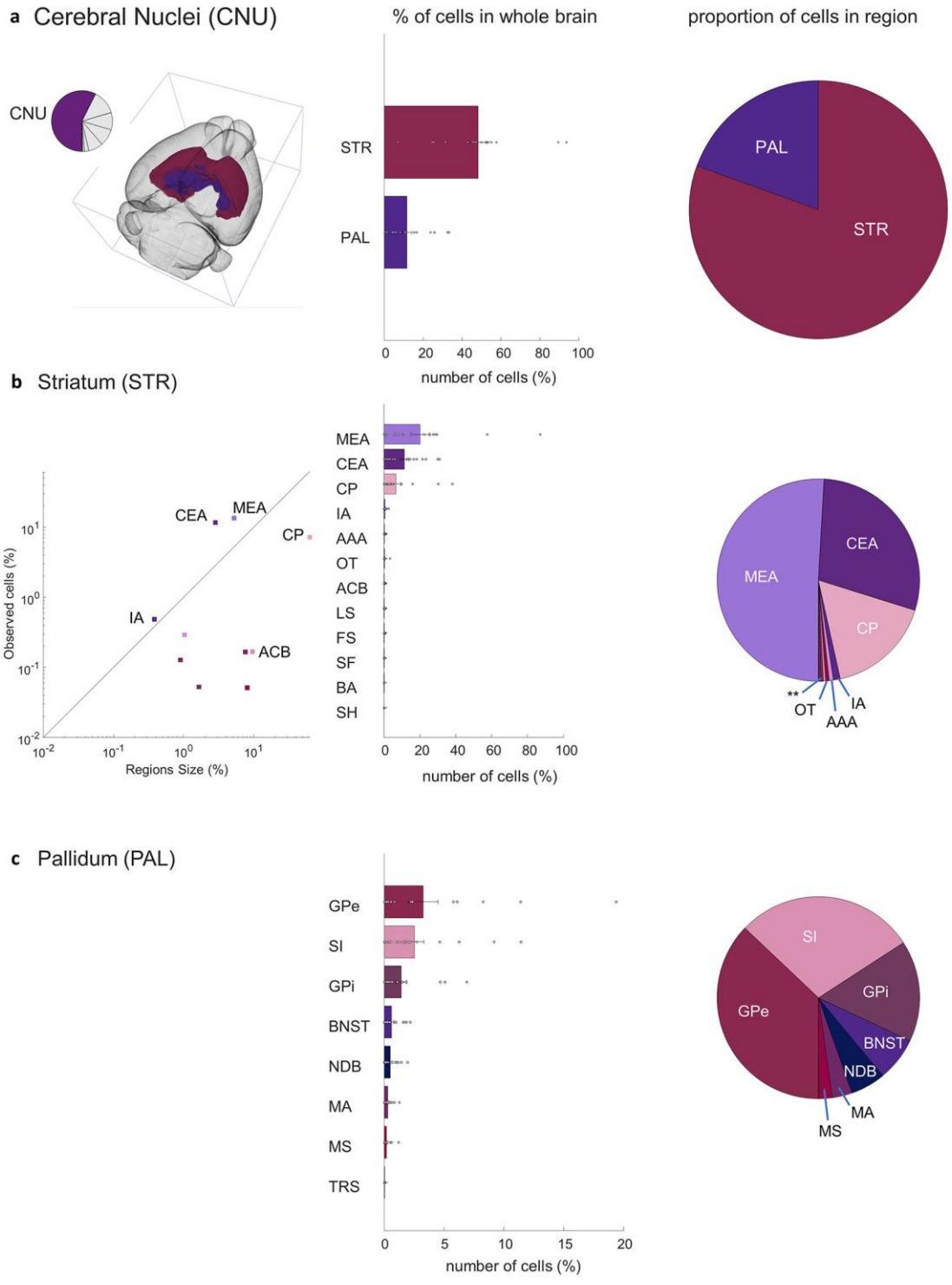
a Cerebral Nuclei (CNU)
% of cells in whole brain
proportion of cells in region
CNU
STR
PAL
0 20 40 60 80 100
number of cells (%)
PAL
STR
b Striatum (STR)
CEA
MEA
CP
IA
ACB
Observed cells (%)
Regions Size (%)
MEA
CEA
CP
IA
AAA
OT
ACB
LS
FS
SF
BA
SH
0 20 40 60 80 100
number of cells (%)
MEA
CEA
CP
**
OT
IA
AAA
c Pallidum (PAL)
GPe
SI
GPi
BNST
NDB
MA
MS
TRS
0 5 10 15 20
number of cells (%)
SI
GPi
GPe
BNST
NDB
MA
MS

Figure 16: MeA arom+ inputome originating in the cerebral nuclei (CNU). a, Left, A pie chart indicates the fraction of all labeled neurons in the CNU and the brain atlas depicts the position of CNU regions. Right, Bar graph depicts the percentages of input cells found in the striatum (STR) and pallidum (PAL) relative to the whole-brain inputome; pie chart shows the relative proportion of those cells within the cerebral nuclei alone. b, Locations of input neurons within the striatum: line graph shows relative density of cells in subregions of the striatum; bar graph shows relative distribution of inputs relative to the whole-brain inputome; pie chart shows the relative proportion of those cells within parts of the striatum. Regions shown: medial amygdala (MEA), central amygdala (CEA), caudoputamen (CP), intercalated amygdalar nucleus (IA), anterior amygdalar area (AAA), nucleus accumbens (ACB), lateral septal nucleus (LS), fundus of striatum (FS), olfactory tubercle (OT), septofimbrial nucleus (SF), bed nucleus of the accessory olfactory tract (BA), and septohippocampal nucleus (SH). c, Locations of input neurons within the pallidum: bar graph shows relative distribution of inputs relative to the whole-brain inputome; pie chart shows the relative proportion of those cells within parts of the pallidum. Regions shown: external globus pallidus (GPe), substantia innominata (SI), internal globus pallidus (GPi), BNST, diagonal band nucleus (NDB), magnocellular nucleus (MA), medial septal nucleus (MS), and triangular nucleus of septum (TRS).

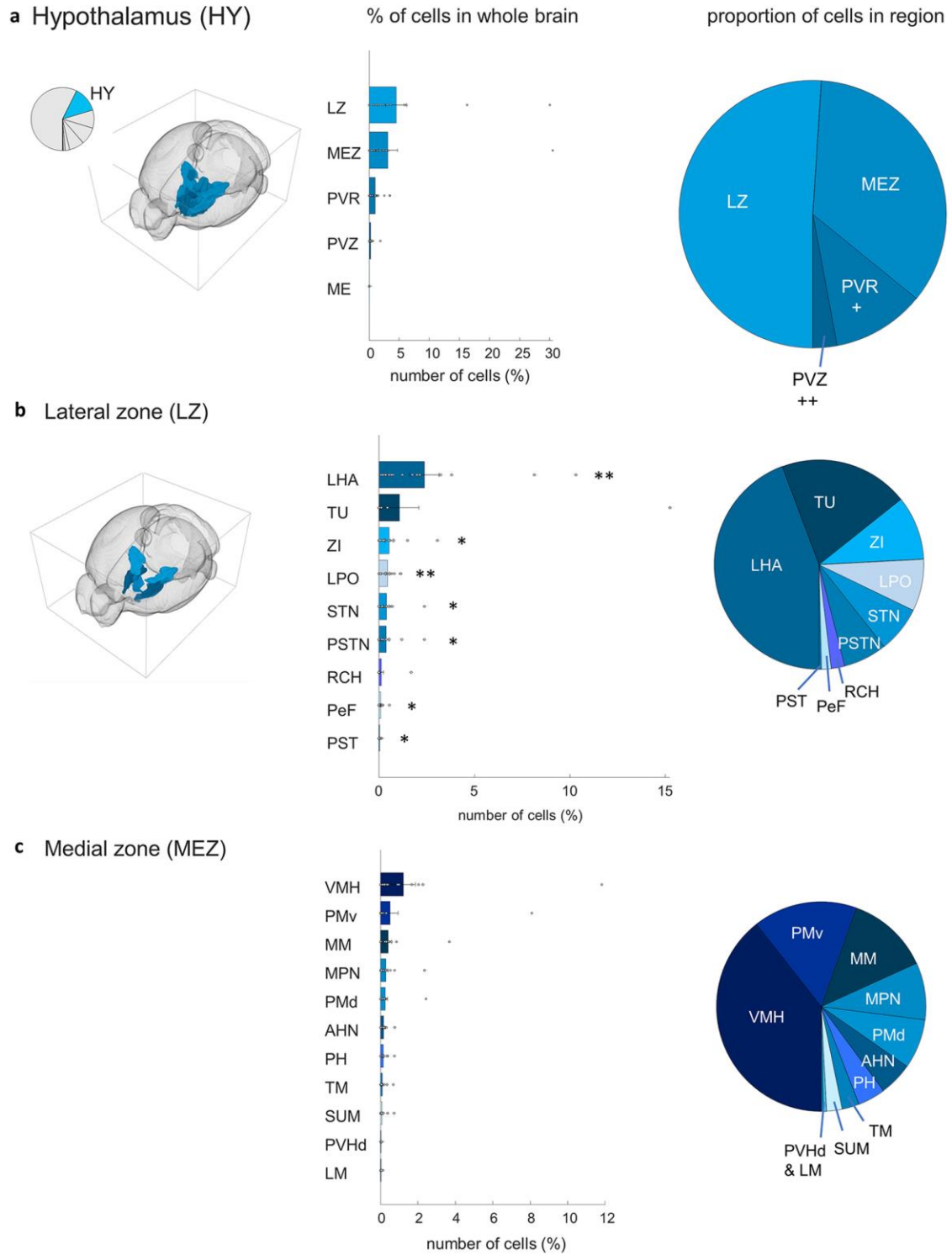

+ Periventricular region (PVR): Areas contain 1.1% of MeA arom+ inputs, most cells originate in the DMH and MPO, with smaller contributions from the AVP, PVp, and AVPV.
++ Periventricular zone (PVZ): Areas contain less than 0.5% of MeA arom+ inputs, most cells originate in the ARH and PVi, with smaller contributions from the PVH and SO.

Figure 17: MeA arom$^+$ inputome originating in the hypothalamus (HY). ***a***, Left, A pie chart indicates the fraction of all labeled neurons in the hypothalamus, and the brain atlas depicts the position of hypothalamic regions. Right, Bar graph depicts the percentages of input cells found in the five subregions of the hypothalamus relative to the whole-brain inputome; pie chart shows the relative proportion of those cells within those hypothalamic regions. Regions shown: lateral zone (LZ), medial zone (MEZ), periventricular region (PVR), periventricular zone (PVZ), and median eminence (ME). ***b***, Locations of input neurons within the lateral zone of the hypothalamus: bar graph shows relative distribution of inputs relative to the whole-brain inputome; and pie chart shows the relative proportion of those cells within parts of the medial zone. Regions shown: lateral hypothalamic area (LHA), Tuberal nucleus (TU), zona incerta (ZI), lateral preoptic area (LPO), subthalamic nucleus (STN), parasubthalamic nucleus (PSTN), retrochiasmatic area (RCH), perifornical nucleus (PeF), and preparasubthalamic nucleus (PST). ***c***, Locations of input neurons within the medial zone of the hypothalamus: bar graph shows relative distribution of inputs relative to the whole-brain inputome; pie chart shows the relative proportion of those cells within parts of the medial zone. Regions shown: ventromedial hypothalamic nucleus (VMH), PMv, medial mammillary nucleus (MM), medial preoptic nucleus (MPN), dorsal premammillary nucleus (PMd), anterior hypothalamic nucleus (AHN), posterior hypothalamic nucleus (PH), tuberomammillary nucleus (TM), supramammillary nucleus (SUM), paraventricular hypothalamic nucleus (PVHd), and lateral mammillary nucleus (LM).

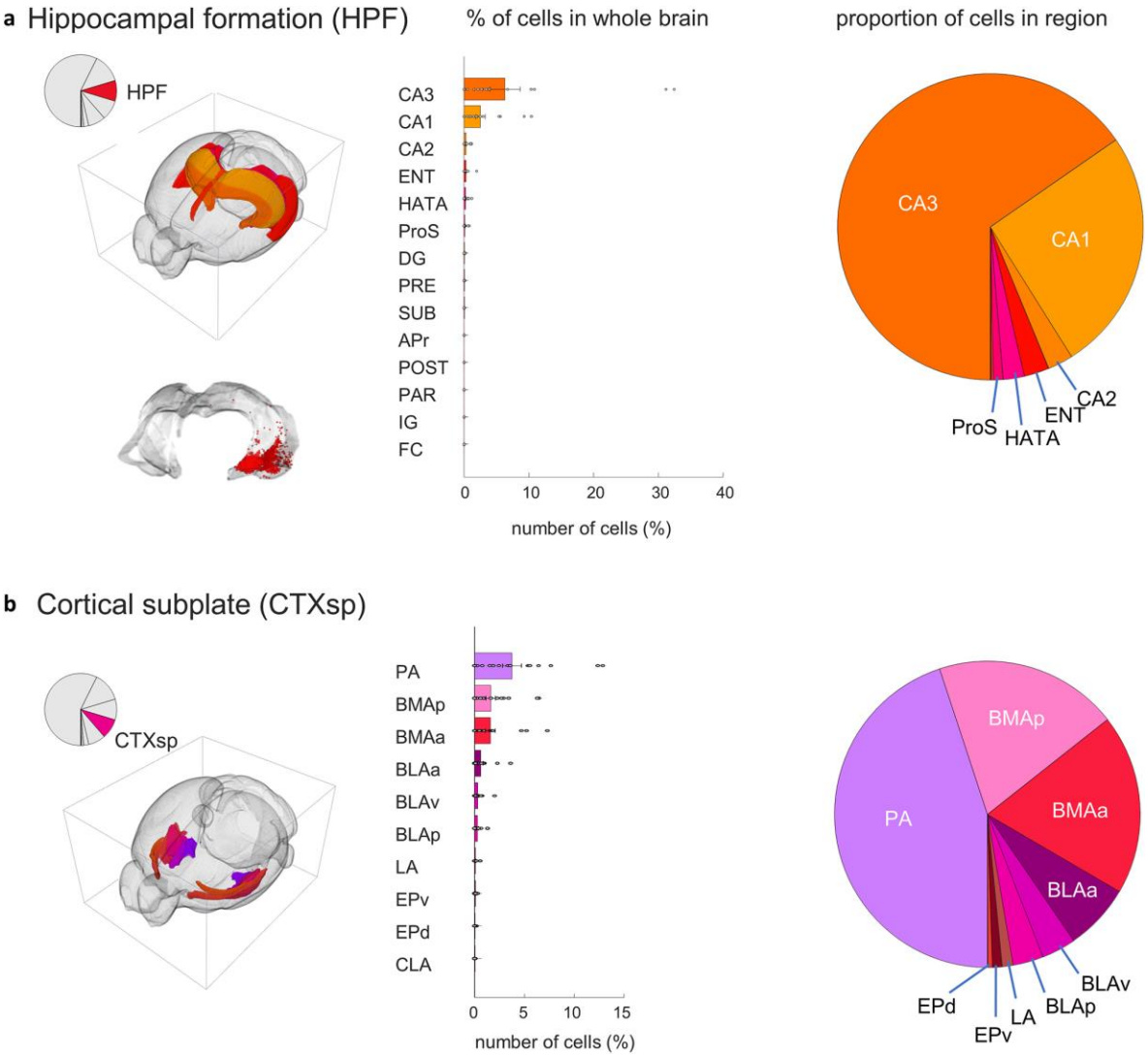
a Hippocampal formation (HPF)
% of cells in whole brain
proportion of cells in region
HPF
CA3
CA1
CA2
ENT
HATA
ProS
DG
PRE
SUB
APr
POST
PAR
IG
FC
0
10
20
30
40
number of cells (%)
CA3
CA1
CA2
ENT
HATA
ProS
b Cortical subplate (CTXsp)
CTXsp
PA
BMAp
BMAa
BLAa
BLAv
BLAp
LA
EPv
EPd
CLA
0
5
10
15
number of cells (%)
PA
BMAp
BMAa
BLAa
BLAv
BLAp
LA
EPv
EPd

Figure 18: MeA arom$^+$ inputome originating in the hippocampal formation (HPF) and the cortical subplate (CTXsp). ***a***, Left, A pie chart indicates the fraction of all labeled neurons in the hippocampus and the brain atlas depicts the position of hippocampal regions. Right, Bar graph depicts the percentages of input cells found in the regions of the hippocampal formation relative to the whole-brain inputome; and pie chart shows the relative proportion of those cells within those regions. The lower inset image illustrates that input cells are located primarily in ventral portions of the HPF. Regions shown: field CA1 (CA1), field CA2 (CA2), field CA3 (CA3), entorhinal area (ENT), hippocampal-amygdalar transition area (HATA), prosubiculum (ProS), dentate gyrus (DG), presubiculum (PRE), subiculum (SUB), area prostriata (APr), postsubiculum (POST), parasubiculum (PAR), induseum griseum (IG), and fasciola cinerea (FC). ***b***, Left, A pie chart indicates the fraction of all labeled neurons in the cortical subplate, and the brain atlas depicts the position of cortical subplate regions. Right, Bar graph depicts the percentages of input cells found in the regions of the cortical subplate relative to the whole-brain inputome; and pie chart shows the relative proportion of those cells within those regions. Regions shown: posterior amygdalar nucleus (PA), anterior BMA (BMAa), posterior BMA (BMAp), anterior BMA (BLAa), ventral basolateral amygdalar nucleus (BLAv), posterior basolateral amygdalar nucleus (BLAp), lateral amygdalar nucleus (LA), ventral endopiriform nucleus (EPv), dorsal endopiriform nucleus (EPd), and claustrum (CLA).

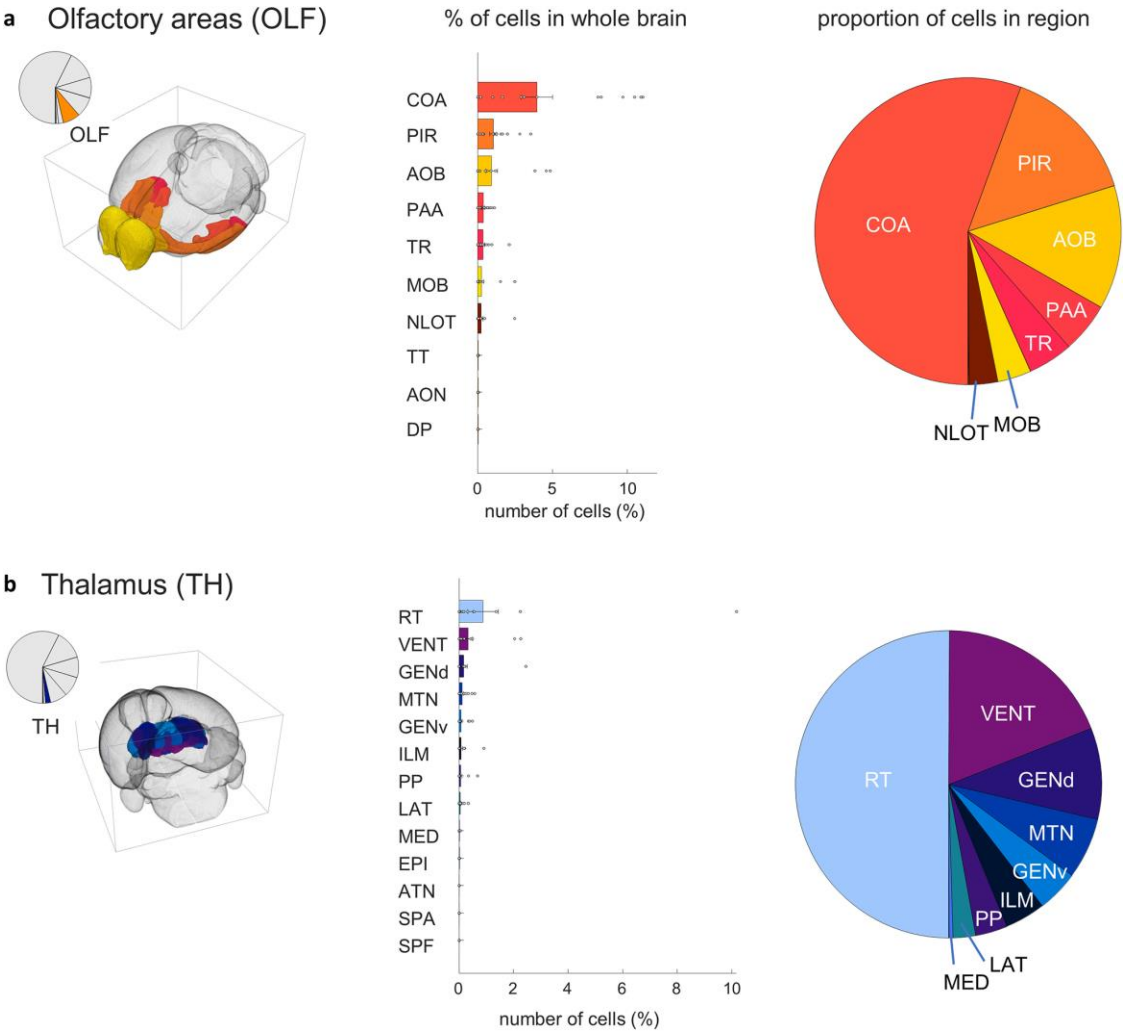

Figure 19: MeA arom^{+} inputome originating in the olfactory areas (OLF) and the thalamus (TH). ***a***, Left, A pie chart indicates the fraction of all labeled neurons in olfactory areas; and the brain atlas depicts the position of olfactory areas. Right, Bar graph depicts the percentages of input cells found in subregions of the olfactory area relative to the whole-brain inputome; and pie chart shows the relative proportion of those cells within those regions. Regions shown: cortical amygdalar area (COA), piriform area (PIR), accessory olfactory bulb (AOB) , piriform-amygdalar area (PAA), postpiriform transition area (TR), nucleus of the lateral olfactory tract (NLOT), main olfactory bulb (MOB), taenia tecta (TT), anterior olfactory nucleus (AON), and dorsal peduncular area (DP). ***b***, Left, A pie chart indicates the fraction of all labeled neurons in the thalamus; and brain atlas depicts the position of thalamic regions. Right, Bar graph depicts the percentages of input cells found in subregions of the thalamus relative to the whole-brain inputome; and pie chart shows the relative proportion of those cells within those regions. Regions shown: reticular nucleus (RT), ventral group of the dorsal thalamus (VENT), dorsal geniculate group (GENd), midline group of the dorsal thalamus (MTN), ventral geniculate group (GENv), intralaminar nuclei of the dorsal thalamus (ILM), peripeduncular nucleus (PP), lateral group of the dorsal thalamus (LAT), medial group of the dorsal thalamus (MED), epithalamus (EPI), anterior group of the dorsal thalamus (ATN), subparafascicular area (SPA), and subparafascicular nucleus (SPF).

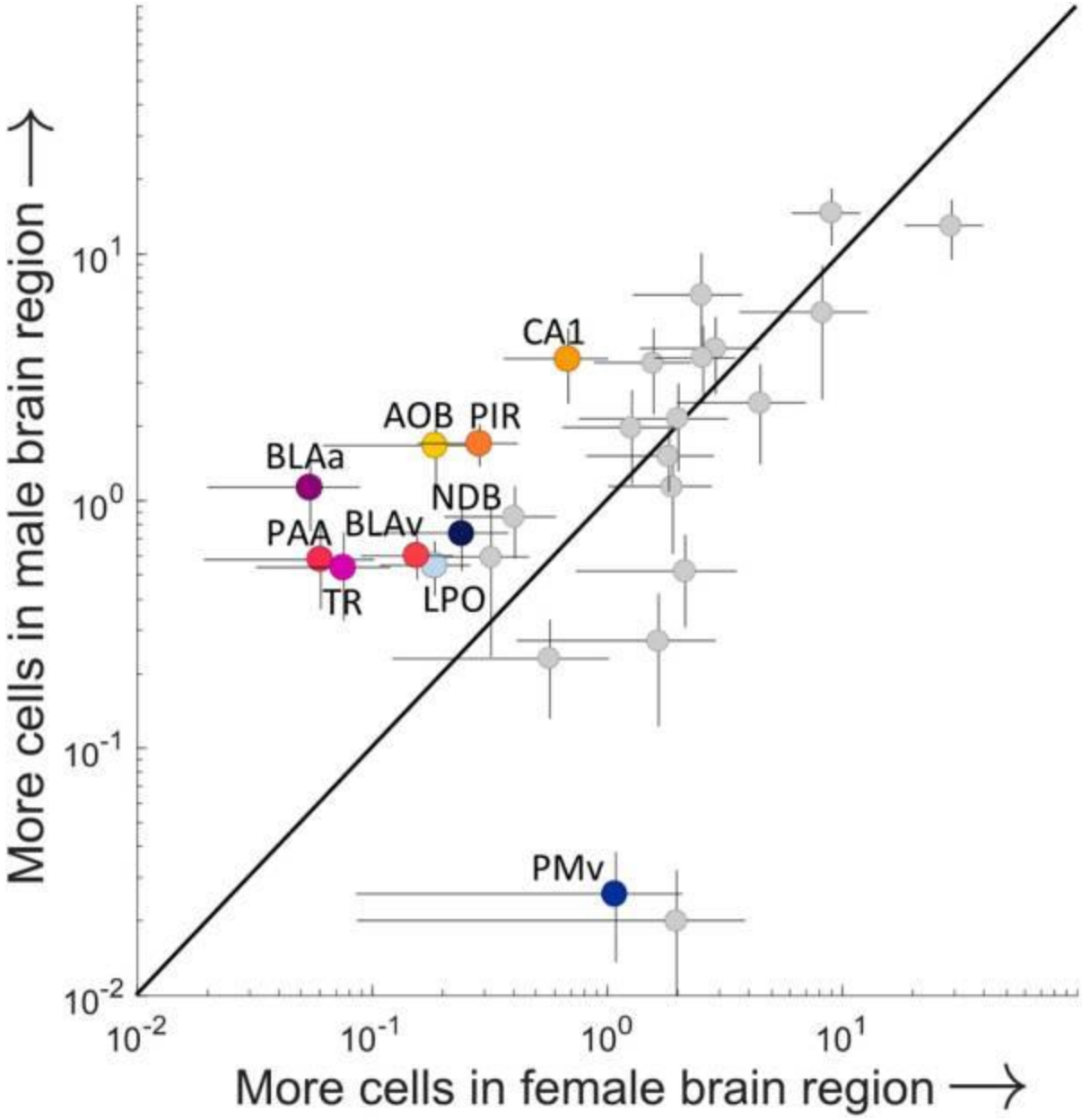

Figure 20: Sex differences in the inputome of aromatase-expressing cells in the MeA. The average percentage of synaptic inputs to MeA arom^{+} neurons compared for each region in males and females. Only regions that provide 0.5% of the overall input are shown, and regions identified as having a statistically significant sex difference are shown in color ($p < 0.05$, permutation *post hoc* test following ANOVA with repeated measures on "sex," "region," and "individual"). These regions include field CA1 (CA1), the accessory olfactory bulb (AOB), piriform area (PIR), piriform-amygdalar area (PAA), postpiriform transition area (TA), basolateral amygdalar nucleus-anterior (BLAa), basolateral amygdalar nucleus-ventral (BLAv), diagonal band nucleus (NDB), lateral preoptic area (LPO), and ventral premammillary nucleus (PMv). Regions lying above the line of unity represent a male bias, and neurons lying to the right of the unity line indicate a female bias. Error bars indicate the SEMs (male, vertical; female, horizontal) for each region.

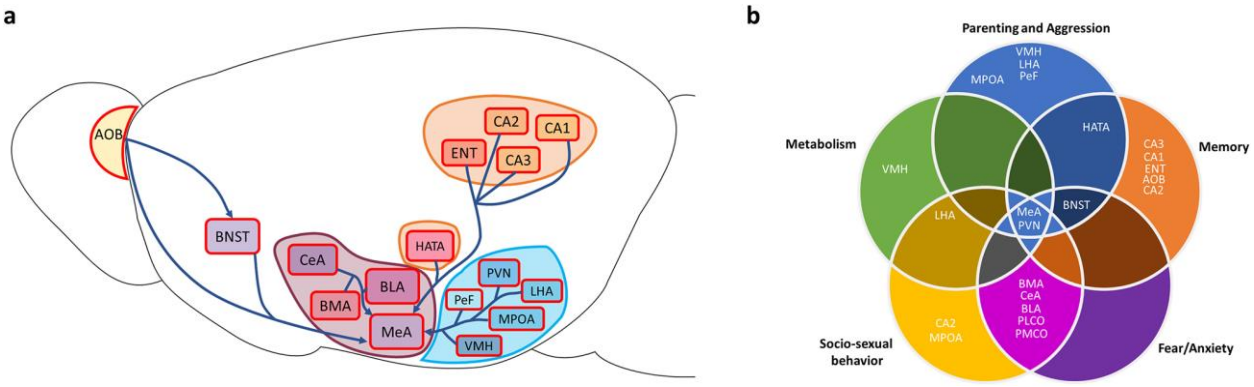

Figure 21: The inputome of MeA arom^{+} neurons. ***a***, Illustration showing the relative locations of the major inputs to the aromatase-expressing MeA cells throughout the brain as defined by our data. Major regions are shaded to demonstrate that the included regions were analyzed in groups and are considered components of a larger analysis region. These inputs were selected based on their relative abundance in the data and behavioral significance as represented in previous literature. ***b***, A Venn diagram showing the relative distribution of the regions displayed in ***a*** sorted by their reported roles in the production or modulation of memory, parenting and aggression, metabolism, sociosexual behaviors, and fear and anxiety behaviors.

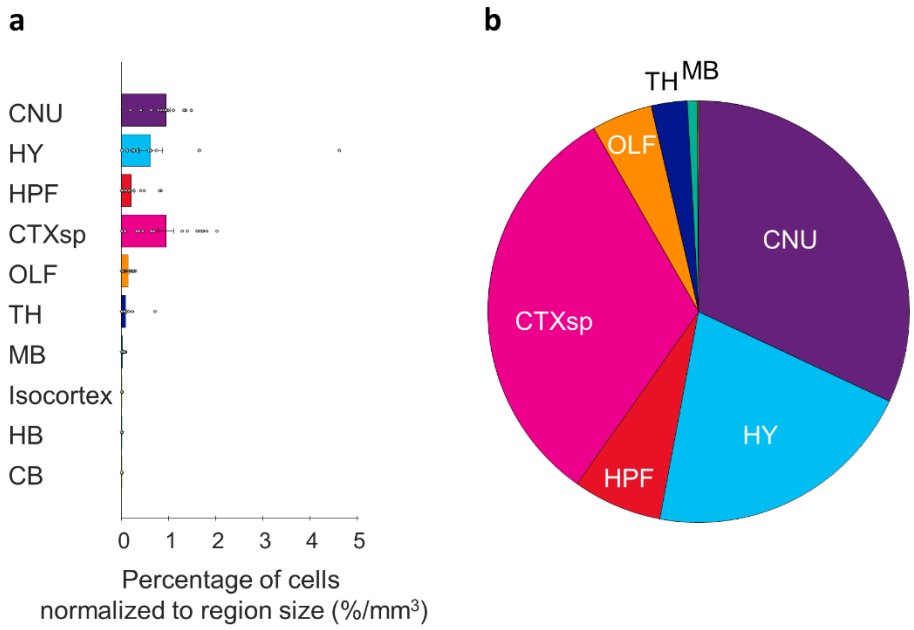

Figure 22: Input cell density in regions brain wide. Percentage of input cells in each coarse region identified in the Allen Brain Atlas normalized to the volume of that region to determine cell densities in each region are presented as graph (a) and pie chart (b). The densest concentration of input cells is found in the cortical subplate (CTXsp).

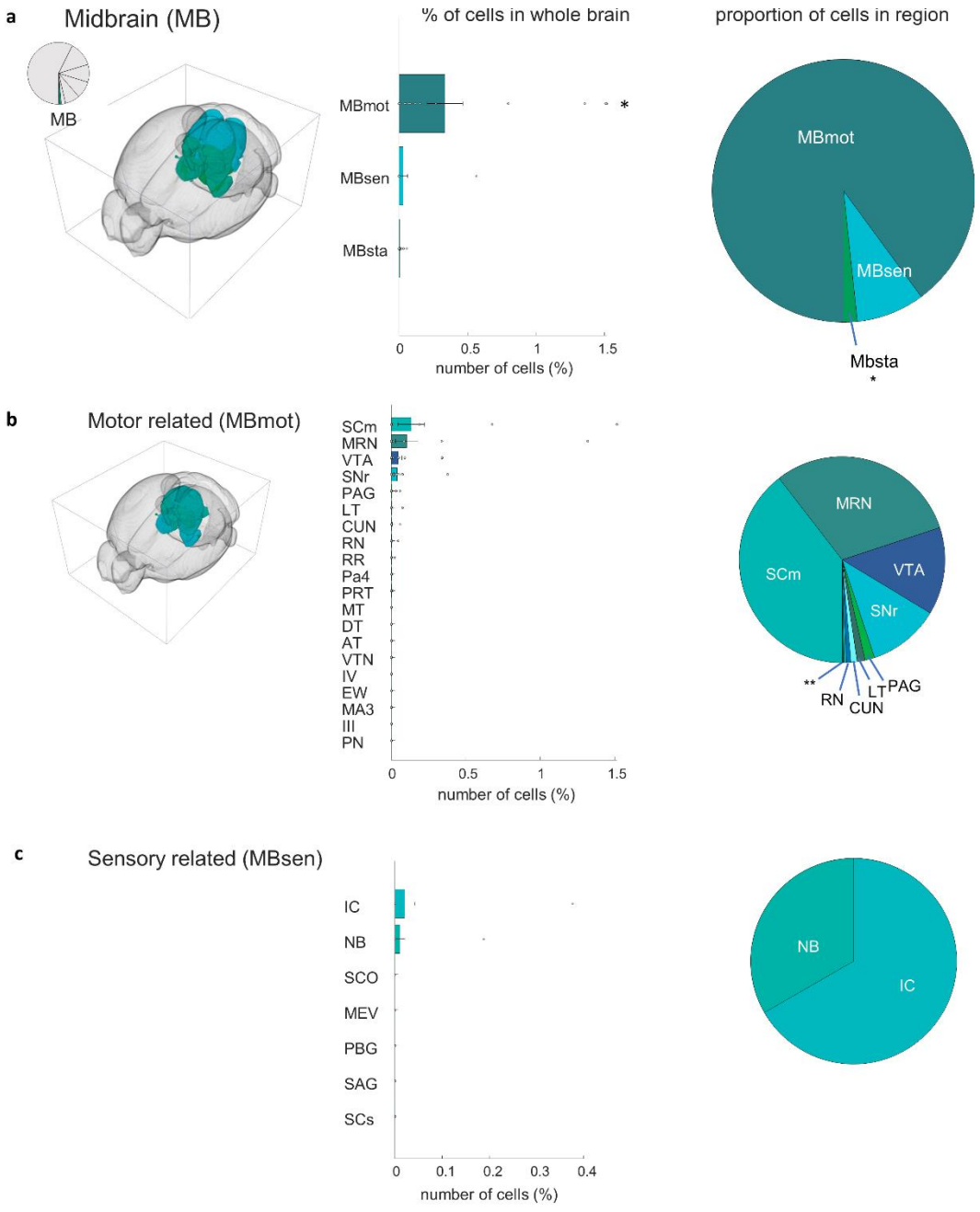

* Behavior related (MBsta): Regions contain less than 0.01% of MeA arom+ inputs, most cells in the DR, PPN, IPN.

Figure 23: MeA arom+ inputome originating in the midbrain (MB). a, Bar graph depicts the percentages of input cells found in major divisions of the midbrain relative to the whole-brain inputome; and pie chart shows the relative proportion of those cells within those regions. Regions shown: motor-related midbrain regions (MBmot), sensory-related midbrain regions (MBsec), and behavior-related midbrain regions (MBsta). b, Inputs from motor-related midbrain regions: bar graph depicts the percentages of input cells found in major divisions of these regions relative to the whole-brain inputome; and pie chart shows the relative proportion of input cells within those regions. Regions shown: midbrain reticular nucleus (MRN), superior colliculus—motor (SCm), VTA, substantia nigra (SNr), periaqueductal gray (PAG), lateral terminal nucleus of accessory optic tract (LT), cuneiform nucleus (CUN), red nucleus (RN), retrorubal area of midbrain reticular nucleus (RR), paratrochlear nucleus (Pa4), pretectal region (PRT), medial terminal nucleus of accessory optic tract (MT), dorsal terminal nucleus of accessory optic tract (DT), anterior tegmental nucleus (AT), ventral tegmental nucleus (VTN), trochlear nucleus (IV), Edinger-Westphal nucleus (EW), medial accessory oculomotor nucleus (MA3), oculomotor nucleus (III), and paranigral nucleus (PN). c, Inputs from sensory-related midbrain regions: bar graph depicts the percentages of input cells found in major divisions of these regions relative to the whole-brain inputome; and pie chart shows the relative proportion of input cells within those regions. Regions shown: inferior colliculus (IC), brachium of inferior colliculus (NB), subcommissural organ (SCO), midbrain trigeminal nucleus (MEV), parabigeminal nucleus (PBG), nucleus sagulum (SAG), and superior colliculus (sensory; SCs). **Less than 0.01% of MeA arom+ inputs originate in behavior-related midbrain area; most of those cells are found in the dorsal raphe nucleus (DR), pedunculopontine nucleus (PPN), and interpeduncular nucleus (IPN).

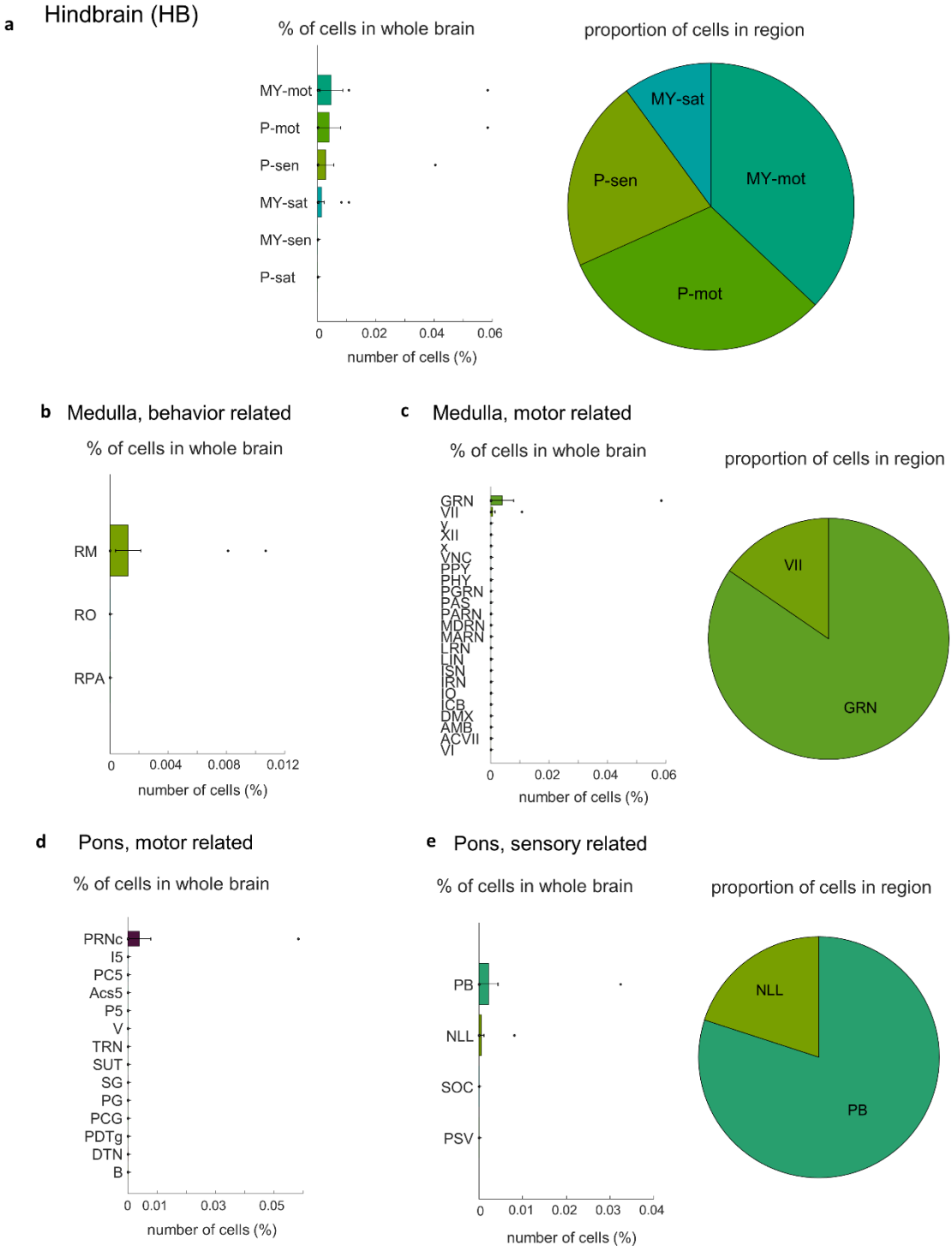
a
Hindbrain (HB)
% of cells in whole brain
MY-mot
P-mot
P-sen
MY-sat
MY-sen
P-sat
0
0.02
0.04
0.06
number of cells (%)
proportion of cells in region
MY-sat
P-sen
MY-mot
P-mot
b
Medulla, behavior related
% of cells in whole brain
RM
RO
RPA
0
0.004
0.008
0.012
number of cells (%)
c
Medulla, motor related
% of cells in whole brain
GRN
VII
V
XII
X
VNC
PPY
PHY
PGRN
PAS
PARN
MDRN
MARN
LRN
LIN
ISN
IRN
IO
ICB
DMX
AMB
ACVII
VI
0
0.02
0.04
0.06
number of cells (%)
proportion of cells in region
VII
GRN
d
Pons, motor related
% of cells in whole brain
PRNc
I5
PC5
Acs5
P5
V
TRN
SUT
SG
PG
PCG
PDTg
DTN
B
0
0.01
0.03
0.05
number of cells (%)
e
Pons, sensory related
% of cells in whole brain
PB
NLL
SOC
PSV
0
0.01
0.02
0.03
0.04
number of cells (%)
proportion of cells in region
NLL
PB

Figure 24: MeA arom+ inputome originating in the hindbrain (HB). a, Whole hindbrain: bar graph depicts the percentages of input cells found in major divisions of the hindbrain relative to the whole-brain inputome; and pie chart shows the relative proportion of input cells within those regions. Regions shown: motor-related medulla (MY-mot), sensory-related medulla (MY-sen), behavioral state medulla (MY-sat), motor-related pons (P-mot), sensory-related pons (P-sen), and behavioral state pons (P-sat). b, Only one of the behavior-state portions of the medulla, the nucleus raphe magnus (RM) contains inputs to arom+ cells in the MeA. c, Bar graph depicts the percentages of input cells found in major divisions of the motor-related medulla relative to the whole-brain inputome; and pie chart shows the relative proportion of input cells within those regions. Two regions of the motor-related medulla provide inputs: the gigantocellular reticular nucleus (GRN) and the facial motor nucleus (VII). d, The caudal part of the pontine reticular nucleus (PRNc) is the only part of the motor-related pons to provide inputs to arom+ MeA cells. e, In the sensory-related pons, inputs originate from the parabrachial nucleus (PB) and the nucleus of the lateral lemniscus (NLL).

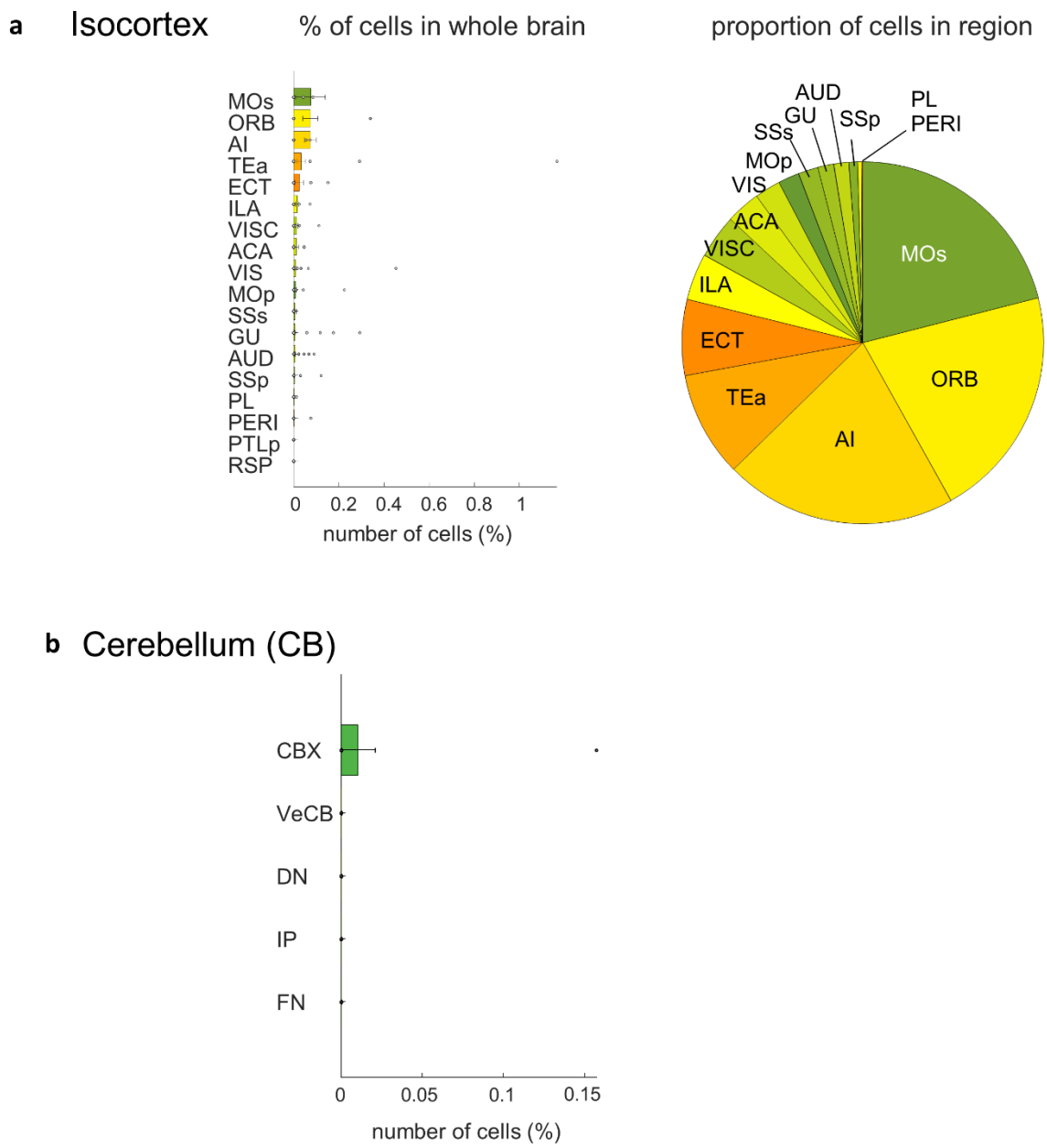

Figure 25: MeA arom+ inputome originating in the isocortex and the cerebellum (CB). a, Bar graph depicts the percentages of input cells found in major divisions of the isocortex relative to the whole-brain inputome; and pie chart shows the relative proportion of input cells within those regions. Regions shown: Secondary motor area (MOs), agranular insular area (AI), orbital area (ORB), temporal association area (Tea), ectorhinal area (ECT), visceral area (VISC), anterior cingulate area (ACA), infralimbic area (ILA), primary motor area (MOp), supplementary somatosensory area (SSs), gustatory areas (GU), auditory areas (AUD), visual areas (VIS), primary somatosensory area (SSp), prelimbic area (PL), perirhinal area (PERI), posterior parietal association areas (PTLps), and retrosplenial area (RSP). b, Inputs from the cerebellum are only found in the cerebellar cortex (CBX).

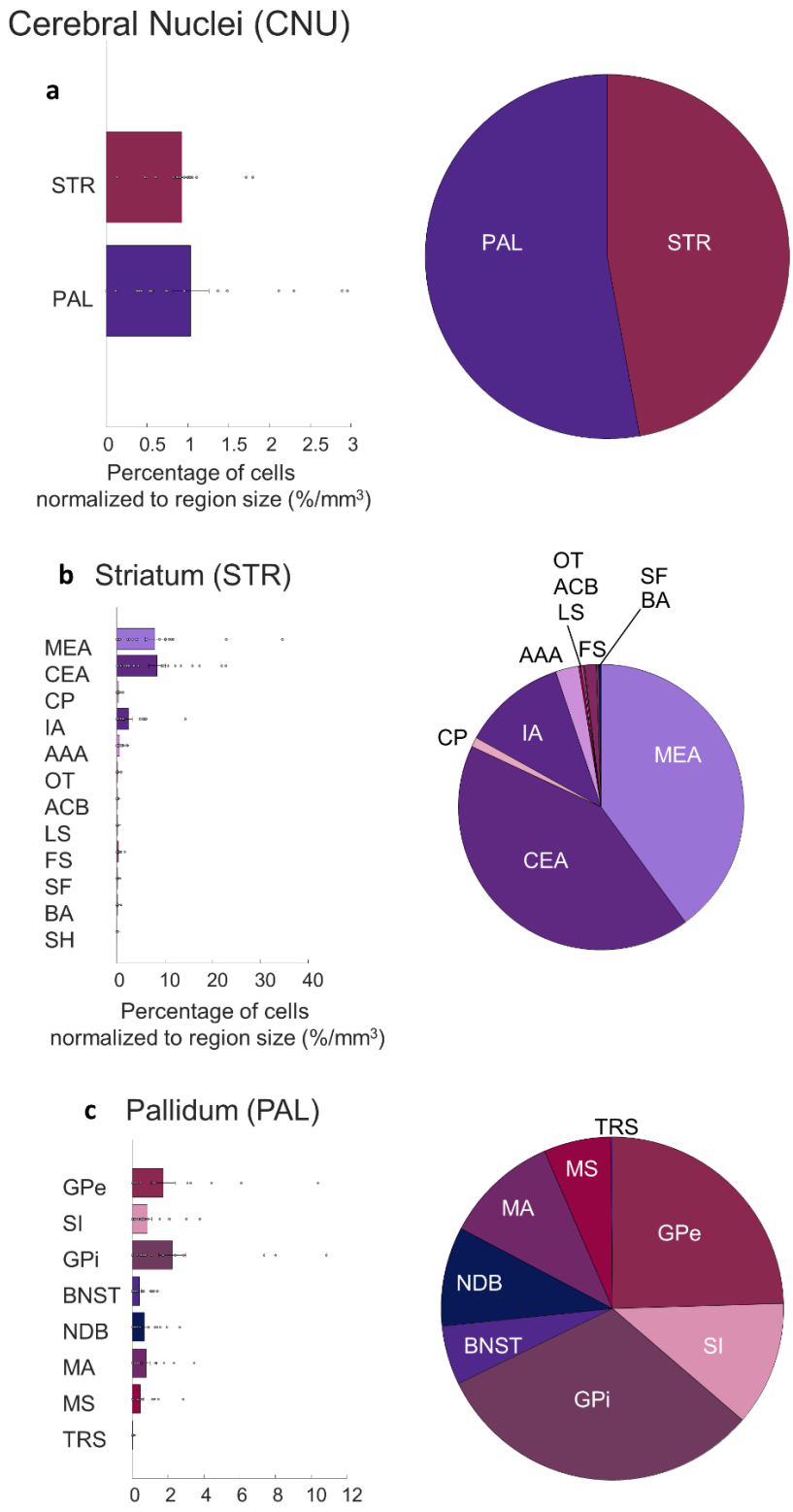

Figure 26: Input cell density in the cerebral nuclei (CNU). a, Input cell densities of constituent regions of the cerebral nuclei. b, Input cell densities of constituent regions in the striatum. c, Input cell densities of constituent regions in the pallidum. Results are presented as both bar chart and pie charts.

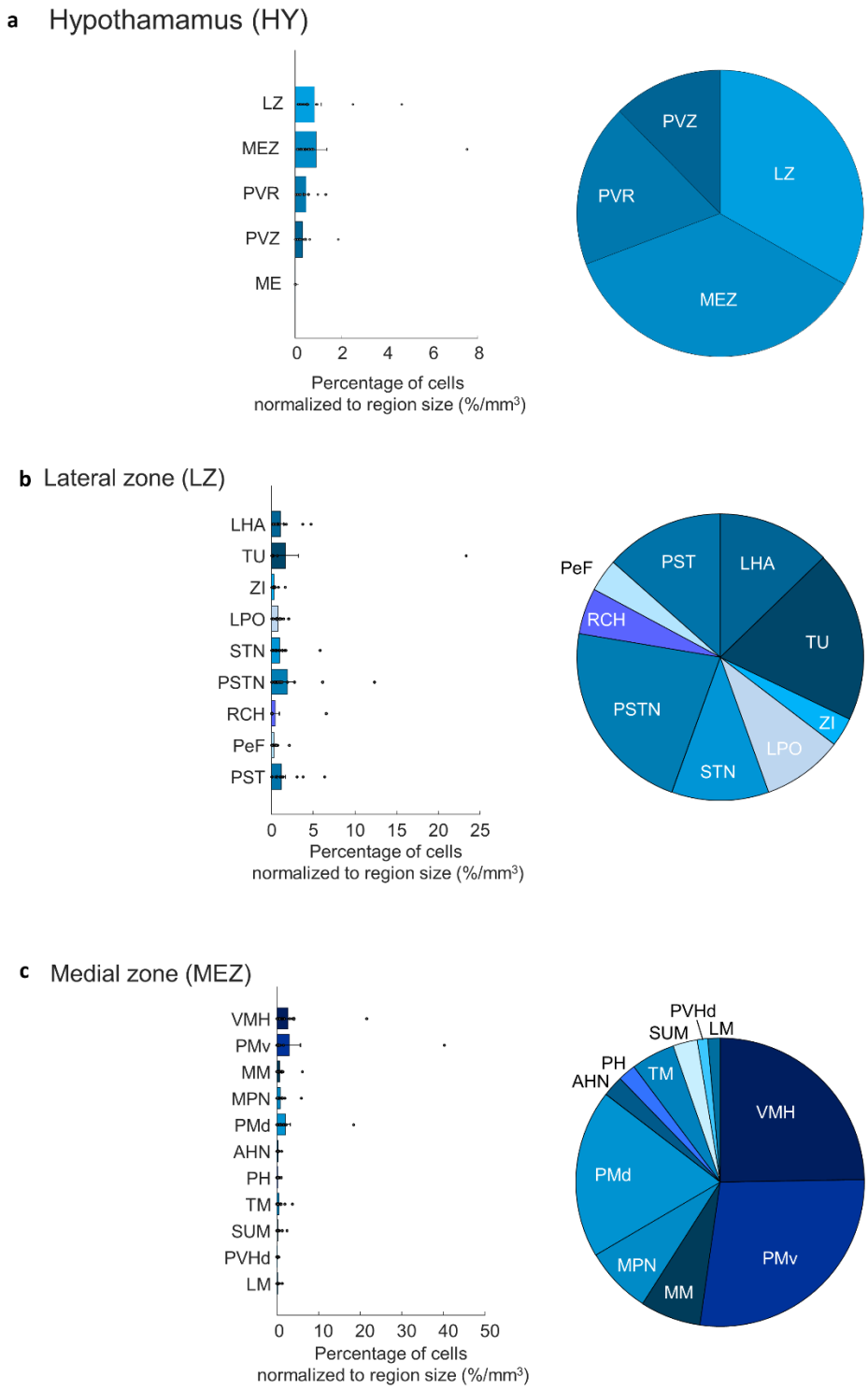

Figure 27: Input cell density in the hypothalamus (HY). a, Input cell densities of constituent regions in the hypothalamus. b, Input cell densities of constituent regions in the lateral zone of the hypothalamus. c, Input cell densities of constituent regions in the medial zone of the hypothalamus. Results are presented as both bar chart and pie charts.

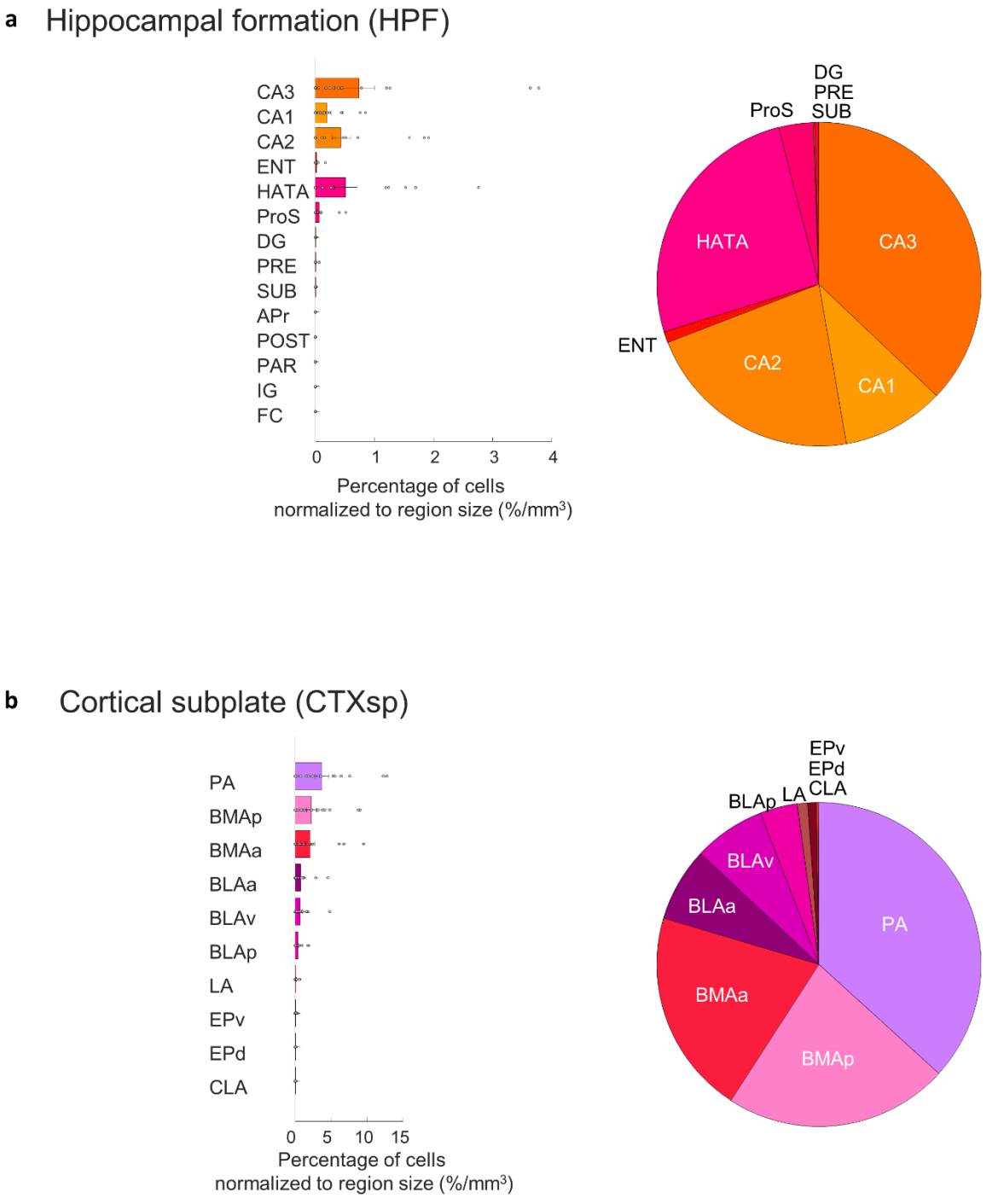

Figure 28: Input cell density in the hippocampal formation (HPF) and the cortical subplate (CTXsp). a, Input cell densities of constituent regions in the hippocampal formation. b, Input cell densities of constituent regions in the cortical subplate. Results are presented as both bar chart and pie charts.

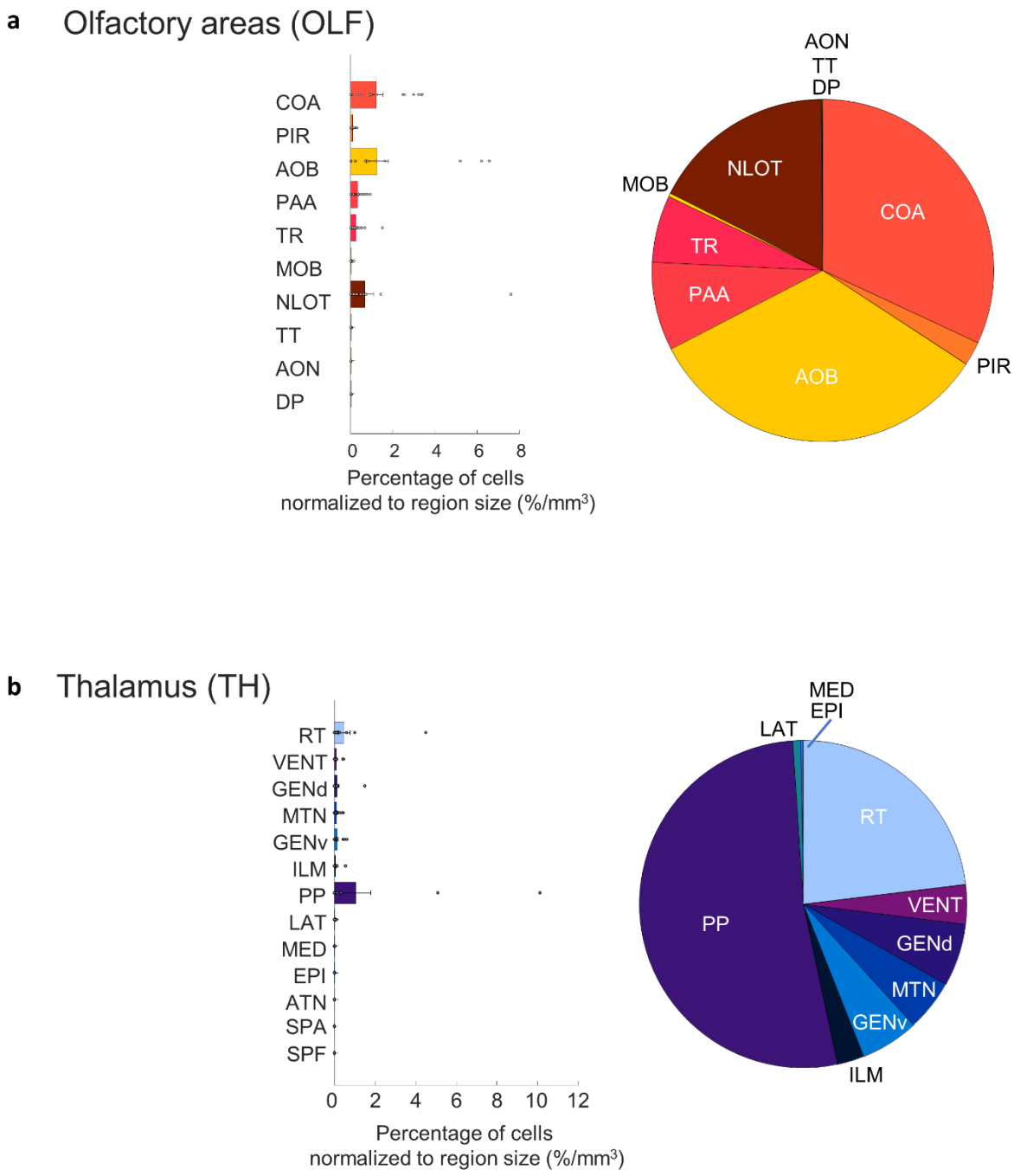

Figure 29: Input cell density in the olfactory areas (OLF) and the thalamus (TH). a, Input cell densities of constituent regions in the olfactory areas. b, Input cell densities of constituent regions in the thalamus. Results are presented as both bar chart and pie charts.

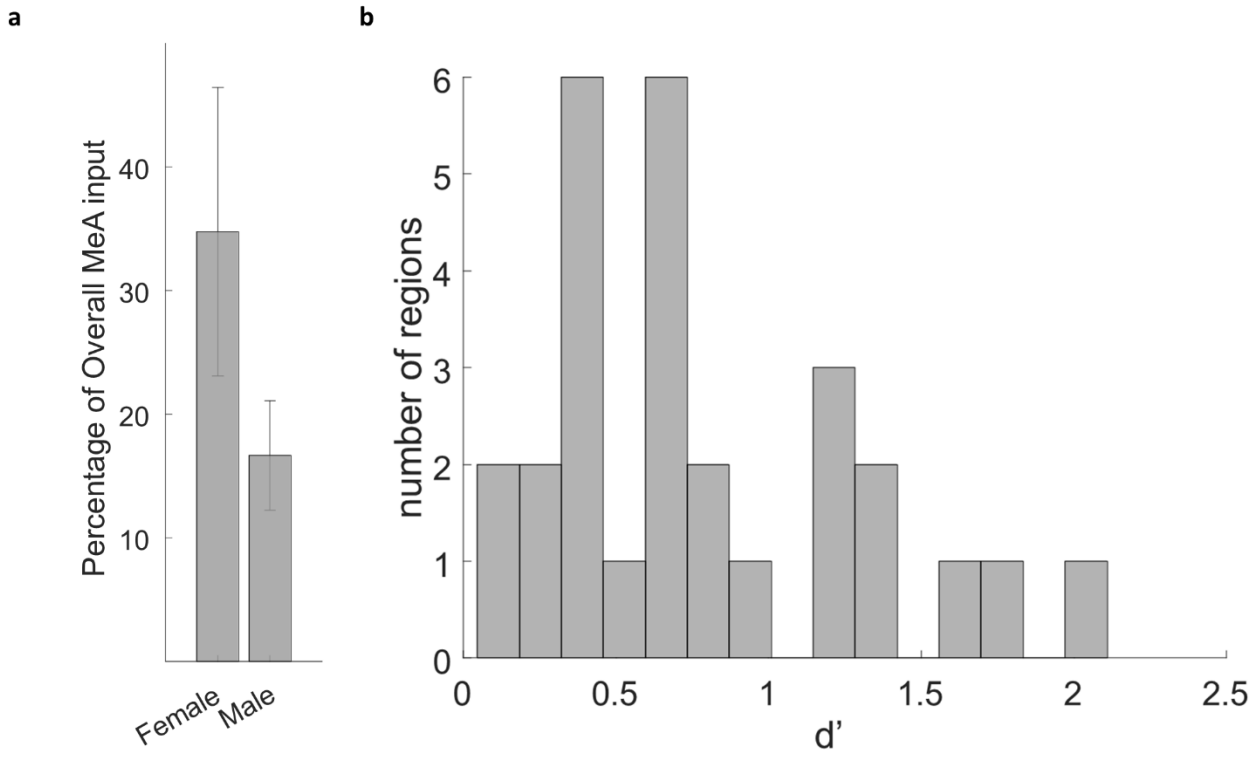

Figure 30: Comparison of sex differences in observed inputs to MeA Arom+ Cells. a, Graph comparing the fraction of labeled neurons in the MeA, local to the injection site, in females and males. b, graph showing the d′ values for sex differences in the regions presented in Figure 9.

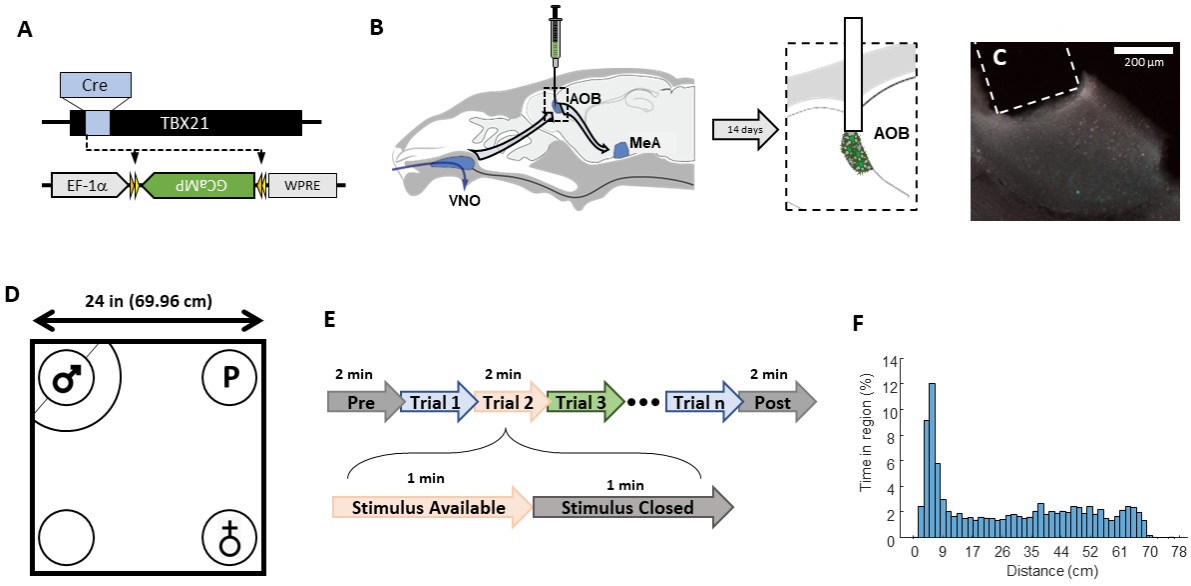

Figure 31: Introduction to fiberphotometry and behavioral testing paradigm A) Conditional AAV vectors were injected in tbet-cre mice to express GCaMP6s in mitral and tufted cells in the AOB. B) Fourteen days after AAV injection, a custom fiberoptic probe was implanted into at the same stereotaxic coordinates to collect light fluctuations in the infected mitral and tufted cells of the AOB. C) Fluorescent images showing infection of mitral and tufted cells of the AOB with fluorescent GCaMP. The fiber placement is identified by the dotted box. D) A diagram showing the setup of the stimulus presentation box when setup for a predator trial. The delineated area around the male stimulus represents an area we identify as 'social interaction' between the stimulus and experimental animal. E) The behavioral paradigm included an initial 2 min habituation to the stimulus presentation box followed by 7 trials. Each trial consisted of a randomized presentation of one of the three stimuli (for predator: Male, Female, and Predator; without predator: Male, Female, and Control) for one minute followed by a one-minute period where no stimulus is presented. This is repeated three times to ensure that each stimulus is presented once per trial. Following the trials, a post-experimental period of 2 minutes is recorded. F) Histogram showing the percentages of time the animals spent at a given distance from an open stimulus while the animal is manually scored and having been in the 'social interaction' area.

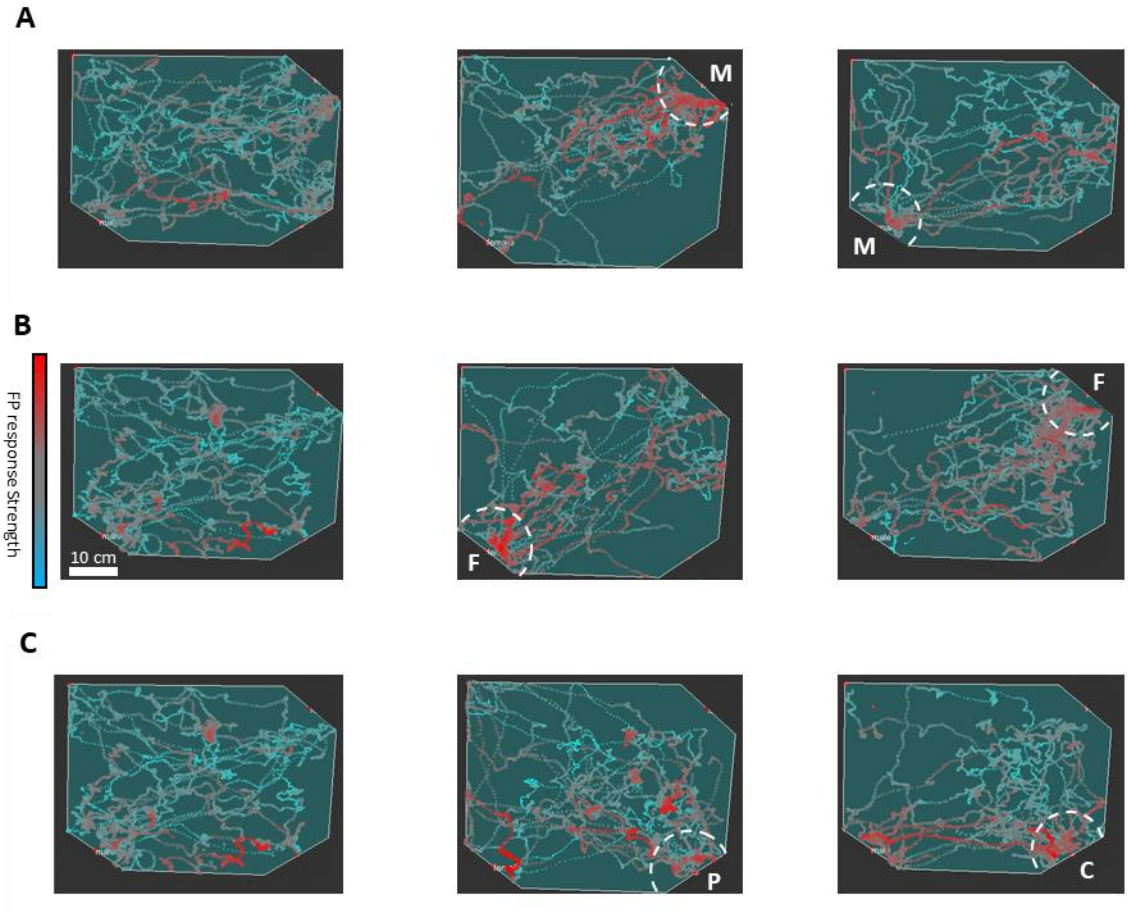

Figure 32: Example behavioral tracking data from female animal. Graphs showing the position of a female animal with respect to the behavior box in response to A) male, B) female, and C) non animal stimuli. Each subset includes an image showing the position of a female animal when all stimuli are unavailable following an interaction (left), when the stimulus is available and the predator stimulus is present (middle), and when the stimulus is available and the predator stimulus is not present (right). The areas designated by the white, dotted line are designated 'social interaction' areas for each presented stimulus. In B) the scale of the images is shown along with a heatbar, which shows the colors that correlate to higher (red) and lower (blue) z-score fiberphotometry responses.

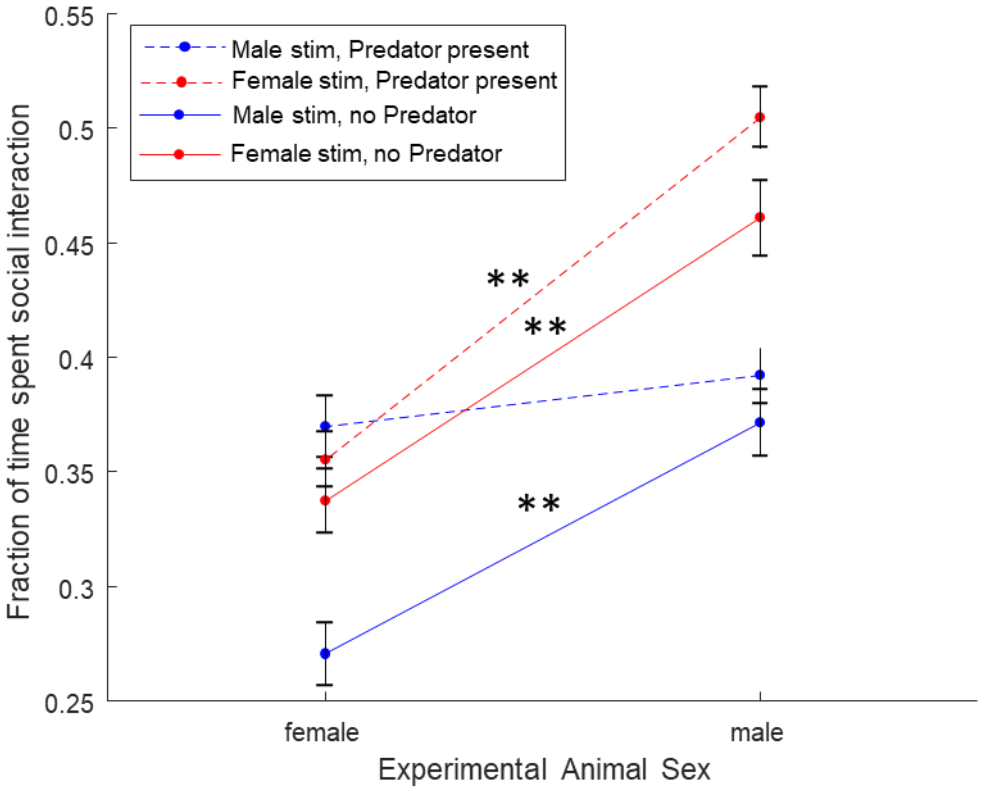

Figure 33: Comparing male and female behavior to various stimuli. Comparison showing the different average amount of time that a given male or female animal spends in the 'social interaction' area of the behavior presentation box when presented with male or female stimuli with and without the predator stimulus present. Error bars show standard error of the mean for each point. ** connotates a significance of $p < 0.001$ between the connected points using a paired samples t-test to compare between measurements for each group (male and female).

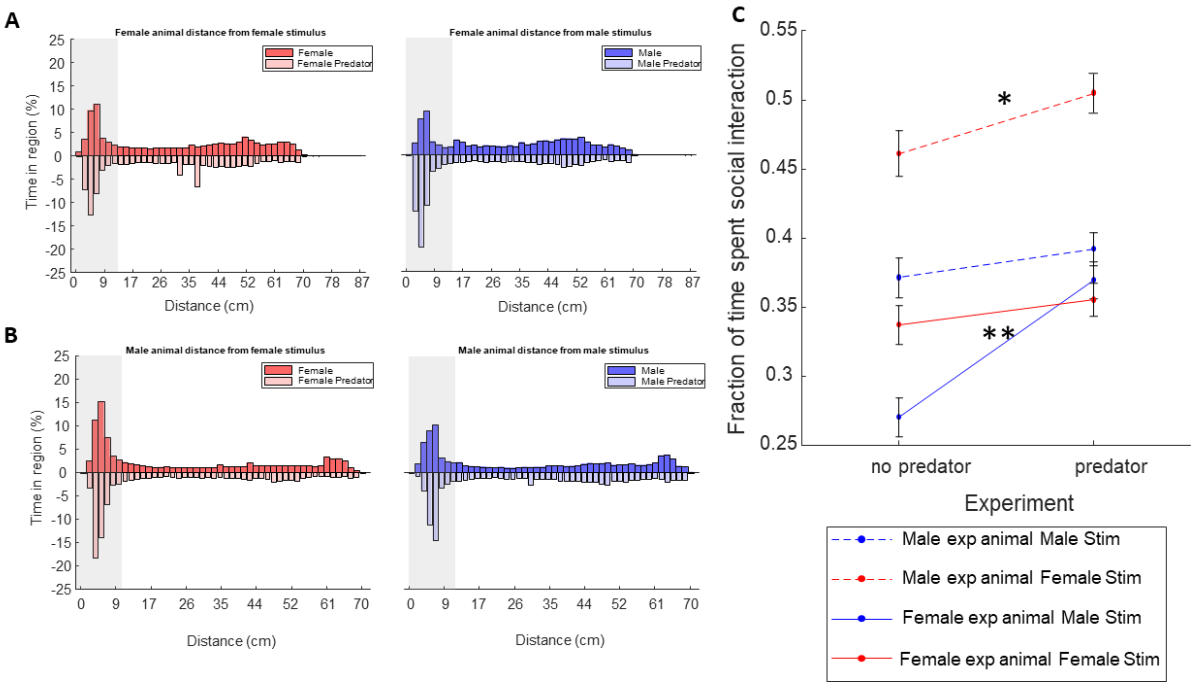

Figure 34: Showing the impact of predator scent on behavior. Histograms showing the percentages of time female A) and male B) animals spend at a given distance from the available female (left) and male (right) stimulus animals with and without the predator stimulus present. The shaded area indicates the area that we designated as 'social interaction' area. C) A graphic comparison showing the different average amount of time that a given animal spends in the 'social interaction' area of the behavior presentation box when presented with male or female stimuli with or without the predator stimulus present. Error bars show standard error of the mean for each point. ** Connotates a significance of $p < 0.001$ between the connected points using a paired samples t-test to compare between measurements for each group (predator present vs no predator present). * Connotates a significance of $p < 0.05$ between the connected points using a paired samples t-test to compare between measurements for each group (predator present vs no predator present).

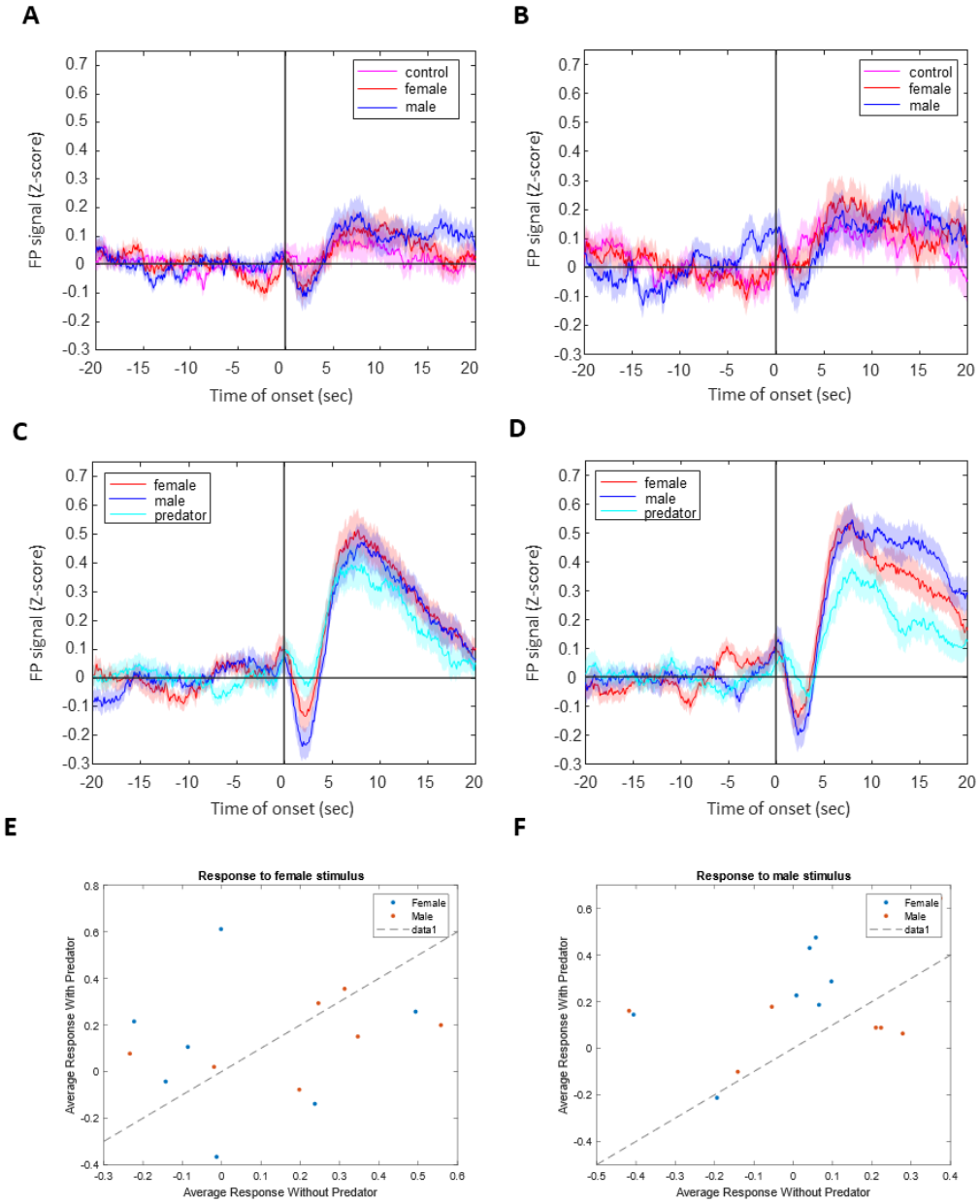

Figure 35: Average recorded neural responses to social interaction. Graphs showing the average recorded neural responses (normalized to z-scores) to sniffing a male (blue), female (red), or control stimulus (violet) in a male A) and female B) animal with respect to the sniffing behavior (0 point on the x-axis). Standard error of the mean is displayed as shaded area in the graphs. C) and D) present the same average neural signals recorded for male C) and female D) responses to sniffing male (blue), female (red) and predator stimuli (cyan) with respect to the sniffing behavior. These graphs show the same data as is displayed in Figures 6 and 7. Graphs E) and F) show the effect of adding the predator stimulus to an experiment on average z-score responses for individual male (blue) and female (red) animals in response to female E) and male F) stimuli.

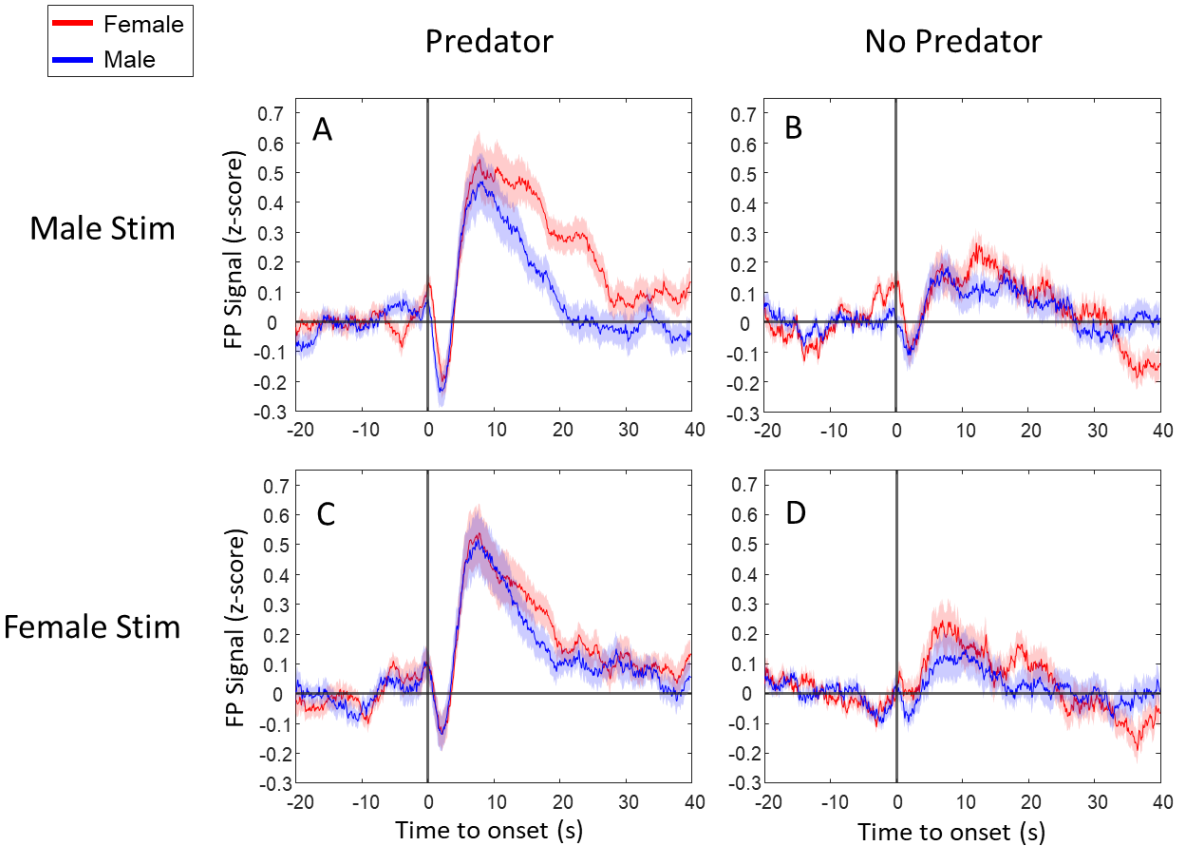

Figure 36: Showing sex-differences in neural responses to various stimuli. Graphs comparing the average recorded neural responses (normalized to z-scores) in male A),C) and female B),D) animals to male A),B) and female C),D) stimuli with respect to the sniffing behavior (0 point on the x-axis) in male (blue) and female (red) experimental animals. Standard error of the mean is displayed as shaded area in the graphs. These graphs show the same data as is displayed in Figures 5 and 7.

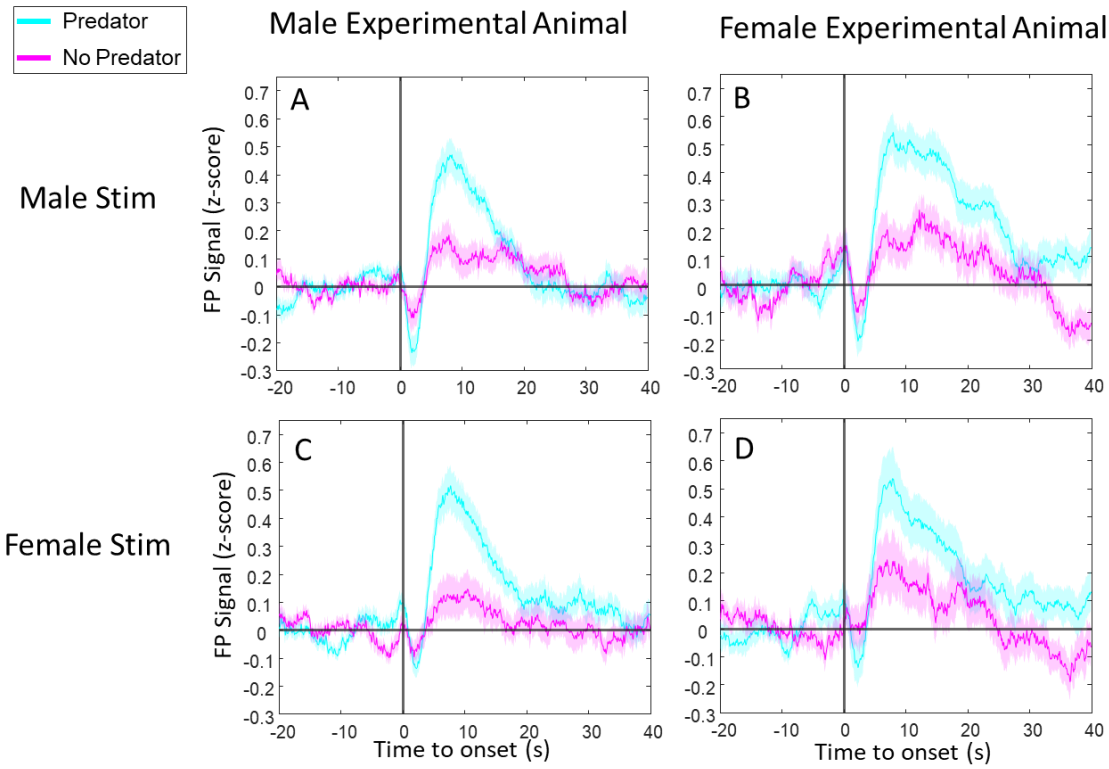

Figure 37: Demonstrating the effect of predator scent on neural responses to a given social stimulus. Graphs comparing the average recorded neural responses (normalized to z-scores) in male A),C) and female B),D) animals to male A),B) and female C),D) stimuli with respect to the sniffing behavior (0 point on the x-axis) in experiments with (cyan) and without (violet) the predator stimulus present. Standard error of the mean is displayed as shaded area in the graphs. These graphs show the same data as is displayed in Figures 5 and 6.

APPENDIX B

TABLES

Technique	Time to clear Full mouse brain (hr)	Antibody Penetration over time (mm/hr)	Level of Difficulty	Cost
MHD-accelerated Clearing	12 - 48	0.15	Low	$
CLARITY (Chung, et al., 2013)	120 – 216	0.0074	High	$$
Stochastic Electrotransport (Kim, SY, et al., 2015)	72	0.20	Very High	$$
ACT-PRESTO (Lee, et al., 2016)	6	0.040	High	$$$
SCALEs (Hama, et al., 2015)	72	0.066	Medium	$
uDISCO (Pan, et al., 2016)	198	0.0046 - 0.010	Low	$
CUBIC/ CUBIC-HistoVIsion (Susaki, et al., 2015; Susaki, et al., 2020)	72 – 168	0.007 - 0.060	Medium	$
Adipo-Clear (Chi, et al., 2016)	24 – 48	0.042 - 0.050	Medium	$
SWITCH (Murray, et al., 2015)	168 – 672	0.083	Low	$

Table 1: A direct comparison of multiple popular clearing techniques, based on literature, that shows the reported time it takes to clear an intact mouse brain, the relative antibody penetration into the tissue over a single hour, the degree of difficulty to setup and use the technique, and the amount of money it costs to implement the technique effectively. Degree of difficulty is a subjective measure of the amount and complexity of steps and solutions required to implement each technique and the level of expertise required construct devices for required for the technique and use these devices to clear mouse tissue. Level of difficulty ranges from easy (easy setup and/or requiring very few easy steps) to very hard (intricate setup that requires a high level of specialized expertise and/or requires many difficult steps) Cost to implement the technique is displayed as less than $1000 ($), less than $10,000 ($$), and over $10,000 ($$$).

Region name	Contra percentage	Total number of contra cells
Inferior colliculus	0	0
Basic cell groups and regions	0.770459457	82
Anterior amygdalar area	0	0
Periventricular hypothalamic nucleus, anterior part	85.71428571	6
Anterior cingulate area	75	3
Paraventricular hypothalamic nucleus	6	3
Infralimbic area	0	0
Intralaminar nuclei of the dorsal thalamus	2.631578947	1
Nucleus accumbens	1.538461538	2
Paraventricular hypothalamic nucleus, descending division	0	0
Lateral terminal nucleus of the accessory optic tract	0	0
Anterodorsal preoptic nucleus	4.347826087	1
Anterior hypothalamic nucleus	0	0
Agranular insular area	3.389830508	2
Interpeduncular nucleus	50	1
Periventricular hypothalamic nucleus, intermediate part	48.35164835	44
Periventricular hypothalamic nucleus, posterior part	8.333333333	3
Midbrain reticular nucleus	6.666666667	1
Lateral amygdalar nucleus	0	0
Periventricular hypothalamic nucleus, preoptic part	22.91666667	11
Lateral group of the dorsal thalamus	0	0
Accessory olfactory bulb	0	0
Anterior olfactory nucleus	0	0
Retrochiasmatic area	0	0
Lateral hypothalamic area	0.412654746	6
Nucleus raphe magnus	50	1
Lateral mammillary nucleus	10	1
Red nucleus	0	0
Arcuate hypothalamic nucleus	12.85714286	9
Lateral preoptic area	1.308900524	5
Lateral septal nucleus	1.015228426	2
Midbrain reticular nucleus, retrorubral area	0	0
Auditory areas	0	0
Reticular nucleus of the thalamus	0	0
Anteroventral preoptic nucleus	1.785714286	2
Anteroventral periventricular nucleus	6.25	5
Suprachiasmatic nucleus	66.66666667	2

Bed nucleus of the accessory olfactory tract	0	0
Superior colliculus, motor related	0	0
Magnocellular nucleus	0	0
Basolateral amygdalar nucleus, anterior part	0	0
Septofimbrial nucleus	5.263157895	2
Basolateral amygdalar nucleus, posterior part	0.307692308	1
Primary somatosensory area	0	0
Basomedial amygdalar nucleus, anterior part	0.102092905	2
Accessory supraoptic group	0	0
Basomedial amygdalar nucleus, posterior part	0.064683053	1
Subfornical organ	0	0
Substantia innominata	0	0
Subparaventricular zone	50	3
Bed nuclei of the stria terminalis	0.333889816	2
Preparasubthalamic nucleus	0	0
Parasubthalamic nucleus	0.641025641	1
Substantia nigra, compact part	100	1
Supplemental somatosensory area	75	3
Substantia nigra, reticular part	0	0
Field CA1	0	0
Supraoptic nucleus	0	0
Medial amygdalar nucleus	0.008221656	1
Field CA2	0	0
Medial group of the dorsal thalamus	10	1
Basolateral amygdalar nucleus, ventral part	0.241545894	1
Median preoptic nucleus	33.33333333	1
Field CA3	0.027307482	1
Subthalamic nucleus	0	0
Medial mammillary nucleus	12.40310078	32
Subiculum	0	0
Main olfactory bulb	84.44444444	38
Medial preoptic nucleus	2.459016393	6
Medial preoptic area	1.742160279	5
Supramammillary nucleus	14.66666667	11
Cerebellar cortex	0	0
Central amygdalar nucleus	0.010026068	1
Temporal association areas	6.25	1
Tuberomammillary nucleus	18.75	9
Medial septal nucleus	15.55555556	35
Postpiriform transition area	0.869565217	4
Midline group of the dorsal thalamus	6.140350877	7
Nucleus of the brachium of the inferior colliculus	0	0
Triangular nucleus of septum	0	0

Claustrum	0	0
Taenia tecta	0	0
Diagonal band nucleus	4.625199362	29
Nucleus of the lateral lemniscus	100	1
Tuberal nucleus	1.587301587	7
Cuneiform nucleus	0	0
Nucleus of the lateral olfactory tract	0	0
Cortical amygdalar area	0.138197899	5
Ventral group of the dorsal thalamus	0	0
Facial motor nucleus	0	0
Visual areas	0	0
Caudoputamen	0.095739588	2
Visceral area	0	0
Ventrolateral preoptic nucleus	0	0
Ventromedial hypothalamic nucleus	8.396946565	55
Orbital area	28.57142857	2
Dentate gyrus	0	0
Ventral tegmental area	0	0
Olfactory tubercle	0	0
Posterior amygdalar nucleus	0.062558649	2
Piriform-amygdalar area	0	0
Periaqueductal gray	20	1
Zona incerta	0	0
Dorsal peduncular area	0	0
Dorsomedial nucleus of the hypothalamus	19.7080292	54
Parabrachial nucleus	0	0
Dorsal nucleus raphe	50	1
Ectorhinal area	0	0
Entorhinal area	0	0
Posterodorsal preoptic nucleus	0	0
Perirhinal area	0	0
Posterior hypothalamic nucleus	13.06818182	23
Endopiriform nucleus, dorsal part	0	0
Epithalamus	50	1
Piriform area	0.415973378	5
Endopiriform nucleus, ventral part	0	0
Prelimbic area	0	0
Dorsal premammillary nucleus	9.395973154	14
Primary motor area	40	2
Secondary motor area	90.47619048	19
Fundus of striatum	0	0
Ventral premammillary nucleus	3.816793893	10
Geniculate group, dorsal thalamus	0	0

Geniculate group, ventral thalamus	0	0
Globus pallidus, external segment	0	0
Globus pallidus, internal segment	0	0
Peripeduncular nucleus	0	0
Gigantocellular reticular nucleus	100	1
Pedunculopontine nucleus	0	0
Gustatory areas	0	0
Presubiculum	0	0
Pontine reticular nucleus, caudal part	100	1
Pretectal region	0	0
Intercalated amygdalar nucleus	0	0
Parastrial nucleus	0	0
Prosubiculum	0	0
Ventromedial preoptic nucleus	25	1
Perifornical nucleus	0	0
Hippocampo-amygdalar transition area	0.534759358	1
Paratrochlear nucleus	0	0

Table 2: Ipsilateral bias across brain regions. The average percentage of cells, as well as the absolute count of cells, are shown for each region on the contralateral hemisphere to the injection site.

Periventricular region	Periventricular zone	Hypothalamic medial zone	Hypothalamic lateral zone
Anterodorsal preoptic nucleus	Paraventricular hypothalamic nucleus	Anterior hypothalamic nucleus	Lateral Hypothalamic area
Anteroventral preoptic nucleus	Periventricular hypothalamic nucleus, anterior	Medial mammillary nucleus	Lateral preoptic area
Anteroventral periventricular nucleus	Periventricular hypothalamic nucleus, intermediate	Supramammillary nucleus	Parasubthalamic nucleus
Dorsomedial nucleus of the hypothalamus	Arcuate hypothalamic nucleus	Tuberomammilary nucleus	Perifornical nucleus
Medial preoptic area		Medial preoptic nucleus	Retrochiasmatic area
Posterodorsal preoptic nucleus		Dorsal premammillary nucleus	Subthalamic nucleus
Parastrial nucleus		Ventral premammillary nucleus	Tuberal nucleus
Periventricular hypothalamic nucleus, posterior		Ventromedial hypothalamic nucleus	Zona incerta
Periventricular hypothalamic nucleus, preoptic		Posterior hypothalamic nucleus	
Ventrolateral preoptic nucleus			

Table 3: Hypothalamic inputs to aromatase+ cells in the MeA. The hypothalamic regions of the aromatase-expressing MeA cells. The top row describes course hypothalamic ->MeAarom+. Each column enumerates the sub-regions in each respective course region ->MeAarom+ cells from the top row.

Superior central nucleus raphe: Mean: 0 +/- 0 SEM
Test against a mean of 0
Superior central nucleus raphe: ttest pval: NaN; tstat : NaN; df : 17; sd : 0
Test against a Expected # of cells based on region size 0.13627
Superior central nucleus raphe: ttest pval (scaled--expected based on size): 1; tstat : -Inf; df : 17; sd : 0

Locus ceruleus: Mean: 0 +/- 0 SEM
Test against a mean of 0
Locus ceruleus: ttest pval: NaN; tstat : NaN; df : 17; sd : 0
Test against a Expected # of cells based on region size 0.0031612
Locus ceruleus: ttest pval (scaled--expected based on size): 1; tstat : -Inf; df : 17; sd : 0

Laterodorsal tegmental nucleus: Mean: 0 +/- 0 SEM
Test against a mean of 0
Laterodorsal tegmental nucleus: ttest pval: NaN; tstat : NaN; df : 17; sd : 0
Test against a Expected # of cells based on region size 0.044372
Laterodorsal tegmental nucleus: ttest pval (scaled--expected based on size): 1; tstat : -Inf; df : 17; sd : 0

Nucleus incertus: Mean: 0 +/- 0 SEM
Test against a mean of 0
Nucleus incertus: ttest pval: NaN; tstat : NaN; df : 17; sd : 0
Test against a Expected # of cells based on region size 0.023008
Nucleus incertus: ttest pval (scaled--expected based on size): 1; tstat : -Inf; df : 17; sd : 0

Pontine reticular nucleus: Mean: 0 +/- 0 SEM
Test against a mean of 0
Pontine reticular nucleus: ttest pval: NaN; tstat : NaN; df : 17; sd : 0
Test against a Expected # of cells based on region size 0.54093
Pontine reticular nucleus: ttest pval (scaled--expected based on size): 1; tstat : -Inf; df : 17; sd : 0

Nucleus raphe pontis: Mean: 0 +/- 0 SEM
Test against a mean of 0
Nucleus raphe pontis: ttest pval: NaN; tstat : NaN; df : 17; sd : 0
Test against a Expected # of cells based on region size 0.020984
Nucleus raphe pontis: ttest pval (scaled--expected based on size): 1; tstat : -Inf; df : 17; sd : 0

Subceruleus nucleus: Mean: 0 +/- 0 SEM
Test against a mean of 0
Subceruleus nucleus: ttest pval: NaN; tstat : NaN; df : 17; sd : 0
Test against a Expected # of cells based on region size 0.0057519

Subceruleus nucleus: ttest pval (scaled--expected based on size): 1; tstat : -Inf; df : 17; sd : 0

Sublaterodorsal nucleus: Mean: 0 +/- 0 SEM
Test against a mean of 0
Sublaterodorsal nucleus: ttest pval: NaN; tstat : NaN; df : 17; sd : 0
Test against a Expected # of cells based on region size 0.010241
Sublaterodorsal nucleus: ttest pval (scaled--expected based on size): 1; tstat : -Inf; df : 17; sd : 0

Nucleus of the lateral lemniscus: Mean: 0.00044941 +/- 0.00011216 SEM
Test against a mean of 0
Nucleus of the lateral lemniscus: ttest pval: 0.16567; tstat : 1; df : 17; sd : 0.0019067
Test against a Expected # of cells based on region size 0.25004
Nucleus of the lateral lemniscus: ttest pval (scaled--expected based on size): 1; tstat : -555.3697; df : 17; sd : 0.0019067

Principal sensory nucleus of the trigeminal: Mean: 0 +/- 0 SEM
Test against a mean of 0
Principal sensory nucleus of the trigeminal: ttest pval: NaN; tstat : NaN; df : 17; sd : 0
Test against a Expected # of cells based on region size 0.24141
Principal sensory nucleus of the trigeminal: ttest pval (scaled--expected based on size): 1; tstat : -Inf; df : 17; sd : 0
---
parabrachial nucleus: Mean: 0.0017976 +/- 0.00044863 SEM
Test against a mean of 0
parabrachial nucleus: ttest pval: 0.16567; tstat : 1; df : 17; sd : 0.0076267
Test against a Expected # of cells based on region size 0.29638
parabrachial nucleus: ttest pval (scaled--expected based on size): 1; tstat : -163.8736; df : 17; sd : 0.0076267

Superior olivary complex: Mean: 0 +/- 0 SEM
Test against a mean of 0
Superior olivary complex: ttest pval: NaN; tstat : NaN; df : 17; sd : 0
Test against a Expected # of cells based on region size 0.20263
Superior olivary complex: ttest pval (scaled--expected based on size): 1; tstat : -Inf; df : 17; sd : 0

Abducens nucleus: Mean: 0 +/- 0 SEM
Test against a mean of 0
Abducens nucleus: ttest pval: NaN; tstat : NaN; df : 17; sd : 0
Test against a Expected # of cells based on region size 0.0080405
Abducens nucleus: ttest pval (scaled--expected based on size): 1; tstat : -Inf; df : 17; sd : 0

Facial motor nucleus: Mean: 0.00059285 +/- 0.00014795 SEM
Test against a mean of 0
Facial motor nucleus: ttest pval: 0.16567; tstat : 1; df : 17; sd : 0.0025152
Test against a Expected # of cells based on region size 0.20784
Facial motor nucleus: ttest pval (scaled--expected based on size): 1; tstat : -349.5866; df : 17; sd : 0.0025152

Accessory facial motor nucleus: Mean: 0 +/- 0 SEM
Test against a mean of 0
Accessory facial motor nucleus: ttest pval: NaN; tstat : NaN; df : 17; sd : 0
Test against a Expected # of cells based on region size 0.0011986
Accessory facial motor nucleus: ttest pval (scaled--expected based on size): 1; tstat : -Inf; df : 17; sd : 0

Nucleus ambiguus: Mean: 0 +/- 0 SEM
Test against a mean of 0
Nucleus ambiguus: ttest pval: NaN; tstat : NaN; df : 17; sd : 0
Test against a Expected # of cells based on region size 0.0093817
Nucleus ambiguus: ttest pval (scaled--expected based on size): 1; tstat : -Inf; df : 17; sd : 0

Dorsal motor nucleus of the vagus nerve: Mean: 0 +/- 0 SEM
Test against a mean of 0
Dorsal motor nucleus of the vagus nerve: ttest pval: NaN; tstat : NaN; df : 17; sd : 0
Test against a Expected # of cells based on region size 0.037822
Dorsal motor nucleus of the vagus nerve: ttest pval (scaled--expected based on size): 1; tstat : -Inf; df : 17; sd : 0

Gigantocellular reticular nucleus: Mean: 0.003247 +/- 0.00081034 SEM
Test against a mean of 0
Gigantocellular reticular nucleus: ttest pval: 0.16567; tstat : 1; df : 17; sd : 0.013776
Test against a Expected # of cells based on region size 0.60393
Gigantocellular reticular nucleus: ttest pval (scaled--expected based on size): 1; tstat : -184.9991; df : 17; sd : 0.013776

Infracerebellar nucleus: Mean: 0 +/- 0 SEM
Test against a mean of 0
Infracerebellar nucleus: ttest pval: NaN; tstat : NaN; df : 17; sd : 0
Test against a Expected # of cells based on region size 0.011742
Infracerebellar nucleus: ttest pval (scaled--expected based on size): 1; tstat : -Inf; df : 17; sd : 0

Inferior olivary complex: Mean: 0 +/- 0 SEM

Test against a mean of 0
Inferior olivary complex: ttest pval: NaN; tstat : NaN; df : 17; sd : 0
Test against a Expected # of cells based on region size 0.11344
Inferior olivary complex: ttest pval (scaled--expected based on size): 1; tstat : -Inf; df : 17; sd : 0

Intermediate reticular nucleus: Mean: 0 +/- 0 SEM
Test against a mean of 0
Intermediate reticular nucleus: ttest pval: NaN; tstat : NaN; df : 17; sd : 0
Test against a Expected # of cells based on region size 0.60413
Intermediate reticular nucleus: ttest pval (scaled--expected based on size): 1; tstat : -Inf; df : 17; sd : 0

Inferior salivatory nucleus: Mean: 0 +/- 0 SEM
Test against a mean of 0
Inferior salivatory nucleus: ttest pval: NaN; tstat : NaN; df : 17; sd : 0
Test against a Expected # of cells based on region size 0.0015619
Inferior salivatory nucleus: ttest pval (scaled--expected based on size): 1; tstat : -Inf; df : 17; sd : 0

Linear nucleus of the medulla: Mean: 0 +/- 0 SEM
Test against a mean of 0
Linear nucleus of the medulla: ttest pval: NaN; tstat : NaN; df : 17; sd : 0
Test against a Expected # of cells based on region size 0.013405
Linear nucleus of the medulla: ttest pval (scaled--expected based on size): 1; tstat : -Inf; df : 17; sd : 0

Lateral reticular nucleus: Mean: 0 +/- 0 SEM
Test against a mean of 0
Lateral reticular nucleus: ttest pval: NaN; tstat : NaN; df : 17; sd : 0
Test against a Expected # of cells based on region size 0.13335
Lateral reticular nucleus: ttest pval (scaled--expected based on size): 1; tstat : -Inf; df : 17; sd : 0

Magnocellular reticular nucleus: Mean: 0 +/- 0 SEM
Test against a mean of 0
Magnocellular reticular nucleus: ttest pval: NaN; tstat : NaN; df : 17; sd : 0
Test against a Expected # of cells based on region size 0.11764
Magnocellular reticular nucleus: ttest pval (scaled--expected based on size): 1; tstat : -Inf; df : 17; sd : 0

Medullary reticular nucleus: Mean: 0 +/- 0 SEM
Test against a mean of 0
Medullary reticular nucleus: ttest pval: NaN; tstat : NaN; df : 17; sd : 0
Test against a Expected # of cells based on region size 0.44487

Medullary reticular nucleus: ttest pval (scaled--expected based on size): 1; tstat : -Inf; df : 17; sd : 0

Parvicellular reticular nucleus: Mean: 0 +/- 0 SEM
Test against a mean of 0
Parvicellular reticular nucleus: ttest pval: NaN; tstat : NaN; df : 17; sd : 0
Test against a Expected # of cells based on region size 0.49066
Parvicellular reticular nucleus: ttest pval (scaled--expected based on size): 1; tstat : -Inf; df : 17; sd : 0

Parasolitary nucleus: Mean: 0 +/- 0 SEM
Test against a mean of 0
Parasolitary nucleus: ttest pval: NaN; tstat : NaN; df : 17; sd : 0
Test against a Expected # of cells based on region size 0.006139
Parasolitary nucleus: ttest pval (scaled--expected based on size): 1; tstat : -Inf; df : 17; sd : 0

Paragigantocellular reticular nucleus: Mean: 0 +/- 0 SEM
Test against a mean of 0
Paragigantocellular reticular nucleus: ttest pval: NaN; tstat : NaN; df : 17; sd : 0
Test against a Expected # of cells based on region size 0.21407
Paragigantocellular reticular nucleus: ttest pval (scaled--expected based on size): 1; tstat : -Inf; df : 17; sd : 0

Perihypoglossal nuclei: Mean: 0 +/- 0 SEM
Test against a mean of 0
Perihypoglossal nuclei: ttest pval: NaN; tstat : NaN; df : 17; sd : 0
Test against a Expected # of cells based on region size 0.07651
Perihypoglossal nuclei: ttest pval (scaled--expected based on size): 1; tstat : -Inf; df : 17; sd : 0

Parapyramidal nucleus: Mean: 0 +/- 0 SEM
Test against a mean of 0
Parapyramidal nucleus: ttest pval: NaN; tstat : NaN; df : 17; sd : 0
Test against a Expected # of cells based on region size 0.02057
Parapyramidal nucleus: ttest pval (scaled--expected based on size): 1; tstat : -Inf; df : 17; sd : 0

Vestibular nuclei: Mean: 0 +/- 0 SEM
Test against a mean of 0
Vestibular nuclei: ttest pval: NaN; tstat : NaN; df : 17; sd : 0
Test against a Expected # of cells based on region size 0.74321
Vestibular nuclei: ttest pval (scaled--expected based on size): 1; tstat : -Inf; df : 17; sd : 0

Nucleus x: Mean: 0 +/- 0 SEM

Test against a mean of 0
Nucleus x: ttest pval: NaN; tstat : NaN; df : 17; sd : 0
Test against a Expected # of cells based on region size 0.01238
Nucleus x: ttest pval (scaled--expected based on size): 1; tstat : -Inf; df : 17; sd : 0

Hypoglossal nucleus: Mean: 0 +/- 0 SEM
Test against a mean of 0
Hypoglossal nucleus: ttest pval: NaN; tstat : NaN; df : 17; sd : 0
Test against a Expected # of cells based on region size 0.061142
Hypoglossal nucleus: ttest pval (scaled--expected based on size): 1; tstat : -Inf; df : 17; sd : 0

Nucleus y: Mean: 0 +/- 0 SEM
Test against a mean of 0
Nucleus y: ttest pval: NaN; tstat : NaN; df : 17; sd : 0
Test against a Expected # of cells based on region size 0.0050966
Nucleus y: ttest pval (scaled--expected based on size): 1; tstat : -Inf; df : 17; sd : 0

Nucleus raphe magnus: Mean: 0.0010423 +/- 0.00018033 SEM
Test against a mean of 0
Nucleus raphe magnus: ttest pval: 0.083673; tstat : 1.4425; df : 17; sd : 0.0030655
Test against a Expected # of cells based on region size 0.031972
Nucleus raphe magnus: ttest pval (scaled--expected based on size): 1; tstat : -42.8057; df : 17; sd : 0.0030655

Nucleus raphe pallidus: Mean: 0 +/- 0 SEM
Test against a mean of 0
Nucleus raphe pallidus: ttest pval: NaN; tstat : NaN; df : 17; sd : 0
Test against a Expected # of cells based on region size 0.01641
Nucleus raphe pallidus: ttest pval (scaled--expected based on size): 1; tstat : -Inf; df : 17; sd : 0

Nucleus raphe obscurus: Mean: 0 +/- 0 SEM
Test against a mean of 0
Nucleus raphe obscurus: ttest pval: NaN; tstat : NaN; df : 17; sd : 0
Test against a Expected # of cells based on region size 0.013928
Nucleus raphe obscurus: ttest pval (scaled--expected based on size): 1; tstat : -Inf; df : 17; sd : 0

Area postrema: Mean: 0 +/- 0 SEM
Test against a mean of 0
Area postrema: ttest pval: NaN; tstat : NaN; df : 17; sd : 0
Test against a Expected # of cells based on region size 0.012733
Area postrema: ttest pval (scaled--expected based on size): 1; tstat : -Inf; df : 17; sd : 0

Cochlear nuclei: Mean: 0 +/- 0 SEM
Test against a mean of 0
Cochlear nuclei: ttest pval: NaN; tstat : NaN; df : 17; sd : 0
Test against a Expected # of cells based on region size 0.41049
Cochlear nuclei: ttest pval (scaled--expected based on size): 1; tstat : -Inf; df : 17; sd : 0

Dorsal column nuclei: Mean: 0 +/- 0 SEM
Test against a mean of 0
Dorsal column nuclei: ttest pval: NaN; tstat : NaN; df : 17; sd : 0
Test against a Expected # of cells based on region size 0.09435
Dorsal column nuclei: ttest pval (scaled--expected based on size): 1; tstat : -Inf; df : 17; sd : 0

External cuneate nucleus: Mean: 0 +/- 0 SEM
Test against a mean of 0
External cuneate nucleus: ttest pval: NaN; tstat : NaN; df : 17; sd : 0
Test against a Expected # of cells based on region size 0.052097
External cuneate nucleus: ttest pval (scaled--expected based on size): 1; tstat : -Inf; df : 17; sd : 0

Nucleus of the trapezoid body: Mean: 0 +/- 0 SEM
Test against a mean of 0
Nucleus of the trapezoid body: ttest pval: NaN; tstat : NaN; df : 17; sd : 0
Test against a Expected # of cells based on region size 0.0397
Nucleus of the trapezoid body: ttest pval (scaled--expected based on size): 1; tstat : -Inf; df : 17; sd : 0

Nucleus of the solitary tract: Mean: 0 +/- 0 SEM
Test against a mean of 0
Nucleus of the solitary tract: ttest pval: NaN; tstat : NaN; df : 17; sd : 0
Test against a Expected # of cells based on region size 0.19355
Nucleus of the solitary tract: ttest pval (scaled--expected based on size): 1; tstat : -Inf; df : 17; sd : 0

Spinal nucleus of the trigeminal, caudal part: Mean: 0 +/- 0 SEM
Test against a mean of 0
Spinal nucleus of the trigeminal, caudal part: ttest pval: NaN; tstat : NaN; df : 17; sd : 0
Test against a Expected # of cells based on region size 0.3686
Spinal nucleus of the trigeminal, caudal part: ttest pval (scaled--expected based on size): 1; tstat : -Inf; df : 17; sd : 0

Spinal nucleus of the trigeminal, interpolar part: Mean: 0 +/- 0 SEM
Test against a mean of 0

Spinal nucleus of the trigeminal, interpolar part: ttest pval: NaN; tstat : NaN; df : 17; sd : 0
Test against a Expected # of cells based on region size 0.4143
Spinal nucleus of the trigeminal, interpolar part: ttest pval (scaled--expected based on size): 1; tstat : -Inf; df : 17; sd : 0

Spinal nucleus of the trigeminal, oral part: Mean: 0 +/- 0 SEM
Test against a mean of 0
Spinal nucleus of the trigeminal, oral part: ttest pval: NaN; tstat : NaN; df : 17; sd : 0
Test against a Expected # of cells based on region size 0.21959
Spinal nucleus of the trigeminal, oral part: ttest pval (scaled--expected based on size): 1; tstat : -Inf; df : 17; sd : 0

Paratrigeminal nucleus: Mean: 0 +/- 0 SEM
Test against a mean of 0
Paratrigeminal nucleus: ttest pval: NaN; tstat : NaN; df : 17; sd : 0
Test against a Expected # of cells based on region size 0.029041
Paratrigeminal nucleus: ttest pval (scaled--expected based on size): 1; tstat : -Inf; df : 17; sd : 0

Barrington's nucleus: Mean: 0 +/- 0 SEM
Test against a mean of 0
Barrington's nucleus: ttest pval: NaN; tstat : NaN; df : 17; sd : 0
Test against a Expected # of cells based on region size 0.0033751
Barrington's nucleus: ttest pval (scaled--expected based on size): 1; tstat : -Inf; df : 17; sd : 0

Dorsal tegmental nucleus: Mean: 0 +/- 0 SEM
Test against a mean of 0
Dorsal tegmental nucleus: ttest pval: NaN; tstat : NaN; df : 17; sd : 0
Test against a Expected # of cells based on region size 0.022536
Dorsal tegmental nucleus: ttest pval (scaled--expected based on size): 1; tstat : -Inf; df : 17; sd : 0

Posterodorsal tegmental nucleus: Mean: 0 +/- 0 SEM
Test against a mean of 0
Posterodorsal tegmental nucleus: ttest pval: NaN; tstat : NaN; df : 17; sd : 0
Test against a Expected # of cells based on region size 0.010397
Posterodorsal tegmental nucleus: ttest pval (scaled--expected based on size): 1; tstat : -Inf; df : 17; sd : 0

Pontine central gray: Mean: 0 +/- 0 SEM
Test against a mean of 0
Pontine central gray: ttest pval: NaN; tstat : NaN; df : 17; sd : 0
Test against a Expected # of cells based on region size 0.14153

Pontine central gray: ttest pval (scaled--expected based on size): 1; tstat : -Inf; df : 17; sd : 0

Pontine gray: Mean: 0 +/- 0 SEM
Test against a mean of 0
Pontine gray: ttest pval: NaN; tstat : NaN; df : 17; sd : 0
Test against a Expected # of cells based on region size 0.21287
Pontine gray: ttest pval (scaled--expected based on size): 1; tstat : -Inf; df : 17; sd : 0

Pontine reticular nucleus, caudal part: Mean: 0.003247 +/- 0.00081034 SEM
Test against a mean of 0
Pontine reticular nucleus, caudal part: ttest pval: 0.16567; tstat : 1; df : 17; sd : 0.013776
Test against a Expected # of cells based on region size 0.54369
Pontine reticular nucleus, caudal part: ttest pval (scaled--expected based on size): 1; tstat : -166.4446; df : 17; sd : 0.013776

Supragenual nucleus: Mean: 0 +/- 0 SEM
Test against a mean of 0
Supragenual nucleus: ttest pval: NaN; tstat : NaN; df : 17; sd : 0
Test against a Expected # of cells based on region size 0.0037724
Supragenual nucleus: ttest pval (scaled--expected based on size): 1; tstat : -Inf; df : 17; sd : 0

Supratrigeminal nucleus: Mean: 0 +/- 0 SEM
Test against a mean of 0
Supratrigeminal nucleus: ttest pval: NaN; tstat : NaN; df : 17; sd : 0
Test against a Expected # of cells based on region size 0.056501
Supratrigeminal nucleus: ttest pval (scaled--expected based on size): 1; tstat : -Inf; df : 17; sd : 0

Tegmental reticular nucleus: Mean: 0 +/- 0 SEM
Test against a mean of 0
Tegmental reticular nucleus: ttest pval: NaN; tstat : NaN; df : 17; sd : 0
Test against a Expected # of cells based on region size 0.18094
Tegmental reticular nucleus: ttest pval (scaled--expected based on size): 1; tstat : -Inf; df : 17; sd : 0

Motor nucleus of trigeminal: Mean: 0 +/- 0 SEM
Test against a mean of 0
Motor nucleus of trigeminal: ttest pval: NaN; tstat : NaN; df : 17; sd : 0
Test against a Expected # of cells based on region size 0.07705
Motor nucleus of trigeminal: ttest pval (scaled--expected based on size): 1; tstat : -Inf; df : 17; sd : 0

Peritrigeminal zone: Mean: 0 +/- 0 SEM
Test against a mean of 0
Peritrigeminal zone: ttest pval: NaN; tstat : NaN; df : 17; sd : 0
Test against a Expected # of cells based on region size 0.069662
Peritrigeminal zone: ttest pval (scaled--expected based on size): 1; tstat : -Inf; df : 17; sd : 0

Accessory trigeminal nucleus: Mean: 0 +/- 0 SEM
Test against a mean of 0
Accessory trigeminal nucleus: ttest pval: NaN; tstat : NaN; df : 17; sd : 0
Test against a Expected # of cells based on region size 0.0031035
Accessory trigeminal nucleus: ttest pval (scaled--expected based on size): 1; tstat : -Inf; df : 17; sd : 0

Parvicellular motor 5 nucleus: Mean: 0 +/- 0 SEM
Test against a mean of 0
Parvicellular motor 5 nucleus: ttest pval: NaN; tstat : NaN; df : 17; sd : 0
Test against a Expected # of cells based on region size 0.018285
Parvicellular motor 5 nucleus: ttest pval (scaled--expected based on size): 1; tstat : -Inf; df : 17; sd : 0

Intertrigeminal nucleus: Mean: 0 +/- 0 SEM
Test against a mean of 0
Intertrigeminal nucleus: ttest pval: NaN; tstat : NaN; df : 17; sd : 0
Test against a Expected # of cells based on region size 0.0095718
Intertrigeminal nucleus: ttest pval (scaled--expected based on size): 1; tstat : -Inf; df : 17; sd : 0

Field CA1: Mean: 2.4885 +/- 0.18631 SEM
Test against a mean of 0
Field CA1: ttest pval: 0.0019677; tstat : 3.3334; df : 17; sd : 3.1672
Test against a Expected # of cells based on region size 2.6586
Field CA1: ttest pval (scaled--expected based on size): 0.58877; tstat : -0.22787; df : 17; sd : 3.1672

Field CA2: Mean: 0.25768 +/- 0.023006 SEM
Test against a mean of 0
Field CA2: ttest pval: 0.0062132; tstat : 2.7953; df : 17; sd : 0.3911
Test against a Expected # of cells based on region size 0.12892
Field CA2: ttest pval (scaled--expected based on size): 0.090217; tstat : 1.3968; df : 17; sd : 0.3911

FieldCa3: Mean: 6.3221 +/- 0.57746 SEM
Test against a mean of 0
FieldCa3: ttest pval: 0.0070927; tstat : 2.7323; df : 17; sd : 9.8169
Test against a Expected # of cells based on region size 1.8646

FieldCa3: ttest pval (scaled--expected based on size): 0.035471; tstat : 1.9264; df : 17; sd : 9.8169

Dentate Gyrus: Mean: 0.018308 +/- 0.0028243 SEM
Test against a mean of 0
Dentate Gyrus: ttest pval: 0.06206; tstat : 1.6177; df : 17; sd : 0.048013
Test against a Expected # of cells based on region size 1.5904
Dentate Gyrus: ttest pval (scaled--expected based on size): 1; tstat : -138.9174; df : 17; sd : 0.048013

Fasciola cinerea: Mean: 0 +/- 0 SEM
Test against a mean of 0
Fasciola cinerea: ttest pval: NaN; tstat : NaN; df : 17; sd : 0
Test against a Expected # of cells based on region size 0.051896
Fasciola cinerea: ttest pval (scaled--expected based on size): 1; tstat : -Inf; df : 17; sd : 0

Induseum griseum: Mean: 0 +/- 0 SEM
Test against a mean of 0
Induseum griseum: ttest pval: NaN; tstat : NaN; df : 17; sd : 0
Test against a Expected # of cells based on region size 0.052127
Induseum griseum: ttest pval (scaled--expected based on size): 1; tstat : -Inf; df : 17; sd : 0

Entorhinal area: Mean: 0.25717 +/- 0.026799 SEM
Test against a mean of 0
Entorhinal area: ttest pval: 0.014209; tstat : 2.3949; df : 17; sd : 0.45559
Test against a Expected # of cells based on region size 2.4996
Entorhinal area: ttest pval (scaled--expected based on size): 1; tstat : -20.8826; df : 17; sd : 0.45559

Parasubiculum: Mean: 0 +/- 0 SEM
Test against a mean of 0
Parasubiculum: ttest pval: NaN; tstat : NaN; df : 17; sd : 0
Test against a Expected # of cells based on region size 0.20365
Parasubiculum: ttest pval (scaled--expected based on size): 1; tstat : -Inf; df : 17; sd : 0

Postsubiculum: Mean: 0 +/- 0 SEM
Test against a mean of 0
Postsubiculum: ttest pval: NaN; tstat : NaN; df : 17; sd : 0
Test against a Expected # of cells based on region size 0.26263
Postsubiculum: ttest pval (scaled--expected based on size): 1; tstat : -Inf; df : 17; sd : 0

Presubiculum: Mean: 0.0087044 +/- 0.0014084 SEM

Test against a mean of 0
Presubiculum: ttest pval: 0.070691; tstat : 1.5424; df : 17; sd : 0.023943
Test against a Expected # of cells based on region size 0.22907
Presubiculum: ttest pval (scaled--expected based on size): 1; tstat : -39.0475; df : 17; sd : 0.023943

Subiculum: Mean: 0.0026964 +/- 0.00067294 SEM
Test against a mean of 0
Subiculum: ttest pval: 0.16567; tstat : 1; df : 17; sd : 0.01144
Test against a Expected # of cells based on region size 0.56318
Subiculum: ttest pval (scaled--expected based on size): 1; tstat : -207.8597; df : 17; sd : 0.01144

Prosubiculum: Mean: 0.09977 +/- 0.012787 SEM
Test against a mean of 0
Prosubiculum: ttest pval: 0.034105; tstat : 1.9473; df : 17; sd : 0.21737
Test against a Expected # of cells based on region size 0.31964
Prosubiculum: ttest pval (scaled--expected based on size): 0.99975; tstat : -4.2914; df : 17; sd : 0.21737

Hippocampo-amygdalar transition area: Mean: 0.21843 +/- 0.020456 SEM
Test against a mean of 0
Hippocampo-amygdalar transition area: ttest pval: 0.0081639; tstat : 2.6649; df : 17; sd : 0.34776
Test against a Expected # of cells based on region size 0.092798
Hippocampo-amygdalar transition area: ttest pval (scaled--expected based on size): 0.07187; tstat : 1.5327; df : 17; sd : 0.34776

Area prostriata: Mean: 0 +/- 0 SEM
Test against a mean of 0
Area prostriata: ttest pval: NaN; tstat : NaN; df : 17; sd : 0
Test against a Expected # of cells based on region size 0.071492
Area prostriata: ttest pval (scaled--expected based on size): 1; tstat : -Inf; df : 17; sd : 0

Median eminence: Mean: 0 +/- 0 SEM
Test against a mean of 0
Median eminence: ttest pval: NaN; tstat : NaN; df : 17; sd : 0
Test against a Expected # of cells based on region size 0.018196
Median eminence: ttest pval (scaled--expected based on size): 1; tstat : -Inf; df : 17; sd : 0

Anterodorsal preoptic nucleus: Mean: 0.015989 +/- 0.0016003 SEM
Test against a mean of 0
Anterodorsal preoptic nucleus: ttest pval: 0.01163; tstat : 2.4934; df : 17; sd : 0.027206

Test against a Expected # of cells based on region size 0.021989
Anterodorsal preoptic nucleus: ttest pval (scaled--expected based on size): 0.81873; tstat : -0.93569; df : 17; sd : 0.027206

Anteroventral preoptic nucleus: Mean: 0.070683 +/- 0.0059333 SEM
Test against a mean of 0
Anteroventral preoptic nucleus: ttest pval: 0.0042651; tstat : 2.9731; df : 17; sd : 0.10087
Test against a Expected # of cells based on region size 0.02003
Anteroventral preoptic nucleus: ttest pval (scaled--expected based on size): 0.024012; tstat : 2.1306; df : 17; sd : 0.10087

Anteroventral periventricular nucleus: Mean: 0.051614 +/- 0.0055466 SEM
Test against a mean of 0
Anteroventral periventricular nucleus: ttest pval: 0.016441; tstat : 2.3224; df : 17; sd : 0.094292
Test against a Expected # of cells based on region size 0.070762
Anteroventral periventricular nucleus: ttest pval (scaled--expected based on size): 0.79953; tstat : -0.86153; df : 17; sd : 0.094292

Dorsomedial nucleus of the hypothalamus: Mean: 0.4397 +/- 0.047233 SEM
Test against a mean of 0
Dorsomedial nucleus of the hypothalamus: ttest pval: 0.016412; tstat : 2.3233; df : 17; sd : 0.80295
Test against a Expected # of cells based on region size 0.081722
Dorsomedial nucleus of the hypothalamus: ttest pval (scaled--expected based on size): 0.037863; tstat : 1.8915; df : 17; sd : 0.80295

Median preoptic nucleus: Mean: 0.001908 +/- 0.00032727 SEM
Test against a mean of 0
Median preoptic nucleus: ttest pval: 0.081943; tstat : 1.455; df : 17; sd : 0.0055635
Test against a Expected # of cells based on region size 0.01748
Median preoptic nucleus: ttest pval (scaled--expected based on size): 1; tstat : -11.8748; df : 17; sd : 0.0055635

Medial preoptic area: Mean: 0.25786 +/- 0.019784 SEM
Test against a mean of 0
Medial preoptic area: ttest pval: 0.0023415; tstat : 3.2528; df : 17; sd : 0.33633
Test against a Expected # of cells based on region size 0.12125
Medial preoptic area: ttest pval (scaled--expected based on size): 0.051482; tstat : 1.7233; df : 17; sd : 0.33633

Vascular organ of the lamina terminalis: Mean: 0 +/- 0 SEM
Test against a mean of 0
Vascular organ of the lamina terminalis: ttest pval: NaN; tstat : NaN; df : 17; sd : 0
Test against a Expected # of cells based on region size 0.0030865

Vascular organ of the lamina terminalis: ttest pval (scaled--expected based on size): 1; tstat : -Inf; df : 17; sd : 0

Posterodorsal preoptic nucleus: Mean: 0.0086461 +/- 0.00093346 SEM
Test against a mean of 0
Posterodorsal preoptic nucleus: ttest pval: 0.0168; tstat : 2.3116; df : 17; sd : 0.015869
Test against a Expected # of cells based on region size 0.0025228
Posterodorsal preoptic nucleus: ttest pval (scaled--expected based on size): 0.059994; tstat : 1.6371; df : 17; sd : 0.015869

Parastrial nucleus: Mean: 0.012037 +/- 0.0015809 SEM
Test against a mean of 0
Parastrial nucleus: ttest pval: 0.037248; tstat : 1.9003; df : 17; sd : 0.026875
Test against a Expected # of cells based on region size 0.02096
Parastrial nucleus: ttest pval (scaled--expected based on size): 0.91151; tstat : -1.4086; df : 17; sd : 0.026875

Periventricular hypothalamic nucleus, posterior part: Mean: 0.069225 +/- 0.0081592 SEM
Test against a mean of 0
Periventricular hypothalamic nucleus, posterior part: ttest pval: 0.024635; tstat : 2.1174; df : 17; sd : 0.13871
Test against a Expected # of cells based on region size 0.031252
Periventricular hypothalamic nucleus, posterior part: ttest pval (scaled--expected based on size): 0.13074; tstat : 1.1615; df : 17; sd : 0.13871

Periventricular hypothalamic nucleus, preoptic part: Mean: 0.035883 +/- 0.0042756 SEM
Test against a mean of 0
Periventricular hypothalamic nucleus, preoptic part: ttest pval: 0.025751; tstat : 2.0945; df : 17; sd : 0.072685
Test against a Expected # of cells based on region size 0.045852
Periventricular hypothalamic nucleus, preoptic part: ttest pval (scaled--expected based on size): 0.71587; tstat : -0.5819; df : 17; sd : 0.072685

Subparaventricular zone: Mean: 0.0041656 +/- 0.00060095 SEM
Test against a mean of 0
Subparaventricular zone: ttest pval: 0.050878; tstat : 1.7299; df : 17; sd : 0.010216
Test against a Expected # of cells based on region size 0.023795
Subparaventricular zone: ttest pval (scaled--expected based on size): 1; tstat : -8.152; df : 17; sd : 0.010216

Suprachiasmatic nucleus: Mean: 0.0046598 +/- 0.0010502 SEM
Test against a mean of 0
Suprachiasmatic nucleus: ttest pval: 0.14178; tstat : 1.1074; df : 17; sd : 0.017853

Test against a Expected # of cells based on region size 0.02074
Suprachiasmatic nucleus: ttest pval (scaled--expected based on size): 0.99932; tstat : -3.8213; df : 17; sd : 0.017853

Subfornical organ: Mean: 0.0011857 +/- 0.00029591 SEM
Test against a mean of 0
Subfornical organ: ttest pval: 0.16567; tstat : 1; df : 17; sd : 0.0050305
Test against a Expected # of cells based on region size 0.025211
Subfornical organ: ttest pval (scaled--expected based on size): 1; tstat : -20.263; df : 17; sd : 0.0050305

Ventromedial preoptic nucleus: Mean: 0.0059082 +/- 0.0010758 SEM
Test against a mean of 0
Ventromedial preoptic nucleus: ttest pval: 0.094157; tstat : 1.3706; df : 17; sd : 0.018288
Test against a Expected # of cells based on region size 0.023541
Ventromedial preoptic nucleus: ttest pval (scaled--expected based on size): 0.99962; tstat : -4.0906; df : 17; sd : 0.018288

Ventrolateral preoptic nucleus: Mean: 0.012442 +/- 0.0026021 SEM
Test against a mean of 0
Ventrolateral preoptic nucleus: ttest pval: 0.12458; tstat : 1.1933; df : 17; sd : 0.044236
Test against a Expected # of cells based on region size 0.02605
Ventrolateral preoptic nucleus: ttest pval (scaled--expected based on size): 0.89539; tstat : -1.3052; df : 17; sd : 0.044236

Supraoptic nucleus: Mean: 0.0081396 +/- 0.0014333 SEM
Test against a mean of 0
Supraoptic nucleus: ttest pval: 0.087242; tstat : 1.4172; df : 17; sd : 0.024367
Test against a Expected # of cells based on region size 0.030766
Supraoptic nucleus: ttest pval (scaled--expected based on size): 0.99947; tstat : -3.9397; df : 17; sd : 0.024367

Accessory supraoptic group: Mean: 0.0012484 +/- 0.00031157 SEM
Test against a mean of 0
Accessory supraoptic group: ttest pval: 0.16567; tstat : 1; df : 17; sd : 0.0052967
Test against a Expected # of cells based on region size 0.0013174
Accessory supraoptic group: ttest pval (scaled--expected based on size): 0.52172; tstat : -0.055272; df : 17; sd : 0.0052967

Paraventricular hypothalamic nucleus: Mean: 0.03159 +/- 0.0059345 SEM
Test against a mean of 0
Paraventricular hypothalamic nucleus: ttest pval: 0.10079; tstat : 1.3285; df : 17; sd : 0.10089
Test against a Expected # of cells based on region size 0.044498

Paraventricular hypothalamic nucleus: ttest pval (scaled--expected based on size): 0.70285; tstat : -0.54283; df : 17; sd : 0.10089

Periventricular hypothalamic nucleus, anterior part: Mean: 0.0051395 +/- 0.00090238 SEM
Test against a mean of 0
Periventricular hypothalamic nucleus, anterior part: ttest pval: 0.086644; tstat : 1.4214; df : 17; sd : 0.015341
Test against a Expected # of cells based on region size 0.014353
Periventricular hypothalamic nucleus, anterior part: ttest pval (scaled--expected based on size): 0.9896; tstat : -2.548; df : 17; sd : 0.015341

Periventricular hypothalamic nucleus, intermediate part: Mean: 0.082574 +/- 0.0049426 SEM
Test against a mean of 0
Periventricular hypothalamic nucleus, intermediate part: ttest pval: 0.00032136; tstat : 4.1694; df : 17; sd : 0.084025
Test against a Expected # of cells based on region size 0.056755
Periventricular hypothalamic nucleus, intermediate part: ttest pval (scaled--expected based on size): 0.10487; tstat : 1.3037; df : 17; sd : 0.084025

Arcuate hypothalamic nucleus: Mean: 0.12561 +/- 0.023991 SEM
Test against a mean of 0
Arcuate hypothalamic nucleus: ttest pval: 0.10435; tstat : 1.3067; df : 17; sd : 0.40784
Test against a Expected # of cells based on region size 0.066881
Arcuate hypothalamic nucleus: ttest pval (scaled--expected based on size): 0.27464; tstat : 0.61099; df : 17; sd : 0.40784

Lateral hypothalamic area: Mean: 2.007 +/- 0.16859 SEM
Test against a mean of 0
Lateral hypothalamic area: ttest pval: 0.0042832; tstat : 2.9711; df : 17; sd : 2.866
Test against a Expected # of cells based on region size 0.47743
Lateral hypothalamic area: ttest pval (scaled--expected based on size): 0.018459; tstat : 2.2643; df : 17; sd : 2.866

Lateral preoptic area: Mean: 0.35671 +/- 0.022095 SEM
Test against a mean of 0
Lateral preoptic area: ttest pval: 0.00043528; tstat : 4.0291; df : 17; sd : 0.37562
Test against a Expected # of cells based on region size 0.12063
Lateral preoptic area: ttest pval (scaled--expected based on size): 0.0081346; tstat : 2.6666; df : 17; sd : 0.37562

Preparasubthalamic nucleus: Mean: 0.017012 +/- 0.0018394 SEM
Test against a mean of 0

Preparasubthalamic nucleus: ttest pval: 0.016913; tstat : 2.3082; df : 17; sd : 0.031269
Test against a Expected # of cells based on region size 0.0039048
Preparasubthalamic nucleus: ttest pval (scaled--expected based on size): 0.04661; tstat : 1.7784; df : 17; sd : 0.031269

Parasubthalamic nucleus: Mean: 0.29958 +/- 0.034813 SEM
Test against a mean of 0
Parasubthalamic nucleus: ttest pval: 0.023226; tstat : 2.1477; df : 17; sd : 0.59182
Test against a Expected # of cells based on region size 0.041815
Parasubthalamic nucleus: ttest pval (scaled--expected based on size): 0.041046; tstat : 1.8479; df : 17; sd : 0.59182

Perifornical nucleus: Mean: 0.065641 +/- 0.0075548 SEM
Test against a mean of 0
Perifornical nucleus: ttest pval: 0.022304; tstat : 2.1684; df : 17; sd : 0.12843
Test against a Expected # of cells based on region size 0.054823
Perifornical nucleus: ttest pval (scaled--expected based on size): 0.36262; tstat : 0.35734; df : 17; sd : 0.12843

Retrochiasmatic area: Mean: 0.093526 +/- 0.023105 SEM
Test against a mean of 0
Retrochiasmatic area: ttest pval: 0.16327; tstat : 1.0102; df : 17; sd : 0.39278
Test against a Expected # of cells based on region size 0.055445
Retrochiasmatic area: ttest pval (scaled--expected based on size): 0.34298; tstat : 0.41134; df : 17; sd : 0.39278

Subthalamic nucleus: Mean: 0.31615 +/- 0.033088 SEM
Test against a mean of 0
Subthalamic nucleus: ttest pval: 0.01451; tstat : 2.3845; df : 17; sd : 0.5625
Test against a Expected # of cells based on region size 0.088897
Subthalamic nucleus: ttest pval (scaled--expected based on size): 0.052349; tstat : 1.714; df : 17; sd : 0.5625

Tuberal nucleus: Mean: 0.88995 +/- 0.21065 SEM
Test against a mean of 0
Tuberal nucleus: ttest pval: 0.15323; tstat : 1.0544; df : 17; sd : 3.581
Test against a Expected # of cells based on region size 0.14193
Tuberal nucleus: ttest pval (scaled--expected based on size): 0.19393; tstat : 0.88623; df : 17; sd : 3.581

Zona incerta: Mean: 0.43925 +/- 0.044104 SEM
Test against a mean of 0
Zona incerta: ttest pval: 0.011818; tstat : 2.4856; df : 17; sd : 0.74977
Test against a Expected # of cells based on region size 0.41362

Zona incerta: ttest pval (scaled--expected based on size): 0.44319; tstat : 0.14505; df : 17; sd : 0.74977

Anterior hypothalamic nucleus: Mean: 0.16055 +/- 0.010375 SEM
Test against a mean of 0
Anterior hypothalamic nucleus: ttest pval: 0.00062553; tstat : 3.8619; df : 17; sd : 0.17638
Test against a Expected # of cells based on region size 0.15438
Anterior hypothalamic nucleus: ttest pval (scaled--expected based on size): 0.44188; tstat : 0.14841; df : 17; sd : 0.17638

Lateral mammillary nucleus: Mean: 0.011553 +/- 0.0016939 SEM
Test against a mean of 0
Lateral mammillary nucleus: ttest pval: 0.053473; tstat : 1.7021; df : 17; sd : 0.028796
Test against a Expected # of cells based on region size 0.020234
Lateral mammillary nucleus: ttest pval (scaled--expected based on size): 0.89096; tstat : -1.279; df : 17; sd : 0.028796

Medial mammillary nucleus: Mean: 0.39412 +/- 0.050426 SEM
Test against a mean of 0
Medial mammillary nucleus: ttest pval: 0.033895; tstat : 1.9506; df : 17; sd : 0.85724
Test against a Expected # of cells based on region size 0.13169
Medial mammillary nucleus: ttest pval (scaled--expected based on size): 0.10567; tstat : 1.2988; df : 17; sd : 0.85724

Supramammillary nucleus: Mean: 0.074357 +/- 0.010899 SEM
Test against a mean of 0
Supramammillary nucleus: ttest pval: 0.053429; tstat : 1.7026; df : 17; sd : 0.18529
Test against a Expected # of cells based on region size 0.066235
Supramammillary nucleus: ttest pval (scaled--expected based on size): 0.42733; tstat : 0.18597; df : 17; sd : 0.18529

Tuberomammillary nucleus: Mean: 0.081479 +/- 0.010209 SEM
Test against a mean of 0
Tuberomammillary nucleus: ttest pval: 0.031348; tstat : 1.9919; df : 17; sd : 0.17355
Test against a Expected # of cells based on region size 0.040192
Tuberomammillary nucleus: ttest pval (scaled--expected based on size): 0.16348; tstat : 1.0093; df : 17; sd : 0.17355

Medial preoptic nucleus: Mean: 0.27183 +/- 0.032809 SEM
Test against a mean of 0
Medial preoptic nucleus: ttest pval: 0.027118; tstat : 2.0677; df : 17; sd : 0.55775

Test against a Expected # of cells based on region size 0.087929
Medial preoptic nucleus: ttest pval (scaled--expected based on size): 0.089916; tstat : 1.3989; df : 17; sd : 0.55775

Dorsal premammillary nucleus: Mean: 0.23528 +/- 0.032657 SEM
Test against a mean of 0
Dorsal premammillary nucleus: ttest pval: 0.044981; tstat : 1.798; df : 17; sd : 0.55517
Test against a Expected # of cells based on region size 0.028634
Dorsal premammillary nucleus: ttest pval (scaled--expected based on size): 0.066362; tstat : 1.5792; df : 17; sd : 0.55517

Ventral premammillary nucleus: Mean: 0.49484 +/- 0.11132 SEM
Test against a mean of 0
Ventral premammillary nucleus: ttest pval: 0.14135; tstat : 1.1094; df : 17; sd : 1.8924
Test against a Expected # of cells based on region size 0.043666
Ventral premammillary nucleus: ttest pval (scaled--expected based on size): 0.16298; tstat : 1.0115; df : 17; sd : 1.8924

Paraventricular hypothalamic nucleus, descending division: Mean: 0.013922 +/- 0.0012852 SEM
Test against a mean of 0
Paraventricular hypothalamic nucleus, descending division: ttest pval: 0.0075325; tstat : 2.7035; df : 17; sd : 0.021848
Test against a Expected # of cells based on region size 0.028634
Paraventricular hypothalamic nucleus, descending division: ttest pval (scaled--expected based on size): 0.99454; tstat : -2.8569; df : 17; sd : 0.021848

Ventromedial hypothalamic nucleus: Mean: 1.2151 +/- 0.16121 SEM
Test against a mean of 0
Ventromedial hypothalamic nucleus: ttest pval: 0.038606; tstat : 1.881; df : 17; sd : 2.7406
Test against a Expected # of cells based on region size 0.11942
Ventromedial hypothalamic nucleus: ttest pval (scaled--expected based on size): 0.054046; tstat : 1.6962; df : 17; sd : 2.7406

Posterior hypothalamic nucleus: Mean: 0.13119 +/- 0.011118 SEM
Test against a mean of 0
Posterior hypothalamic nucleus: ttest pval: 0.0045287; tstat : 2.9449; df : 17; sd : 0.189
Test against a Expected # of cells based on region size 0.15853
Posterior hypothalamic nucleus: ttest pval (scaled--expected based on size): 0.72627; tstat : -0.61383; df : 17; sd : 0.189

Substantia nigra, reticular part: Mean: 0.037884 +/- 0.0052302 SEM

Test against a mean of 0
Substantia nigra, reticular part: ttest pval: 0.044192; tstat : 1.8077; df : 17; sd : 0.088913
Test against a Expected # of cells based on region size 0.43287
Substantia nigra, reticular part: ttest pval (scaled--expected based on size): 1; tstat : -18.8472; df : 17; sd : 0.088913

Ventral tegmental area: Mean: 0.045944 +/- 0.0064395 SEM
Test against a mean of 0
Ventral tegmental area: ttest pval: 0.046427; tstat : 1.7806; df : 17; sd : 0.10947
Test against a Expected # of cells based on region size 0.11082
Ventral tegmental area: ttest pval (scaled--expected based on size): 0.98886; tstat : -2.5143; df : 17; sd : 0.10947

Paranigral nucleus: Mean: 0 +/- 0 SEM
Test against a mean of 0
Paranigral nucleus: ttest pval: NaN; tstat : NaN; df : 17; sd : 0
Test against a Expected # of cells based on region size 0.004774
Paranigral nucleus: ttest pval (scaled--expected based on size): 1; tstat : -Inf; df : 17; sd : 0

Midbrain reticular nucleus, retrorubral area: Mean: 0.0012484 +/- 0.00031157 SEM
Test against a mean of 0
Midbrain reticular nucleus, retrorubral area: ttest pval: 0.16567; tstat : 1; df : 17; sd : 0.0052967
Test against a Expected # of cells based on region size 0.030233
Midbrain reticular nucleus, retrorubral area: ttest pval (scaled--expected based on size): 1; tstat : -23.2169; df : 17; sd : 0.0052967

Midbrain reticular nucleus: Mean: 0.10224 +/- 0.018492 SEM
Test against a mean of 0
Midbrain reticular nucleus: ttest pval: 0.092747; tstat : 1.3799; df : 17; sd : 0.31436
Test against a Expected # of cells based on region size 1.1584
Midbrain reticular nucleus: ttest pval (scaled--expected based on size): 1; tstat : -14.2545; df : 17; sd : 0.31436

Superior colliculus, motor related: Mean: 0.13275 +/- 0.022439 SEM
Test against a mean of 0
Superior colliculus, motor related: ttest pval: 0.079047; tstat : 1.4765; df : 17; sd : 0.38146
Test against a Expected # of cells based on region size 1.2407
Superior colliculus, motor related: ttest pval (scaled--expected based on size): 1; tstat : -12.3225; df : 17; sd : 0.38146

Periaqueductal gray: Mean: 0.0050446 +/- 0.00090285 SEM

Test against a mean of 0
Periaqueductal gray: ttest pval: 0.090573; tstat : 1.3944; df : 17; sd : 0.015348
Test against a Expected # of cells based on region size 1.0825
Periaqueductal gray: ttest pval (scaled--expected based on size): 1; tstat : -297.8342; df : 17; sd : 0.015348

Pretectal region: Mean: 0.00044941 +/- 0.00011216 SEM
Test against a mean of 0
Pretectal region: ttest pval: 0.16567; tstat : 1; df : 17; sd : 0.0019067
Test against a Expected # of cells based on region size 0.47598
Pretectal region: ttest pval (scaled--expected based on size): 1; tstat : -1058.1259; df : 17; sd : 0.0019067

Cuneiform nucleus: Mean: 0.003247 +/- 0.00081034 SEM
Test against a mean of 0
Cuneiform nucleus: ttest pval: 0.16567; tstat : 1; df : 17; sd : 0.013776
Test against a Expected # of cells based on region size 0.1289
Cuneiform nucleus: ttest pval (scaled--expected based on size): 1; tstat : -38.6973; df : 17; sd : 0.013776

Red nucleus: Mean: 0.0024969 +/- 0.00062314 SEM
Test against a mean of 0
Red nucleus: ttest pval: 0.16567; tstat : 1; df : 17; sd : 0.010593
Test against a Expected # of cells based on region size 0.17216
Red nucleus: ttest pval (scaled--expected based on size): 1; tstat : -67.9517; df : 17; sd : 0.010593

Oculomotor nucleus: Mean: 0 +/- 0 SEM
Test against a mean of 0
Oculomotor nucleus: ttest pval: NaN; tstat : NaN; df : 17; sd : 0
Test against a Expected # of cells based on region size 0.0070762
Oculomotor nucleus: ttest pval (scaled--expected based on size): 1; tstat : -Inf; df : 17; sd : 0

Medial accesory oculomotor nucleus: Mean: 0 +/- 0 SEM
Test against a mean of 0
Medial accesory oculomotor nucleus: ttest pval: NaN; tstat : NaN; df : 17; sd : 0
Test against a Expected # of cells based on region size 0.0035313
Medial accesory oculomotor nucleus: ttest pval (scaled--expected based on size): 1; tstat : -Inf; df : 17; sd : 0

Edinger-Westphal nucleus: Mean: 0 +/- 0 SEM
Test against a mean of 0
Edinger-Westphal nucleus: ttest pval: NaN; tstat : NaN; df : 17; sd : 0
Test against a Expected # of cells based on region size 0.0056501

Edinger-Westphal nucleus: ttest pval (scaled--expected based on size): 1; tstat : -Inf; df : 17; sd : 0

Trochlear nucleus: Mean: 0 +/- 0 SEM
Test against a mean of 0
Trochlear nucleus: ttest pval: NaN; tstat : NaN; df : 17; sd : 0
Test against a Expected # of cells based on region size 0.0015415
Trochlear nucleus: ttest pval (scaled--expected based on size): 1; tstat : -Inf; df : 17; sd : 0

Paratrochlear nucleus: Mean: 0.00044941 +/- 0.00011216 SEM
Test against a mean of 0
Paratrochlear nucleus: ttest pval: 0.16567; tstat : 1; df : 17; sd : 0.0019067
Test against a Expected # of cells based on region size 0.0034804
Paratrochlear nucleus: ttest pval (scaled--expected based on size): 1; tstat : -6.7444; df : 17; sd : 0.0019067

Ventral tegmental nucleus: Mean: 0 +/- 0 SEM
Test against a mean of 0
Ventral tegmental nucleus: ttest pval: NaN; tstat : NaN; df : 17; sd : 0
Test against a Expected # of cells based on region size 0.0082103
Ventral tegmental nucleus: ttest pval (scaled--expected based on size): 1; tstat : -Inf; df : 17; sd : 0

Anterior tegmental nucleus: Mean: 0 +/- 0 SEM
Test against a mean of 0
Anterior tegmental nucleus: ttest pval: NaN; tstat : NaN; df : 17; sd : 0
Test against a Expected # of cells based on region size 0.0093647
Anterior tegmental nucleus: ttest pval (scaled--expected based on size): 1; tstat : -Inf; df : 17; sd : 0

Lateral terminal nucleus of the accessory optic tract: Mean: 0.0042103 +/- 0.0010508 SEM
Test against a mean of 0
Lateral terminal nucleus of the accessory optic tract: ttest pval: 0.16567; tstat : 1; df : 17; sd : 0.017863
Test against a Expected # of cells based on region size 0.004044
Lateral terminal nucleus of the accessory optic tract: ttest pval (scaled--expected based on size): 0.48447; tstat : 0.039508; df : 17; sd : 0.017863

Dorsal terminal nucleus of the accessory optic tract: Mean: 0 +/- 0 SEM
Test against a mean of 0
Dorsal terminal nucleus of the accessory optic tract: ttest pval: NaN; tstat : NaN; df : 17; sd : 0
Test against a Expected # of cells based on region size 0.0029235

Dorsal terminal nucleus of the accessory optic tract: ttest pval (scaled--expected based on size): 1; tstat : -Inf; df : 17; sd : 0

Medial terminal nucleus of the accessory optic tract: Mean: 0 +/- 0 SEM
Test against a mean of 0
Medial terminal nucleus of the accessory optic tract: ttest pval: NaN; tstat : NaN; df : 17; sd : 0
Test against a Expected # of cells based on region size 0.0094734
Medial terminal nucleus of the accessory optic tract: ttest pval (scaled--expected based on size): 1; tstat : -Inf; df : 17; sd : 0

Superior colliculus, sensory related: Mean: 0 +/- 0 SEM
Test against a mean of 0
Superior colliculus, sensory related: ttest pval: NaN; tstat : NaN; df : 17; sd : 0
Test against a Expected # of cells based on region size 0.47634
Superior colliculus, sensory related: ttest pval (scaled--expected based on size): 1; tstat : -Inf; df : 17; sd : 0

Inferior colliculus: Mean: 0.020925 +/- 0.0052222 SEM
Test against a mean of 0
Inferior colliculus: ttest pval: 0.16567; tstat : 1; df : 17; sd : 0.088777
Test against a Expected # of cells based on region size 0.96665
Inferior colliculus: ttest pval (scaled--expected based on size): 1; tstat : -45.1962; df : 17; sd : 0.088777

Nucleus of the brachium of the inferior colliculus: Mean: 0.010462 +/- 0.0026111 SEM
Test against a mean of 0
Nucleus of the brachium of the inferior colliculus: ttest pval: 0.16567; tstat : 1; df : 17; sd : 0.044388
Test against a Expected # of cells based on region size 0.029602
Nucleus of the brachium of the inferior colliculus: ttest pval (scaled--expected based on size): 0.95753; tstat : -1.8293; df : 17; sd : 0.044388

Nucleus sagulum: Mean: 0 +/- 0 SEM
Test against a mean of 0
Nucleus sagulum: ttest pval: NaN; tstat : NaN; df : 17; sd : 0
Test against a Expected # of cells based on region size 0.021344
Nucleus sagulum: ttest pval (scaled--expected based on size): 1; tstat : -Inf; df : 17; sd : 0

Parabigeminal nucleus: Mean: 0 +/- 0 SEM
Test against a mean of 0
Parabigeminal nucleus: ttest pval: NaN; tstat : NaN; df : 17; sd : 0
Test against a Expected # of cells based on region size 0.0096839

Parabigeminal nucleus: ttest pval (scaled--expected based on size): 1; tstat : -Inf; df : 17; sd : 0

Midbrain trigeminal nucleus: Mean: 0 +/- 0 SEM
Test against a mean of 0
Midbrain trigeminal nucleus: ttest pval: NaN; tstat : NaN; df : 17; sd : 0
Test against a Expected # of cells based on region size 0.0022003
Midbrain trigeminal nucleus: ttest pval (scaled--expected based on size): 1; tstat : -Inf; df : 17; sd : 0

Subcommissural organ: Mean: 0 +/- 0 SEM
Test against a mean of 0
Subcommissural organ: ttest pval: NaN; tstat : NaN; df : 17; sd : 0a
Test against a Expected # of cells based on region size 0.0092832
Subcommissural organ: ttest pval (scaled--expected based on size): 1; tstat : -Inf; df : 17; sd : 0

Substantia nigra, compact part: Mean: 0.00044941 +/- 0.00011216 SEM
Test against a mean of 0
Substantia nigra, compact part: ttest pval: 0.16567; tstat : 1; df : 17; sd : 0.0019067
Test against a Expected # of cells based on region size 0.043051
Substantia nigra, compact part: ttest pval (scaled--expected based on size): 1; tstat : -94.7958; df : 17; sd : 0.0019067

Pedunculopontine nucleus: Mean: 0.0012484 +/- 0.00031157 SEM
Test against a mean of 0
Pedunculopontine nucleus: ttest pval: 0.16567; tstat : 1; df : 17; sd : 0.0052967
Test against a Expected # of cells based on region size 0.2086
Pedunculopontine nucleus: ttest pval (scaled--expected based on size): 1; tstat : -166.0893; df : 17; sd : 0.0052967

Interfascicular nucleus raphe: Mean: 0 +/- 0 SEM
Test against a mean of 0
Interfascicular nucleus raphe: ttest pval: NaN; tstat : NaN; df : 17; sd : 0
Test against a Expected # of cells based on region size 0.020156
Interfascicular nucleus raphe: ttest pval (scaled--expected based on size): 1; tstat : -Inf; df : 17; sd : 0

Interpeduncular nucleus: Mean: 0.00089881 +/- 0.00022431 SEM
Test against a mean of 0
Interpeduncular nucleus: ttest pval: 0.16567; tstat : 1; df : 17; sd : 0.0038133
Test against a Expected # of cells based on region size 0.079699
Interpeduncular nucleus: ttest pval (scaled--expected based on size): 1; tstat : -87.671; df : 17; sd : 0.0038133

Rostral linear nucleus raphe: Mean: 0 +/- 0 SEM

Test against a mean of 0
Rostral linear nucleus raphe: ttest pval: NaN; tstat : NaN; df : 17; sd : 0
Test against a Expected # of cells based on region size 0.016071
Rostral linear nucleus raphe: ttest pval (scaled--expected based on size): 1; tstat : -Inf; df : 17; sd : 0

Central linear nucleus raphe: Mean: 0 +/- 0 SEM
Test against a mean of 0
Central linear nucleus raphe: ttest pval: NaN; tstat : NaN; df : 17; sd : 0
Test against a Expected # of cells based on region size 0.020332
Central linear nucleus raphe: ttest pval (scaled--expected based on size): 1; tstat : -Inf; df : 17; sd : 0

Dorsal nucleus raphe: Mean: 0.0036964 +/- 0.0008115 SEM
Test against a mean of 0
Dorsal nucleus raphe: ttest pval: 0.1357; tstat : 1.1368; df : 17; sd : 0.013795
Test against a Expected # of cells based on region size 0.033422
Dorsal nucleus raphe: ttest pval (scaled--expected based on size): 1; tstat : -9.1417; df : 17; sd : 0.013795

Primary motor area: Mean: 0.006686 +/- 0.0012921 SEM
Test against a mean of 0
Primary motor area: ttest pval: 0.10693; tstat : 1.2913; df : 17; sd : 0.021966
Test against a Expected # of cells based on region size 2.6186
Primary motor area: ttest pval (scaled--expected based on size): 1; tstat : -504.4714; df : 17; sd : 0.021966

Secondary motor area: Mean: 0.074756 +/- 0.016114 SEM
Test against a mean of 0
Secondary motor area: ttest pval: 0.13147; tstat : 1.1578; df : 17; sd : 0.27393
Test against a Expected # of cells based on region size 2.9481
Secondary motor area: ttest pval (scaled--expected based on size): 1; tstat : -44.5026; df : 17; sd : 0.27393
---
primary somatosensory area: Mean: 0.0027917 +/- 0.0004482 SEM
Test against a mean of 0
primary somatosensory area: ttest pval: 0.069247; tstat : 1.5545; df : 17; sd : 0.0076194
Test against a Expected # of cells based on region size 5.5681
primary somatosensory area: ttest pval (scaled--expected based on size): 1; tstat : -3098.8479; df : 17; sd : 0.0076194

Supplemental somatosensory area: Mean: 0.0063329 +/- 0.0011044 SEM
Test against a mean of 0
Supplemental somatosensory area: ttest pval: 0.085266; tstat : 1.4311; df : 17; sd : 0.018775

Test against a Expected # of cells based on region size 2.0429
Supplemental somatosensory area: ttest pval (scaled--expected based on size): 1; tstat : -460.2201; df : 17; sd : 0.018775

Gustatory areas: Mean: 0.0050837 +/- 0.00097392 SEM
Test against a mean of 0
Gustatory areas: ttest pval: 0.10502; tstat : 1.3027; df : 17; sd : 0.016557
Test against a Expected # of cells based on region size 0.38663
Gustatory areas: ttest pval (scaled--expected based on size): 1; tstat : -97.7722; df : 17; sd : 0.016557

Visceral area: Mean: 0.013856 +/- 0.0013483 SEM
Test against a mean of 0
Visceral area: ttest pval: 0.010045; tstat : 2.5647; df : 17; sd : 0.022921
Test against a Expected # of cells based on region size 0.52504
Visceral area: ttest pval (scaled--expected based on size): 1; tstat : -94.6193; df : 17; sd : 0.022921

Auditory areas: Mean: 0.0047348 +/- 0.00071797 SEM
Test against a mean of 0
Auditory areas: ttest pval: 0.05908; tstat : 1.6458; df : 17; sd : 0.012206
Test against a Expected # of cells based on region size 1.3473
Auditory areas: ttest pval (scaled--expected based on size): 1; tstat : -466.6904; df : 17; sd : 0.012206

Visual areas: Mean: 0.008255 +/- 0.0014136 SEM
Test against a mean of 0
Visual areas: ttest pval: 0.081613; tstat : 1.4574; df : 17; sd : 0.024031
Test against a Expected # of cells based on region size 3.1429
Visual areas: ttest pval (scaled--expected based on size): 1; tstat : -553.4224; df : 17; sd : 0.024031

Anterior cingulate area: Mean: 0.010989 +/- 0.0024326 SEM
Test against a mean of 0
Anterior cingulate area: ttest pval: 0.13762; tstat : 1.1274; df : 17; sd : 0.041355
Test against a Expected # of cells based on region size 1.3819
Anterior cingulate area: ttest pval (scaled--expected based on size): 1; tstat : -140.646; df : 17; sd : 0.041355

Prelimbic area: Mean: 0.0012484 +/- 0.00031157 SEM
Test against a mean of 0
Prelimbic area: ttest pval: 0.16567; tstat : 1; df : 17; sd : 0.0052967
Test against a Expected # of cells based on region size 0.54511
Prelimbic area: ttest pval (scaled--expected based on size): 1; tstat : -435.6325; df : 17; sd : 0.0052967

Infralimbic area: Mean: 0.014772 +/- 0.0015668 SEM
Test against a mean of 0
Infralimbic area: ttest pval: 0.01546; tstat : 2.3531; df : 17; sd : 0.026635
Test against a Expected # of cells based on region size 0.20061
Infralimbic area: ttest pval (scaled--expected based on size): 1; tstat : -29.6022; df : 17; sd : 0.026635

Orbital area: Mean: 0.030667 +/- 0.0049647 SEM
Test against a mean of 0
Orbital area: ttest pval: 0.070793; tstat : 1.5416; df : 17; sd : 0.0844
Test against a Expected # of cells based on region size 1.3105
Orbital area: ttest pval (scaled--expected based on size): 1; tstat : -64.3337; df : 17; sd : 0.0844

Agranular insular area: Mean: 0.074015 +/- 0.0062399 SEM
Test against a mean of 0
Agranular insular area: ttest pval: 0.0043832; tstat : 2.9602; df : 17; sd : 0.10608
Test against a Expected # of cells based on region size 1.7341
Agranular insular area: ttest pval (scaled--expected based on size): 1; tstat : -66.3957; df : 17; sd : 0.10608

Retrosplenial area: Mean: 0 +/- 0 SEM
Test against a mean of 0
Retrosplenial area: ttest pval: NaN; tstat : NaN; df : 17; sd : 0
Test against a Expected # of cells based on region size 2.5553
Retrosplenial area: ttest pval (scaled--expected based on size): 1; tstat : -Inf; df : 17; sd : 0

Posterior parietal association areas: Mean: 0 +/- 0 SEM
Test against a mean of 0
Posterior parietal association areas: ttest pval: NaN; tstat : NaN; df : 17; sd : 0
Test against a Expected # of cells based on region size 0.57144
Posterior parietal association areas: ttest pval (scaled--expected based on size): 1; tstat : -Inf; df : 17; sd : 0

Temporal association areas: Mean: 0.033418 +/- 0.0048174 SEM
Test against a mean of 0
Temporal association areas: ttest pval: 0.05076; tstat : 1.7312; df : 17; sd : 0.081896
Test against a Expected # of cells based on region size 0.71655
Temporal association areas: ttest pval (scaled--expected based on size): 1; tstat : -35.3897; df : 17; sd : 0.081896

Perirhinal area: Mean: 0.00044941 +/- 0.00011216 SEM
Test against a mean of 0
Perirhinal area: ttest pval: 0.16567; tstat : 1; df : 17; sd : 0.0019067

Test against a Expected # of cells based on region size 0.17514
Perirhinal area: ttest pval (scaled--expected based on size): 1; tstat : -388.7036; df : 17; sd : 0.0019067

Ectorhinal area: Mean: 0.02416 +/- 0.0046767 SEM
Test against a mean of 0
Ectorhinal area: ttest pval: 0.10728; tstat : 1.2893; df : 17; sd : 0.079503
Test against a Expected # of cells based on region size 0.39531
Ectorhinal area: ttest pval (scaled--expected based on size): 1; tstat : -19.8065; df : 17; sd : 0.079503
---
cerebellar cortex: Mean: 0.0087391 +/- 0.002181 SEM
Test against a mean of 0
cerebellar cortex: ttest pval: 0.16567; tstat : 1; df : 17; sd : 0.037077
Test against a Expected # of cells based on region size 12.5699
cerebellar cortex: ttest pval (scaled--expected based on size): 1; tstat : -1437.3559; df : 17; sd : 0.037077

Fastigial nucleus: Mean: 0 +/- 0 SEM
Test against a mean of 0
Fastigial nucleus: ttest pval: NaN; tstat : NaN; df : 17; sd : 0
Test against a Expected # of cells based on region size 0.19496
Fastigial nucleus: ttest pval (scaled--expected based on size): 1; tstat : -Inf; df : 17; sd : 0

Interposed nucleus: Mean: 0 +/- 0 SEM
Test against a mean of 0
Interposed nucleus: ttest pval: NaN; tstat : NaN; df : 17; sd : 0
Test against a Expected # of cells based on region size 0.30222
Interposed nucleus: ttest pval (scaled--expected based on size): 1; tstat : -Inf; df : 17; sd : 0

Dentate nucleus: Mean: 0 +/- 0 SEM
Test against a mean of 0
Dentate nucleus: ttest pval: NaN; tstat : NaN; df : 17; sd : 0
Test against a Expected # of cells based on region size 0.13733
Dentate nucleus: ttest pval (scaled--expected based on size): 1; tstat : -Inf; df : 17; sd : 0

Vestibulocerebellar nucleus: Mean: 0 +/- 0 SEM
Test against a mean of 0
Vestibulocerebellar nucleus: ttest pval: NaN; tstat : NaN; df : 17; sd : 0
Test against a Expected # of cells based on region size 0.018814
Vestibulocerebellar nucleus: ttest pval (scaled--expected based on size): 1; tstat : -Inf; df : 17; sd : 0

Ventral group of the dorsal thalamus: Mean: 0.33454 +/- 0.039723 SEM
Test against a mean of 0
Ventral group of the dorsal thalamus: ttest pval: 0.025392; tstat : 2.1018; df : 17; sd : 0.6753
Test against a Expected # of cells based on region size 1.0937
Ventral group of the dorsal thalamus: ttest pval (scaled--expected based on size): 0.99991; tstat : -4.7692; df : 17; sd : 0.6753

Subparafascicular nucleus: Mean: 0 +/- 0 SEM
Test against a mean of 0
Subparafascicular nucleus: ttest pval: NaN; tstat : NaN; df : 17; sd : 0
Test against a Expected # of cells based on region size 0.044905
Subparafascicular nucleus: ttest pval (scaled--expected based on size): 1; tstat : -Inf; df : 17; sd : 0

Subparafascicular area: Mean: 0 +/- 0 SEM
Test against a mean of 0
Subparafascicular area: ttest pval: NaN; tstat : NaN; df : 17; sd : 0
Test against a Expected # of cells based on region size 0.028753
Subparafascicular area: ttest pval (scaled--expected based on size): 1; tstat : -Inf; df : 17; sd : 0

Peripeduncular nucleus: Mean: 0.058784 +/- 0.010232 SEM
Test against a mean of 0
Peripeduncular nucleus: ttest pval: 0.084889; tstat : 1.4338; df : 17; sd : 0.17395
Test against a Expected # of cells based on region size 0.01455
Peripeduncular nucleus: ttest pval (scaled--expected based on size): 0.14785; tstat : 1.0789; df : 17; sd : 0.17395

Geniculate group, dorsal thalamus: Mean: 0.16823 +/- 0.033751 SEM
Test against a mean of 0
Geniculate group, dorsal thalamus: ttest pval: 0.1152; tstat : 1.244; df : 17; sd : 0.57377
Test against a Expected # of cells based on region size 0.35506
Geniculate group, dorsal thalamus: ttest pval (scaled--expected based on size): 0.90749; tstat : -1.3815; df : 17; sd : 0.57377

Lateral group of the dorsal thalamus: Mean: 0.041493 +/- 0.0052111 SEM
Test against a mean of 0
Lateral group of the dorsal thalamus: ttest pval: 0.031631; tstat : 1.9872; df : 17; sd : 0.088588
Test against a Expected # of cells based on region size 0.68209
Lateral group of the dorsal thalamus: ttest pval (scaled--expected based on size): 1; tstat : -30.6791; df : 17; sd : 0.088588

Anterior group of the dorsal thalamus: Mean: 0 +/- 0 SEM

Test against a mean of 0
Anterior group of the dorsal thalamus: ttest pval: NaN; tstat : NaN; df : 17; sd : 0
Test against a Expected # of cells based on region size 0.57039
Anterior group of the dorsal thalamus: ttest pval (scaled--expected based on size): 1; tstat : -Inf; df : 17; sd : 0

Medial group of the dorsal thalamus: Mean: 0.00711 +/- 0.00096338 SEM
Test against a mean of 0
Medial group of the dorsal thalamus: ttest pval: 0.041505; tstat : 1.8419; df : 17; sd : 0.016378
Test against a Expected # of cells based on region size 0.45517
Medial group of the dorsal thalamus: ttest pval (scaled--expected based on size): 1; tstat : -116.072; df : 17; sd : 0.016378

Midline group of the dorsal thalamus: Mean: 0.11222 +/- 0.010624 SEM
Test against a mean of 0
Midline group of the dorsal thalamus: ttest pval: 0.0086697; tstat : 2.6359; df : 17; sd : 0.18062
Test against a Expected # of cells based on region size 0.28566
Midline group of the dorsal thalamus: ttest pval (scaled--expected based on size): 0.99961; tstat : -4.0743; df : 17; sd : 0.18062

Intralaminar nuclei of the dorsal thalamus: Mean: 0.074545 +/- 0.012797 SEM
Test against a mean of 0
Intralaminar nuclei of the dorsal thalamus: ttest pval: 0.082118; tstat : 1.4537; df : 17; sd : 0.21756
Test against a Expected # of cells based on region size 0.36311
Intralaminar nuclei of the dorsal thalamus: ttest pval (scaled--expected based on size): 0.99998; tstat : -5.6275; df : 17; sd : 0.21756

Reticular nucleus of the thalamus: Mean: 0.87295 +/- 0.14077 SEM
Test against a mean of 0
Reticular nucleus of the thalamus: ttest pval: 0.070059; tstat : 1.5477; df : 17; sd : 2.3931
Test against a Expected # of cells based on region size 0.49022
Reticular nucleus of the thalamus: ttest pval (scaled--expected based on size): 0.25328; tstat : 0.67855; df : 17; sd : 2.3931

Geniculate group, ventral thalamus: Mean: 0.076796 +/- 0.0089385 SEM
Test against a mean of 0
Geniculate group, ventral thalamus: ttest pval: 0.023384; tstat : 2.1442; df : 17; sd : 0.15195
Test against a Expected # of cells based on region size 0.17279
Geniculate group, ventral thalamus: ttest pval (scaled--expected based on size): 0.99209; tstat : -2.6803; df : 17; sd : 0.15195

Epithalamus: Mean: 0.00089881 +/- 0.00022431 SEM
Test against a mean of 0
Epithalamus: ttest pval: 0.16567; tstat : 1; df : 17; sd : 0.0038133
Test against a Expected # of cells based on region size 0.22435
Epithalamus: ttest pval (scaled--expected based on size): 1; tstat : -248.6063; df : 17; sd : 0.0038133

Caudoputanum: Mean: 6.5636 +/- 0.63899 SEM
Test against a mean of 0
Caudoputanum: ttest pval: 0.010071; tstat : 2.5635; df : 17; sd : 10.8628
Test against a Expected # of cells based on region size 6.55
Caudoputanum: ttest pval (scaled--expected based on size): 0.49791; tstat : 0.0053252; df : 17; sd : 10.8628

Nucleus accumbens: Mean: 0.14857 +/- 0.014201 SEM
Test against a mean of 0
Nucleus accumbens: ttest pval: 0.0091294; tstat : 2.611; df : 17; sd : 0.24141
Test against a Expected # of cells based on region size 0.99813
Nucleus accumbens: ttest pval (scaled--expected based on size): 1; tstat : -14.9302; df : 17; sd : 0.24141

Fundus of striatum: Mean: 0.11367 +/- 0.011312 SEM
Test against a mean of 0
Fundus of striatum: ttest pval: 0.011294; tstat : 2.5077; df : 17; sd : 0.19231
Test against a Expected # of cells based on region size 0.093834
Fundus of striatum: ttest pval (scaled--expected based on size): 0.33359; tstat : 0.43761; df : 17; sd : 0.19231

Olfactory Tubercle: Mean: 0.22479 +/- 0.044624 SEM
Test against a mean of 0
Olfactory Tubercle: ttest pval: 0.11284; tstat : 1.2572; df : 17; sd : 0.75861
Test against a Expected # of cells based on region size 0.84157
Olfactory Tubercle: ttest pval (scaled--expected based on size): 0.99847; tstat : -3.4494; df : 17; sd : 0.75861

Lateral septal nucleus: Mean: 0.14769 +/- 0.012135 SEM
Test against a mean of 0
Lateral septal nucleus: ttest pval: 0.0037178; tstat : 3.0375; df : 17; sd : 0.20629
Test against a Expected # of cells based on region size 0.79092
Lateral septal nucleus: ttest pval (scaled--expected based on size): 1; tstat : -13.2287; df : 17; sd : 0.20629

Septofimbrial nucleus: Mean: 0.046789 +/- 0.0060092 SEM
Test against a mean of 0
Septofimbrial nucleus: ttest pval: 0.034372; tstat : 1.9432; df : 17; sd : 0.10216
Test against a Expected # of cells based on region size 0.17297

Septofimbrial nucleus: ttest pval (scaled--expected based on size): 0.99997; tstat : -5.2403; df : 17; sd : 0.10216

Septohippocampal nucleus: Mean: 0 +/- 0 SEM
Test against a mean of 0
Septohippocampal nucleus: ttest pval: NaN; tstat : NaN; df : 17; sd : 0
Test against a Expected # of cells based on region size 0.0097178
Septohippocampal nucleus: ttest pval (scaled--expected based on size): 1; tstat : -Inf; df : 17; sd : 0

Anterior amygdalar area: Mean: 0.25848 +/- 0.021208 SEM
Test against a mean of 0
Anterior amygdalar area: ttest pval: 0.003685; tstat : 3.0416; df : 17; sd : 0.36054
Test against a Expected # of cells based on region size 0.10747
Anterior amygdalar area: ttest pval (scaled--expected based on size): 0.046736; tstat : 1.7769; df : 17; sd : 0.36054

Bed nucleus of the accessory olfactory tract: Mean: 0.0012484 +/- 0.00031157 SEM
Test against a mean of 0
Bed nucleus of the accessory olfactory tract: ttest pval: 0.16567; tstat : 1; df : 17; sd : 0.0052967
Test against a Expected # of cells based on region size 0.0054463
Bed nucleus of the accessory olfactory tract: ttest pval (scaled--expected based on size): 0.99815; tstat : -3.3625; df : 17; sd : 0.0052967

Central amygdalar nucleus: Mean: 11.3864 +/- 0.59917 SEM
Test against a mean of 0
Central amygdalar nucleus: ttest pval: 9.4177e-05; tstat : 4.7427; df : 17; sd : 10.1858
Test against a Expected # of cells based on region size 0.2958
Central amygdalar nucleus: ttest pval (scaled--expected based on size): 0.00012234; tstat : 4.6195; df : 17; sd : 10.1858

Intercalated amygdalar nucleus: Mean: 0.43087 +/- 0.039931 SEM
Test against a mean of 0
Intercalated amygdalar nucleus: ttest pval: 0.0077006; tstat : 2.6929; df : 17; sd : 0.67883
Test against a Expected # of cells based on region size 0.039897
Intercalated amygdalar nucleus: ttest pval (scaled--expected based on size): 0.012874; tstat : 2.4436; df : 17; sd : 0.67883

Medial amygdalar nucleus: Mean: 20.0323 +/- 1.3142 SEM
Test against a mean of 0
Medial amygdalar nucleus: ttest pval: 0.00070912; tstat : 3.8041; df : 17; sd : 22.3418
Test against a Expected # of cells based on region size 0.5476

Medial amygdalar nucleus: ttest pval (scaled--expected based on size): 0.00088875; tstat : 3.7001; df : 17; sd : 22.3418

Globus pallidus, external segment: Mean: 3.2419 +/- 0.30863 SEM
Test against a mean of 0
Globus pallidus, external segment: ttest pval: 0.0089331; tstat : 2.6215; df : 17; sd : 5.2467
Test against a Expected # of cells based on region size 0.40648
Globus pallidus, external segment: ttest pval (scaled--expected based on size): 0.017442; tstat : 2.2928; df : 17; sd : 5.2467

Globus pallidus, internal segment: Mean: 1.4163 +/- 0.11891 SEM
Test against a mean of 0
Globus pallidus, internal segment: ttest pval: 0.004272; tstat : 2.9723; df : 17; sd : 2.0215
Test against a Expected # of cells based on region size 0.1381
Globus pallidus, internal segment: ttest pval (scaled--expected based on size): 0.00787; tstat : 2.6825; df : 17; sd : 2.0215

Substantia innominata: Mean: 2.5134 +/- 0.19436 SEM
Test against a mean of 0
Substantia innominata: ttest pval: 0.0024738; tstat : 3.2273; df : 17; sd : 3.3041
Test against a Expected # of cells based on region size 0.65833
Substantia innominata: ttest pval (scaled--expected based on size): 0.014584; tstat : 2.382; df : 17; sd : 3.3041

Magnocellular nucleus: Mean: 0.27731 +/- 0.021054 SEM
Test against a mean of 0
Magnocellular nucleus: ttest pval: 0.0021749; tstat : 3.2871; df : 17; sd : 0.35792
Test against a Expected # of cells based on region size 0.079227
Magnocellular nucleus: ttest pval (scaled--expected based on size): 0.015619; tstat : 2.348; df : 17; sd : 0.35792

Medial septal nucleus: Mean: 0.18787 +/- 0.018921 SEM
Test against a mean of 0
Medial septal nucleus: ttest pval: 0.012004; tstat : 2.4779; df : 17; sd : 0.32167
Test against a Expected # of cells based on region size 0.09107
Medial septal nucleus: ttest pval (scaled--expected based on size): 0.10943; tstat : 1.2767; df : 17; sd : 0.32167

Diagonal band nucleus: Mean: 0.48947 +/- 0.033737 SEM
Test against a mean of 0
Diagonal band nucleus: ttest pval: 0.0010556; tstat : 3.6208; df : 17; sd : 0.57353
Test against a Expected # of cells based on region size 0.16087
Diagonal band nucleus: ttest pval (scaled--expected based on size): 0.013211; tstat : 2.4308; df : 17; sd : 0.57353

Triangular nucleus of septum: Mean: 0.0064051 +/- 0.00088501 SEM
Test against a mean of 0
Triangular nucleus of septum: ttest pval: 0.044312; tstat : 1.8062; df : 17; sd : 0.015045
Test against a Expected # of cells based on region size 0.11501
Triangular nucleus of septum: ttest pval (scaled--expected based on size): 1; tstat : -30.6272; df : 17; sd : 0.015045

BNST: Mean: 0.61112 +/- 0.043287 SEM
Test against a mean of 0
BNST: ttest pval: 0.0013042; tstat : 3.5234; df : 17; sd : 0.73588
Test against a Expected # of cells based on region size 0.33723
BNST: ttest pval (scaled--expected based on size): 0.066372; tstat : 1.5791; df : 17; sd : 0.73588

MainOlfactoryBulb: Mean: 0.25171 +/- 0.038879 SEM
Test against a mean of 0
MainOlfactoryBulb: ttest pval: 0.062276; tstat : 1.6158; df : 17; sd : 0.66094
Test against a Expected # of cells based on region size 4.2909
MainOlfactoryBulb: ttest pval (scaled--expected based on size): 1; tstat : -25.9276; df : 17; sd : 0.66094

AccessoryOlfactoryBulb: Mean: 0.92978 +/- 0.097154 SEM
Test against a mean of 0
AccessoryOlfactoryBulb: ttest pval: 0.014397; tstat : 2.3884; df : 17; sd : 1.6516
Test against a Expected # of cells based on region size 0.16047
AccessoryOlfactoryBulb: ttest pval (scaled--expected based on size): 0.032296; tstat : 1.9762; df : 17; sd : 1.6516

AnteriorOlfactoryNucleus: Mean: 0.0037733 +/- 0.00069434 SEM
Test against a mean of 0
AnteriorOlfactoryNucleus: ttest pval: 0.096383; tstat : 1.3562; df : 17; sd : 0.011804
Test against a Expected # of cells based on region size 1.168
AnteriorOlfactoryNucleus: ttest pval (scaled--expected based on size): 1; tstat : -418.465; df : 17; sd : 0.011804

Taenia tecta: Mean: 0.003908 +/- 0.00062019 SEM
Test against a mean of 0
Taenia tecta: ttest pval: 0.06712; tstat : 1.5726; df : 17; sd : 0.010543
Test against a Expected # of cells based on region size 0.31398
Taenia tecta: ttest pval (scaled--expected based on size): 1; tstat : -124.7746; df : 17; sd : 0.010543

Dorsal peduncular area: Mean: 0.001602 +/- 0.0002845 SEM

Test against a mean of 0
Dorsal peduncular area: ttest pval: 0.088968; tstat : 1.4053; df : 17; sd : 0.0048365
Test against a Expected # of cells based on region size 0.12319
Dorsal peduncular area: ttest pval (scaled--expected based on size): 1; tstat : -106.657; df : 17; sd : 0.0048365

Piriform area: Mean: 1.0382 +/- 0.05887 SEM
Test against a mean of 0
Piriform area: ttest pval: 0.00019501; tstat : 4.4014; df : 17; sd : 1.0008
Test against a Expected # of cells based on region size 2.6015
Piriform area: ttest pval (scaled--expected based on size): 1; tstat : -6.6274; df : 17; sd : 1.0008

Nucleus of the lateral olfactory tract: Mean: 0.21477 +/- 0.033776 SEM
Test against a mean of 0
Nucleus of the lateral olfactory tract: ttest pval: 0.06548; tstat : 1.5869; df : 17; sd : 0.5742
Test against a Expected # of cells based on region size 0.070684
Nucleus of the lateral olfactory tract: ttest pval (scaled--expected based on size): 0.15097; tstat : 1.0646; df : 17; sd : 0.5742

Cortical amygdalar area: Mean: 3.9576 +/- 0.26051 SEM
Test against a mean of 0
Cortical amygdalar area: ttest pval: 0.0007289; tstat : 3.7914; df : 17; sd : 4.4286
Test against a Expected # of cells based on region size 0.70976
Cortical amygdalar area: ttest pval (scaled--expected based on size): 0.0031734; tstat : 3.1114; df : 17; sd : 4.4286

Piriform-amygdalar area: Mean: 0.37813 +/- 0.021107 SEM
Test against a mean of 0
Piriform-amygdalar area: ttest pval: 0.00016796; tstat : 4.4711; df : 17; sd : 0.35881
Test against a Expected # of cells based on region size 0.25921
Piriform-amygdalar area: ttest pval (scaled--expected based on size): 0.088843; tstat : 1.4062; df : 17; sd : 0.35881

Postpiriform transition area: Mean: 0.33813 +/- 0.030562 SEM
Test against a mean of 0
Postpiriform transition area: ttest pval: 0.0066758; tstat : 2.7612; df : 17; sd : 0.51955
Test against a Expected # of cells based on region size 0.30535
Postpiriform transition area: ttest pval (scaled--expected based on size): 0.3961; tstat : 0.26765; df : 17; sd : 0.51955

Claustrum: Mean: 0.0042561 +/- 0.00083431 SEM
Test against a mean of 0

Claustrum: ttest pval: 0.11005; tstat : 1.2731; df : 17; sd : 0.014183
Test against a Expected # of cells based on region size 0.12164
Claustrum: ttest pval (scaled--expected based on size): 1; tstat : -35.113; df : 17; sd : 0.014183

Endopiriform nucleus-dorsal: Mean: 0.039201 +/- 0.0035084 SEM
Test against a mean of 0
Endopiriform nucleus-dorsal: ttest pval: 0.0063029; tstat : 2.7885; df : 17; sd : 0.059643
Test against a Expected # of cells based on region size 0.43775
Endopiriform nucleus-dorsal: ttest pval (scaled--expected based on size): 1; tstat : -28.3509; df : 17; sd : 0.059643

Endopiriform nucleus-ventral: Mean: 0.085026 +/- 0.0061553 SEM
Test against a mean of 0
Endopiriform nucleus-ventral: ttest pval: 0.0015377; tstat : 3.4474; df : 17; sd : 0.10464
Test against a Expected # of cells based on region size 0.21637
Endopiriform nucleus-ventral: ttest pval (scaled--expected based on size): 0.99997; tstat : -5.3255; df : 17; sd : 0.10464

Lateral amygdalar nucleus: Mean: 0.096562 +/- 0.010483 SEM
Test against a mean of 0
Lateral amygdalar nucleus: ttest pval: 0.017234; tstat : 2.2988; df : 17; sd : 0.17821
Test against a Expected # of cells based on region size 0.20089
Lateral amygdalar nucleus: ttest pval (scaled--expected based on size): 0.98814; tstat : -2.4838; df : 17; sd : 0.17821

Basolateral amygdalar nucleus-anterior: Mean: 0.59024 +/- 0.056393 SEM
Test against a mean of 0
Basolateral amygdalar nucleus-anterior: ttest pval: 0.0091088; tstat : 2.6121; df : 17; sd : 0.95868
Test against a Expected # of cells based on region size 0.17252
Basolateral amygdalar nucleus-anterior: ttest pval (scaled--expected based on size): 0.040991; tstat : 1.8486; df : 17; sd : 0.95868

Basolateral amygdalar nucleus-posterior: Mean: 0.26929 +/- 0.023909 SEM
Test against a mean of 0
Basolateral amygdalar nucleus-posterior: ttest pval: 0.0060123; tstat : 2.811; df : 17; sd : 0.40645
Test against a Expected # of cells based on region size 0.15594
Basolateral amygdalar nucleus-posterior: ttest pval (scaled--expected based on size): 0.1265; tstat : 1.1833; df : 17; sd : 0.40645

Basolateral amygdalar nucleus-ventral: Mean: 0.30243 +/- 0.0294 SEM

Test against a mean of 0
Basolateral amygdalar nucleus-ventral: ttest pval: 0.0099945; tstat : 2.5672; df : 17; sd : 0.4998
Test against a Expected # of cells based on region size 0.091039
Basolateral amygdalar nucleus-ventral: ttest pval (scaled--expected based on size): 0.045276; tstat : 1.7944; df : 17; sd : 0.4998

Basomedial amygdalar nucleus -anterior: Mean: 1.5901 +/- 0.12207 SEM
Test against a mean of 0
Basomedial amygdalar nucleus -anterior: ttest pval: 0.0023508; tstat : 3.251; df : 17; sd : 2.0751
Test against a Expected # of cells based on region size 0.16715
Basomedial amygdalar nucleus -anterior: ttest pval (scaled--expected based on size): 0.0048844; tstat : 2.9093; df : 17; sd : 2.0751

Basomedial amygdalar nucleus-posterior: Mean: 1.623 +/- 0.12082 SEM
Test against a mean of 0
Basomedial amygdalar nucleus-posterior: ttest pval: 0.0018883; tstat : 3.3525; df : 17; sd : 2.054
Test against a Expected # of cells based on region size 0.15629
Basomedial amygdalar nucleus-posterior: ttest pval (scaled--expected based on size): 0.0037805; tstat : 3.0296; df : 17; sd : 2.054

Posterior amygdalar nucleus: Mean: 3.7539 +/- 0.23612 SEM
Test against a mean of 0
Posterior amygdalar nucleus: ttest pval: 0.00049723; tstat : 3.9677; df : 17; sd : 4.014
Test against a Expected # of cells based on region size 0.21998
Posterior amygdalar nucleus: ttest pval (scaled--expected based on size): 0.00082354; tstat : 3.7352; df : 17; sd : 4.014

Table 4: Statistical analysis of sex differences in major input regions. The average percentage of input cells observed in each region for males (mean column 2; SEM column 3) and females (mean column 4; SEM column 5). The p-value obtained from performing a posthoc permutation test comparing the percentage of inputs for each region in male versus female mice (column 6). Posthoc analyses followed an ANOVA with repeated samples.

APPENDIX C

SUPPLEMENTARY INFORMATION

Solutions

- Hydrogel monomer solution: 4% acrylamide (Sigma Aldrich; A3553); 0.05% bis acrylamide (Bio Rad; 1610142); 0.25% Initiator (Fisher Scientific; NC0632395); 0.01 M PBS (Fisher Scientific; BP2944100)
- Clearing Solution: 4% sodium dodecyl sulfate in 200 mM Boric Acid brought to pH 8.5 with 0.1 M NaOH
- Electrophoresis Buffer: 0.1 M Borate Buffer and 0.1% Triton X-100 (Fisher Scientific; 85111) brought to pH 9.5 with 0.1 M LiOH
- Optiview: Sodium Diatrizoate: 0.173 M (Sigma Alrdrich; **S4506**), Meglumine Diatrizoate: 0.816 M (Sigma Aldrich; **M5266),** Diatrizoic Acid 0.816 M (Chem Impex; 24150), pH 8 EDTA: 0.00005 M, Tween-20: 9×10^{-7}M (Sigma Aldrich; **P1379)**

MHD-accelerated tissue clearing protocol

1. Incubate sample of PFA-perfused tissue in hydrogel monomer solution overnight at 4˚ C.
    - Hydrogel: (4% acrylamide (Sigma Aldrich; A3553); 0.05% bis acrylamide (Bio Rad; 1610142); 0.25% Initiator (Fisher Scientific; NC0632395); 0.01 M PBS (Fisher Scientific; BP2944100)).
2. Degas hydrogel with sample in it with one liter of nitrogen gas
3. Polymerize sample by placing in a water bath at 37 ˚ C for 2 – 3 hours
4. Remove excess hydrogel from the surface of the sample
5. Place in sample in 40 mL clearing solution (4% SDS solution in 200 mM Boric Acid) at 37 ˚ C for 2 days
6. Transfer sample to the basket in the central channel of the MHD-accelerated clearing device and submerge in a five-liter bath of clearing solution
7. Apply 0.3 to 0.5 Amps across the tissue at 36.7 ˚ C (we find 0.3 Amps for 12 hours to be an effective starting point).

Refractive Index-Matching

1. Wash tissue sample in 0.01 PBS at 37 ˚ C overnight or for 8 to 12 hours
2. Incubate tissue in 30 mL Optiview for two days

MHD-accelerated antibody labeling protocol

Preparation

1. Cut dialysis (6-8 kDa Spectra Por1) tubing to 2.25" + size of tissue sample (along the longest axis)
2. Equilibrate dialysis tubing in dH_2O for at least 30 min at RT in bath of electrophoresis buffer
3. Fill dialysis tubing and one-liter chamber with Electrophoresis Buffer
    a. Electrophoresis Buffer: 0.1 M Borate Buffer brought to pH 9.5 with 0.1 M LiOH and 0.1% Triton X-100
4. Place tissue in the center of the dialysis tubing
5. Submerge dialysis tubing with tissue inside in one-liter chamber filled with Electrophoresis Buffer
6. Prepare a concentrated 300 µL solution of antibody in electrophoresis buffer
    a. 1:30 antibody, 1% Heparin
7. Load antibody solution into a syringe

Device setup

8. Submerge the torus-shaped tube in electrophoresis buffer
    a. Ensure that all air in the tubing is replaced with electrophoresis buffer
9. Attach each end of the dialysis tubing, with the tissue inside, to the corresponding ends of the torus-shaped tubing
    a. Run the dialysis tubing through the two openings on either side of the acrylic device
    b. Fit the ends of the dialysis tubing over the barbs on the ends of the torus-shaped tubing
    c. Use nylon screws to tighten an acrylic plate onto the end of the barbs on the outer edges of the acrylic device, pushing them into the angled fittings
10. Ensure that the entire tubing system is water-tight with no leaks and no air bubbles

Active antibody incubation:

11. Place the device, with the tube intact, over a waterproofed N52 neodymium magnet and affix the electrode array over the device to create a channel that is held in place, with an electrode on either side of the tissue, by the attraction between the top and bottom magnets
12. Submerge the intact device in electrophoresis buffer in the one-liter chamber
13. Use the inputs to the torus-shaped tube to flush the concentrated antibody solution in the syringe into the intact torus and dialysis tube system
14. Ensure that there are no bubbles or leaks in the system and that the tissue is positioned in the center of the dialysis tubing at the intersection of the magnetic and electric fields
15. Provide power to the electrode array by activating the power supply at 30-60 VDC and 0.2 to 0.3 Amps

16. Every two hours turn off power to the electrodes and use the torus tube input to flush 300 µL electrophoresis buffer into the system for the entirety of the labeling session (12 hours)

Active wash:

17. Flush the antibody solution out of the system and refill with pure electrophoresis solution
18. Repeat the 'active antibody incubation' protocol without additional antibody for an additional 6 to 12 hours

Antibodies used

Zebrafish:

Primary: Mouse IgG anti-Acetylated Tubulin antibody (Sigma-Aldrich)
Secondary: Goat IgG anti-mouse Alexa 647 nm (ThermoFisher)

Nudibranch:

Primary: Rabbit anti-5-HT (Immunostar)
Secondary: Goat anti-rabbit Alexa 488 nm (ThermoFisher)

Mouse:

Primary 1: Rabbit anti-oxytocin antibody (Immunostar)
Primary 2: Rabbit anti-AVP antibody (AbCam)
Primary 3: Rat anti-mCherry (ThermoFisher)
Secondary 1: Goat IgG anti-rabbit Alexa 647 nm (Jackson ImmunoResearch)
Secondary 2: Goat IgG anti-rabbit Alexa 488 nm (ThermoFisher)
Secondary 3: Donkey IgG anti-rat Alexa 488 nm (ThermoFisher)

Materials used to build clearing device:

0.25 mm diameter 99.9% platinum wire (Sigma-Aldrich; 349402)
Silicone adhesive (Grainger; 4UH03)
1" x 2" x 1" N52 Neodymium magnet (Applied magnets; NB057-6-N52)
1/8" thickness acrylic sheet (Delvie's Plastics)
Nylon bolts (Mcmaster-Carr; 93939A734)

Materials used to build antibody labeling device:

1" x 2" x 0.5" N52 Neodymium Magnet (Applied magnets; NB057-6-N52)
0.25 mm diameter 99.9% platinum wire (Sigma-Aldrich; 349402)
1" thickness acrylic sheet (Delvie's Plastics)
1/8" thickness acrylic sheet (Delvie's Plastics)
0.25" diameter Spectra Por 1 6-8 kDa dialysis tubing (Spectra Por; 132645)
0.5" cubed N52 Neodymium Magnet (Applied magnets; NB022-N52)
1/8" inner diameter vinyl tubing (ThermoFisher: S504591)
1/4" to 1/8" male-to-male tubing adapters (Cole-Parmer; UX-45501-20)
Nylon bolts (Mcmaster-Carr; 93939A734)
25-gauge winged infusion needle and IV (Fisher Scientific; 22-289913

BIBLIOGRAPHY

1. Adhikari, A., Lerner, T., Finkelstein, J., Pak, S., Jennings, J.H., Davidson, T.J., Ferenczi, E., Gunaydin, L.A., Mirzabekov, J.J., Ye, L., Kim, S.Y., Lei, A., Deisseroth, K., (2015). Basomedial amygdala mediates top-down control of anxiety and fear. Nature 527, 179–185
2. Amano, Duvarci, Popa, Paré, (2011). The Fear Circuit Revisited: Contributions of the Basal Amygdala Nuclei to Conditioned Fear. Journal of Neuroscience, 31(43):15481-9
3. Anderson PK., (1986). Foraging Range in Mice and Voles - the Role of Risk. Can J Zool. 1986;64:2645–2653.
4. Apfelbach R, Blanchard CD, Blanchard RJ, Hayes RA, McGregor IS., (2005). The effects of predator odors in mammalian prey species: a review of field and laboratory studies. Neurosci Biobehav Rev. 2005;29(8):1123-44. doi: 10.1016/j.neubiorev.2005.05.005.
5. Autry AE, Wu Z, Kapoor V, Kohl J, Bambah-Mukku D, Rubinstein ND, Marin-Rodriguez B, Carta I, Sedwick V, Tang M, Dulac C (2021) Urocortin-3 neurons in the mouse perifornical area promote infant-directed neglect and aggression. Elife 10:e64680. doi:10.7554/eLife.64680
6. Baier, F., & Hoekstra, H. E. (1914). The genetics of morphological and behavioural island traits in deer mice. In Proceedings of the Royal Society B: Biological Sciences 286(1914): 20191697. https://doi.org/10.1098/rspb.2019.1697

7. Bakker, J., Honda, S., Harada, N., & Balthazart, J. (2002). The aromatase knock-out mouse provides new evidence that estradiol is required during development in the female for the expression of sociosexual behaviors in adulthood. The Journal of neuroscience, 22(20), 9104–9112.
8. Bansal, R., Nagel, M., Stopkova, R., Sofer, Y., Kimchi, T., Stopka, P., Spehr, M., Ben-Shaul, Y., (2021). Do all mice smell the same? Chemosensory cues from inbred and wild mouse strains elicit stereotypic sensory representations in the accessory olfactory bulb. BMC Biol 19, 133
9. Bastock, M. (1967). Courtship: An ethological study. Chicago: Aldine Publishing Company.
10. Bedoya-Pérez, M. A., Smith, K. L., Kevin, R. C., Luo, J. L., Crowther, M. S., & McGregor, I. S. (2019). Parameters That Affect Fear Responses in Rodents and How to Use Them for Management. In Frontiers in Ecology and Evolution (Vol. 7). Frontiers Media SA. https://doi.org/10.3389/fevo.2019.00136
11. Beery and Kaufer, (2015). Stress, social behavior, and resilience: Insights from rodents. Neurobiology of Stress, 1:116-127
12. Bendesky, A., Kwon, Y. M., Lassance, J. M., Lewarch, C. L., Yao, S., et al., (2017). The genetic basis of parental care evolution in monogamous mice. Nature, 544(7651), 434-439.
13. Ben-Shaul Y, Katz LC, Mooney R, Dulac C., (2010). In vivo vomeronasal stimulation reveals sensory encoding of conspecific and allospecific cues by the mouse accessory olfactory bulb. Proc Natl Acad Sci U S A. 2010 Mar 16;107(11):5172-7. doi: 10.1073/pnas.0915147107.

14. Bergan JF, Ben-Shaul Y, Dulac C. (2014). Sex-specific processing of social cues in the medial amygdala. Elife. 2014 Jun 3;3:e02743. doi: 10.7554/eLife.02743. PMID: 24894465; PMCID: PMC4038839.
15. Berthoud H-R, Munzberg H (2011) The lateral hypothalamus as integrator of metabolic and environmental needs: from electrical self-stimulation to opto-genetics. Physiol Behav 104:29–39. doi:10.1016/j.physbeh.2011.04.051
16. Billing, A, Correia, M, Kelly, D, Li, G, Bergan, J, (2020). Synaptic Connections of Aromatase Circuits in the Medial Amygdala Are Sex Specific. eNeuro, 7(3), 0489-19.2020. DOI: https://doi.org/10.1523/ENEURO.0489-19.2020
17. Binns, KE, Brennan, PA, (2005). Changes in electrophysiological activity in the accessory olfactory bulb and medial amygdala associated with mate recognition in mice. European Journal of Neuroscience, 21(9):2529-37.
18. Bradley SR, Pieribone VA, Wang W, Severson CA, Jacobs RA, Richerson GB, (2002) Chemosensitive serotonergic neurons are closely associated with large medullary arteries. Nat Neurosci 5:401–402. doi:10.1038/nn848 pmid:11967547
19. Bressler and Baum, (1996). Sex comparison of neuronal fos immunoreactivity in the rat vomeronasal projection circuit after chemosensory stimulation. Neuroscience, 71(4):1063-72
20. Brown, C.H. (2016). Magnocellular Neurons and Posterior Pituitary Function. In Comprehensive Physiology, R. Terjung (Ed.).
21. Burnett Heyes S, Jih YR, Block P, Hiu CF, Holmes EA, Lau JY., (2015). Relationship Reciprocation Modulates Resource Allocation in Adolescent Social

Networks: Developmental Effects. Child Dev. 2015 Sep-Oct;86(5):1489-506. doi: 10.1111/cdev.12396.

22. Butler, J.M., Whitlow, S.M., Roberts, D.A. et al. Neural and behavioural correlates of repeated social defeat. Sci Rep 8, 6818 (2018). https://doi.org/10.1038/s41598-018-25160-x
23. Byrne, H., (2008). Learning and Memory: A Comprehensive Reference. Elsevier, Academic Press.
24. Cádiz-Moretti, B, Abellán-Álvaro, M., Pardo-Bellver, C., Martínez-García, Lanuza, E., (2016). Afferent and Efferent Connections of the Cortex-Amygdala Transition Zone in Mice. Frontiers in Neuroanatomy, 10:125
25. Canteras, Simerly, and Swanson, (1995). Organization of projections from the medial nucleus of the amygdala: A PHAL study in the rat. Journal of Comparative Neurology, 360(2):213-45
26. Castellano and Tena-Sempere (2016) Metabolic control of female puberty: potential therapeutic targets, Expert Opinion on Therapeutic Targets, 20:10, 1181-1193
27. Chalfin, L., Dayan, M., Levy, D., Austad, Miller, Iraqi, Dulac, Kimchi, (2014). Mapping ecologically relevant social behaviours by gene knockout in wild mice. Nat Commun 5, 4569 (2014).
28. Chamero P, Marton TF, Logan DW, Flanagan K, Cruz JR, Saghatelian A, Cravatt BF, Stowers L., (2007). Identification of protein pheromones that promote aggressive behaviour. Nature. 2007 Dec 6;450(7171):899-902. doi: 10.1038/nature05997. PMID: 18064011.

29. Chen and Hong, (2018). Neural Circuit Mechanisms of Social Behavior. Neuron, 98(1):16-30

30. Chen, P. B., Hu, R. K., Wu, Y. E., Pan, L., Huang, S., Micevych, P. E., & Hong, W. (2019). Sexually Dimorphic Control of Parenting Behavior by the Medial Amygdala. Cell, 176(5), 1206–1221.e18.

31. Chi, J., Crane, A., Wu, Z., & Cohen, P. (2018). Adipo-Clear: A Tissue Clearing Method for Three-Dimensional Imaging of Adipose Tissue. Journal of Visualized Experiments, (137). doi:10.3791/58271

32. Chou, Xl., Wang, X., Zhang, Zg., Shen, L., Zingg, B., Huang, J., Zhong, W., Mesik, L., Zhang, L.I., Tao, H.W., (2018). Inhibitory gain modulation of defense behaviors by zona incerta. Nat Commun 9, 1151

33. Chung, K., Wallace, J., Kim, SY., Kalyanasundaram, S., Andalman, A.S., Davidson, T.J., Mirzabekov, J.J., Zalocusky, K.A., Mattis, J., Denisin, A.K., Pak, S., Bernstein, H., Ramakrishnan, C., Grosenick, L., Gradinaru, V., Deisseroth, K., (2013). Structural and molecular interrogation of intact biological systems. Nature 497, 332–337

34. Ciocchi, S., Herry, C., Grenier, F., Wolff, S. B. E., Letzkus, J. J., Vlachos, I., Ehrlich, I., Sprengel, R., Deisseroth, K., Stadler, M. B., Müller, C., & Lüthi, A. (2010). Encoding of conditioned fear in central amygdala inhibitory circuits. In Nature (Vol. 468, Issue 7321, pp. 277–282). Springer Science and Business Media LLC. https://doi.org/10.1038/nature09559

35. Clemens, Girardin, Coen, Guan, Dickson, and Murthy, (2015). Connecting Neural Codes with Behavior in the Auditory System of Drosophila. Neuron, 87(6):1332-43

36. Contreras JL, Agmo A. Sensory control of the male rat's copulatory thrusting patterns (1993). Behav. Neural Biol. 1993;60:234–240.
37. Cooke and Woolley, (2005). Sexually Dimorphic Synaptic Organization of the Medial Amygdala. Journal of Neuroscience. 25(46): 10759-67.
38. Cooke, B, Tabibnia, G, and Breedlove, M, (1999). A brain sexual dimorphism controlled by adult circulating androgens. PNAS, 96(13):7538-40.
39. Creel, Schuette, Christianson, (2014). Effects of predation risk on group size, vigilance, and foraging behavior in an African ungulate community, *Behavioral Ecology*, Volume 25, Issue 4, July-August 2014, Pages 773–784, https://doi.org/10.1093/beheco/aru050
40. Darwin, C. & Kebler, L. (1859) On the origin of species by means of natural selection, or The preservation of favoured races in the struggle for life.
41. Darwin, C. (1871). The descent of man, and Selection in relation to sex, Vol. 1. John Murray. https://doi.org/10.1037/12293-000
42. de Olmos , J.S., G.F. A Lheid & C.A. B Eltramino, (1985). Amygdala. In The Rat Nervous System. 1st Edition. G. Paxinos, Ed.: 223–334. Academic Press.
43. De Olmos J, Hardy H, Heimer L (1978) The afferent connections of the main and accessory olfactory bulb formations in the rat. An experimental HRP study. J Comp Neurol 181:213–244
44. De Vries GJ, Buijs RM, Van Leeuwen FW (1984) Sex differences in vasopressin and other neurotransmitter systems in the brain. Prog Brain Res 61: 185-203.

45. DeAngelis, R, Dodd, L, Snyder, A, Rhodes, JS, (2018). Dynamic regulation of brain aromatase and isotocin receptor gene expression depends on parenting status. Hormones and Behavior, 103:62-70

46. Del Punta, K, Puche, A, Adams, Adams, N, Rodriguez, I, Mombaerts, P, (2002). A Divergent Pattern of Sensory Axonal Projections Is Rendered Convergent by Second-Order Neurons in the Accessory Olfactory Bulb. Neuron, 35(6):1057-1066.

47. Di Marino V., Etienne Y., Niddam M. (2016) The Concept of "Extended Amygdala". In: The Amygdaloid Nuclear Complex.

48. Dina K N Dechmann, Rachel A Page, Gerald G Carter, Jenna E Kohles (2020). Socially foraging bats discriminate between group members based on search-phase echolocation calls. Behavioral Ecology, 2020; DOI: 10.1093/beheco/araa056

49. Donato J Jr, Elias CF. (2011). The ventral premammillary nucleus links metabolic cues and reproduction. Front Endocrinol (Lausanne). Oct 25;2:57. doi: 10.3389/fendo.2011.00057. PMID: 22649378; PMCID: PMC3355867.

50. Donato J Jr., Cravo RM, Frazão R, Gautron L, Scott MM, Lachey J, Castro IA, Margatho LO, Lee S, Lee C, Richardson JA, Friedman J, Chua S Jr., Coppari R, Zigman JM, Elmquist JK, Elias CF (2011) Leptin's effect on puberty in mice is relayed by the ventral premammillary nucleus and does not require signaling in Kiss1 neurons. J Clin Invest 121:355–368. doi:10.1172/JCI45106 pmid:21183787

51. Dudek SM, Alexander GM, Farris S (2016) Rediscovering area CA2: unique properties and functions. Nat Rev Neurosci 17:89–102. doi:10.1038/nrn.2015.22 pmid:26806628

52. Dulac C, O'Connell LA, Wu Z., (2014). Neural control of maternal and paternal behaviors. Science. 2014 Aug 15;345(6198):765-70. doi: 10.1126/science.1253291. Epub 2014 Aug 14. PMID: 25124430; PMCID: PMC4230532.

53. Dulac C, Torello AT., (2003). Molecular detection of pheromone signals in mammals: from genes to behaviour. Nat Rev Neurosci. 2003 Jul;4(7):551-62. doi: 10.1038/nrn1140. PMID: 12838330.

54. Dulac, C. and Axel, R., (1995). A Novel Family of Genes Encoding Putative Pheromone Receptors in Mammals. Cell, 83:195-206.

55. Duvarci, S, Popa, D, Paré, Denis, (2011). Central Amygdala Activity during Fear Conditioning. Journal of Neuroscience, 31(1):289-294

56. Dwyer J, Kelly DA, Bergan J., (2022). Brain-Wide Synaptic Inputs to Aromatase-Expressing Neurons in the Medial Amygdala Suggest Complex Circuitry for Modulating Social Behavior. eNeuro. 2022 Mar 11;9(2): ENEURO.0329-21.2021.

57. Dwyer, J, Ramirez, MD, Katz, PS, Karlstrom, RO, Bergan, J, (2019). Accelerated clearing and molecular labeling of large tissue samples using magnetohydrodynamic force. bioRxiv 819292;

58. Efron. B and Tibshirani F, (1986). Bootstrap Methods for Standard Errors, Confidence Intervals, and Other Measures of Statistical Accuracy. Statist. Sci. 1 (1) 54 – 75

59. Elias, C.F., (2010). Leptin's effect on puberty in mice is relayed by the ventral premammillary nucleus and does not require signaling in Kiss1 neurons. The Journal of Clinical Investigation, 121(1):355-68

60. Ferguson J, Aldag J, Insel T, Young L (2001) Oxytocin in the medial amygdala is essential for social recognition in the mouse. J Neurosci 21:8278–8285. doi:10.1523/JNEUROSCI.21-20-08278.2001 pmid:11588199

61. Ferrero DM, Moeller LM, Osakada T, Horio N, Li Q, Roy DS, Cichy A, Spehr M, Touhara K, Liberles SD., (2013). A juvenile mouse pheromone inhibits sexual behaviour through the vomeronasal system. Nature. 2013 Oct 17;502(7471):368-71. doi: 10.1038/nature12579. Epub 2013 Oct 2. PMID: 24089208; PMCID: PMC3800207.

62. Ferretti, Maltese, Contarini, Nigro, Bonavia, Huang, Gigliucci, Morelli, Scheggia, Managó, Castellini, Lefevre, Cancedda, Chini, Grinevich, Papaleo, (2019). Oxytocin Signaling in the Central Amygdala Modulates Emotion Discrimination in Mice. Current Biology, 29(12):1938-53.e6

63. Fischer, E. K., Roland, A. B., Moskowitz, N. A., Tapia, E. E., Summers, K., Coloma, L. A., & O'Connell, L. A. (2019). The neural basis of tadpole transport in poison frogs. In Proceedings of the Royal Society B: Biological Sciences (Vol. 286, Issue 1907, p. 20191084). The Royal Society. https://doi.org/10.1098/rspb.2019.1084

64. Fisher MM, Eugster EA., (2014). What is in our environment that effects puberty? Reprod Toxicol. 2014 Apr;44:7-14. doi: 10.1016/j.reprotox.2013.03.012. Epub 2013 Apr 17.

65. Gersick, A., & Kurzban, R. (2014). Covert Sexual Signaling: Human Flirtation and Implications for other Social Species. In Evolutionary Psychology (Vol. 12, Issue 3, p. 147470491401200). SAGE Publications. https://doi.org/10.1177/147470491401200305

66. Gonzalez, F., Witzgall, P. & Walker, W. (2017). Antennal transcriptomes of three tortricid moths reveal putative conserved chemosensory receptors for social and habitat olfactory cues. Sci Rep 7, 41829

67. Goodson J. L. (2005). The vertebrate social behavior network: evolutionary themes and variations. Hormones and behavior, 48(1), 11–22.

68. Goodson, J.L. and Kingsbury, M.A., (2013). What's in a name? Considerations of homologies and nomenclature for vertebrate social behavior networks. Hormones and Behavior, 64(1):103-112.

69. Green, S.M., & Marler, P.R. (1979). The Analysis of Animal Communication.

70. Guo, X., Guo, H., Zhao, L., Zhang, Y.H., Zhang, J.X., (2018). Two predominant MUPs, OBP3 and MUP13, are male pheromones in rats. Front Zool 15, 6.

71. Haller, J, Tóth, Halasz, De Boer, (2006). Patterns of violent aggression-induced brain c-fos expression in male mice selected for aggressiveness. Physiology and Behavior 88(1-2):173-182

72. Haller, J. (2018). The role of central and medial amygdala in normal and abnormal aggression: A review of classical approaches..Neuroscience and Biobehavior Reviews, 85:34-43

73. Hama, H, Kurokawa, H, Kawano, H, Ando, R, Shimorgori, T, et al., (2011). Scale: a chemical approach for fluorescence imaging and reconstruction of transparent mouse brain. Nature Neuroscience, (14): 1481-1488.

74. Hama, Hiroshi, Hioki, Hiroyuki, Namiki, Kana, Hoshida, Tetsushi, Kurokawa, Hiroshi, et al., (2015). ScaleS: an optical clearing palette for biological imaging. Nat Neurosci, 18(10): 1518-1529.

75. Hammen, G. F., Turaga, D., Holy, T. E., & Meeks, J. P. (2014). Functional organization of glomerular maps in the mouse accessory olfactory bulb. Nature neuroscience, 17(7), 953–961.

76. Harris, G., Wimmer, M. & Aston-Jones, G., (2005). A role for lateral hypothalamic orexin neurons in reward seeking. Nature 437, 556–559 (2005).

77. Hashikawa, K., Hashikawa, Y., Falkner, A., & Lin, D. (2016). The neural circuits of mating and fighting in male mice. In Current Opinion in Neurobiology (Vol. 38, pp. 27–37). Elsevier BV. https://doi.org/10.1016/j.conb.2016.01.006

78. Hassabis D, Spreng RN, Rusu AA, Robbins CA, Mar RA, Schacter DL., (1979). Imagine all the people: how the brain creates and uses personality models to predict behavior. Cereb Cortex. 2014 Aug;24(8):1979-87. doi: 10.1093/cercor/bht042. Epub 2013 Mar 5. PMID: 23463340; PMCID: PMC4089378.

79. Hattori T, Kanno K, Nagasawa M, Nishimori K, Mogi K, Kikusui T., (2015). Impairment of interstrain social recognition during territorial aggressive behavior in oxytocin receptor-null mice. Neurosci Res. 2015 Jan;90:90-4. doi: 10.1016/j.neures.2014.05.003. Epub 2014 Jun 12. PMID: 24929102.

80. Haxby, J, Hoffman, E, Gobbini, M, (2002). Human neural systems for face recognition and social communication. Biological Psychiatry, 51(1):59-67.

81. Herbert-Read, J. E., Rosén, E., Szorkovszky, A., Ioannou, C. C., Rogell, B., Perna, A., Ramnarine, I. W., Kotrschal, A., Kolm, N., Krause, J., & Sumpter, D. J. T. (2017). How predation shapes the social interaction rules of shoaling fish. In Proceedings of the Royal Society B: Biological Sciences (Vol. 284, Issue 1861, p. 20171126). The Royal Society. https://doi.org/10.1098/rspb.2017.1126

82. Hu RK, Zuo Y, Ly T, Wang J, Meera P, Wu YE, Hong W (2021) An amygdala-to-hypothalamus circuit for social reward. Nat Neurosci 24:831–842. doi:10.1038/s41593-021-00828-2

83. Huffman LS, O'Connell LA, Hofmann HA., (2013). Aromatase regulates aggression in the African cichlid fish Astatotilapia burtoni. Physiol Behav. 2013 Mar 15;112-113:77-83. doi: 10.1016/j.physbeh.2013.02.004. Epub 2013 Feb 21.

84. Ishii KK, Osakada T, Mori H, Miyasaka N, Yoshihara Y, Miyamichi K, Touhara K., (2017). A Labeled-Line Neural Circuit for Pheromone-Mediated Sexual Behaviors in Mice. Neuron. 2017 Jul 5;95(1):123-137.e8. doi: 10.1016/j.neuron.2017.05.038. Epub 2017 Jun 22. PMID: 28648498.

85. Isogai Y, Wu Z, Love MI, Ahn MH, Bambah-Mukku D, Hua V, Farrell K, Dulac C., (2018). Multisensory Logic of Infant-Directed Aggression by Males. Cell. 2018 Dec 13;175(7):1827-1841.e17. doi: 10.1016/j.cell.2018.11.032. PMID: 30550786; PMCID: PMC6558521.

86. Isogai, Y., Richardson, D., Dulac, C., and Bergan, J.F. (2017) Optimized protocol for imaging cleared neural issues using light microscopy, in Synapse Development, Methods in Molecular Biology, Springer, 1538: 137-153.

87. Isogai, Y., Si, S., Pont-Lezica, L., Tan, T., Kapoor, V., Murthy, V. N., & Dulac, C. (2011). Molecular organization of vomeronasal chemoreception. Nature, 478(7368), 241–245.

88. Iwasa, T., Matsuzaki, T., Yano, K., Mayila, Y., Yanagihara, R., Yamamoto, Y., Kuwahara, A., & Irahara, M. (2018). Effects of Low Energy Availability on Reproductive Functions and Their Underlying Neuroendocrine Mechanisms. In

Journal of Clinical Medicine (Vol. 7, Issue 7, p. 166). MDPI AG. https://doi.org/10.3390/jcm7070166

89. Jamalabadi, MY, (2014). Analytical Study of Magnetohydrodynamic Propulsion Stability. J. Marine Sci. Appl. 13:281-290.
90. Jasnow, Schulkin, Pfaff, (2006). Estrogen facilitates fear conditioning and increases corticotropin-releasing hormone mRNA expression in the central amygdala in female mice. Hormones and Behavior, 49(2):197-205
91. Jordan, S.D., Könner, A.C. & Brüning, J.C., (2010). Sensing the fuels: glucose and lipid signaling in the CNS controlling energy homeostasis. Cell. Mol. Life Sci. 67, 3255–3273 (2010). https://doi.org/10.1007/s00018-010-0414-7
92. Katz-Wise SL, Priess HA, Hyde JS., (2010) Gender-role attitudes and behavior across the transition to parenthood. Dev Psychol. 2010 Jan;46(1):18-28. doi: 10.1037/a0017820. PMID: 20053003; PMCID: PMC3764615.
93. Keller M, Douhard Q, Baum MJ, Bakker J *(*2006a*)* Destruction of the main olfactory epithelium reduces female sexual behavior and olfactory investigation in female mice. *Chem Senses* 31:315–*323.* doi:10.1093/chemse/bjj035 pmid:16484502
94. Keller M, Pierman S, Douhard Q, Baum MJ, Bakker J *(*2006b*)* The vomeronasal organ is required for the expression of lordosis behaviour, but not sex discrimination in female mice. *Eur J Neurosci* 23:521–*530.* doi:10.1111/j.1460-9568.2005.04589.x
95. Keller M, Pierman S, Douhard Q, Baum MJ, Bakker J., (2006c). The vomeronasal organ is required for the expression of lordosis behaviour, but not sex discrimination in female mice. Eur J Neurosci. 2006c;23:521–530.

96. Keys, A., Brožek, J., Henschel, A., Mickelsen, O., Taylor, H. L., Simonson, E., Skinner, A. S., Wells, S. M., Drummond, J. C., Wilder, R. M., King, C. G., & Williams, R. R. (1950). Growth and Development. In The Biology of Human Starvation: Volume II (NED-New edition, pp. 974–1001). University of Minnesota Press. http://www.jstor.org/stable/10.5749/j.cttttqzj.12

97. Kim B, Im HI *(*2019*)* The role of the dorsal striatum in choice impulsivity. *Ann N Y Acad Sci* 1451*:*92*–111.* doi:10.1111/nyas.13961 pmid:30277562

98. Kim, Im, (2018). The role of the dorsal striatum in choice impulsivity. Anals of the New York academy of sciences, 1451(1):92-111

99. Kim, SY, Cho, JH, Murray, E, Bakh, N, Choi, H, et al., (2015). Stochastic electrotransport selectively enhances the transport of highly electromobile molecules, PNAS, 112(46): E6274-83. doi:10.1073/pnas.1510133112.

100. Kim, Y, Yan, GR, Pradhan, K, Venkataraju, KU, Bota, García Del Molino, L.C., Fitzgerald, G., Ram, K., He, M., Levine, J.M., Mitra, P., Huang, Z., Wang, X.J., Osten, P., (2017). Brain-wide Maps Reveal Stereotyped Cell Type-based Cortical Architecture and Subcortical Sexual Dimorphism. Cell, 171(2)-456-69.e22

101. King, (2006). The rise, fall, and resurrection of the ventromedial hypothalamus in the regulation of feeding behavior and body weight. Physiology and Behavior, 87(2):221-44

102. Klein, Staring, Murphy, Viergever, Pluim., (2010) elastix: a toolbox for intensity based medical image registration. IEEE Transactions on Medical Imaging, 29(1): 196 - 205

103. Kohl J, Babayan BM, Rubinstein ND, Autry AE, Marin-Rodriguez B, Kapoor V, Miyamishi K, Zweifel LS, Luo L, Uchida N, Dulac C. (2018). Functional circuit architecture underlying parental behaviour. Nature. 556(7701):326-331. doi: 10.1038/s41586-018-0027-0. Epub 2018 Apr 11. PMID: 29643503; PMCID: PMC5908752.

104. Kohl, J., Autry, A. E., & Dulac, C. (2016). The neurobiology of parenting: A neural circuit perspective. In BioEssays (Vol. 39, Issue 1, p. e201600159). Wiley. https://doi.org/10.1002/bies.201600159

105. Kohler SL, Mcpeek MA., (1989) Predation Risk and the Foraging Behavior of Competing Stream Insects. Ecology. 1989;**70**:1811–1825.

106. Kollack-Walker S, Watson SJ, Akil H., (1997). Social stress in hamsters: defeat activates specific neurocircuits within the brain. J Neurosci. 1997 Nov 15;17(22):8842-55. doi: 10.1523/JNEUROSCI.17-22-08842.1997. PMID: 9348352; PMCID: PMC6573068.

107. Krapp, Hengstenberg, and Egelhaaf, (2001). Binocular Contributions to Optic Flow Processing in the Fly Visual System. Journal of Neurophysiology, 85(2):724-34

108. Krebs, J. R., & Kroodsma, D. E. (1980). Repertoires and Geographical Variation in Bird Song. In Advances in the Study of Behavior (pp. 143–177). Elsevier. https://doi.org/10.1016/s0065-3454(08)60117-5

109. Lebow MA, Chen A. (2016). Overshadowed by the amygdala: the bed nucleus of the stria terminalis emerges as key to psychiatric disorders. Mol Psychiatry. 21(4):450-63. doi: 10.1038/mp.2016.1. Epub 2016 Feb 16. Erratum in: Mol Psychiatry. 2021 Aug;26(8):4561. PMID: 26878891; PMCID: PMC4804181.

110. Lee, Eunsoo, Choi, JC, Jo, Y, Kim, JY, Jang, YJ, et. al., (2016). ACT-PRESTO: Rapid and consistent tissue clearing and labeling method for 3-dimensional (3D) imaging. Scientific Reports, 6(1863). doi: 10.1038/srep18631

111. Lee, H., Kim, D. W., Remedios, R., Anthony, T. E., Chang, A., Madisen, L., Zeng, H., & Anderson, D. J. (2014). Scalable control of mounting and attack by Esr1+ neurons in the ventromedial hypothalamus. Nature, 509(7502), 627–632.

112. Lee, JH., Latchoumane, CF.V., Park, J., Kim, J., Jeong, J., Lee, K.W., Shin, H.S., (2019). The rostroventral part of the thalamic reticular nucleus modulates fear extinction. Nat Commun 10, 4637

113. Li and Dulac, (2018). Neural coding of sex-specific social information in the mouse brain. Current Opinion in Neurobiology, 53:120-30

114. Li Yusha, Xu Jianyi, Wan Peng, Yu Tingting, Zhu Dan, (2018). Optimization of GFP Fluorescence Preservation by a Modified uDISCO Clearing Protocol. Frontiers in Neuroanatomy 12:67.

115. Li, Y., Mathis, A., Grewe, B. F., Osterhout, J. A., Ahanonu, B., Schnitzer, M. J., Murthy, V. N., & Dulac, C. (2017). Neuronal Representation of Social Information in the Medial Amygdala of Awake Behaving Mice. In Cell (Vol. 171, Issue 5, pp. 1176-1190.e17). Elsevier BV. https://doi.org/10.1016/j.cell.2017.10.015

116. Lin D, Boyle M, Dollar P, Lee H, Lein ES, Perona P, Anderson DJ (2011) Functional identification of an aggression locus in the mouse hypothalamus. Nature 470:221–226. doi:10.1038/nature09736

117. Luo, M, Fee, M, and Katz, L, (2003). Encoding Pheromonal Signals in the Accessory Olfactory Bulb of Behaving Mice. Science, 299(5610):1196-1201

118. Luo, SX, Huang, J, Li, Q, Mohammad, H, Lee, Chun-Yao, Krishna, K., Kok, A.M.Y., Tan, Y.L., Lim, J.Y., Li, H., Yeow, L.Y., Sun, J.J., He, M., Jean, J.G., Sajikumar,, S., Han, W., Fu, Y., (2018). Regulation of feeding by somatostatin neurons in the tuberal nucleus. Science, 361(6397):76-81

119. Madisen L; Zwingman TA; Sunkin SM; Oh SW; Zariwala HA; Gu H; Ng LL; Palmiter RD; Hawrylycz MJ; Jones AR; Lein ES; Zeng H, (2010). A robust and high-throughput Cre reporting and characterization system for the whole mouse brain. Nat Neurosci 13(1):133-40

120. Maras PM, Petrulis A., (2008). The posteromedial cortical amygdala regulates copulatory behavior, but not sexual odor preference, in the male Syrian hamster (Mesocricetus auratus). Neuroscience. 2008 Oct 15;156(3):425-35. doi: 10.1016/j.neuroscience.2008.08.004.

121. Marler, P (1961). The logical analysis of animal communication. J. Theoret. Bioi. 1 :295 - 3 1 7

122. Mathis, A., Mamidanna, P., Cury, K.M., Abe, Murthy, Mathis, MW, Bethge, (2018). DeepLabCut: markerless pose estimation of user-defined body parts with deep learning. *Nat Neurosci* **21**, 1281–1289 (2018). https://doi.org/10.1038/s41593-018-0209-y

123. McCarthy MM, (1994). Molecular aspects of sexual differentiation of the rodent brain. Psychoneuroendocrinology. 1994;19(5-7):415-27. doi: 10.1016/0306-4530(94)90029-9. PMID: 7938343.

124. McCarthy, Nugent BM and Lenz KM (2017) Neuroimmunology and neuroepigenetics in the establishment of sex differences in the brain. Nature Neuroscience Reviews 18: 471-484. PMID:28638119

125. Melis, M.R., Succu, S., Sanna, F., Boi, A. and Argiolas, A. (2009), Oxytocin injected into the ventral subiculum or the posteromedial cortical nucleus of the amygdala induces penile erection and increases extracellular dopamine levels in the nucleus accumbens of male rats. European Journal of Neuroscience, 30: 1349-1357. https://doi.org/10.1111/j.1460-9568.2009.06912.x

126. Menegas, W., Bergan, J. F., Ogawa, S. K., Isogai, Y., Umadevi Venkataraju, et al., (2015). Dopamine neurons projecting to the posterior striatum form an anatomically distinct subclass. eLife, 4, e10032. http://doi.org/10.7554/eLife.10032

127. Meredith and Westberry, (2004). Distinctive Responses in the Medial Amygdala to Same-Species and Different-Species Pheromones. Journal of Neuroscience, 24 (25) 5719-5725

128. Meredith, M., & Fernandez-Fewell, G. (1994). Vomeronasal system, LHRH, and sex behaviour. In Psychoneuroendocrinology (Vol. 19, Issues 5–7, pp. 657–672). Elsevier BV. https://doi.org/10.1016/0306-4530(94)90048-5

129. Merriam, C. H. (1902). The prairie dog of the Great Plains. [s.n.]. https://doi.org/10.5962/bhl.title.101960

130. Mitoyen C, Quigley C, Fusani L., (2019). Evolution and function of multimodal courtship displays. Ethology. 2019 Aug;125(8):503-515. doi: 10.1111/eth.12882. Epub 2019 May 10.

131. Moltz H, Lubin M, Leon M, Numan M., (1970). Hormonal induction of maternal behavior in the ovariectomized nulliparous rat. Physiology & Behavior. 1970;**5**:1373–7.

132. Mombaerts, P., Wang, F., Dulac, C., Chao, S. K., Nemes, A., Mendelsohn, M., Edmondson, J., & Axel, R. (1996). Visualizing an Olfactory Sensory Map. In Cell (Vol. 87, Issue 4, pp. 675–686). Elsevier BV. https://doi.org/10.1016/s0092-8674(00)81387-2

133. Moncho-Bogani, J, Martinez-Garci, Novejarque, Lanuza, (2005). Attraction to sexual pheromones and associated odorants in female mice involves activation of the reward system and basolateral amygdala. European Journal of Neuroscience, 21(8):2186-98

134. Morris JA, Jordan CL, Breedlove SM, (2008). Sexual dimorphism in neuronal number of the posterodorsal medial amygdala is independent of circulating androgens and regional volume in adult rats. J Comp Neurol. 506(5):851-9.

135. Motta, S.C., Guimarães, C.C., Furigo, I.C., Sukikara, M.H., Baldo, M.V.C., Lonstein, J.S., Canteras, N.S., (2013). Ventral premammillary nucleus as a critical sensory relay to the maternal aggression network. PNAS, 110(35):14438-43

136. Murray, E., Cho, J., Goodwin, D., Ku, T., Swaney, J., et al., (2015). Simple, Scalable Proteomic Imaging for High-Dimensional Profiling of Intact Systems. Cell, 163(6), 1500-1514. doi:10.1016/j.cell.2015.11.025

137. Naftolin F, Ryan KJ, Davies IJ, Reddy VV, Flores F, Petro Z, Kuhn M, White RJ, Takaoka Y, Wolin L. (1975). The formation of estrogens by central neuroendocrine tissues. Recent Prog Horm Res. 31:295-319. doi: 10.1016/b978-0-12-571131-9.50012-8. PMID: 812160.

138. Negron R, Martin A, Almog M, Balbierz A, Howell EA., (2013). Social support during the postpartum period: mothers' views on needs, expectations, and mobilization of support. Matern Child Health J. 2013 May;17(4):616-23. doi: 10.1007/s10995-012-1037-4. PMID: 22581378; PMCID: PMC3518627.

139. Newman, S. W. (1999). The Medial Extended Amygdala in Male Reproductive Behavior A Node in the Mammalian Social Behavior Network. In Annals of the New York Academy of Sciences (Vol. 877, Issue 1 ADVANCING FRO, pp. 242–257). Wiley. https://doi.org/10.1111/j.1749-6632.1999.tb09271.x

140. Nguyen, A. J., Hoyer, E., Rajhans, P., Strathearn, L., & Kim, S. (2019). A tumultuous transition to motherhood: Altered brain and hormonal responses in mothers with postpartum depression. In Journal of Neuroendocrinology (Vol. 31, Issue 9). Wiley. https://doi.org/10.1111/jne.12794

141. Nisbett, R. E. (1972). Hunger, obesity, and the ventromedial hypothalamus. Psychological Review, 79(6), 433–453. Nishizuka M, Arai Y. (1981). Sexual dimorphism in synaptic organization in the amygdala and its dependence on neonatal hormone environment. Brain Res.212(1):31-8.

142. Nishizuka, M., & Arai, Y. (1981). Sexual dimorphism in synaptic organization in the amygdala and its dependence on neonatal hormone environment. In Brain

Research (Vol. 212, Issue 1, pp. 31–38). Elsevier BV. https://doi.org/10.1016/0006-8993(81)90029-9

143. Nodari F, Hsu FF, Fu X, Holekamp TF, Kao LF, Turk J, Holy TE., (2008). Sulfated steroids as natural ligands of mouse pheromone-sensing neurons. J Neurosci. 2008 Jun 18;28(25):6407-18. doi: 10.1523/JNEUROSCI.1425-08.2008. PMID: 18562612; PMCID: PMC2726112.

144. Nomoto, Lima, (2015). Enhanced Male-Evoked Responses in the Ventromedial Hypothalamus of Sexually Receptive Female Mice. Current Biology, 25(5):589-94

145. Numan M, Insel TR., (2011). The Neurobiology of Parental Behavior. Springer; 2011.

146. Numan, (1988). Neural basis of maternal behavior in the rat. Psychoneuroendocrinology, 13(1-2):47-62

147. O'Connell, L and Hofmann, H. (2011). Genes, hormones, and circuits: An integrative approach to study the evolution of social behavior. Frontiers in Neuroendocinology, 32(3):320-35

148. O'Connell and Hofmann, (2012). Evolution of a Vertebrate Social Decision-Making Network. Science 336:1154-1157

149. Okuyama, T., Kitamura, T., Roy, D. S., Itohara, S., & Tonegawa, S. (2016). Ventral CA1 neurons store social memory. Science, 353(6307), 1536–1541.

150. Padilla SL, Qiu J, Soden ME, Sanz E, Nestor CC, Barker FD, Quintana A, Zweifel LS, Rønnekleiv OK, Kelly MJ, Palmiter RD., (2016). Agouti-related peptide neural circuits mediate adaptive behaviors in the starved state. Nat Neurosci. 2016

May;19(5):734-741. doi: 10.1038/nn.4274. Epub 2016 Mar 28. PMID: 27019015; PMCID: PMC4846501.

151. Pan, C, Cai, R, Quacquarelli, FP, Ghasemigharagoz, A, Lourbopoulos, A, et al., (2016). Shrinkage-mediated imaging of entire organs and organisms using uDISCO. Nature Methods 13(10):859-67.

152. Papes F, Logan DW, Stowers L., (2010). The vomeronasal organ mediates interspecies defensive behaviors through detection of protein pheromone homologs. Cell. 2010 May 14;141(4):692-703. doi: 10.1016/j.cell.2010.03.037.

153. Pardo-Bellver C, Cádiz-Moretti B, Novejarque A, Martínez-García F and Lanuza E (2012) Differential efferent projections of the anterior, posteroventral, and posterodorsal subdivisions of the medial amygdala in mice. Front. Neuroanat. 6:33. doi: 10.3389/fnana.2012.00033

154. Parmigiani, S., & vom Saal, F. (Eds.). (1994). Infanticide And Parental Care (1st ed.). Routledge. https://doi.org/10.4324/9781315539133

155. Pearlstein, T., Howard, M., Salisbury, A., & Zlotnick, C. (2009). Postpartum depression. In American Journal of Obstetrics and Gynecology (Vol. 200, Issue 4, pp. 357–364). Elsevier BV. https://doi.org/10.1016/j.ajog.2008.11.033

156. Perez-Gomez, A, Stein, B, Leinders-Zufall, T, Chamero, P, (2014). Signaling mechanisms and behavioral function of the mouse basal vomeronasal neuroepithelium. Frontiers in Neuroanatomy, 8:135

157. Petrovich GD, Canteras NS, Swanson LW., (2001). Combinatorial amygdalar inputs to hippocampal domains and hypothalamic behavior systems. Brain Res Brain Res Rev. 2001 Dec;38(1-2):247-89. doi: 10.1016/s0165-0173(01)00080-7.

158. Pierman S, Sica M, Allieri F, Viglietti-Panzica C, Panzica GC, Bakker J., (2008). Activational effects of estradiol and dihydrotestosterone on social recognition and the arginine-vasopressin immunoreactive system in male mice lacking a functional aromatase gene. Horm Behav. 2008 Jun;54(1):98-106. doi: 10.1016/j.yhbeh.2008.02.001. Epub 2008 Feb 15.

159. Piperno, G., & Fuller, M. T. (1985). Monoclonal antibodies specific for an acetylated form of alpha-tubulin recognize the antigen in cilia and flagella from a variety of organisms. The Journal of cell biology, 101(6), 2085-94.

160. Pomerantz SM, Nunez AA, Bean NJ., (1983). Female behavior is affected by male ultrasonic vocalizations in house mice. Physiol Behav. 1983;31:91–96.

161. Raisman, G. An experimental study of the projection of the amygdala to the accessory olfactory bulb and its relationship to the concept of a dual olfactory system. Exp Brain Res 14, 395–408 (1972). https://doi.org/10.1007/BF00235035

162. Renier, N, Wu, Z, Simon, D, Yang, J, Ariel, P, et al., (2014). iDISCO: A Simple, Rapid Method to Immunolabel Large Tissue Samples for Volume Imaging. Cell, 159(4):896-910.

163. Renier, N., Adams, E. L., Kirst, C., Wu, Z., Azevedo, R., Kohl, J., et al. (2016). Mapping of Brain Activity by Automated Volume Analysis of Immediate Early Genes. Cell, 165(7), 1789–1802. doi:10.1016/j.cell.2016.05.007

164. Root, C., Denny, C., Hen, R., Axel, R., (2014). The participation of cortical amygdala in innate, odour-driven behaviour. Nature 515, 269–273

165. Ross, Leon, Madara, JC, Schafer, Fergani, et al., (2018). PACAP neurons in the ventral premammillary nucleus regulate reproductive function in the female mouse. eLife 2018;7:e35960

166. Rutter, M. (1998) Developmental Catch-Up, and Deficit, Following Adoption after Severe Global Early Privation. Journal of Child Psychology and Psychiatry, 39, 465-476.

167. Samuelson and Meredith (2009). The vomeronasal organ is required for the male mouse medial amygdala response to chemical-communication signals, as assessed by immediate early gene expression. Neuroscience, 164(4):1468-74

168. Sarnoff, I., & Zimbardo, P. G. (1961). Anxiety, fear, and social isolation. The Journal of Abnormal and Social Psychology, 62(2), 356–363.

169. Scalia F, Winans SS (1975) The differential projections of the olfactory bulb and accessory olfactory bulb in mammals. J Comp Neurol 161:31–55. doi:10.1002/cne.901610105 pmid:1133226

170. Schmidt, M.H., Valatx, J.L., Sakai, K., Fort, P., Jouvet, M., (2000). Role of the Lateral Preoptic Area in Sleep-Related Erectile Mechanisms and Sleep Generation in the Rat. JNeurosci, 20(17):6640-7

171. Schnupp and Carr, (2009). On hearing with more than one ear: lessons from evolution. Nature neuroscience, 12(6):692-7

172. Schultze, O. (1897). Über Herstellung and Conservirung durchsichtigen Embryonen zum Stadium der Skeletbildung. In Verhandlungen der Anatomischen Gesellschaft (Anatomischer Anzeiger), pg. 3-5.

173. Schwanzel-Fukuda, Marlene; Pfaff, Donald W. (1991). Migration of LHRH-immunoreactive neurons from the olfactory placode rationalizes olfacto-hormonal relationships. , 39(4), 565–572. doi:10.1016/0960-0760(91)90254-3

174. Schwarz, S.-L. Liang, S.M Thompson and M.M. McCarthy (2008) Estradiol induces hypothalamic dendritic spines by enhancing glutamate release: A mechanism for organizational sex differences. Neuron, 58: 584-598. PMCID: PMC2570057

175. Scoville, W. B. & Milner, B., (1957). Loss of recent memory after bilateral hippocampal lesions. J. Neurol. Neurosurg. Psychiatry 20, 11–21 (1957).

176. Shamonin, DP, Bron, Lelieveldt, Smits, Klein and Staring, (2014). Fast Parallel Image Registration on CPU and GPU for Diagnostic Classification of Alzheimer's Disease. Frontiers in Neuroinformatics, 7(50):1-15

177. Sosulski, D., Bloom, M., Cutforth, T., Axel, R., Datta, S.R., (2011). Distinct representations of olfactory information in different cortical centres. Nature 472, 213–216

178. Spreng, R. N. (2013). Examining the role of memory in social cognition. In Frontiers in Psychology (Vol. 4). Frontiers Media SA. https://doi.org/10.3389/fpsyg.2013.00437

179. St-Cyr, S., Abuaish, S., Spinieli, R. L., & McGowan, P. O. (2018). Maternal Predator Odor Exposure in Mice Programs Adult Offspring Social Behavior and Increases Stress-Induced Behaviors in Semi-Naturalistic and Commonly-Used Laboratory Tasks. In Frontiers in Behavioral Neuroscience (Vol. 12). Frontiers Media SA. https://doi.org/10.3389/fnbeh.2018.00136

180. Steinke, H and Wolff, W (2001). A modified Spalteholz technique with preservation of the histology. Annals of Anatomy, 183:91-95.

181. Stettler, D, Axel, R, (2009). Representations of Odor in the Piriform Cortex. Neuron, 63(6):854-64

182. Stowers, L., Holy, T. E., Meister, M., Dulac, C., & Koentges, G. (2002). Loss of Sex Discrimination and Male-Male Aggression in Mice Deficient for TRP2. In Science (Vol. 295, Issue 5559, pp. 1493–1500). American Association for the Advancement of Science (AAAS). https://doi.org/10.1126/science.1069259

183. Strasser S, Dixon AK., (1986). Effects of visual and acoustic deprivation on agonistic behaviour of the albino mouse (M. musculus L.) Physiol Behav. 1986;36:773–778.

184. Susaki, E.A., Shimizu, C., Kuno, A. et al., (2020). Versatile whole-organ/body staining and imaging based on electrolyte-gel properties of biological tissues. Nat Commun 11, 1982 (2020). https://doi.org/10.1038/s41467-020-15906-5

185. Susaki, EA, Tainaka, K, Perrin, D, Kishino, F, Tawara, T, et al., (2014). Whole-Brain Imaging with Single-Cell Resolution Using Chemical Cocktails and Computational Analysis. Cell, 157(3): 726–739.

186. Susaki, EA, Tainaka, K, Perrin, D, Yukinaga, H, Kuno, A, et al., (2015). Advanced CUBIC protocols for whole-brain and whole-body clearing and imaging. Nature Protocols, 10(11): 1709-27.

187. Tainaka, K, Murakami, T, Susaki, E, Shimizu, C, Saito, C, et al., (2018). Chemical Landscape for Tissue Clearing Based on Hydrophilic Reagents. Cell Reports, 24(8):2196-2210.

188. Tanisumi, Y., Shiotani, K., Hirokawa, J., Sakurai, Y., & Manabe, H. (2021). Bi-directional encoding of context-based odors and behavioral states by the nucleus of the lateral olfactory tract. In iScience (Vol. 24, Issue 4, p. 102381). Elsevier BV. https://doi.org/10.1016/j.isci.2021.102381

189. Thor, DH and Holloway, WR, (1982). Social Memory in the Male Laboratory Rat. Journal of Comparative and Physiological Psychology, 96(9): 1000-1006

190. Tinbergen, N. (1951). The study of instinct. Clarendon Press/Oxford University Press.

191. Tinbergen, N. (1963). On aims and methods of Ethology. In Zeitschrift für Tierpsychologie (Vol. 20, Issue 4, pp. 410–433). Wiley. https://doi.org/10.1111/j.1439-0310.1963.tb01161.x

192. Ueda, HR, Dodt, HU, Osten, P, Economo, MN, Chandrashekar, J, Keller, P.J., (2020). Whole-Brain Profiling of Cells and Circuits in Mammals by Tissue Clearing and Light-Sheet Microscopy. Neuron, 106(3):369-87

193. Unger, E. K., Burke, K. J., Jr, Yang, C. F., Bender, K. J., Fuller, P. M., & Shah, N. M. (2015). Medial amygdalar aromatase neurons regulate aggression in both sexes. Cell reports, 10(4), 453–462.

194. Vaz, R.P., Cardoso, A., Sá, S.I., Pereira, P.A., Madeira, M.D., (2017). The integrity of the nucleus of the lateral olfactory tract is essential for the normal functioning of the olfactory system. Brain Struct Funct 222, 3615–3637

195. Vochteloo, Koolhaas, (1987). Medial amygdala lesions in male rats reduce aggressive behavior: interference with experience. Physiology and Behavior, 41(2):99-102

196. Wagner S, Gresser AL, Torello AT, Dulac C., (2006). A multireceptor genetic approach uncovers an ordered integration of VNO sensory inputs in the accessory olfactory bulb. Neuron. 2006 Jun 1;50(5):697-709. doi: 10.1016/j.neuron.2006.04.033. PMID: 16731509.

197. Walker, David L., Donna J. Toufexis, and Michael Davis. (2003). Role of the bed nucleus of the stria terminalis versus the amygdala in fear, stress, and anxiety. European journal of pharmacology463.1-3: 199-216.

198. Wang L, Chen IZ, Lin D *(*2015*)* Collateral pathways from the ventromedial hypothalamus mediate defensive behaviors. *Neuron* 85*:*1344*–1358.* doi:10.1016/j.neuron.2014.12.025 pmid:25754823

199. Wang Li, Zhang Zhijian, Chen Jiacheng, Manyande Anne, Haddad Rafi, Liu Qing, Xu Fuqiang, (2020a). Cell-Type-Specific Whole-Brain Direct Inputs to the Anterior and Posterior Piriform Cortex. Frontiers in Neural Circuits, 14:4

200. Wang, Li, Chen, Irene Z., Lin, Dayu, (2015). Collateral Pathways from the Ventromedial Hypothalamus Mediate Defensive Behaviors. Neuron, 85(6):1344-1358

201. Wang, Q, et al., (2020b). The Allen Mouse Brain Common Coordinate Framework: A 3D Reference Atlas. Cell, 181(4):936-53.E20

202. Watabe-Uchida M, Zhu L, Ogawa SK, Vamanrao A, Uchida N., (2012). Whole-brain mapping of direct inputs to midbrain dopamine neurons. Neuron. 2012 Jun 7;74(5):858-73. doi: 10.1016/j.neuron.2012.03.017. PMID: 22681690.

203. Wei Y-C, Wang S-R, Jiao Z-L, Zhang W, Lin J-K, Li X-Y, Li S-S, Zhang X, Xu X-H *(*2018*)* Medial preoptic area in mice is capable of mediating sexually dimorphic behaviors regardless of gender. *Nat Commun* 9*:*279.

204. Whitham J, Mathis A., (2000). Effects of hunger and predation risk on foraging behavior of graybelly salamanders, Eurycea multiplicata. J Chem Ecol. 2000;**26**:1659–1665.

205. Wickersham, I. R., Finke, S., Conzelmann, K. K., & Callaway, E. M. (2007). Retrograde neuronal tracing with a deletion-mutant rabies virus. Nature methods, 4(1), 47–49.

206. Winans SS, Scalia F., (1970). Amygdaloid nucleus: new afferent input from the vomeronasal organ. Science. 1970 Oct 16;170(3955):330-2. doi: 10.1126/science.170.3955.330. PMID: 5460037.

207. Wonch, K. E., de Medeiros, C. B., Barrett, J. A., Dudin, A., Cunningham, W. A., Hall, G. B., Steiner, M., & Fleming, A. S. (2016). Postpartum depression and brain response to infants: Differential amygdala response and connectivity. In Social Neuroscience (Vol. 11, Issue 6, pp. 600–617). Informa UK Limited. https://doi.org/10.1080/17470919.2015.1131193

208. Worm, M, Landgraf, T, Prume, J, Nguyen, H, Kirschbaum, F, von der Emde, (2018). Evidence for mutual allocation of social attention through interactive signaling in a mormyrid weakly electric fish. PNAS, 115(26): 6852–6857

209. Wortham J, Miller A., (2017). Social interactions in different environments impacts and motivates reproductive displays in college students. Heliyon. 2017 Jun 22;3(6):e00320. doi: 10.1016/j.heliyon.2017.e00320.

210. Wu Z, Autry AE, Bergan JF, Watabe-Uchida M, Dulac CG (2014). Galanin neurons in the medial preoptic area govern parental behaviour. Nature. 2014 May 15;509(7500):325-30. doi: 10.1038/nature13307. PMID: 24828191; PMCID: PMC4105201.

211. Wu, M, Manoli, D, Fraser, E, Coats, J, Tollkuhn, J., Honda, S.I., Harada, N., Shah, N, (2009). Estrogen Masculinizes Neural Pathways and Sex-Specific Behaviors. Cell, 139(1):61-72.

212. Wysocki, C.J. (1989). Vomeronasal chemoreception: its role in reproductive fitness and physiology. In Neural Control of Reproductive Function (New York: Alan R. Liss), pp. 545-566.

213. Wysocki, C.J., and Lepri, J.J. (1991). Consequences of removing the vomeronasal organ. J. Steroid Biochem. Mol. Biol. 39, 661-669

214. Yang, Chiang, Grag, Unger, Wells, Shah, N.M., (2013). Sexually Dimorphic Neurons in the Ventromedial Hypothalamus Govern Mating in Both Sexes and Aggression in Males. Cell, 153(4):896-909

215. Yang, Y., Wang Jian-Zhi, (2017). From Structure to Behavior in Basolateral Amygdala-Hippocampus Circuits. Frontiers in Neural Circuits, 11:86

216. Yao, S, Bergan, J, Lanjuin, A, Dulac, C, (2017). Oxytocin signaling in the medial amygdala is required for sex discrimination of social cues. eLife 2017;6:e31373.

217. Yu, B., Zhang, Q., Lin, L. et al., (2023). Molecular and cellular evolution of the amygdala across species analyzed by single-nucleus transcriptome profiling. Cell Discov 9, 19. https://doi.org/10.1038/s41421-022-00506-y

218. Yun, DH, Park, Y, Cho, J, Kamentsky, L, Evans, N, et al., (2019). Ultrafast immunostaining of organ-scale tissues for scalable proteomic phenotyping. bioRxiv. doi: https://doi.org/10.1101/660373

219. Zikopoulos, Barbas, (2012). Pathways for Emotions and Attention Converge on the Thalamic Reticular Nucleus in Primates. Journal of neuroscience, 32(15):5338-50